Development of POLARBEAR-2 receiver system for cosmic microwave background polarization experiment

Yuki Inoue

Doctor of Philosophy

Department of Particle and Nuclear Physics
School of High Energy Accelerator Science
SOKENDAI (The Graduate University for Advanced Studies)

Development of POLARBEAR-2 receiver system for cosmic microwave background polarization experiment

Yuki Inoue

Graduate University
for
Advanced Studies

Spring 2016

Abstract

POLARBEAR-2 is a cosmic microwave background (CMB) polarization experiment that will be located in the Atacama highland in Chile at an altitude of 5200 m. Its main science goal is to measure the CMB B-mode polarization signal which is originating from primordial gravitational waves and weak lensing. The POLARBEAR-2 experiment is designed to measure the tensor to scalar ratio, r, with precision $\sigma(r) < 0.01$, and the sum of neutrino masses, Σm_ν, with $\sigma(\Sigma m_\nu) < 100$ meV. To achieve these goals, POLARBEAR-2 will employ 7588 transition-edge sensor bolometers at 95 GHz and 150 GHz, which is cooled at 250 mK. In this thesis, I describe the thermal and optical design, development and characterization of the POLARBEAR-2 system. The POLARBEAR-2 receiver system consists of the detector section and cold optical section. The detector and the readout system are placed into the detector section. The cold optical elements, such as lenses, infrared (IR) filters, cold aperture, and a vacuum window, are mounted on the cold optical section. The cryogenic system employs the combination of two pulse tube coolers and a sorption cooler. To reduce the thermal noise from the optical elements, these are cooled at each thermal stage.

POLARBEAR-2 has a larger focal plane than any other CMB experiment so far deployed. The large focal plane causes the large aberration. The large focal plane also receives a large thermal load of IR radiation from the window.

We developed the optical system to solve these problems. We constructed the optical system with high index of reflection material to reduce the aberration due to the large diameter. We used and characterized alumina as the new candidate material for the optical system. Since alumina is high-reflectance material, we need anti-reflection (AR) coating. We newly developed two-layer AR coating with thermally-sprayed mullite and expanded polyimide (Skybond Foam) for use at the 50 K stage where the maximum diameter of 530 mm is required.

For reducing the thermal loading from the 50 K IR filter, we also used alumina as the material for the IR filter. The temperature of the conventional absorptive filters rises when a window with a large diameter is used because of its lower thermal conductivity. On the other hand, the thermal conductivity of alumina is three orders of magnitude as large as those of the conventional filters. We have confirmed with measurements that the transmittance, the 3 db cutoff (700 GHz) and temperature rise (2.3 ± 0.1 K) all satisfy our requirements at cold stage. In particular, the temperature rise is reduced to only 2.3 K, which is 50 times as low as the case with conventional filters.

We also invented the new millimeter-wave absorber, which we call "KEK Black", to reduce the stray light from the window. The performance of the KEK Black is better than conventional absorbers. In particular, we achieved much lower reflectance than before, which is important to reduce effects of stray lights and loading.

We installed the optical elements mentioned above into the receiver system and characterize the large cold optics with prototype of dual-color TES bolometers on the focal plane. We have confirmed that all the detectors realize the diffraction limited optics based on the optical simulation and the measured values. All the results of the optical characterization meet our requirements. The thermal loadings at each stage based on the measured temperature are less than the cooling power of the cryogenic system. We have achieved the hold time of 38 hours and the detectors are cooled at 270 mK. The estimated noise equivalent temperature is $3.39\mu\mathrm{K}\sqrt{\mathrm{sec}}$, which is sufficient for us to achieve our science goals mentioned above.

We prepare an end-to-end system for the characterization of beam and sensitivity. All the optical components are mounted. Prototype dual-color TES bolometers are placed on the focal plane. We have successfully observed signals from a 77 K load. The cross section of the beam at the front of the window is measured with the knife edge method. The results are consistent with the simulation within 1 σ. The optical efficiency and power at each band are also measured. The measured powers meet the expected values.

As the validation of optical design and alignment of the optical elements, we also measured the beam map at the window, and optical efficiency defined as the measured power divided by the input power to the receiver system. We confirmed they reasonably agreed with the simulation and calculation.

We conclude that we have established the technologies to realize the optical system with a large focal plane for the next generation CMB polarization experiment, POLARBEAR-2.

Acknowledgments

この博士論文は沢山の人に支えられて執筆する事ができました。ここでは敢えて母国語である日本語で感謝を述べたいと思っています。

私は 5 年間指導教官である羽澄教授の元で POLARBEAR-2 実験に参加させて頂きとても感謝しています。この 5 年間は宇宙マイクロ波背景放射 (CMB) にとっても日本の CMB にとっても非常に重要な 5 年間になりました。私が初めて羽澄教授と出会ったのは学部の 3 年生のサマーチャレンジに参加した時です。当時は CMB について何も知らなかったのですが、勉強をしていく間に CMB の研究を行いたいと強く思う様になりました。蓋を開けてみるとその通りになりましたが、5 年間の研究の間にきっと CMB は面白い時代になると考え、迷う事無くこの研究分野を選びました。今考えると、サマーチャレンジの時に羽澄教授と出会わなかったら、今の自分は無かっただろうと思います。また、羽澄教授はどんな小さなアイデアの種でも相談にのって頂き、新技術の実現の為の可能性に投資をして頂きました。実学の中で学んだものは非常に大きく、世界一級の教育をして頂きました。その結果を博士論文としてまとめる事ができました。本当にありがとうございました。

私は長谷川助教にとても感謝しております。長谷川助教は昼夜休日問わず研究の相談にのって頂きました。人の入れ替わりで実験室が 2 人だけになったときは本当にどうなる事かと思いました。今、改めてこの博士論文を客観的に眺めると、あの時にギリギリの中で長谷川助教と議論しながら試行錯誤して生まれた技術やアイデアの種が随所に散りばめられています。精神面でも、研究面でも長谷川助教に鍛えて頂いた 1 つ 1 つがこの博士論文につながりました。本当にありがとうございました。

陰に陽に 5 年間支えて下さった都丸准教授には感謝してもしくせない思いでいっぱいです。都丸准教授は研究に行き詰まった時、アイデアが浮かんだとき、一番に相談にのって頂き適切なアドバイスをして頂きました。特に修士の頃に都丸准教授に鍛えて頂いた低温物理や物性はこの博士論文ではなくてはならない技術です。この 5 年間で、1 番と言っても過言ではないくらい楽しかったのは都丸准教授と「こういうのはどうですかねぇ」と、今の物理の 2 歩先をあれこれ議論している時です。時には「残念、実は 10 年前に特許を持ってるんだよね」と言われる事もありました。そういった議論の積み重ねが博士論文につながったと確信しています。本当にありがとうございました。

入学後間もない頃に研究の右も左もわからない私を厳しく指導していただいた松村氏には大変感謝しています。ログノートによると入学して間もない 4 月 26 日に「飯を抜いた日数だけ Ph.D. が近くなるよ」と言われた事は実際に博士論文を執筆している今でも鮮明に覚えています。実際の所は飯を抜いたわけではありませんが、その様な決意で実験を行った経験は今でも自分の中に生きています。アルミナ光学系という既存の技術の延長ではなし得ない、世界の最先端の技術を試行錯誤しながら確立していった毎日があっ

てこそ、この博士論文を書く事ができたとおもいます。本当にありがとうございました。

良き相談相手であり、ライバルでもあった鈴木有春氏には感謝しても仕切れません。アルミナ光学系の持つ問題点や課題、そして可能性を誰よりも良く理解していていたのは他の誰でもなく鈴木氏だと思っています。何年にも渡る鈴木氏との議論のおかげで、本当の意味の実力を鍛えて頂きました。博士論文を執筆するにあたって、鈴木氏との議論の中で実現し得た技術がいたる所にあります。鈴木氏無しには今の自分はいないと思います。大変ありがとうございました。

Adrian 氏には研究面で大変お世話になりました。特にミーティングの中で何時でも新しいアイデアを持ってくる姿にはとても尊敬しています。特にアルミナフィルターの開発やレンズの開発で沢山の意見を頂きました。Adrian 氏の助力がなければ博士論文は完成できませんでした。大変ありがとうございました。

バークレーの堀氏には大変お世話になりました。KEK に滞在されていた時は毎日深夜まで議論につきあって頂きました。年代が近くて議論の行える人が少なかったので、毎日の議論がとても刺激的で楽しかったです。また、アルミナレンズの測定や AR コーティングでも大変お世話になりました。また、最後の検出器の準備の際にも LC レゾナンスフィルターの開発に協力して頂きました。また、日本にもどられて議論ができる時をおまちしております。

IPMU の服部氏は、学部の時からのつながりでお世話になりました。バークレーに行ってからの服部氏が活躍を、自分も頑張らないとと行けないなと鼓舞しながら見ていました。博士論文では特に最後の Wafer を用いた試験でお世話になりました。また、進路についても相談にのって頂きました。大変ありがとうございました。

良き先輩であり、時に厳しく、時に優しく相談に乗って下さった茅根氏には大変感謝しています。バークレーに滞在しながらもテレビ電話で研究の相談にのって頂き、様々なアドバイスを頂きました。特に修士の頃は茅根氏からお預かりした書物を片っ端から読んで、早く茅根氏に追いつきたいと言う思いで研究を行っていました。茅根氏に物理を教えて貰う為にテレビ電話でアメリカとつなぎながらゼミを行った事は今でも忘れません。あの時の経験があったからこそ博士論文の 2 章の執筆できました。本当にありがとうございました。

関係者以外で初めてアルミナフィルターの重要性を認識していただいたのが修士 2 年生当時の日下氏でした。当時は ABS 実験におられましたが、今では POLARBEAR のメンバーとしてご指導して頂いております。特に光学シミュレーションやアルミナフィルターの議論では大変お世話になりました。大変感謝しております。

鈴木先任技師は装置開発や設計、評価について相談にのって頂きました。装置の事がわからない中、色々なアドバイスを頂きました。また、強度シミュレーションや引っぱり強度試験等を見て頂きました。鈴木先任技師がいなければ、ミラーも受信器システムも実現し得なかったと思います。大変ありがとうございます。

Fred 氏は特にシミュレーションの議論や光学系の相談にのって頂きました。特にラボテストの準備について大変お世話になりました。

秋葉氏は最初の後輩として学部の 4 年生の頃から一緒に研究を行いました。非常に理解力が良く、私と相補的な研究を行っている為沢山の事を学ばせて頂きました。特に最後の読み出し試験では、デバッグやオペレーションの相談にのって頂きました。この博士論文は秋葉氏の協力無しでは完成できませんでした。

瀬川氏は 300K と 50K ステージの間の熱設計を共同研究しました。真空窓の開発は POLARBEAR-2 および博士論文にとっては無くてはならない技術であり、それらの技術が現在の研究に活かされている様で素晴らしい事だと思います。非常に重要な研究なので以後も主導的に頑張って下さい。

高取氏とはレンズのトレランス解析で共同研究を行いました。高取氏は 1 年生ながらトレランス解析に取り組み、今後の活躍が期待されるホープです。重要性の高い仕事がまかされる分、責任も重くなりますが、あきらめずにやり遂げるときっと花開くと思います。びっしり書いたログノートはいつも感心させられます。勉強熱心なのは高取氏の武器なので、周りの人から沢山の事を学んで、それをさらに議論としてぶつけて行ってください。ますますグループで活躍を期待しています。

濱田氏はビームマッパーの開発で共同研究を行いました。濱田氏は一人でとことん考えて問題を解決していく事ができる CMB の若手のエースです。特にギアの振動問題や、ステージの安定性など問題点にぶつかった時に、問題を切り分けて解決まで持っていけるのは素晴らしい事です。また、ゼミの際の予習もしっかり頑張っていました。これからは検出器が統合されていく中で、壮大なデバッグ作業が始まります。そういった中で、濱田君の考察力はますます光るのではと思います。

岡村准教授には低温試験やヘリウムのトランスファー方法について教えて頂きました。冷凍機の扱い方や温度計、低温物性試験について教えて頂きました。これらの試験はアルミナフィルターのプロトタイプ開発には無くてはならない試験でした。大変感謝いたします。

田島准教授には特にチリでのミラー試験や永久凍土の掘り起こしでお世話になりました。また、CAMB の使い方やプログラミングについても教えて頂きました。大変感謝しています。

いつもアイデアの相談に乗って下さる高田助教には大変感謝いたします。光源と黒体の研究はまだ発展途上ですが、引き続きご教授ください。よろしくおねがいします。

西野特認助教はチリでのオペレーションや偏光試験についての相談にのって頂きました。また、Systematic error の原因についても議論を行い、博士論文でもそれらの議論を元にした試験を行う事ができました。大変感謝しております。

高倉氏と初めて出会ったのは 2005 年なのでかれこれ 10 年になります。あの頃は高校の力学で風船の膨張モデルを考えて宇宙年齢が 90 億年くらいになると言う問題を考えていましたが、本当に宇宙の研究を一緒にやる事になるとは驚きでした。高倉君はチリでのデータを触る時や HWP の設置試験の時に研究を行いました。また、チリでは塩湖までドライブしたり、チリのキッチンでうどんを作ったりと色々行いました。

修士 1 年の頃に宇宙論ゼミを毎週見て頂いた永田氏には大変感謝いたします。お忙しい中でご指導して頂いたおかげで、CMB の物理の理解を深める事ができました。

鈴木敏一教授は低温技術の相談をはじめ、進路や TES と KAGRA を用いた Hidden photon の探索の相談にものって頂きました。大変感謝いたします。Bill 氏には F2F meeting の際に黒体に関するコメントを頂きました。Mike 氏には Zotefoam window の開発や熱設計で相談にのって頂きました。Kam 氏にはミーティングを通じて様々なコメントを頂きました。特に AR coating の開発では親身にメールを送って頂きました。Ziggy 氏には PB-1 についての情報を教えて頂き、スタック型のフィルター設計についてのアドバイスを頂きました。Oliver 氏とは AR coating の開発で議論を行いました。Charlie 氏はサファイアの測定を通じて議論を交わしました。大変感謝します。高山氏にはセラミックの物性や応用について教えて頂き

ました。金子氏には天文台の測定でお世話になりました。IST 株式会社の源様、坂田様、平井様にはスカイボンドフォームの作成加工で大変お世話になりました。IST 様のご尽力が無ければこの博士論文を初めとする反射防止膜技術の開発はなし得ませんでした。今後とも宜しくお願いいたします。トーカロ株式会社の小野様、西迫様、神野様には溶射についての R&D で大変お世話になりました。石徹白氏には Hidden photon 探索の相談にのって頂き、色々な計算の仕方を教えて頂きました。また、修士の頃はご飯に連れて行って頂いて色々議論にものってもらいました。大変ありがとうございました。筑波大学の永井氏にはアルミナレンズの焦点測定の際にご相談にのって頂きました。また、修士の頃はご飯にも連れて行って頂きました。森井氏にはバークレーで FTS 試験を見て頂きました。日本に戻られてからも、沢山の相談にのって頂きました。大阪府立大学の木村氏にはホーンの計算や、レンズの焦点測定のご相談にのって頂きました。山口氏にはメタルメッシュフィルターの議論でお世話になりました。CERN の灰野副研究員にはセミナーに御招待して頂いたり、色々な面でご相談させて頂きました。村上氏、豊田氏、五十嵐氏には加工や実験の準備等で大変お世話になりました。IPMU の片山教授は進路の相談やすばると POLARBEAR を用いた重力レンズ効果の探索の相談にのって頂きました。大変感謝しております。萩原氏、小原氏、平澤氏には CAD の作成、修正、図面化で大変お世話になりました。小林氏、工藤氏、東氏には機械加工で大変お世話になりました。渡辺氏、清水氏には修士の頃から学生生活面でお世話になりました。作田教授、石野准教授、小倉氏、三澤氏には CMB の研究を選ぶにあたって、大変お世話になりました。高富氏、牛谷氏には大型ミラーの開発で大変お世話になりました。国立天文台の松尾准教授、新田氏、関本准教授、関口氏、唐津氏、関根氏には FTS の測定の際に大変お世話になりました。理化学研究所の美馬氏は学部の 3 年生の頃からお世話になり、相談にも乗って頂きました。本当にありがとうございます。服部誠准教授には東北大学での滞在の間に FTS やホーンについて教えて頂きました。また、ビームマッパーの開発にむけて相談にのって頂きました。大変ありがとうございます。石塚氏は同級生として時に議論したり、ゼミを行ったりしました。時々、中々近い年代がいない中、飲みにいって研究の話や、物理の話、世間の話をする事がとても楽しかったです。GroundBIRD の Jihoon 氏には光学系の測定についての議論とホーンの設計についての議論をさせて頂きました。小栗氏には TES の応用の議論や研究生活面で大変お世話になりました。長崎氏、富田氏には議論につきあって頂き、RT-MLI などの導入で相談させて頂きました。大変感謝いたします。

Contents

Chapter 1

Introduction

Recent observations have proven the standard model of cosmology, called the"ΛCDM model" of the universe [1, 2, 3]. However, there are yet unresolved problems, such as "flatness problem", "horizon problem" ,"relic problem", and "origin of perturbation" that the current standard theory of the universe cannot explain. The inflation theory is one of the most powerful theories to solve these problems. It assumes rapid expansion of the early universe [4, 5, 6]. However, "gravitational waves", which are the direct evidence for inflation have not been observed [7]. The dark sector in the universe is another mystery. The observation of the large scale structure, which rised from the fluctuation of energy density with dark matter, is one of the powerful methods to shed light on this problem [8]. It allows us to reach the precision for the sum of neutrino masses and the dark energy. However, we are not able to observe the large scale structure of dark mater directly. We estimate it using other information such as the galaxy distribution, the cosmic infrared background [9], or gravitational lensing [10, 11]. Accurate measurements with these probes are useful to resolve the problems of cosmology [12].

The cosmic microwave background (CMB) has immensely improved our understanding of the early universe [13]. The odd parity of CMB polarization pattern, called the B-mode is a promising tool to measure the inflationary gravitational waves and gravitational lensing effects [14]. The B-mode pattern of the inflationary gravitational waves is accessible on large angular scales, while gravitational lensing can be examined on small scales. Here the large scale typically means ~ 2 degrees or even larger, and the small scale corresponds to ~ 0.1 degrees. Theoretical and astronomical uncertainties of the measurements with the CMB B-mode are much smaller than the other methods mentioned above.

The intensity of the inflationary gravitational waves is measured as the tensor to scalar ratio, r. The observational upper limit of the tensor to scalar ratio is $r < 0.07$ (95 %C.L.) according to the joint analysis of data from BICEP2, the Keck array and the Planck satellite [15]. The next-generation experiments are required to probe at the level of $r \sim 0.01$.

The POLARBEAR-2 (PB-2) is one of such CMB polarization experiments [16]. The PB-2 receiver system will be mounted on one of Simons array telescopes in the Atacama desert in Chile at the altitude of 5200 m. We plan to start science observations in 2017. The PB-2 is designed to measure the tensor

to scalar ratio, r, with precision $\sigma(r) < 0.01$, and the sum of neutrino masses, Σm_ν, with $\sigma(\Sigma m_\nu) <$ 100 meV. Here $\sigma(r)$ and $\sigma(\Sigma m_\nu)$ are the uncertainties of the measurements. When combined with galaxy survey data, $\sigma(\Sigma m_\nu) < 40$ meV is expected. To achieve these science goals, the PB-2 receiver system has the following features:

- It has 7588 transition edge sensor (TES) bolometers at the 250 mK stage in order to achieve high sensitivity;
- Each detector pixel measures 150 and 95 GHz bands simultaneously to reduce the foreground, such as dust and synchrotron emissions;
- It has the optical system with the diffraction limited optics.

To realize these features, we have developed four key technologies.

(i) Development and characterization of the cold alumina optics We used alumina as the material for lenses. We have characterized and developed the large-diameter alumina optics to match a large area of the detector array [17]. To reduce the aberration to all the detectors, large and thin lenses are essential. We measured the material property of the alumina at low temperatures. We made alumina lenses and installed them in the cryogenic receiver system. We have confirmed that the measured temperatures and optical properties of the lenses meet our requirements.

(ii) Development of alumina infrared filter We newly developed a high-thermal-conductivity infrared (IR) filter using alumina [18]. We estimated the 3 dB cutoff frequency using Fourier transform spectroscopy. The 3 dB cutoff frequency is 650 GHz. The cut-off shape is steeper than that of conventional filters. The high thermal conductivity of an alumina minimizes thermal gradients. The temperature rise of the alumina filter is only 3 % of the conventional filter. In fact, after we published our results, other projects including SPT3G and BICEP3 followed to employ this technology. Hence we achieved to establish the new world-standard in the CMB community.

(iiI) Two-layer anti-reflection coating We established a new two-layer anti-reflection (AR) coating method with thermally-sprayed mullite and expanded polyimide (called Skybond Foam developed by IST corporation). We applied this technique to an alumina filter with a diameter of 450 mm and a thickness of 2 mm. The transmittance for this filter is larger than 95 %, which is sufficiently high. Two-layer AR coating on thin and large alumina is one of the most important technologies in the next-generation CMB experiments. Our technology is thus a breakthrough to make the cold optics with a large diameter.

(iv) Development of the blackbody absorber In order to reduce the instrumental polarization and stray light at the inner metal shell, we placed the millimeter absorber on the 4 K shell. The absorber is required to be kept in the low temperature, with low reflectance and high absorption. We invented the new absorber of the millimeter wavelength. The result of characterization with the absorber meets

our requirements.

We established these technologies and applied them to the PB-2 optical system. For the validation of the system, we first characterized the alignment of the lenses. The mismatch of the alignment may generate the aberration of the optics. The large aberration optics breaks the diffraction limit, which will lead to worse sensitivity for the small-scale fluctuation of the B-mode. From the alignment test, all the lenses meet the diffraction limit optics.

We simulated mainlobe and sidelobe patterns with GRASP [19], assuming the diffraction limited optics. To reduce the sidelobe amplitude level, we design and optimize the Lyot stop. These results meet our requirements

We then placed all the optical elements in the PB-2 receiver system. We measured the temperature of each element. The sensitivity of the PB-2 experiment is calculated based on the measured temperature and optical properties of each element. The estimated sensitivity meets our requirement. Finally, we validated the optical system with the prototype dual-color TES bolometers. All the optical components are placed on each thermal stage. We detect the signals from a load at the liquid nitrogen temperature. First, we measure the beam profile. The cross section of the beam is characterized with the knife edge method. The results meet the simulation within 1 σ. Second, we measure the polarization efficiency with two orthogonal-axis detectors using the rotating polarizer. The measured polarization signals agree with our polarization model. The optical efficiency and power at 95 and 150 GHz band are also measured. The measured powers agree with the expected values.

This thesis is organized in the following way. In Chap. 2, we explain the science overview and science requirements for B-mode measurements. In Chap. 3, we give an instrumental overview and system requirements of the POLARBEAR-2 experiment. In Chap. 4, we introduce the key technologies and explain the design, fabrication, and characterizations of new technologies. In Chap. 5, we simulate the beam width of detection bands by changing the Strehl ratio using GRASP simulation. In Chap. 6, we explain the alignment of alumina lenses and show that we achieve the diffraction-limited optics. In Chap. 7, we estimate the PB-2 sensitivity using the beam, temperature and detector information. In Chap. 8, we describe our optics tube and its validation. Discussion and conclusion are given in Chap. 9 and 10.

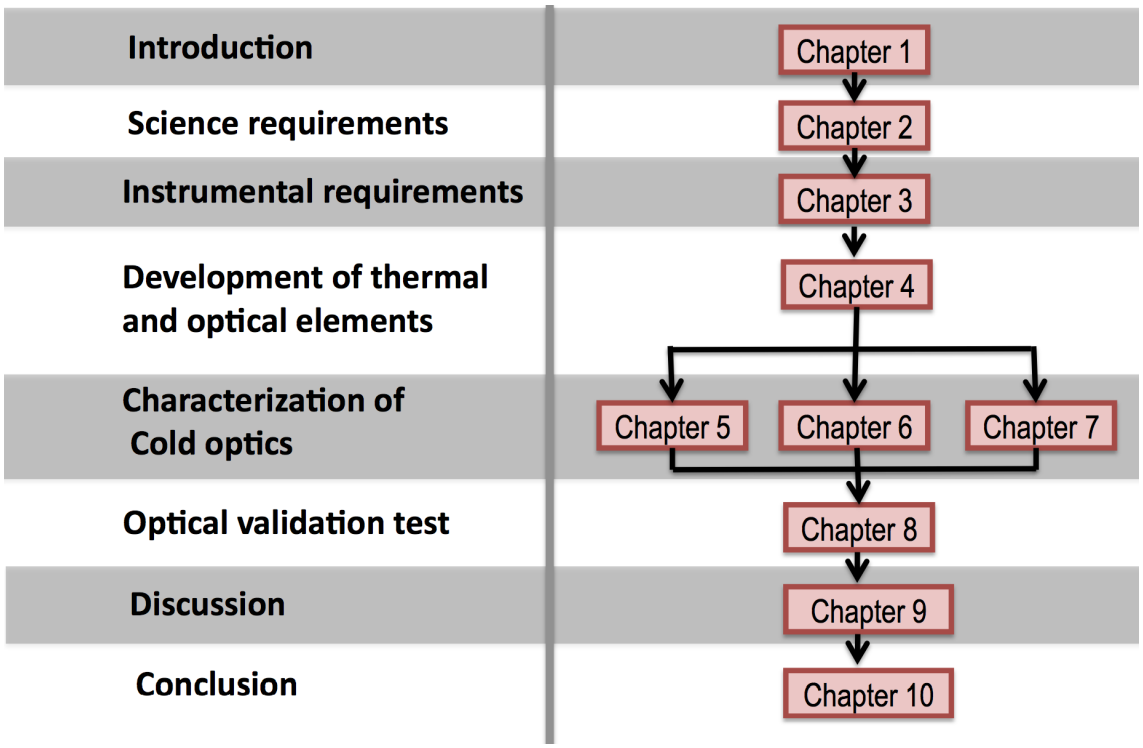

Figure 1.1: Chart diagram of this thesis.

Chapter 2

CMB science

The cosmic microwave background (CMB) has been enormously contributing to modern cosmology. Observations of the CMB have established the standard cosmological model, in which the scale-invariant adiabatic Gaussian fluctuations are responsible for the large-scale structure formation. [20] It has been supported not only by the CMB data, but also with large-scale structure data [21] and type Ia supernovae data [22][23][2].

In this chapter, we discuss CMB science and expected precisions of B-mode observations.

2.1 Friedmann-Robertson-Walker (FRW) universe

Modern cosmology is based on the hypothesis of homogeneous and isotropic universe on a large scale, which is called the 'cosmological principle'. Based on this principle, the Friedmann-Robertson-Walker (FRW) metric is given as

$$ds^2 = g_{\mu\nu}dx^\mu dx^\nu = dt^2 - a^2(t)\left[\frac{dr^2}{1-Kr^2} + r^2 d\theta^2 + r^2\sin^2\theta d\phi^2\right], \tag{2.1}$$

where $a(t)$ is the scale factor of the universe, K is the curvature of the universe [24]. The equation of motion for the FRW universe is given by the Einstein equation:

$$G_{\mu\nu} + \Lambda g_{\mu\nu} = 8\pi G T_{\mu\nu}. \tag{2.2}$$

The energy-momentum tensor with the symmetry of space-time is given by

$$T_{\mu\nu} = \begin{bmatrix} -\rho & 0 & 0 & 0 \\ 0 & P & 0 & 0 \\ 0 & 0 & P & 0 \\ 0 & 0 & 0 & P \end{bmatrix}, \tag{2.3}$$

where ρ and P are the energy and pressure of perfect fluid, respectively. In the FRW universe, the Einstein equation is reduced to the following Friedmann equations,

$$\left(\frac{\dot{a}}{a}\right)^2 = \frac{8\pi G}{3}\rho + \frac{\Lambda}{3} - \frac{K}{a^2}, \tag{2.4}$$

$$2\frac{\ddot{a}}{a} + \frac{\dot{a}^2}{a^2} = -8\pi G P + \Lambda - \frac{K}{a^2}. \tag{2.5}$$

We also find the conservation equation, $T^{\mu\nu}_{;\mu} = 0$, as

$$\dot{\rho} = -3(\rho + P)\left(\frac{\dot{a}}{a}\right). \tag{2.6}$$

The solution of Eq. (2.6) is written as

$$\rho = \rho_0 (a_0/a)^{3(1+w)}, \tag{2.7}$$

where ρ_0 and a_0 denote the current values of the energy density and scale factor, respectively. Here we use the equation of state $w \equiv P/\rho =$ constant. We hereafter use a widely-adopted normalization of $a_0 = 1$. We define the cosmological parameters for the relative energy densities as

$$\Omega_i = \frac{\rho_i}{\rho_{\rm cr}}, \tag{2.8}$$

where $\rho_{\rm cr}$ is the critical density. The quantities $\Omega_i h^2$ are proportional to the density of the species i in the universe today. We define the total density as $\Omega_{\rm tot} = \Sigma\Omega_i$. Here, the subscript, i, denotes species in the universe as listed in Table 2.1.

Table 2.1: The value of w and scale factor dependence of the energy density for different species.

	w	ρ
Radiation (CMB, neutrinos)	$\frac{1}{3}$	a^{-4}
Matter	0	a^{-3}
Cosmological constant	-1	const

2.2 Cosmic microwave background (CMB)

The existence of CMB is one of the most important predictions of the big bang theory. The CMB photons were emitted from the last scattering surface of the plasma made of electrons, protons and photons. The CMB photons were scattered by electrons and photons at $z \sim 1100$. It provides important pieces of information of the universe at the age of 380,000 years. The scattered photons have traveled freely through the universe. The most important fact about the thermal history of the early universe is that the collisions with electrons before the last scattering ensured that the photons were in equilibrium. The

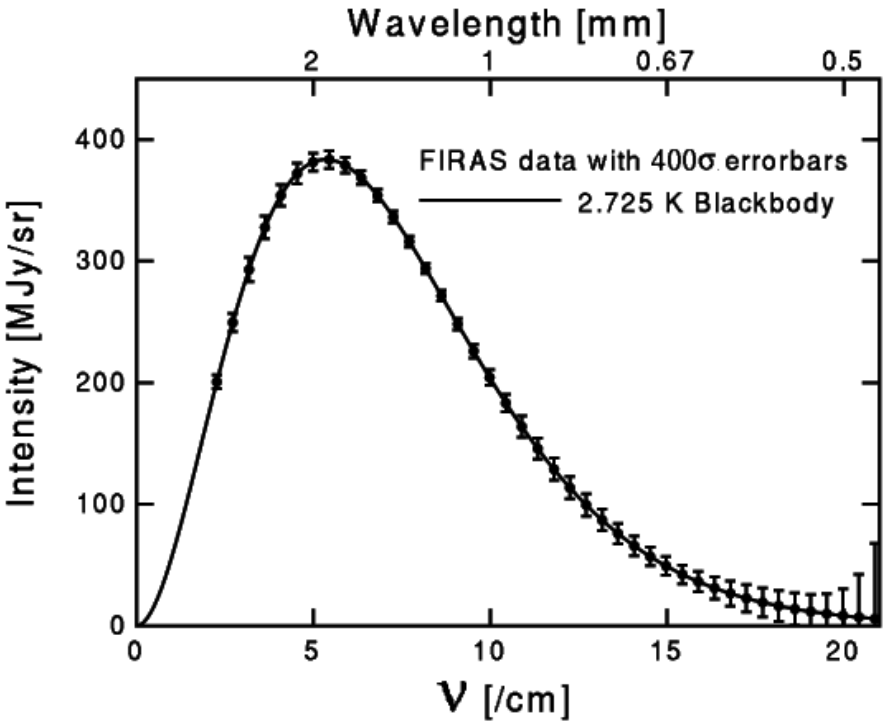

Figure 2.1: CMB spectrum with 400 sigma error bars measured by FIRAS. This spectrum is consistent with a black body at 2.725 K [25].

distribution of the photons is nearly isotropic and is described by the Planck distribution (black-body radiation),

$$I_\nu(T) = \left(\frac{2h\nu^3}{c^2}\right) \frac{1}{\exp\left(\frac{h\nu}{kT_{\rm cmb}}\right) - 1}, \tag{2.9}$$

with a temperature of $T = 2.725$ K now. This is due to the fact that photons were decoupled from the thermal bath at $T \sim 3000$ K and $z \sim 1100$. The discovery of the CMB provides us with the firm evidence for the state of heat bath at the early universe and the big bang cosmology. Figure 2.1 shows the remarkable agreement between this prediction and the observation by the Far Infrared Absolute Spectrometer (FIRAS) experiment on the Cosmic Background Explorer (COBE) satellite [26].

By the more accurate observations, the spacial fluctuation of the temperature of the CMB photons at a level of 1/1000,000 was discovered. The accurate measurement of this fluctuation provides us with the cosmological parameters and initial condition of the universe. The details of this fluctuation are described in Sec. 2.4.

2.3 Inflationary universe

In spite of the great success of the big bang theory, there are several unresolved issues. This leads to a new theory beyond the naive big bang model In this section, we outline the problems of the big bang theory and introduce the inflation hypothesis as a solution [4][5].

2.3.1 Horizon problem

The horizon problem is a problem that the CMB is too uniform beyond the causally-connected regions. In the FRW universe, the scale of the causal horizon is well approximated with the Hubble length l_H. Since $H \propto 1/t$ and during matter-dominated era $a \propto t^{2/3}$, the Hubble length of photon decoupling was

$$l_{\rm H}(t_{\rm dec}) = H_{\rm dec}^{-1} \sim l_H^0 (1+z_{\rm dec})^{-3/2}, \tag{2.10}$$

where $z_{\rm dec} \sim 1100$. Then, the current physical distance is described by

$$d = (1+z_{\rm dec}) l_H(T_{\rm dec}) = (1+z_{\rm dec})^{-1/2} l_H^0. \tag{2.11}$$

We need to estimate the number of independent causal regions. The observable surface of the CMB sphere, in which we are contained today, is $4\pi^2 H_0^{-2}$. Thus, the number of the observed independent causal regions is

$$\frac{4\pi d^2}{4\pi l_H^2(t_{\rm dec})} = \left(\frac{l_H^0}{l_H(t_{\rm dec})(1+z_{\rm dec})} \right)^2 \sim (1+z_{\rm dec}) \sim 10^3. \tag{2.12}$$

This result implies that we are actually observing $\sim$ 1000 causal regions. These regions have never contacted each other thermally. However, the observation shows a mysterious uniformity; i.e. all the regions have the same temperature to the order of 10^{-5}. This fine tuning problem is called 'the horizon problem'.

2.3.2 Flatness problem

In the Friedmann equation, Eq. (2.4) , the curvature term is proportional to a^{-2}. We define the cosmological parameter of curvature as

$$\Omega_K(t) = \frac{\rho(t)}{\rho_{\rm cr}} = \frac{1}{a^2(t) H^2(t)} \sim 1. \tag{2.13}$$

According to Planck 2015 results [27], the estimated curvature and the Hubble constant are

$$H_0 = 67.8 \pm 0.9 \text{ km/s/Mpc}, \tag{2.14}$$

$$\Omega_{\rm K0} = -0.0008^{+0.0040}_{-0.0039}. \tag{2.15}$$

Then, we can calculate the ratio at the Planck epoch:

$$\frac{\Omega_K(t_{\rm pl})}{\Omega_{\rm K0}} = \left(\frac{a_0}{a(t_{\rm pl})} \right)^2 \left(\frac{H_0}{H(t_{\rm pl})} \right)^2 \sim \left(\frac{M_{\rm pl}}{T_0} \right)^2 \left(\frac{H_0}{M_{\rm pl}} \right)^2 = \left(\frac{H_0}{T_0} \right)^2 \sim 10^{-58}. \tag{2.16}$$

We see that the big bang theory indeed reproduces the observed universe only if the following initial condition is imposed,

$$|\Omega_K(t_{\rm pl})| < 10^{-61}. \tag{2.17}$$

Thus our universe requires a large order of the fine tuning at the beginning, which we call the 'flatness problem'.

2.3.3 Relic problem

Most particle physics models beyond the standard model predict some stable relic particles, such as gravitinos, neutralinos, and monopoles, when the universe was at very high temperature. Although the universe cooled down, we should observe them in the present universe. But we do not find any of them so far. This is the 'relic particles problem'.

2.3.4 Origin of the initial perturbation

The red galaxy survey reported the large scale structure in our universe. We do not have a solution within the naive big bang theory to explains the origin of the large scale structure.

2.3.5 One of the solutions for the these problem, "Inflation theory"

The inflation theory provides us with solutions to all the problems described above at once [6][28]. The inflation theory assumes the exponentially expanding universe. If the inflation really occurred in the very early universe, all the aforementioned problems of the big-bang models are naturally solved as follows.

The horizon problem is solved thanks to the rapid reduction of the comoving Hubble length during inflation, which means that our observable universe today was from a small region that was well within the region of causal contact before inflation. The flatness problem is also solved as the accelerating expansion during inflation resulted in a very flat universe at the end of inflation. The relics density is not a problem any more because the universe was much diluted by inflation, leading to a very small number densities of any relic particles.

2.3.6 Inflation theory

We now study the most common solution of the 'inflationary phase'. We assume that the dynamics of the universe is dominated by a scalar field, ϕ, which is called the 'inflaton'. The Lagrangian with the inflaton is given by

$$\mathcal{L}_\phi = -\frac{1}{2}\partial_\mu\phi\partial^\mu\phi - W(\phi), \tag{2.18}$$

where a metric signature is $(-,+,+,+)$.

Since the energy and pressure are dominated by contribution during the inflation, we assume that interaction of the field ϕ can be neglected. The energy-momentum tensor of ϕ is then obtained as

$$T_{\mu\nu} = \frac{-2}{\sqrt{-g}}\frac{\partial}{\partial g^{\mu\nu}}(\sqrt{-g}\mathcal{L}_\phi), \tag{2.19}$$

where $g = det(g_{\mu\nu})$. We yield the energy density and pressure as

$$\rho_\phi = -T^0_0 = \frac{1}{2a^2}\dot{\phi}^2 + \frac{1}{2a^2}(\nabla\phi)^2 + W(\phi), \tag{2.20}$$

and

$$P_\phi = \frac{1}{3}T^i_i = \frac{1}{2a^2}\dot{\phi}^2 - \frac{1}{6a^2}(\nabla\phi)^2 - W(\phi). \tag{2.21}$$

Assuming that both the spatial and time derivatives of the field ϕ are much smaller than the potential at some initial time t_i:

$$\nabla\phi(\mathbf{x}, t_i) \ll \dot{\phi}(\mathbf{x}, t_i) \ll W(\phi). \tag{2.22}$$

Here we assume that the potential is positive, i.e. $W(\phi_i) > 0$. We then obtain

$$\rho = \rho_\phi = \frac{1}{2a^2}\dot{\phi}^2 + W(\phi) \cong W(\phi), \tag{2.23}$$

$$P = P_\phi = \frac{1}{2a^2}\dot{\phi}^2 - W(\phi) \cong -W(\phi). \tag{2.24}$$

Therefore the energy density and pressure are described as $P_\phi \cong -\rho_\phi$ and $\rho_\phi + 3P_\phi < 0$.

When we neglect spatial derivatives, the equation of motion of the inflaton is

$$\phi'' + 3\left(\frac{a'}{a}\right)\phi' + W_{,\phi} = 0. \tag{2.25}$$

During the slow roll, the first term of this equation is negligibly smaller than other terms. Therefore we obtain

$$3\left(\frac{a'}{a}\right)\phi' \cong -W_{,\phi}. \tag{2.26}$$

We then assume the so-called slow roll conditions, which are

$$\frac{1}{2}\phi'^2 \ll W, \tag{2.27}$$

$$|\phi''| \ll 3H|\phi'|, \tag{2.28}$$

so that the slow roll leads to $H' \ll H^2$. Taking the time derivative of Eq. (2.23) and replacing ϕ' by Eq. (2.26), we come to the following slow roll condition;

$$\epsilon_1 \equiv -\frac{H'}{H^2} = \frac{m_{\rm pl}^2}{16\pi}\left(\frac{W_{,\phi}}{W}\right)^2 \cong \frac{3}{2}\frac{\phi'^2}{W} \ll 1, \tag{2.29}$$

where $G \sim m_{\rm pl}$. The second condition of Eq. (2.28) gives

$$\left|\frac{\phi''}{3H\phi'}\right| \ll 1. \tag{2.30}$$

We now set

$$\epsilon_2 \equiv \frac{m_{\rm pl}^2}{24\pi}\left(\frac{W_{,\phi\phi}}{W}\right)^2, \tag{2.31}$$

where $|\epsilon_2| \ll 1$. Then ϵ_1 is always positive. The ϵ_1 and ϵ_2 are often called slow roll parameters. The inflation terminates when ϵ_1 approaches unity.

The perturbation to the FRW metric [29] and the inflation field are given by

$$g_{\mu\nu}(\mathbf{x}, t) = \bar{g}_{\mu\nu}(t) + \delta g_{\mu\nu}(\mathbf{x}, t), \tag{2.32}$$

$$\phi(\mathbf{x}, t) = \bar{\phi}(t) + \delta\phi(\mathbf{x}, t), \tag{2.33}$$

where

$$\delta g_{\mu\nu} = 2\begin{bmatrix} -\Psi & 0 & 0 & 0 \\ 0 & \Phi & 0 & 0 \\ 0 & 0 & \Phi & 0 \\ 0 & 0 & 0 & \Phi \end{bmatrix} + a^2\begin{bmatrix} 0 & 0 & 0 & 0 \\ 0 & 0 & 0 & h_{\rm xz} \\ 0 & 0 & 0 & h_{\rm yz} \\ 0 & h_{\rm xz} & h_{\rm yz} & 0 \end{bmatrix} + a^2\begin{bmatrix} 0 & 0 & 0 & 0 \\ 0 & h_\times & h_+ & 0 \\ 0 & h_+ & h_\times & 0 \\ 0 & 0 & 0 & 0 \end{bmatrix}. \tag{2.34}$$

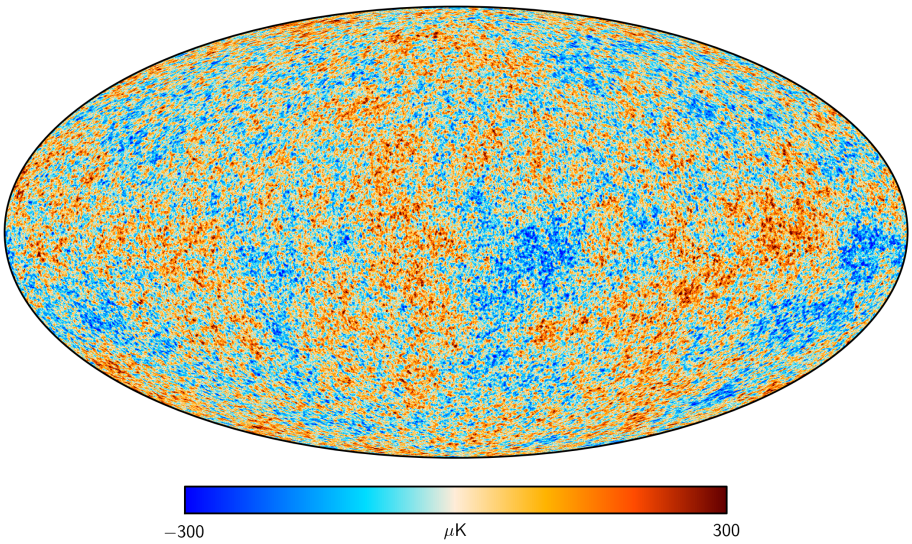

Figure 2.2: CMB anisotropy map of Plank [27]. The color scales show temperature fluctuation from the average value of 2.725 K.

These terms correspond to scalar, vector and tensor perturbation components, which are decomposed by spin eigenstates, spin-0, 1 and 2, respectively. The terms of $h_\times$ and h_+ are known as the gravitational waves.

2.4 CMB power spectrum

The power spectrum is the most important observable for us, when we compare measurements with theoretical calculations [7]. The CMB anisotropy for temperature is defined as $\Theta = \Delta T/T(\mathbf{x_0}, t_0, \mathbf{n})$. We can calculate spherical-harmonic transform of this equation as

$$\Theta(\mathbf{x_0}, \mathbf{n}, t) = \sum_{lm} a_{lm}(\mathbf{x_0}) Y_{lm}(\mathbf{n}), \tag{2.35}$$

$$\langle a_{lm} \cdot a^*_{l'm'} \rangle = \delta_{ll'}\delta_{mm'} C_l, \tag{2.36}$$

where C_l's are the CMB power spectra. The two-point correlation function is

$$\langle \Theta(\mathbf{n})\Theta(\mathbf{n}') \rangle = \sum_{l,l',m,m'} \langle a_{lm} \cdot a^*_{l'm'} \rangle Y_{lm}(\mathbf{n}) Y_{l'm'}(\mathbf{n}) \tag{2.37}$$

$$= \sum_l C_l \sum_{m=-l}^{l} Y_{lm}(\mathbf{n}) Y_{l'm'}(\mathbf{n}) \tag{2.38}$$

$$= \frac{1}{4\pi} \sum_l (2l+1) C_l P_l(\mu), \tag{2.39}$$

where the P_l is the Legendre polynomial. The a_{lm}'s from scalar, vector and tensor perturbations are uncorrelated, i.e.

$$\langle a^{(S)}_{lm} \cdot a^{(V)}_{l'm'} \rangle = \langle a^{(S)}_{lm} \cdot a^{(T)}_{l'm'} \rangle = \langle a^{(V)}_{lm} \cdot a^{(T)}_{l'm'} \rangle = 0. \tag{2.40}$$

The $C_l's$ consist of three types, $C_{\rm Sl}$, $C_{\rm Vl}$ and $C_{\rm Tl}$. Since the vector mode is known to decay soon after entering the horizon, the $C'_{\rm Vl}$ are negligible in models with adiabatic perturbations.

2.4.1 Scalar perturbation

In the case of scalar perturbations, the dominant contribution on the super horizon scale is the ordinary Sachs-Wolfe (OSW) effect shown as

$$\Theta_S^{(SW)}(\mathbf{x_0},\mathbf{n},t_0) \cong \frac{1}{3}\Psi(\mathbf{x_0},\mathbf{n},t_0), \tag{2.41}$$

where Ψ_i is the Bardeen potential. The two point correlation function for scalar perturbation is given by

$$\begin{aligned}
&\langle\Theta_S^{(SW)}(\mathbf{x_0},\mathbf{n},t_0)\Theta_S^{(SW)}(\mathbf{x_0},\mathbf{n'},t_0)\rangle && (2.42)\\
=\;& \frac{1}{(2\pi)^6}\int d^3k d^3k' e^{i\mathbf{x_0}\cdot(\mathbf{k}-\mathbf{k'})}\langle\Theta_S^{(SW)}(\mathbf{k},\mathbf{n},t_0)\Theta_S^{(SW)*}(\mathbf{k'},\mathbf{n'},t_0)\rangle && (2.43)\\
=\;& \frac{1}{(2\pi)^6 9}\int d^3k d^3k' e^{i\mathbf{x_0}\cdot(\mathbf{k}-\mathbf{k'})}\langle\Psi(\mathbf{k})\Psi(\mathbf{k'})\rangle\sum_{l,l'=0}^{\infty}(2l+1)(2l'+1)i^{l-l'} && (2.44)\\
&\cdot j_l(k(t_0-t_{\rm dec}))j'_l(k'(t_0-t_{\rm dec}))P_l(\mathbf{k}\cdot\mathbf{n})\cdot P_{l'}(\mathbf{k'}\cdot\mathbf{n})\\
=\;& \frac{1}{(2\pi)^6 9}\int d^3k P_\Psi\sum_{l,l'=0}^{\infty}(2l+1)(2l'+1)i^{l-l'} && (2.45)\\
&\cdot j_l(k(t_0-t_{\rm dec}))j'_l(k'(t_0-t_{\rm dec}))P_l(\mathbf{k}\cdot\mathbf{n})\cdot P_{l'}(\mathbf{k'}\cdot\mathbf{n})\\
=\;& \sum_l\frac{2l+1}{4\pi}\frac{2}{\pi}\int\frac{dk}{k}\frac{1}{9}P_\Psi(k)k^3 j_l^2(k(t_0-t_{\rm dec})). && (2.46)
\end{aligned}$$

Computing this equation and from Eq. (2.39), we obtain the power spectrum for adiabatic perturbation on scale $2<l\ll\chi(t_0-t_{\rm dec})/t_{\rm dec}\sim 100$:

$$C_{\rm Sl}^{(SW)} \cong \frac{2}{9\pi}\int_0^\infty\frac{dk}{k}P_\Psi(k)k^3 j_l^2(k(t_0-t_{\rm dec})), \tag{2.47}$$

where $j_l^2(k(t_0-t_{\rm dec}))$ peaks roughly at $(k(t_0-t_{\rm dec}))\sim kt_0\sim l$.

We also need to consider the integrated Sachs-Wolfe (ISW) effect. This effect is expressed as

$$\Theta_S^{(ISW)}(\mathbf{x_0},\mathbf{n},t_0) \cong \int_{t_{\rm dec}}^{t_0}(\dot\Phi+\dot\Psi)(t,\mathbf{x}(t))dt \tag{2.48}$$

and the power spectrum is

$$C_{\rm Sl}^{(ISW)} \cong \frac{8}{\pi}\int d\ln k\left|\int_{t_{\rm dec}}^{t_0}\dot\Psi j_0^2(k(t_0-t))dt\right|^2 \tag{2.49}$$

The power spectrum of scalar perturbation can be obtained as

$$k^3P_\Psi(k) = A_s(k/k_0)^{n_s-1}, \tag{2.50}$$

which can also be expressed by using the inflationary potential V as

$$k^3P_\Psi(k) = \frac{16\pi^2}{3}\left[\frac{V}{\epsilon m_{pl}^4}\right]_{k=aH}. \tag{2.51}$$

2.4.2 Tensor perturbation

The CMB anisotropy of Sachs-Wolfe effect from tensor perturbation is

$$\Theta_T^{(ISW)} = -\int \frac{\partial h_{ij}}{\partial t} n^i n^j dt, \tag{2.52}$$

where h_{ij} is from Eq. (2.34). Similarly to Eq. (2.47), we obtain the following power spectrum

$$C_{\mathrm{Tl}}^{(ISW)} = \frac{2}{\pi}\int dk^2 k^2 \left| \int_{t_{\mathrm{dec}}}^{t_0} dt \dot{H}^{(T)}(t,k), \frac{j_l(k(t_0-t))}{(k(t_0-t))} \right|^2 \frac{(l+2)!}{(l-2)!}, \tag{2.53}$$

where $H^T =< h_{ij} n^i n^j h^*_{i'j'} n^{i'} n^{j'} >$. For super-horizon scales, we can assume $\dot{H}^{(T)} = 0$. We also see that $\int dt \dot{H}^{(T)} j_l(t_0 - t) \sim H^(T)(t = 1/k) j_l(kt_0)$ holds as a crude approximation. Then, Eq. (2.53) becomes

$$C_{\mathrm{Tl}}^{(ISW)} = \frac{2}{T}\int \frac{dk}{k} P_h \frac{j_l^2\left(\frac{k}{k_0}\right)}{k(t_0-t)} \frac{(l+2)!}{(l-2)!}. \tag{2.54}$$

We calculate the power low as

$$k^3 P_h = k^3 |H(k, r = 1/k)|^2 = A_T (k/k_0)^{n_T}. \tag{2.55}$$

Here the power spectrum can also be shown with the inflationary potential V as

$$k^3 P_{\mathrm{h}}(k) = \frac{256\pi^2}{3} \left[\frac{V}{m_{\mathrm{pl}}^4}\right]_{\mathrm{k=aH}}. \tag{2.56}$$

2.4.3 Energy scale

Models of cosmic inflation can be characterized by the parameter, r, the tensor to scalar ratio as

$$r = \frac{C_{\mathrm{Sl}}}{C_{\mathrm{Tl}}}. \tag{2.57}$$

This equation implies that r depends on the inflationary potential V. Therefore, measurements of the tensor to scalar ratio are not only testing inflation models, but also relate r to the inflationary energy scale with the following equation,

$$V^{1/4} = 1.06 \times 10^{16}\ \mathrm{GeV} \left(\frac{r}{0.01}\right)^{1/4}. \tag{2.58}$$

This scale $O(10^{16})$ GeV is known as the GUT scale, where GUT stands for the Grand Unified Theory, which is a model in particle physics that unifies electromagnetic, weak and strong interactions at the GUT scale [30].Therefore, observations of r would shed light on ultra high energy physics.

2.5 CMB polarization

The B-mode polarization of the CMB provides us with the direct evidence for primordial gravitational waves. The CMB temperature anisotropy observation uses the information of CMB photon intensity. On the other hand, CMB photon has another aspect of 'polarization'. For generating CMB polarization,

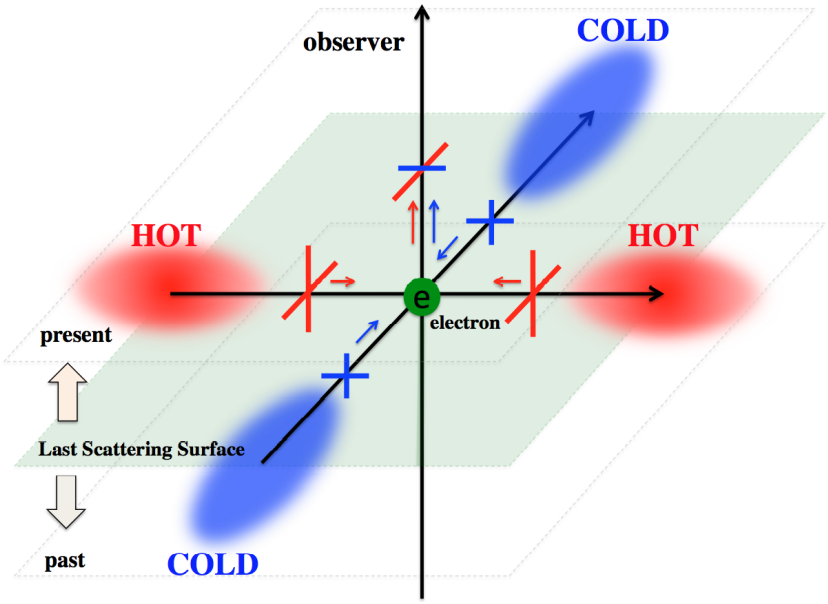

Figure 2.3: A local quadruple of the temperature anisotropy generates linear polarization. The quadrupole temperature anisotropy creates regions of red and blue shifts. The amplitude of the red and blue shifted photons are different. The electron at the last scattering surface scattered the photons from the hot and cold regions. The scattered photons are polarized and a polarization pattern was imprinted on the last scattering surface.

the CMB photons are required to scatter on electrons at the last scattering surface. The density of CMB photons around each electron should also have quadrupole anisotropy as shown in Fig. 2.3.

The scattering into a direction $\mathbf{n}$ is described by the Thomson scattering formula,

$$\frac{d\sigma}{d\Omega_n} = \frac{3}{8\pi}\sigma_T(\epsilon_{\rm in}\cdot\epsilon_{\rm out}), \tag{2.59}$$

where $\epsilon_{\rm in(out)}$ is a polarization vector of the incident (outgoing) photon.

2.5.1 E-mode and B-mode

The polarization map of the CMB can be separated to the E-mode and B-mode. Figure 2.4 shows that the E-mode is symmetric with respect to spatial inversion and the B-mode is obtained by tilting the E-mode pattern by 45 degrees, which is asymmetric with respect to space inversion. In this way, CMB polarization can be characterized with these two modes. In this section, we explain the science details of the E-mode and B-mode polarization.

We first consider the classical decomposition of polarized electromagnetic radiation. For a plane wave

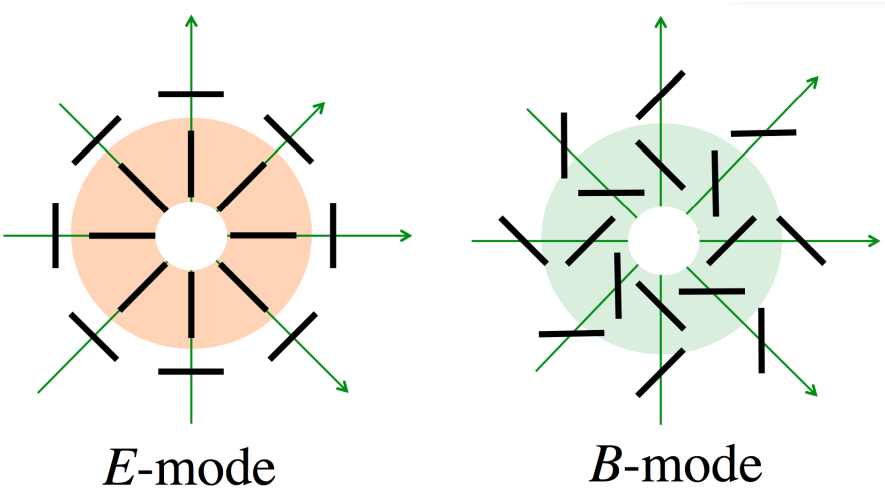

Figure 2.4: E-mode and B-mode

coming to the observer from the +z direction, we define the electric field as

$$E_x(t) = E_x \cos(\omega t - \delta_1), \tag{2.60}$$

$$E_y(t) = E_y \cos(\omega t - \delta_2). \tag{2.61}$$

$$\tag{2.62}$$

The polarization is characterized by the following 'Stokes parameters': intensity, I; two directions of polarization, Q and U; circular polarization V [31]. The Thomson scattering generates linear polarization only. Figure 2.5 shows the Q and U polarization maps that were measured by the POLARBEAR-1 experiment. We should consider Q and U vectors and define these vectors as

$$Q =< E_x^2 - E_y^2 > \tag{2.63}$$

and

$$U =< E_a^2 - E_b^2 >= 2 < E_x E_y^* >, \tag{2.64}$$

where <> is an average over frequency and E_a and E_b defined by

$$E_x = \frac{1}{\sqrt{2}}(E_a + iE_b), \tag{2.65}$$

$$E_y = \frac{1}{\sqrt{2}}(E_a - iE_b). \tag{2.66}$$

Rotating the x and y axes gives new Stokes parameters. When the angle $\phi = 45$ degree, pure $Q > 0$ is transformed into pure $U < 0$. Therefore, the representation of Q, U matrix is

$$\begin{bmatrix} Q' \\ U' \end{bmatrix} = \begin{bmatrix} \cos 2\psi & \sin 2\psi \\ -\sin 2\psi & \cos 2\psi \end{bmatrix} \begin{bmatrix} Q \\ U \end{bmatrix}, \tag{2.67}$$

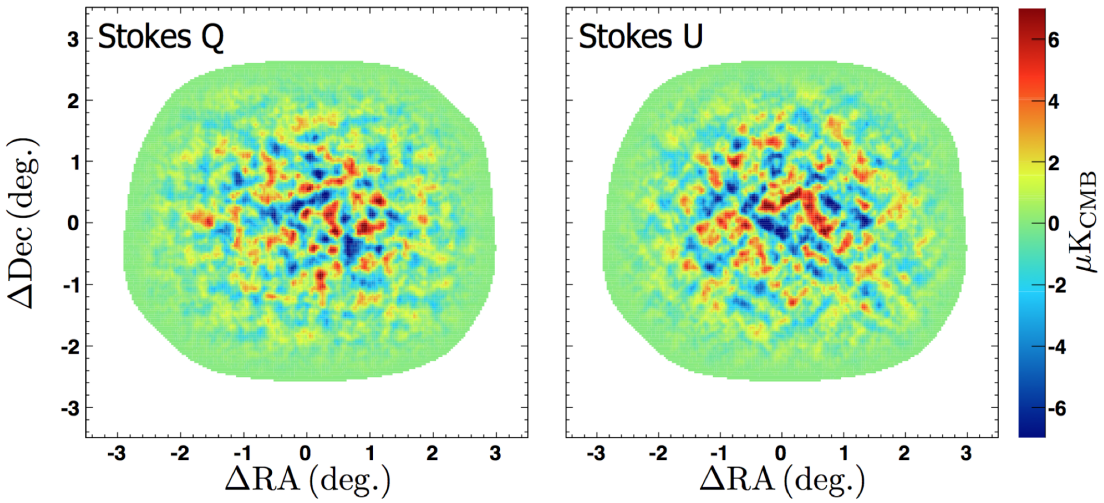

Figure 2.5: Measured Q and U polarization maps in the POLARBEAR-1 experiment. We originally measure the Stokes Q and U maps. The B-mode is reconstructed from them [32].

where bases of x and y axis are transformed by

$$\begin{bmatrix} e'_x \\ e'_y \end{bmatrix} = \begin{bmatrix} \cos\psi & \sin\psi \\ -\sin\psi & \cos\psi \end{bmatrix} \begin{bmatrix} e_x \\ e_y \end{bmatrix}. \tag{2.68}$$

It is convenient to define 'cosmological Stokes parameters' by

$$\begin{bmatrix} \Theta \\ \mathcal{Q} \\ \mathcal{U} \end{bmatrix} = \frac{1}{4} \begin{bmatrix} \delta I/I \\ Q/I \\ U/I \end{bmatrix}. \tag{2.69}$$

It is often more convenient to work with a complex linear combination as

$$\mathcal{Q} + i\mathcal{U}. \tag{2.70}$$

From Eq. (2.67), a clockwise rotation by angle ψ has the effect

$$\mathcal{Q}' + i\mathcal{U}' = e^{\mp i2\psi}(\mathcal{Q} + i\mathcal{U}). \tag{2.71}$$

This property shows that $\mathcal{Q} \pm i\mathcal{U}$ has the spin of ± 2. It is important to note that we can not decompose $\mathcal{Q} \pm i\mathcal{U}$.

We have to decompose by using spin-2. For spin-2 decomposition, a formula analogous to Eq. (2.34) can be obtained as

$$[\mathcal{Q} \pm i\mathcal{U}](\mathbf{n}) = \sum_{lm} a^{\pm 2}_{lm}\, {}_{\pm 2}Y_{lm}(\mathbf{n}) \tag{2.72}$$

$$= \sum_{lm} (E_{lm} \pm iB_{lm})\, {}_{\pm 2}Y_{lm}(\mathbf{n}), \tag{2.73}$$

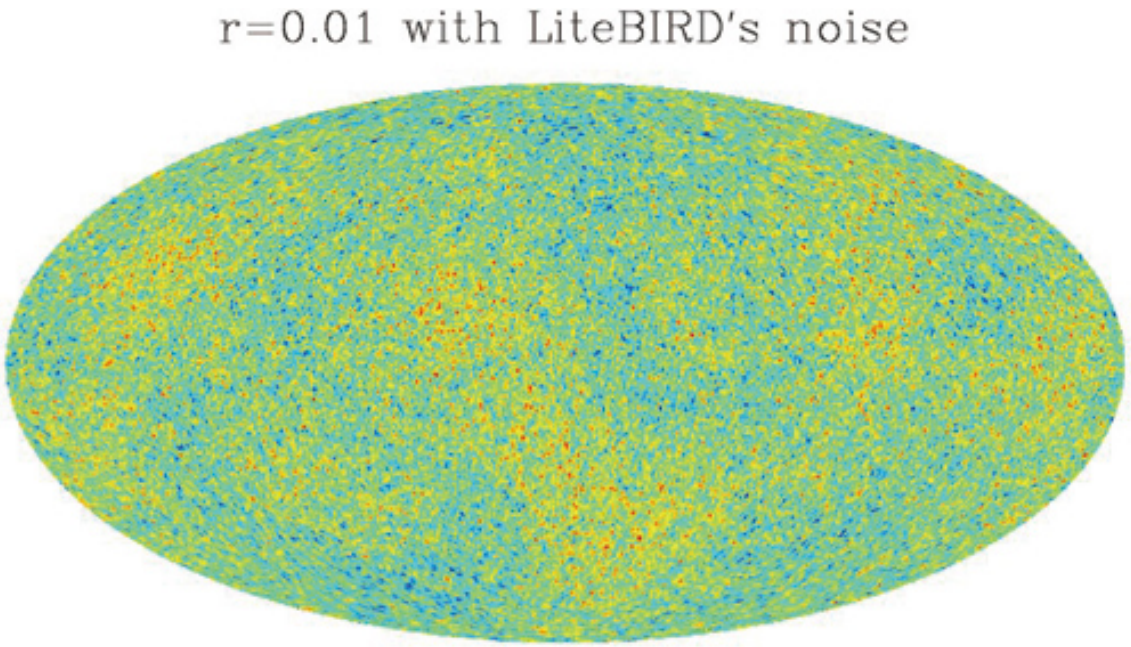

Figure 2.6: Full sky B-mode map simulated by LiteBIRD [33].

where ${}_{\pm 2}Y$ is a spin-2 spherical harmonics function. The components of E-mode, E_{lm}, and B-mode, B_{lm}, are defined by

$$E_{lm} = -\frac{1}{2}({}_{+2}a_{lm} + {}_{-2}a_{lm}), \tag{2.74}$$

$$B_{lm} = \frac{1}{2i}({}_{+2}a_{lm} - {}_{-2}a_{lm}). \tag{2.75}$$

Under parity transformation, $\mathbf{n} \to -\mathbf{n}$, $a_{lm}^{+2} \to a_{lm}^{-2}$, and $a_{lm}^{-2} \to a_{lm}^{+2}$ occur so that the E-mode remains invariant while B-mode changes its sign. Figure 2.6 shows the simulation of a full sky B-mode map.

Moreover, we can define power spectra and cross power spectra as

$$< a_{lm}a_{lm}^* >= \delta_{ll'}\delta_{mm'}C_l^{TT}, \tag{2.76}$$

$$< a_{lm}E_{lm}^* >= \delta_{ll'}\delta_{mm'}C_l^{TE}, \tag{2.77}$$

$$< E_{lm}E_{lm}^* >= \delta_{ll'}\delta_{mm'}C_l^{EE}, \tag{2.78}$$

$$< E_{lm}B_{lm}^* >= \delta_{ll'}\delta_{mm'}C_l^{EB}, \tag{2.79}$$

$$< B_{lm}B_{lm}^* >= \delta_{ll'}\delta_{mm'}C_l^{BB}. \tag{2.80}$$

2.5.2 B-mode from Primordial gravitational waves (PGWs)

We now consider the polarization from the gravitational waves. In Eq.(2.34), we regard the tensor perturbation as gravitational waves, which we call primordial gravitational waves. We distinguish between primordial and astronomical gravitational waves. Recently, the Laser Interferometer Gravitational-Wave Observatory (LIGO) observed the first astronomical gravitational signal GW150914 from a binary black

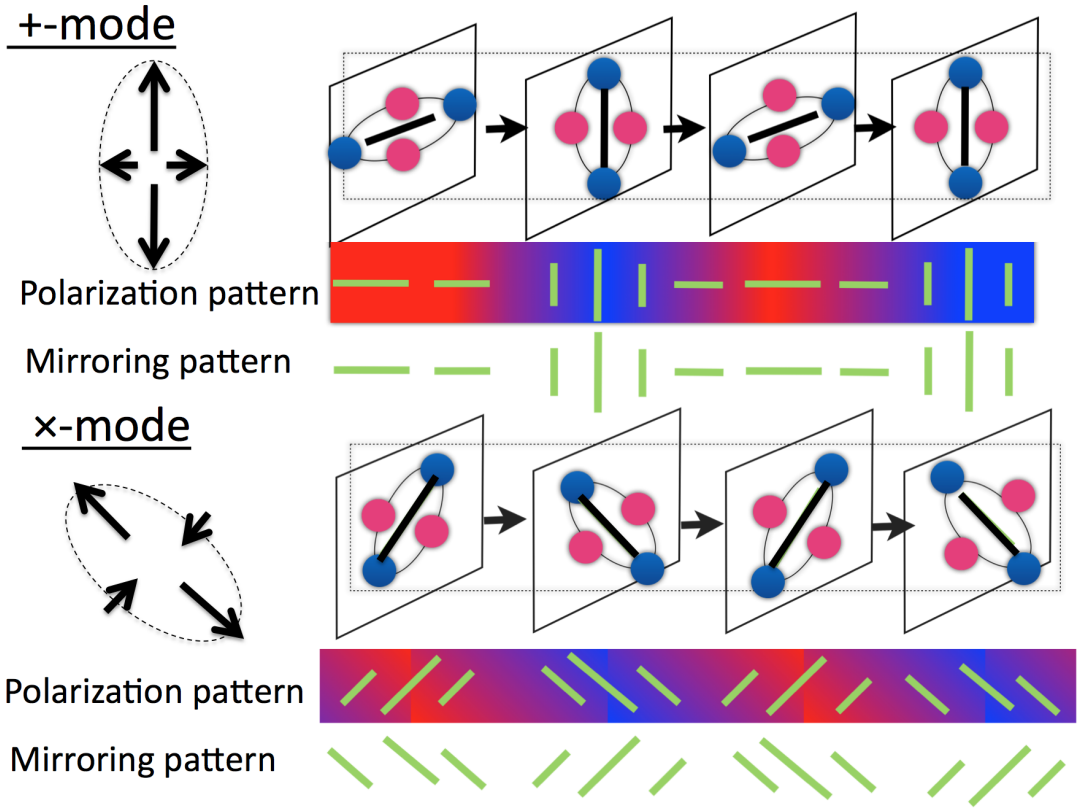

Figure 2.7: The theory of the primordial gravitational waves predicted to be imprinted as degree scale rotation-like polarization patterns. + and × mode fluctuation patterns generate the quadrupole temperature fluctuation pattern. The + mode generates the even parity pattern, E-mode. The × mode generates the odd parity polarization pattern, B-mode.

hole merger [34]. Therefore, there is no doubt about the existence of gravitational waves.

The primordial gravitational waves are transmitted in the universe with expansion and contraction of the space. The space expands and contracts perpendicular to the direction of the wave propagation like the photon transmission. The gravitational waves consist of two modes that are corresponding to the XY axis (the +mode) and the tilted pattern by 45 degrees (the × mode). This mode is equal to the tensor component in metric perturbation in Eq. (2.34).

Since gravitational waves transform geometry, these modes generate temperature anisotropy with red shift or blue shift. Figure 2.7 shows the h_+ mode and $h_\times$ mode anisotropy patterns.

This picture implies that gravitational waves generate × and + mode polarization. These modes generate E-mode and B-mode patterns on the sky. On the other hand, scalar perturbation is only generating the E-mode perturbation, not the B-mode. Therefore, B-mode can be firm evidence for inflationary gravitational waves [35]. We can express the CMB power spectra with primordial inflationary

perturbations as

$$C_l^{TT} = 4\pi \int_0^\infty dlnkT_\Theta^2 P_\Phi(k), \tag{2.81}$$

$$C_l^{TE} = 4\pi \int_0^\infty d\ln kT_\Theta T_E E P_\Phi(k), \tag{2.82}$$

$$C_l^{EE} = 4\pi \int_0^\infty d\ln kT_E^2 P_\Phi(k), \tag{2.83}$$

$$C_l^{BB} = 4\pi \int_0^\infty d\ln kT_B^2 P_{\rm h}(k), \tag{2.84}$$

where $T_X(X = \{T, E, B\})$ is a transfer function, which involves the effect of dynamics in the universe.

2.5.3 Lensing B-mode

The CMB polarization map also contains information on the gravitational lensing at 0.1 deg angular scales [10]. The lensing CMB temperature and polarization anisotropies can be obtained in terms of a remapping of the CMB by a deflection angle $\nabla\phi$:

$$\Theta(\tilde{\mathbf{n}}) = \Theta(\hat{\mathbf{n}} + \nabla\phi(\hat{\mathbf{n}})) \tag{2.85}$$

$$(\mathcal{Q} \pm i\mathcal{U})(\tilde{\mathbf{n}}) = (\mathcal{Q} + i\mathcal{U})(\hat{\mathbf{n}} + \nabla\phi(\hat{\mathbf{n}})) \tag{2.86}$$

The deflection angle is given by the gradient of the gravitational potential,

$$\phi(\hat{\mathbf{n}}) = -2\int_0^{z_{\rm rec}} \frac{dz}{H(z)} \Psi(z, D(z)\hat{\mathbf{n}}) \left(\frac{D(z_{\rm rec}) - D(z)}{D_{z_{\rm rec}} D_z}\right), \tag{2.87}$$

where $D(z)$ is the comoving distance to redshift z in a flat universe and Ψ is the Bardeen potential. By using the Limber approximation, the power spectrum of the gravitational potential is given by

$$C_l^{\phi\phi} = \frac{8\pi^2}{l^3} \int_0^{z_{\rm rec}} \frac{dz}{H(z)} D(z) \left(\frac{D(z_{\rm rec}) - D(z)}{D_{z_{rec}} D_z}\right)^2 P_\Phi(z, k). \tag{2.88}$$

The spectrum of the lensing B-mode can be expressed as

$$C_l^{BB} = \int \frac{d^2L}{(2\pi)^2} W^2(\mathbf{l}, \mathbf{l} - \mathbf{L}) C_{l-L}^{EE} C_L^{\phi\phi}, \tag{2.89}$$

where $\mathbf{l} = (l\cos\psi_l, l\sin\psi_l)$, and $W(\mathbf{l}, \mathbf{l}') = \mathbf{l}' \cdot (\mathbf{l} - \mathbf{l}') \sin 2(\psi_l - \psi_{l'})$ is the mode coupling weighting.

2.6 Recent CMB observation

The precise measurements of CMB temperature anisotropies have been provided by WMAP, ACT, SPT and Plank [3, 36, 37, 27]. The Planck experiment is a satellite experiment for CMB measurements. They measured the 100, 143, and 217 GHz bands with the full sky. The Planck experiment measured the power spectra of the CMB anisotropy and polarization pattern as shown in Fig. 2.8, 2.9, and 2.10. The measured power spectra are consistent with the model. The estimated parameters from the results are listed in Table 2.2.

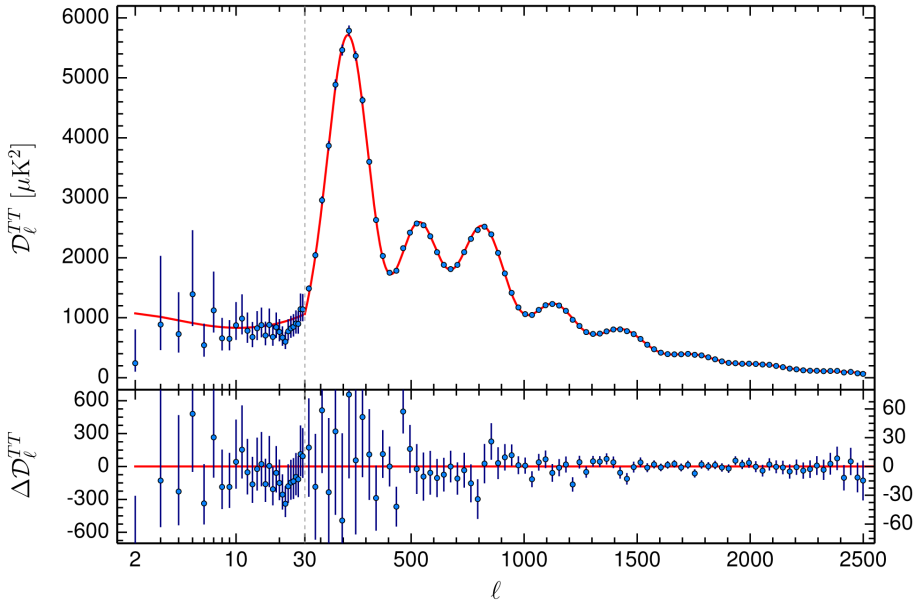

Figure 2.8: The power spectrum of CMB temperature anisotropy according to the Planck 2015 result [27]. The red curve is the best fit of the ΛCDM model. The error bars show $\pm 1\sigma$ uncertainty. The y-axis is $D_l = l(l+1)C_l^{TT}/2\pi$.

The POLARBEAR-1, BICEP-2, KECK Array, and SPTpol experiments detected the lensing B-mode directly as shown in Fig. 2.11. The red points are measured by POLARBEAR-1. The POLARBEAR-1 observed the B-mode polarization at the multipole range of $500 < l < 2100$. POLARBEAR-1 first reported the result of the direct measurement of the lensing B-mode. BICEP-2 and KEK Array also measured the B-mode polarization at the multipole range of $20 < l < 340$. The green points, BK14, are the result of the combined analysis of the BICEP-2 and KEK Array data. SPTpol also measured the B-mode polarization at the multipole range of $300 < l < 2300$.

2.7 Science targets with CMB B-mode

The B-mode signal consists of the primordial and lensing components as described above. Through the measurements of the B-modes, we will probe the inflation and large scale structure.

Cosmic inflation As discussed in 2.5.2, tensor perturbation (primordial gravitational wave) generated during inflation created B-mode polarization pattern on the sky at the recombination and re-ionization era. Because the B-mode is not generated from the scalar perturbation, observing the B-mode is the direct evidence for the inflationary universe. The amplitude of the B-mode signal, which is characterized with r, is directly related with the energy scale of the inflation potential. If we detect the B-mode signal at the level of $r \sim 0.01$, it would suggest that inflation occurred at the GUT scale. The B-mode signal has not been detected. The most stringent upper limit of r is set at 0.07 (95 % C.L.) by BICEP2 and KECK Array [15].

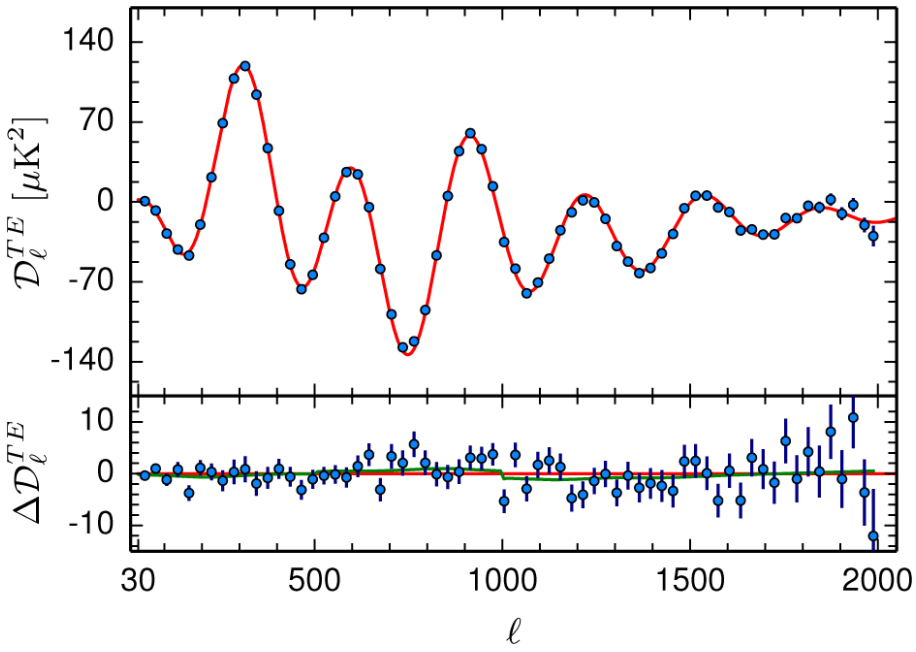

Figure 2.9: The cross correlation spectrum of the CMB temperature anisotropy and E-mode according to the Planck 2015 result [27]. The red curve is the best fit of the ΛCDM model. The error bars show $\pm 1\sigma$ uncertainty. The y-axis is $D_l = l(l+1)C_l^{TE}/2\pi$.

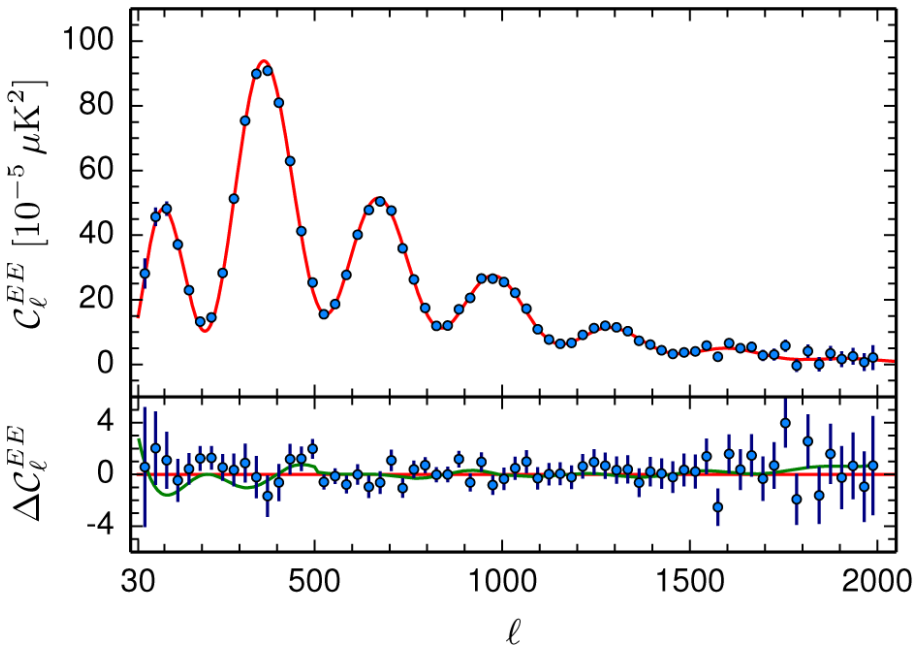

Figure 2.10: The power spectrum of E-mode polarization according to the Planck 2015 result [27]. The red curve is the best fit of the ΛCDM model. The error bars show $\pm 1\sigma$ uncertainty.

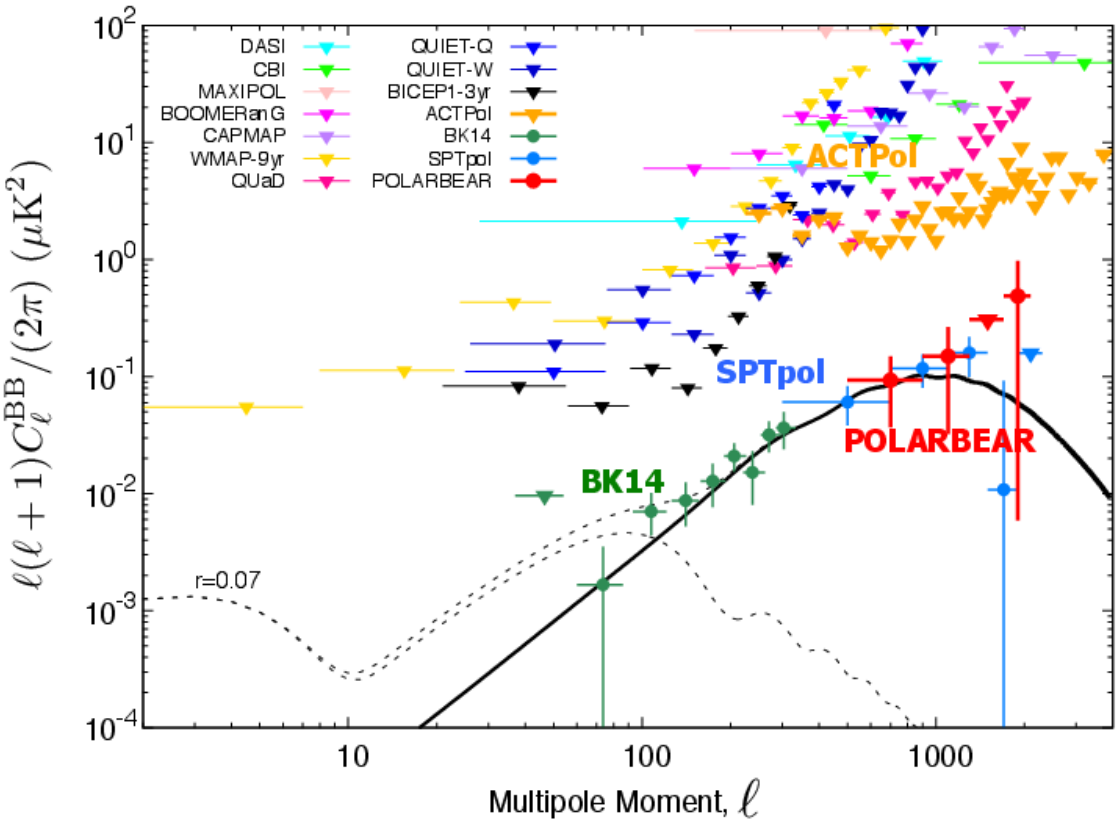

Figure 2.11: Current experimental status of primordial B-mode search and measurements of lensing B-mode. Primordial B-mode has not been detected, and its upper limit is set with BK14 data. The lensing B-mode is measured by POLARBEAR, SPTpol and BK14. Results are consistent with the ΛCDM model. Private complication by Yuji Chinone.

Table 2.2: The measured cosmological parameters from Planck 2015 result [27].

Parameter	TT+lowP	TT+ lowP + lensing	TT+lowP lensing+ext	TT,TE,EE +lowP	TT,TE,EE +lowP+lensing	TT,TE,EE+lowP +lensing+ext
$\Omega_b h^2$	0.02222±0.00023	0.02226±0.00023	0.02227±0.00020	0.02225±0.00016	0.02226±0.00016	0.02230±0.00014
$\Omega_c h^2$	0.1197±0.0022	0.1186±0.0020	0.1184±0.0012	0.1198±0.0015	0.1193±0.0014	0.1188±0.0010
$100\theta_{\rm MC}$	1.04085±0.00047	1.04103±0.00046	1.04103±0.00046	1.04077±0.00032	1.04087±0.00032	1.04093±0.00030
τ	0.078±0.019	0.066±0.016	0.067±0.013	0.079±0.017	0.063±0.014	0.066±0.012
$\ln(10^{10}A_s)$	3.089±0.036	3.062±0.029	3.064±0.024	3.094±0.034	3.059±0.025	3.064±0.023
n_s	0.9655±0.0062	0.9677±0.0060	0.9681±0.0049	0.9645±0.0049	0.9653±0.0048	0.9667±0.0040
H_0	67.31±0.96	67.81±0.92	67.90±0.55	67.27±0.66	67.51±0.64	67.74±0.46
Ω_Λ	0.685±0.013	0.692±0.012	0.6935±0.0072	0.6844±0.0091	0.6879±0.0087	0.6911±0.0062
Ω_m	0.315±0.013	0.308±0.012	0.3065±0.0072	0.3156±0.0091	0.3121±0.0087	0.3089±0.0062
$\Omega_m h^2$	0.1426±0.0020	0.1415±0.0019	0.1413±0.0011	0.1427±0.0014	0.1422±0.0013	0.14170±0.00097
σ_8	0.829±0.014	0.8149±0.0093	0.8154±0.0090	0.831±0.013	0.8150±0.0087	0.8159±0.0086
$z_{\rm re}$	$9.9^{+1.8}_{-1.6}$	$8.8^{+1.7}_{-1.4}$	$8.9^{+1.3}_{-1.4}$	$10.0^{+1.7}_{-1.5}$	$8.5^{+1.3}_{-1.2}$	$8.8^{+1.2}_{-1.1}$
$10^9 A_s$	$2.198^{0.076}_{0.085}$	2.139±0.063	2.143±0.051	2.207±0.074	2.130±0.053	2.142±0.049
Age/Gyr	13.813±0.038	13.799±0.038	13.796±0.029	13.813±0.026	13.807±0.026	13.799±0.021
$z_{\rm eq}$	3393±49	3365±44	3361±27	3395±33	3382±32	3371±23
Ω_k	$-0.052^{+0.049}_{-0.055}$	$-0.005^{+0.016}_{-0.017}$	$-0.0001^{+0.0054}_{-0.0052}$	$-0.040^{+0.038}_{-0.041}$	$-0.004^{+0.015}_{-0.015}$	$-0.0008^{+0.0040}_{-0.0039}$
Σm_ν	<0.715	<0.675	<0.234	<0.492	<0.589	<0.194
$N_{\rm eff}$	$3.13^{+0.64}_{-0.63}$	$3.13^{+0.62}_{-0.61}$	$3.15^{+0.41}_{-0.40}$	$2.99^{+0.41}_{-0.39}$	$2.94^{+0.38}_{-0.38}$	$3.04^{+0.33}_{-0.33}$
$Y_{\rm p}$	$0.252^{+0.041}_{-0.042}$	$0.251^{+0.040}_{-0.039}$	$0.251^{+0.035}_{-0.042}$	$0.250^{+0.026}_{-0.027}$	$0.247^{+0.026}_{-0.027}$	$0.249^{+0.025}_{-0.026}$
$r_{0.002}$	<0.103	<0.114	<0.114	<0.0987	<0.112	<0.113
w	$-1.54^{+0.62}_{-0.50}$	$-1.41^{+0.64}_{-0.56}$	$-1.006^{+0.085}_{-0.091}$	$-1.55^{+0.58}_{-0.48}$	$-1.42^{+0.62}_{-0.56}$	$-1.019^{+0.079}_{-0.080}$

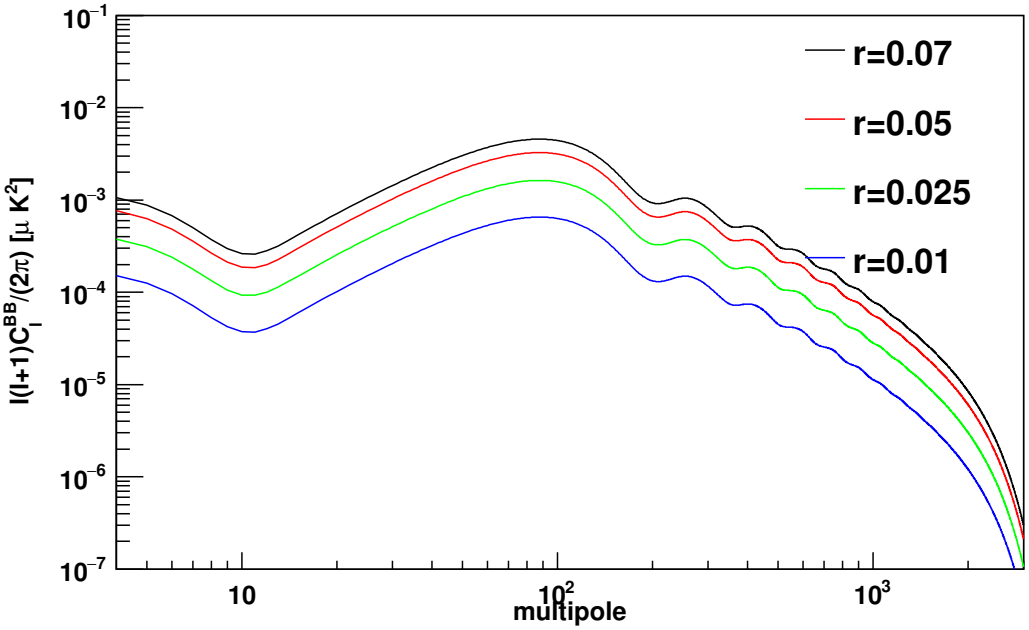

Figure 2.12: The calculated inflationary B-mode power spectrum for various tensor to scalar ratios, r from 0.01 to 0.07. Each spectrum is calculated with CAMB [38]. The assumed parameters are from Planck 2015 results shown in Table 2.2 . Many inflation models favor the r value greater than 0.01.

Many of inflation models suggest $r > 0.01$, and the next generation ground-based experiments target the sensitivity of that level. The clearer target is a theoretical bound of 0.002 on single field inflations, often called the Lyth bound [30]. Measurements at $r \sim 10^{-3}$ level will be conducted by future satellite missions, e.g. LiteBIRD.

Sum of neutrino masses The CMB is the oldest observable light. Traveling from the recombination era to the present time,trajectories of CMB photons were bent by the large-scale structure of the universe [11]. The amplitude of large-scale structure of the universe corresponds to the sum of neutrino masses. This effect is prominent in particular in small angular scales of the B-mode polarization. Figure. 2.13 shows the lensing B-mode as a function of the sum of neutrino masses. The sum of neutrino masses may provide us with the solution to the neutrino hierarchy problem.

The neutrino masses have been measured by experiments observing the neutrino oscillation. The measurements of solar neutrinos have determined the mass squared difference between m_1 and m_2 [39],

$$|m_1^2 - m_2^2| = 7.59^{+0.19}_{-0.21} \times 10^{-5}\text{eV}^2. \tag{2.90}$$

Atmospheric neutrino measurements [40] have also determined

$$|m_1^2 - m_3^2| = 2.43^{+0.13}_{-0.13} \times 10^{-3}\text{eV}^2. \tag{2.91}$$

However, these experiments can only measure the absolute values of m_1, m_2 and m_3. It does not tell us

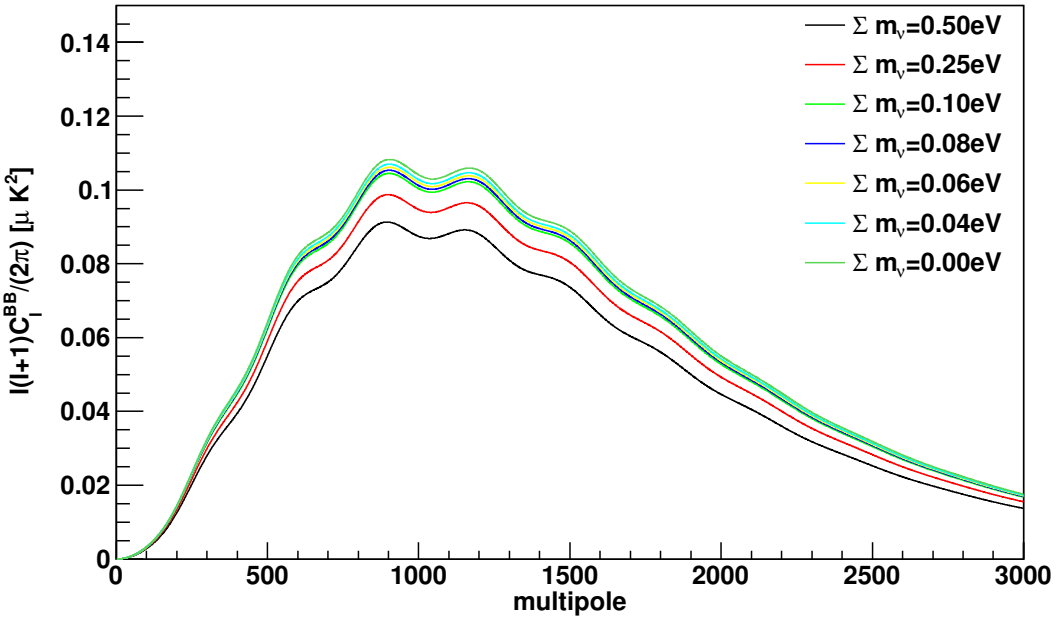

Figure 2.13: The calculated lensing B-mode power spectra as a function of the sum of neutrino masses. These curves are calculated by CAMB [38]. The assumed parameters are from Planck 2015 results as listed in Table. 2.2. The amplitude of lensing B-mode corresponds to the sum of neutrino masses.

whether or not m_2 is heavier than m_3. This question is known as the "neutrino hierarchy problem". If m_3 is larger than m_2, the hierarchy is called the "normal hierarchy". On the other hand, if it is smaller, the hierarchy is called the "inverted hierarchy" as shown in Fig. 2.14.

The accurate measurements of lensing B-mode can solve the "neutrino hierarchy problem" because they allow us to estimate the sum of neutrino masses. From the results of the neutrino oscillation experiments, the lower limit of the sum of neutrino masses is described as

$$\Sigma m_\nu > 100 \text{ meV(inverted)}, \tag{2.92}$$

$$\Sigma m_\nu > 60 \text{ meV(normal)}. \tag{2.93}$$

Therefore, at least, we are able to detect the non-zero neutrino masses if the precision of our measurements is much better than 60 meV.

2.8 Statistic errors

Based on the detector Noise equivalent power, NEP (aW/$\sqrt{\text{Hz}}$), the noise equivalent temperature (NET) in the unit of $\mu\text{K}\sqrt{\text{s}}$ is calculated as follows:

$$\text{NET}_{\text{tot}} = \frac{\text{NEP}_{\text{tot}}}{\sqrt{2}\frac{dP}{dT}|_{T_{\text{cmb}}}}. \tag{2.94}$$

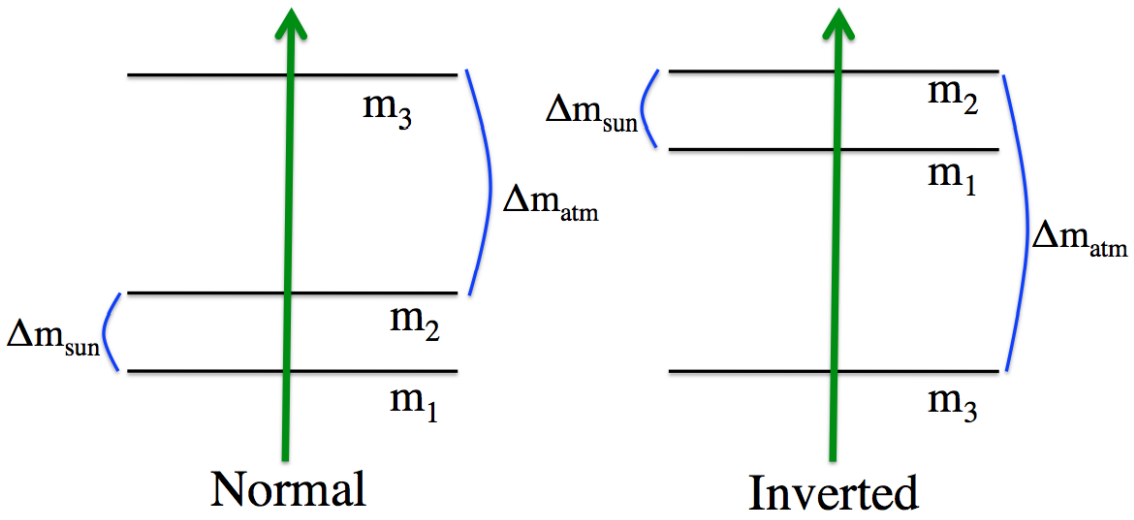

Figure 2.14: The normal and inverted hierarchy of neutrino masses. The current limit allows both scenarios.

We can calculate the mapping speed as

$$S = \frac{N_{\rm bolo}}{NET^2_{\rm tot}}, \tag{2.95}$$

where N_{bolo} is the number of bolometers. The NET array sensitivity is described as inverse of mapping speed:

$$\mathrm{NET}_{\rm array} = \sqrt{1/S} = \frac{\mathrm{NET}_{\rm tot}}{\sqrt{N_{\rm bolo}}}. \tag{2.96}$$

We define the CMB temperature noise as a measurement of pixel noise on the sky in a unit pixel size:

$$\sigma_N = \sqrt{\frac{2\mathrm{NET}^2_{\rm array}\Omega}{t_{\rm obs}}}, \tag{2.97}$$

where $t_{\rm obs}$ and Ω are the observation time and patch size, respectively. The noise of temperature and polarization anisotropy are expressed as

$$N_l = w_T^{-1} W_l^{-1} = \sigma_N^2 e^{l(l+1)\sigma_B^2}, \tag{2.98}$$

$$N_l^{pol} = w_{pol}^{-1} W_l^{-1} = \frac{\sigma_N^2}{\sqrt{2}} e^{l(l+1)\sigma_B^2}, \tag{2.99}$$

where the noise in temperature and polarization are related by $\sigma_N = w_T^{-1/2} = w_{pol}^{-1/2}/\sqrt{2}$, W_l is a window function of beam resolution, σ_B is the standard deviation of the Gaussian beam, i.e. $\sigma_B = FWHM/\sqrt{8\ln 2}$. The detail of W_l is discussed in Chap. 5.

The statistical errors of CMB power spectra for the temperature and polarization anisotropy are

written as

$$\Delta C_l^{TT} = \sqrt{\frac{2}{(2l+1)f_{sky}}}\,[C_l^{TT} + N_l], \tag{2.100}$$

$$\Delta C_l^{EE} = \sqrt{\frac{2}{(2l+1)f_{sky}}}\,[C_l^{EE} + N_l^{pol}], \tag{2.101}$$

$$\Delta C_l^{BB} = \sqrt{\frac{2}{(2l+1)f_{sky}}}\,[C_l^{BB} + N_l^{pol}], \tag{2.102}$$

$$\Delta C_l^{TE} = \sqrt{\frac{2}{(2l+1)f_{sky}}}\,[(C_l^{TE})^2 + (C_l^{TT} + N_l)(C_l^{EE} + N_l^{pol})]^{1/2}, \tag{2.103}$$

$$\Delta C_l^{EB} = \sqrt{\frac{2}{(2l+1)f_{sky}}}\,[(C_l^{EB})^2 + (C_l^{EE} + N_l^{pol})(C_l^{BB} + N_l^{pol})]^{1/2}, \tag{2.104}$$

where f_{sky} is a fraction of the observed sky. These equations are known as the Knox formula [41].

2.9 Systematic errors

For the bolometric detectors, the polarization signal is usually measured as the difference between signals from two orthogonal bolometers. If the property of gain, beam, and polarization are different between two detectors, systematic errors are generated [42]. Here, modeling each detector beam with a Gaussian beam yields

$$I(x,y) = \frac{1}{2\pi\sigma_x\sigma_y} exp\left(-\frac{(x-\rho_x)^2}{2\sigma_x^2} - \frac{(y-\rho_y)^2}{2\sigma_y^2}\right). \tag{2.105}$$

The beam ellipticity is defined as $e = (\sigma_x - \sigma_y)/(\sigma_x + \sigma_y)$. Then, the differential beam properties and systematic errors of B-mode are defined in Table 2.3.

Table 2.3: Beam systematic parameters [42]. The each parameters are defined as $c_\phi = \cos(2\phi_1) - \cos(2\phi_2)$, $s_\phi = \sin(2\phi_1) - \sin(2\phi_2)$,$c_\theta = \cos 2\theta$, $s_\theta = \sin(2\theta)$. I_n and J_n are the cyclindrical Bessel functions, respectively, where the parameter $z = (l\sigma)^2(1+\mu)^2 e$.

Effect	Definition	ΔC_l^{BB}
Differential gain	$g = g_1 - g_2$	$g^2 f_1 C_l^{TT}$
Differential beam width	$\mu = \frac{\sigma_1 - \sigma_2}{\sigma_1 + \sigma_2}$	$4\mu^2 (l\sigma)^4 f_1 C_l^{TT}$
Differential pointing	$\rho = \rho_1 - \rho_2$	$s_\theta^2 C_l^{TT} J_2^2(l\rho) - J_1^2(l\rho) C_l^{TT} f_2$
Differential ellipticity	$e = \frac{e_1 - e_2}{2}$	$I_1^2(z) s_\phi^2 C_l^{TT}$
Differential rotation	$\epsilon = \frac{1}{2}(\epsilon_1 + \epsilon_2)$	$4\epsilon^2 C_l^{EE}$

2.10 Discussion

The statistical errors from the detector are calculated by the Knox formula. Then, we estimate the significance with several parameters. The significance level for r and Σm_ν is calculated with the following

equation:

$$\sigma = \sqrt{\Sigma \left(\frac{(C_l^{BB}(r=0, \Sigma m_\nu = 0) - C_l^{BB}(r, \Sigma m_\nu))^2}{(\Delta C_l^{BB}(f_{sky}, NET_{array}, \sigma_b, t_{obs}))^2} \right)}, \tag{2.106}$$

where the power spectrum is based on the cosmological parameters listed in Table. 2.2 and POLARBEAR-2 instrumental parameters listed in Table. 2.4. In this calculation, we assume that the observation frequencies are 150 and 95 GHz.

Table 2.4: The POLARBEAR-2 instrumental parameters used for the estimation of significance, where σ_B is the beam width and t_{obs} is the observation time. The Efficiency row shows observation efficiencies expected from the POLARBEAR-2 experiment.

	95 GHz	150 GHz
f_{sky}	65 %	65 %
σ_b	6.0 arcmin	3.5 arcmin
t_{obs}	3 years	3 years
Efficiency	0.18	0.18

Figures. 2.15 and 2.16 show the significance as a function of the array NET. When we estimate the significance of inflationary B-mode, we subtract the lensing B-mode. The uncertainty of the lensing B-mode is taken from the Planck 2015 result [27]:

$$A_{lens} = 0.983 \pm 0.025. \tag{2.107}$$

The significance of inflationary B-mode becomes larger when the sum of neutrino masses is larger. This is because the lensing B-mode power as an additional noise is suppressed with increase of sum of neutrino masses. When $\Sigma m_\nu = 0$, therefore, the significance of the r measurement becomes the smallest. In order to achieve more than 2 sigma detection of the inflationary B-mode for $r = 0.01$ at $\Sigma m_\nu = 0$, $\mathrm{NET}_{\mathrm{array}} < 4.32\ \mu\mathrm{K}\sqrt{\mathrm{sec}}$ is required.On the other hand, the significance of the lensing B-mode becomes larger with the larger value of the tensor to scalar ratio. The requirement of the 1 sigma detection of $\Sigma m_\nu = 100$ meV is $NET_{\mathrm{array}} < 4.44\ \mu\mathrm{K}\sqrt{\mathrm{sec}}$. Therefore, our requirement of NET array is $4.30\ \mu\mathrm{K}\sqrt{(\mathrm{sec})}$ for achieving the 2 sigma detection of inflationary B-mode and 1 sigma detection of the lensing B-mode with $\Sigma m_\nu = 100$ meV.

2.11 Summary of this chapter

The CMB has played a key role to establish modern cosmology. In particular, the accurate measurements of the CMB temperature and E-mode polarization anisotropies are essential to precisely determine cosmological parameters. The accurate measurements of B-mode will provide us with the new physics of inflation and neutrinos. To access the level of $r = 0.01$ and $\Sigma m_\nu = 100$ meV, we need to achive the array sensitivity of $NET_{\mathrm{array}} = 4.30\ \mu\mathrm{K}\sqrt{\mathrm{sec}}$.

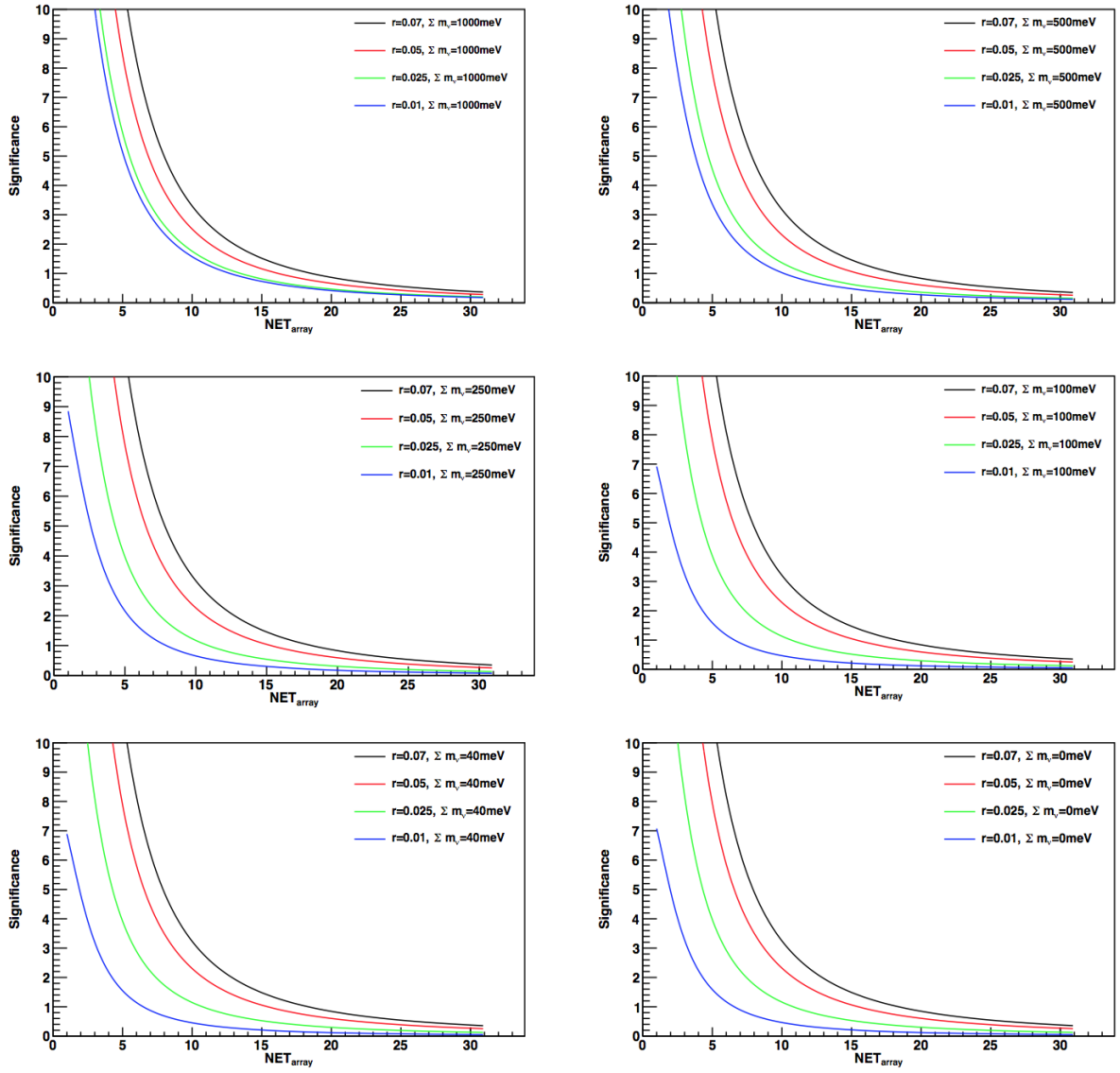

Figure 2.15: The calculated significance of inflationary B-mode. We assume the measured parameters from the Planck 2015 results as listed in Table. 2.2. The significance is calculated with Eq. (2.106) for r=0.07, 0.05, 0.025, and 0.01.

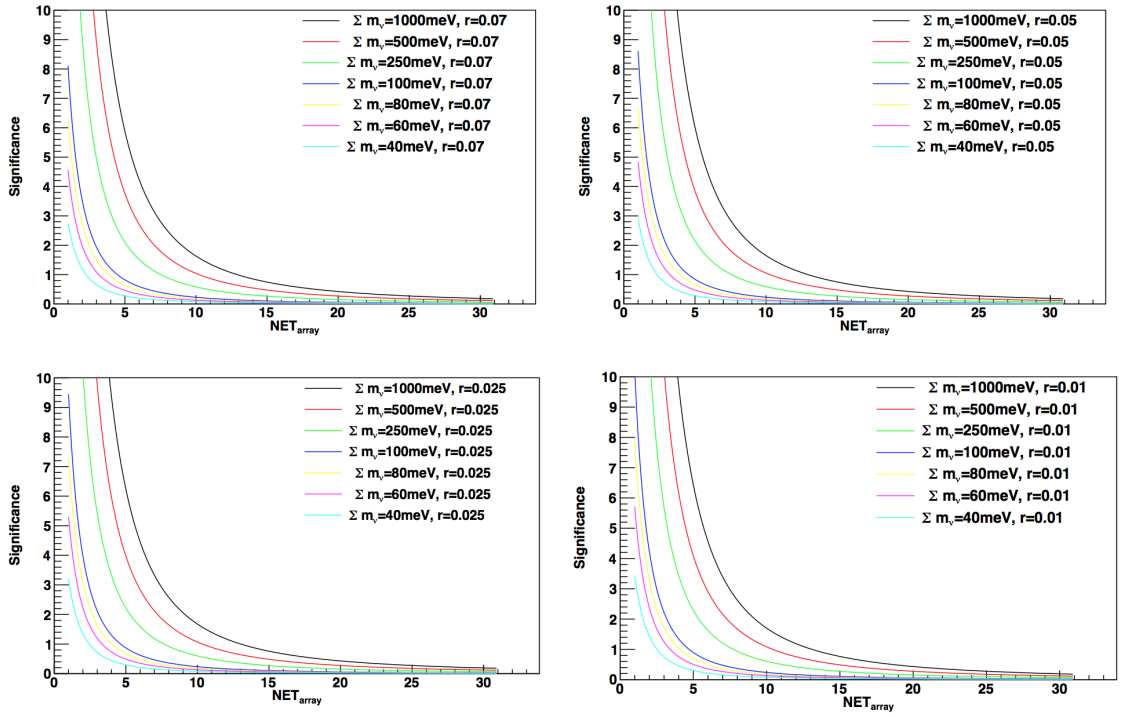

Figure 2.16: The calculated significance of lensing B-mode for 1000 meV, 500 meV, 250 meV, 100 meV, 80 meV, 60 meV, and 40 meV. When we estimate the inflationary B-mode, we subtract lensing B-mode. Then, we assumed lensing B-mode amplitude from the Planck 2015 results.

Chapter 3

POLARBEAR-2 experiment

POLARBEAR-2 (PB-2) is a ground-based CMB polarization experiment with a large detector array [17, 16, 43, 44]. The PB-2 receiver employs 7588 Al-Mn bilayer transition edge sensor (TES) bolometers at 250 mK on the focal plane with a diameter of 365 mm [45]. The detectors are placed on a 250 mK stage and sensitive to two frequencies (95 and 150 GHz) simultaneously. This receiver will be mounted on a telescope of the Simons Array at the Atacama desert in Chile in early 2017. Figure 3.1 shows the observation site of PB-2.

3.1 Science goals of PB-2

As described in the previous chapter, the science goals of PB-2 are

- to obtain the evidence for the inflationary universe,
- to estimate the sum of the neutrino masses from the gravitational lensing (GL) effect.

The main target of PB-2 is the odd-parity polarization pattern, the B-mode. The B-mode is created by the primordial gravitational waves (PGW) during the inflation and by the large scale structure in history of the universe. The detection of the PGW B-mode will shed light on the initial condition of the universe (e.g. energy scale of inflation). On the other hand, the GL B-mode contains information of the structure formation (e.g. the sum of neutrino masses).

The sensitivity curve of PB-2 is shown in Fig. 3.2. Our scientific goals are $r \leq 0.01$ at 95 % C.L. for the tensor to scalar ratio and $\Sigma m_\nu \leq 100$ meV at 68 % C.L. The PB-2 will measure the power spectrum at a multipole range of $25 < l < 2500$.

3.2 PB-2 Instruments overview

The PB-2 instrument consists of two parts, the HTT and the PB-2 receiver system as shown in Fig. 3.3. The PB-2 receiver system is the high sensitive detector array. The specifications of the PB-2 and the

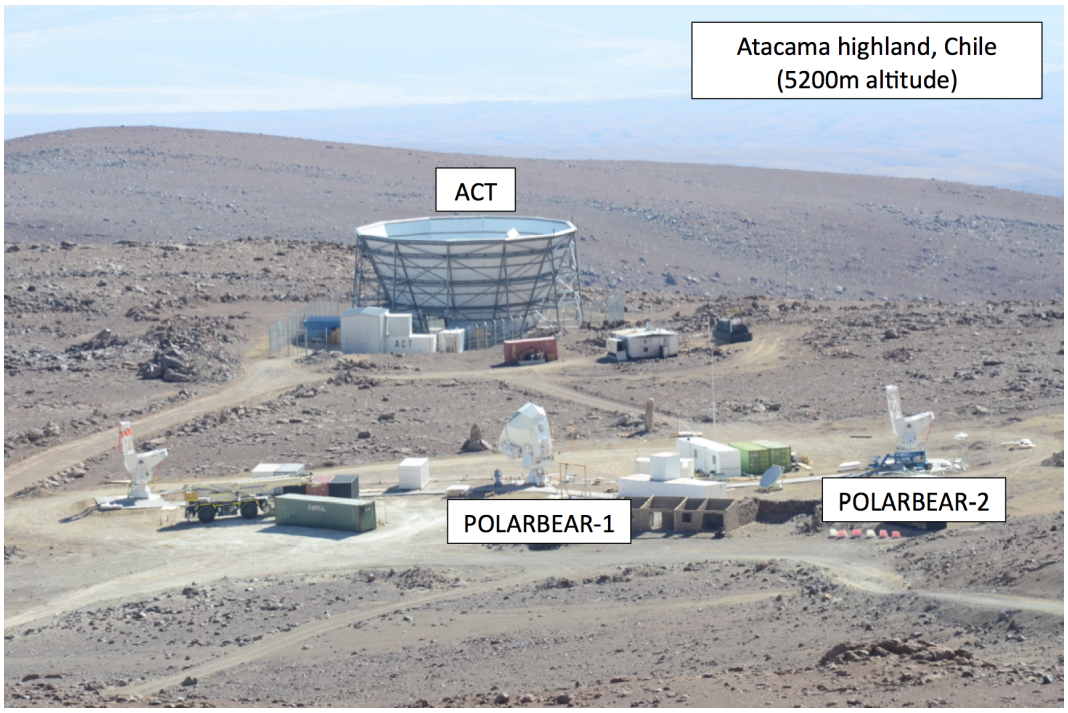

Figure 3.1: Observation site. The telescope in the picture is the Huan tran telescope with the PB-1 receiver system. For the PB-2 we plan to place another telescope near the PB-1 telescope. The design of the telescope of PB-2 is the same as that for PB-1 [46, 44].

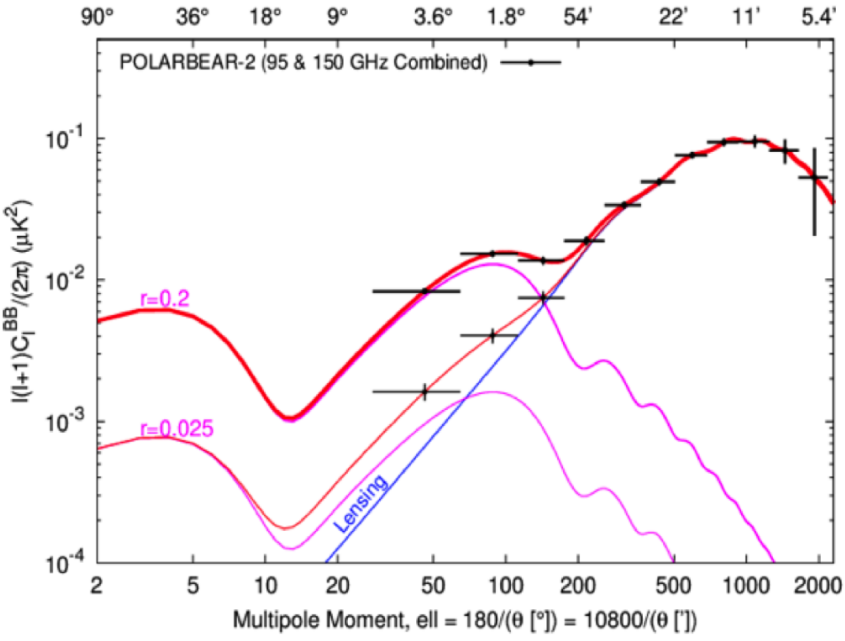

Figure 3.2: Expected sensitivity of PB-2 for B-mode detection within 1 sigma errors for 2 years of observation. Pink and blue curves are the power spectra for PGW and GL B-modes, respectively. Private communication with Yuji Chinone.

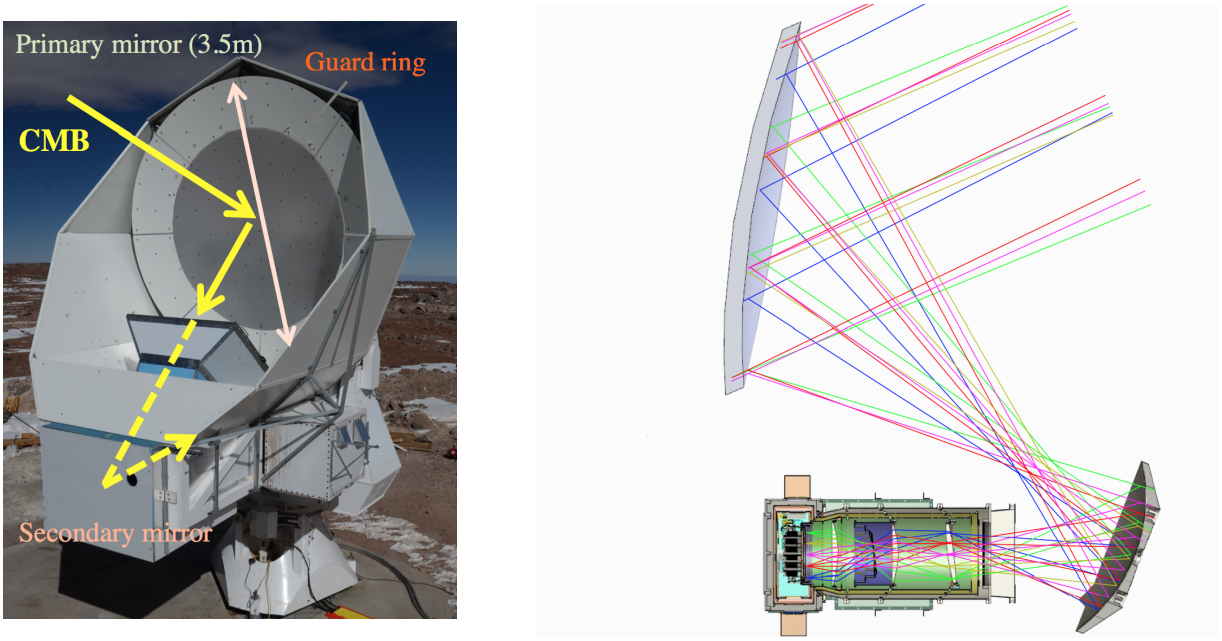

Figure 3.3: Left: The picture of Huan Tran telescope from a PB-2 official picture. Right: The cross sectional view of the PB-2 system.

PB-1 are summarized in Table 3.1. We highlight three features in the PB-2 system as follows:

- 7588 Al-Mn bilayer TES bolometers at 250 mK,
- the observation frequencies of 150 and 95 GHz,
- the cold alumina optics.

In the case of the ground-based experiments, the sensitivity of each pixel is limited with the emission from the atmosphere. We need to increase the number of detectors for the high sensitivity measurements. The current-generation experiments PB-1 and BICEP-2 have employed 1274 and 512 detectors, respectively. The number of the detectors at PB-2 is about ten times as large as those of the current-generation experiments. To accommodate a large number of detectors, we need to place the large focal plane. We employ the alumina optics for the PB-2 experiment. The alumina allows us to make the large optics keeping a low aberration of each detector. Therefore, the technology of large alumina optics must be developed for the B-mode detection.

3.3 Cryogenic system

The receiver system is designed to cool the focal plane at 250 mK. The 250 mK refrigeration system consists of two pulse tube coolers (PTCs) [47] and a helium sorption cooler with two ^{3}He stages and a ^{4}He stage. [48] The nominal cooling power of the PTC is 30 W at 50 K and 1.5 W at 4 K. We measure the PTC performance with the thermal loading as shown in Fig. 3.4. The heat links are between each thermal stage and PTC heads. Our target temperatures are 55 K and 4 K at the 50 K and 4 K stage,

Table 3.1: PB-2 receiver specifications [16].

	POLARBEAR-1	**POLARBEAR-2**
Frequencies	150 GHz	95 GHz and 150 GHz
Number of pixels	637 (1274 bolometers)	1897 (7588 bolometers)
NET (bolometer)	480 μK$\sqrt{\text{s}}$ (150 GHz)	360/360 μK$\sqrt{\text{s}}$ (95/150 GHz)
NET (array)	13.4 μK$\sqrt{\text{s}}$ (150 GHz)	5.6/5.6 μK$\sqrt{\text{s}}$ (95/150 GHz) 4.0 μK$\sqrt{\text{s}}$ (95 and 150 GHz combination)
Focal plane Temperature	250 mK	250 mK
Field of View	2.4 °	4.8 °
Beam Size	3.5 arcmin.	6 arcmin. @95 GHz, 3.5 arcmin. @150 GHz
Sky Coverage	1.7 %	65 %
Observation Time	5 years	3 years

respectively. We place the annealed 5.8N-purity aluminum and annealed 7N-purity copper sheet on the outer surface of each thermal stage to reduce the thermal gradient. The high purity aluminum with a thickness of 0.5 mm is made by Sumitomo chemical corporation. [49] The high purity copper with 0.2 mm thick is made by Mitsubishi material [50]. We place 30 and 50 stacked MLIs which are made by Kaneka corporation. [51]. Figure 3.5 shows an example refrigerator cycle. The measured hold time at the 250 mK stage is 38 hours, which meets our requirement.

3.4 Optics

The HTT is an off-axis Gregorian telescope, which has two mirrors, primary and secondary mirrors [52]. Re-imaging alumina lenses make the focus telecentric over the whole 365 mm diameter focal plane. The projected beam shapes on the sky at detection frequencies are defined with the design of the Lyot stop. The Lyot stop is placed between the aperture lens and collimator lens, with which we make the optical aperture. We employ a new black-body compound named KEK black that I invented, as a material of the Lyot stop. The simulated beam at each pixel is shown in Fig. 3.6. We also place the KEK black at the inner surface of the 4 K shell to reduce the stray light and pseudo polarization due to reflection.

3.4.1 Optical elements

We explain the optical elements of our system in this section. The list of the optical elements of the PB-2 receiver system is shown in Fig. 3.7. The details of the optical elements are shown in the following subsections.

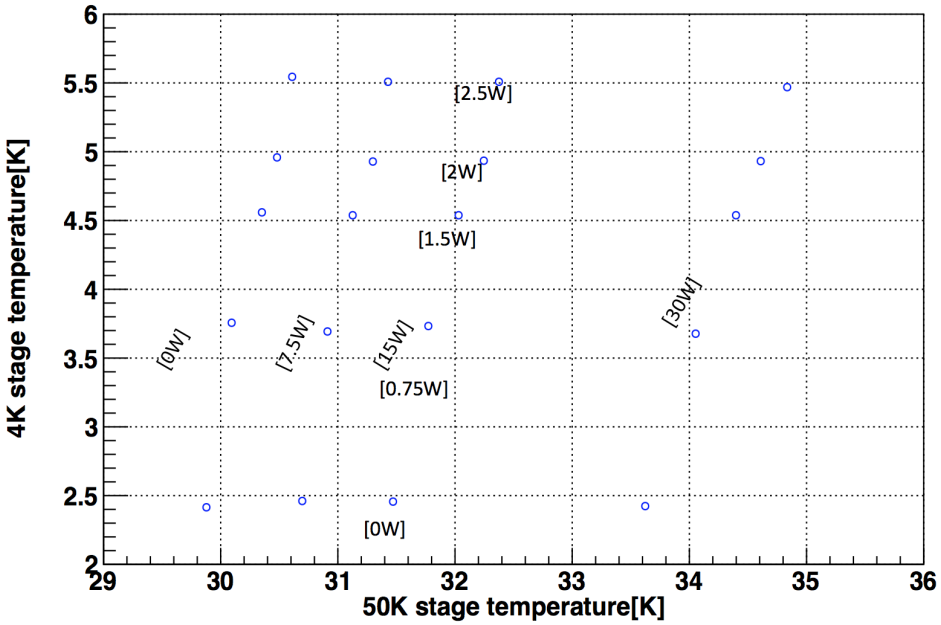

Figure 3.4: Results of the thermal loading test for the PTC. We place a PtCo thermometer and a heater on each head.

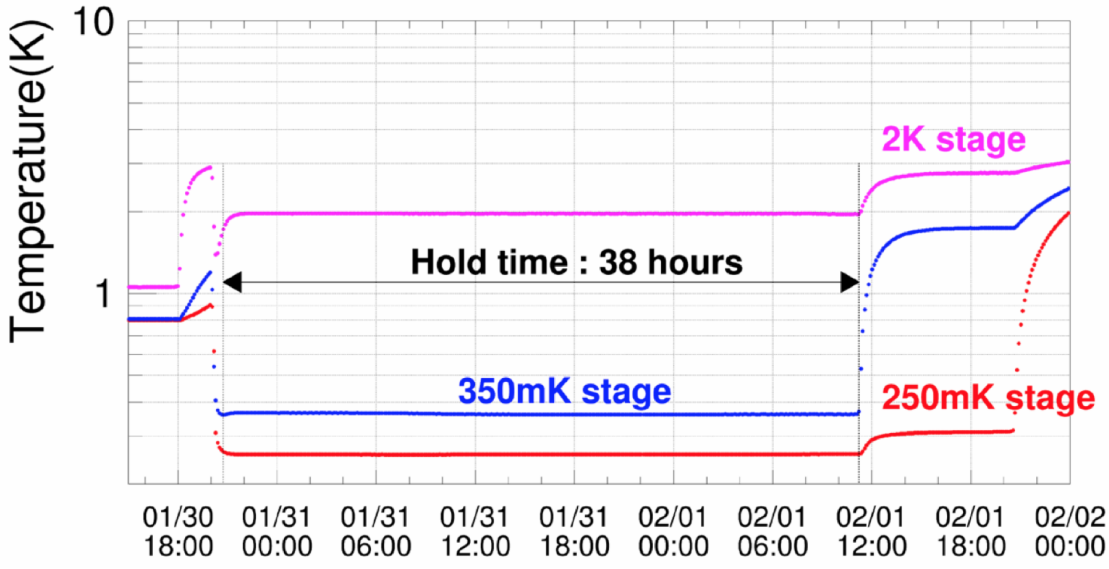

Figure 3.5: The measured hold time of the sorption cooler. Private communication with Masaya Hasegawa.

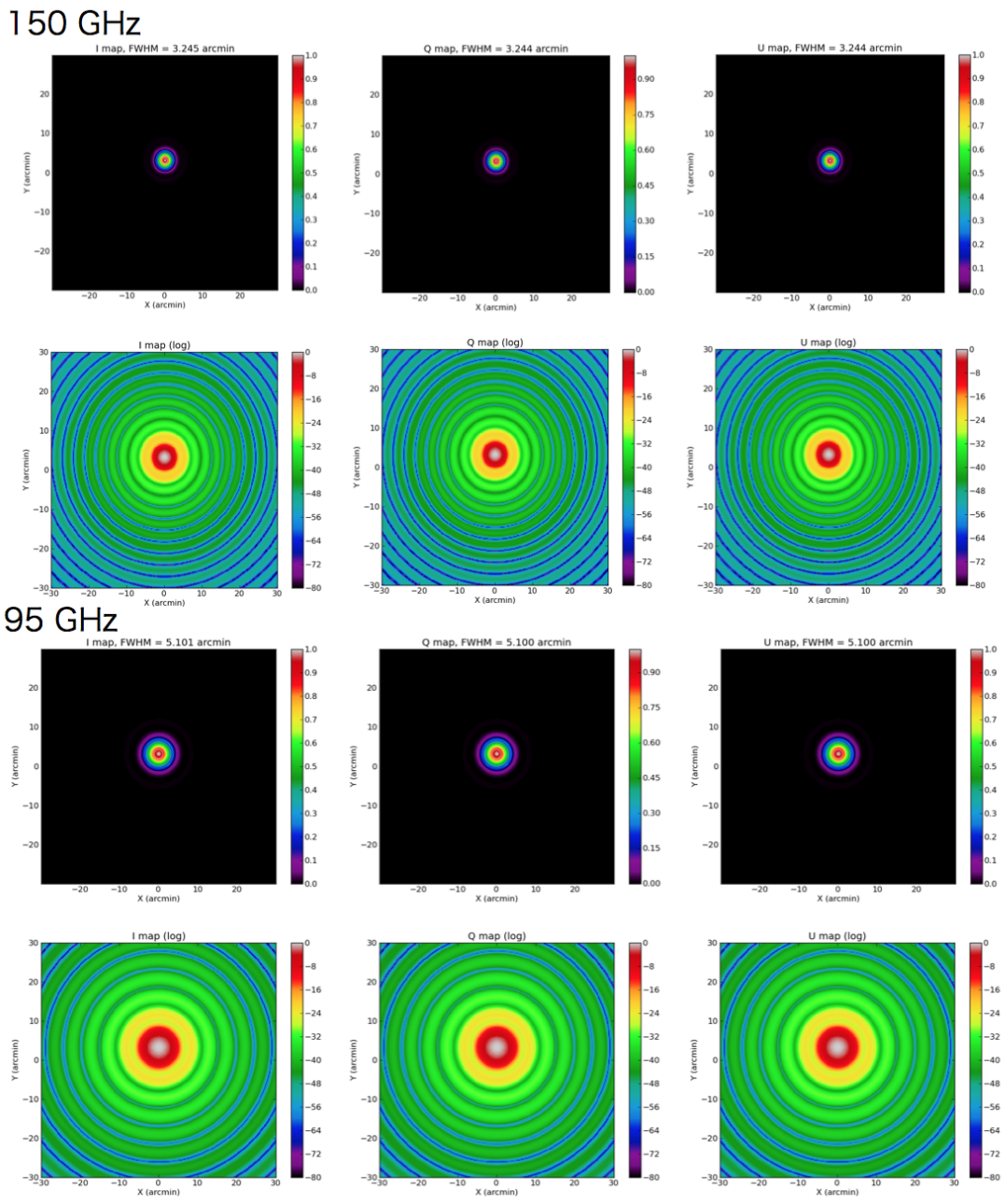

Figure 3.6: The simulated beams with the QUAST simulation [53]. Private communication with F. Matsuda.

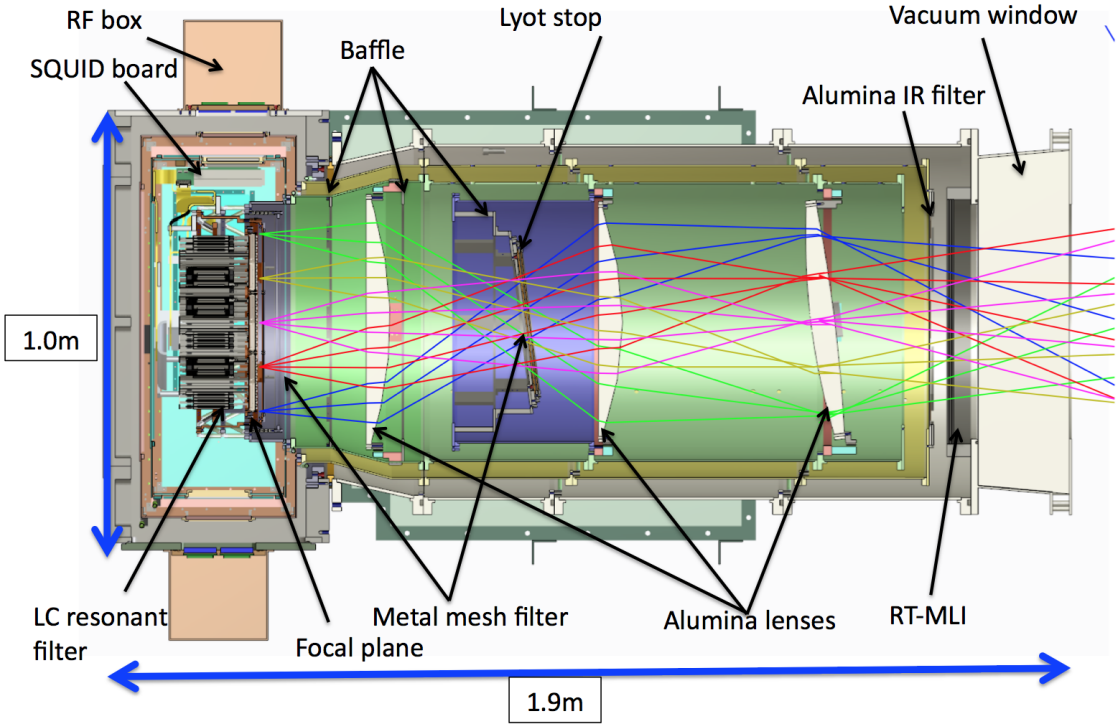

Figure 3.7: Side view of the PB-2 receiver system with optical components and readout system.

3.4.1.1 Primary and secondary mirror

The primary and secondary mirrors reflect the incident beams. The mirrors are made of aluminum. Projected along boresight, the size of the primary mirror is 3.5 m in diameter, with 2.5 m high-precision monolithic mirror and a 1 m guard ring. The secondary mirror is 1.5 m in diameter. The incoming parallel beam is reflected by the primary mirror and is focused at the primary focus, which is placed between the primary and secondary mirrors. The secondary mirror converts the prime focus to the Gregorian focus corresponding to the field lens.

3.4.1.2 Zotefoam window

The Zotefoam [54] is known as a high transmittance material in detection bands and high absorption in the IR band. The thickness of the PB-2 window is 200 mm as shown in Fig. 3.8. The measured temperature of the Zotefoam at the vacuum side is 252 K. The measured transmittance is 98 %.

3.4.1.3 RT-MLI

The first element after the Zotefoam window is the radio-transparent multi-layer insulation (RT-MLI) [55] as shown in Fig. 3.9.

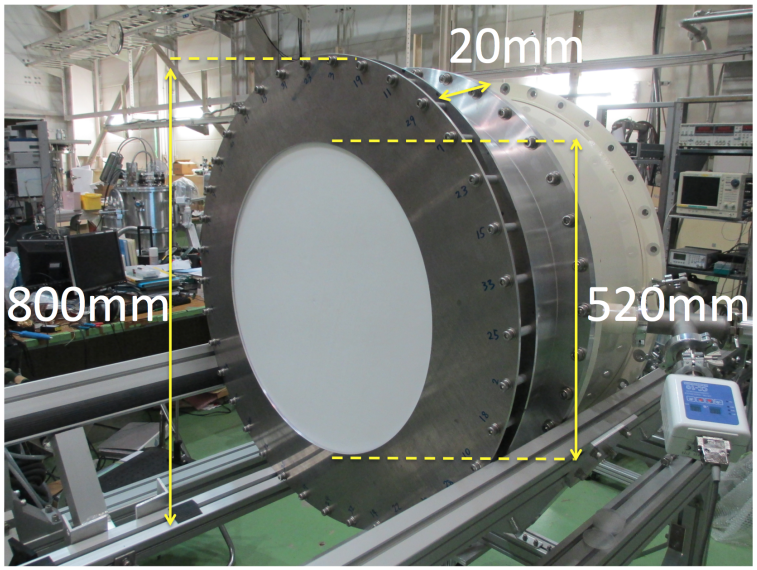

Figure 3.8: Photograph of a Zotefoam window.

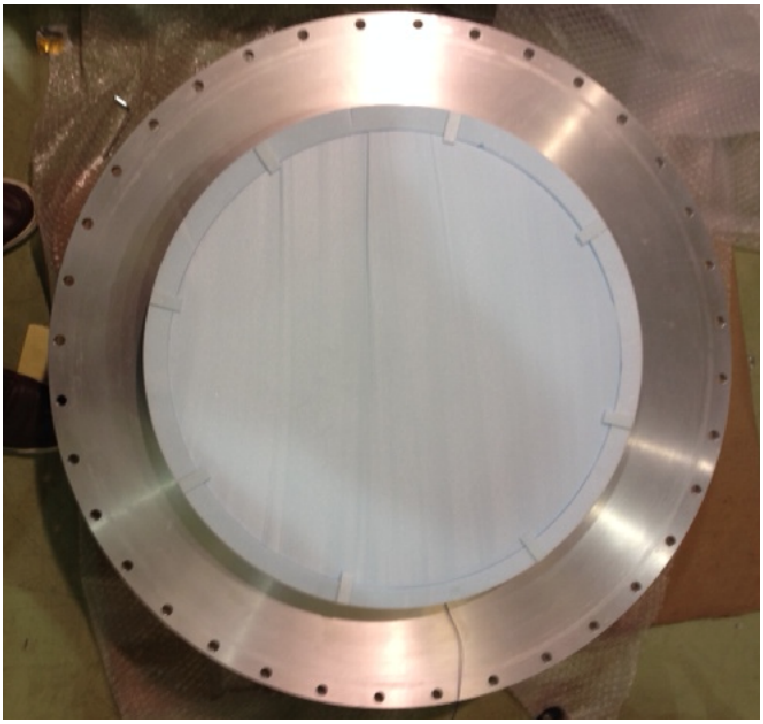

Figure 3.9: Photograph of a RT-MLI as a 300 K IR filter.

3.4.1.4 Alumina filter

We employ alumina with 99.5 % purity as IR absorption filters of the PB-2 receiver system because the loss-tangent difference from the millimeter to sub-mm wavelengths was the largest among the samples we tested [18]. The alumina filter with the AR coating is mounted on a 50 K shell that is located next to the RT-MLI. The thickness and diameter of the alumina filter are 2 mm and 460 mm, respectively. The filter is conductively cooled at the filter edge. We use the method of the mullite and Skybond Foam anti-reflection (AR) coating to the alumina filter. The detail of AR coating and alumina filter is explained in Chap. 4.

3.4.1.5 Alumina lenses

We employ the alumina with 99.9 % purity for re-imaging lenses [17]. To achieve the large field of view over 4.8 degrees with diffraction limited optics, high purity alumina is used for 500 mm in diameter of re-imaging lenses because of its high index of refraction (~ 3.1). There are three lenses, which from the sky side are the field lens, the aperture lens and the collimator lens. We place the AR coating on both surfaces of lenses. We apply epoxy AR coating on curved surfaces, while the technology with mullite and Skybond Foam is adopted on the flat surfaces. That means that the epoxy AR coating is placed on the both surfaces of the field lens. The aperture lens and collimator lens have a hybrid configuration with both AR coating techniques, which is effective in reducing the dip of the fringe. The detail of AR coating and alumina lenses is explained in Chap. 4.

3.4.1.6 Metal mesh filter

The metal mesh filter (MMF) is an IR filter made of the stacks of the metal meshes and polypropylene [56]. It is used as a low pass filter for the incoming radiation. We place three types of MMFs whose cut-off frequencies are 171 GHz (5.7 icm), 261 GHz (8.7icm), and 360 GHz (12 icm). Seven MMFs with a 171 GHz cut-off is placed at the 350 mK stage with each of them corresponding to one wafer as shown in Fig. 3.10. The MMFs with the cut-off frequencies of 261 and 360 GHz are placed at 4 K stage with stacking. Their diameters are 300mm, which are sufficiently large. The measured transmittances of MMFs are explained in Chap. 7.

3.4.1.7 Lyot stop

The Lyot stop defines the beam edge with absorber aperture. The aperture is placed between the collimator and aperture lenses. From the optical design, the diameter of Lyot stop is defined to be 180 mm. To reduce the side lobe with diffraction at the edge of Lyot stop, we should design the smooth edge of window function. To this end, we use the KEK black as a material of the Lyot stop. The composition of KEK black by mass is: 64 % Stycast 1090 (Emerson & Cuming, Inc., Woburn, MA [57]); 6 % Catalyst 9 [57]; 26 % Carbon black(MITSUBISHI Carbon Black #10 [58]); 4 % Powder Beads (Mogu corporation [59]). The millimeter absorber is placed on the inner surface of the 4 K shell and

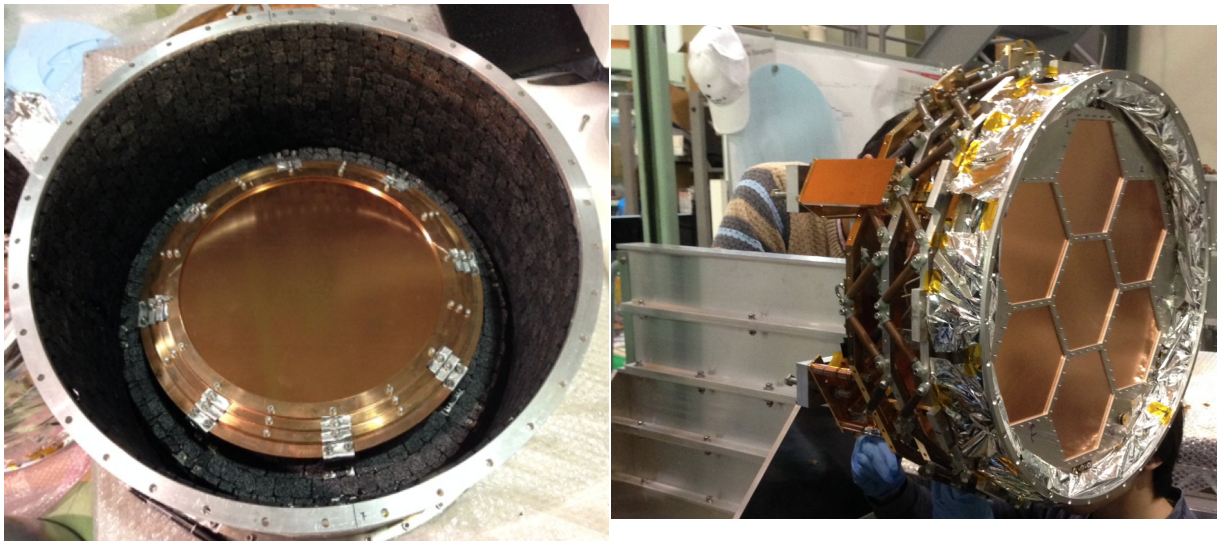

Figure 3.10: Left: Picture of a stack of metal mesh filters at the 4 K stage. Right: Picture of metal mesh filters at the 350 mKstage.

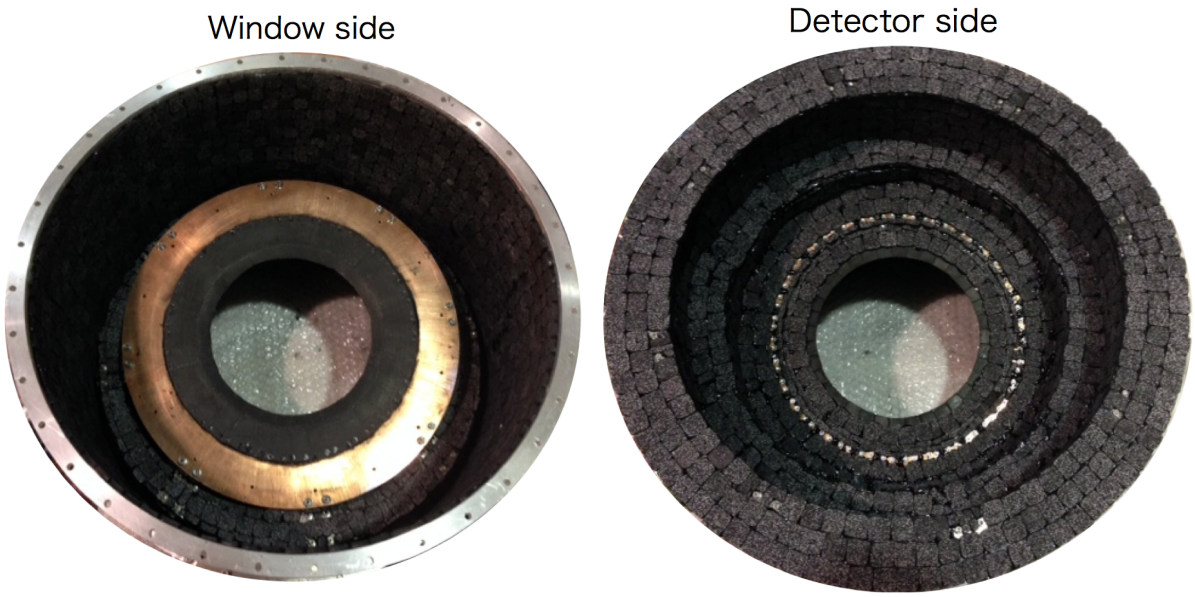

Figure 3.11: Left: The developed Lyot stop viewed from the side of the vacuum window. Right: The developed Lyot stop viewed from the the detector side. The Lyot stop is made of KEK black.

the Lyot stop as shown in Fig. 3.11. The millimeter absorber blocks the stray light for reducing the unexpected loading to the focal plane.

3.5 Detector and Focal plane

The focal plane is separated into 7 wafers. Each wafer has 271 dual linear-polarization pixels which are sensitive to 95 and 150 GHz bands [45]. A silicon lenslet is placed on each pixel. Incoming radiation is

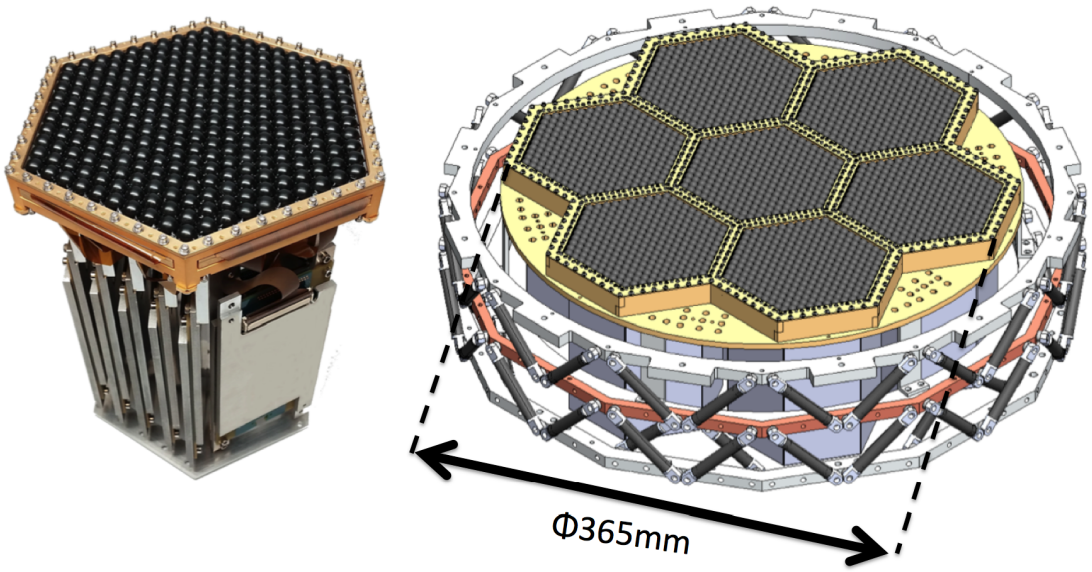

Figure 3.12: The focal plane design of PB-2. The diameter of receiver system is 365 mm. A silicon lenslet with the epoxy AR coating is mounted on each pixel [46].

coupled with a sinuous antenna. Micro-strip filters on the pixel split the signal onto two detection bands. The intensity of each band is detected by TES bolometers. The entire focal plane is cooled to ~ 250 mK by a helium sorption cooler.

The sinuous antenna is sensitive to two polarization directions, which we call "top" and "bottom" detectors. The "top" and "bottom" detectors measure the E_a^2 and E_b^2 polarization of the electromagnetic waves, respectively. It can observe the linear polarization by taking the difference between the "top" and "bottom" bolometer as described in Eq. (2.63) and (2.64).

The observed signals by a pair of detectors are affected by the fluctuations of the atmosphere. However, the atmosphere is known as the non-polarized light to a good approximation. Two detectors have observed the same atmosphere so that it cancels the fluctuation of the atmosphere with the difference in signals. Therefore, it can measure the polarization from the ground without the fluctuation of the atmosphere to a good precision.

3.6 Readout system

Figure 3.14 shows a schematic view of the readout circuit [60, 61, 62]. The signal from each bolometer is amplified by a superconducting quantum interference device (SQUID) and read out by multiplexed readout system based on the digital implementation of the frequency domain technique [63]. For each bolometer that is represented as the resistor R_{bolo} in Fig. 3.14, we form a LCR resonant circuit with the same inductance L and different capacitance C_i, where i runs from 1 to 40 indicating the bolometer ID. By sending the carrier signal that corresponds to each resonant frequency, one can detect the change of

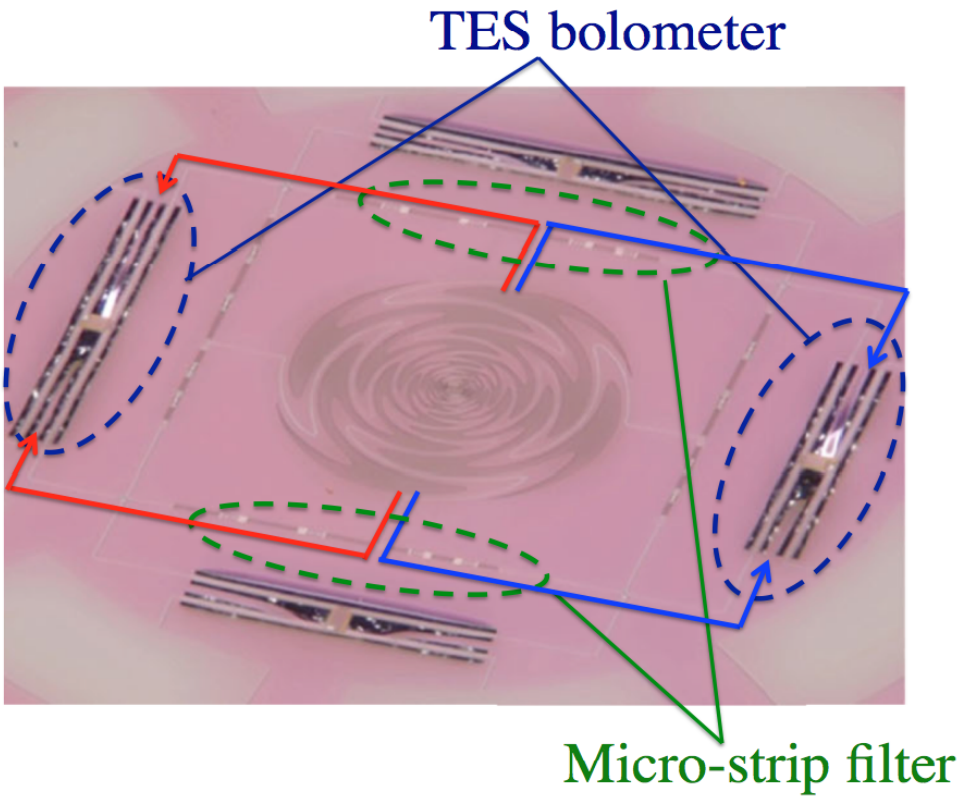

Figure 3.13: PB-2 detector system. A sinuous antenna, micro-strip filters, and TES bolometers are placed on the each pixel [45].

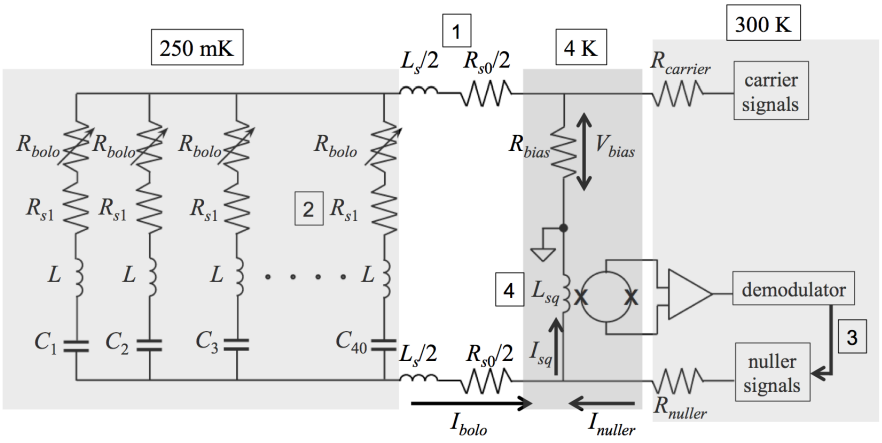

Figure 3.14: Overview of the PB-2 readout system. The frequency-domain multiplexing is adopted to readout 40 bolometers with the same signal line [62] .

the bolometer resistance by watching the output current from the resonant circuit. The following design considerations were made for stable operations of the readout system: (1) Parasitic inductance, L_s, and resistance, R_{s0}, should be small enough not to change the bias resistance R_{bias} seen by the detectors; (2) The equivalent series resistance, R_{s1} should also be small enough not to affect the resonant frequency. Sum of R_{s0}, R_{s1}, and R_{bias} generate the non-linearity of TES bolometers as a parasitic resistance; (3) We have adopted the Digital Active Nulling (DAN) scheme [64], which can extend the band width of the SQUID amplifier and allow the high frequency readout; (4) The current on the input coil at the SQUID chip is canceled by DAN, i.e. $I_{sq} = I_{bolo} + I_{null}$=0. [62] The SQUID board is placed on the 4 K stage. The increase in the detector number requires an increase in the multiplexing factor; while the number of detectors read out per SQUID was 8 at PB-1, it is increased to 40 for PB-2. PB-2 readout system consists of a set of 40 LC resonance chips with different resonance frequencies, $f = 1/2\pi\sqrt{LC}$. Figure. 3.15 shows simulated LCR peaks. The signal from the SQUID board is read out with the custom-made digital board called the Ice board. The Ice board is specialized for high multiplexing readout system.

3.7 Calibrators

We mounted the calibrator into the telescope to reduce the systematic errors of our measurement. We explain the calibration system as follows.

3.7.1 Gain calibrator

A chopped thermal source with ∼1000 K is the relative gain calibrator of the PB-2 system as shown in Fig. 3.16. This source is coupled to the detector beam through a 8 mm light-pipe penetrating the secondary mirror. We estimate the relative gain of each bolometer. The response of the detector depends on the frequency due to the time constant of the detector. We change the chopper frequencies between

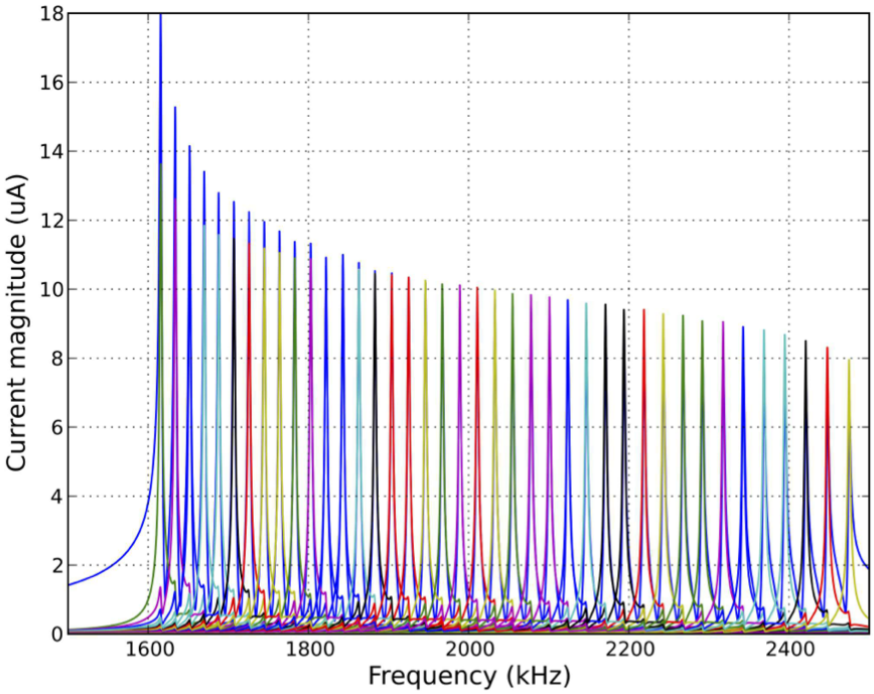

Figure 3.15: The simulated LC resonance peaks [63].

4 Hz and 44 Hz during each calibration.

3.7.2 Polarization modulator

At PB-2, we plan to modulate the polarization signal with a continuously-rotating half-wave plate (HWP) whose diameter is 500 mm. Figure 3.17 shows the picture of the PB-2 HWP. The HWP rotates the polarization angle of the incident polarized signal. We use sapphire, which is a birefringent material. The thickness of our HWP is 3.6 mm, with which the difference of the optical path length between the ordinary axis and extraordinary axis is equal to a half wavelength of the average of two band centers (120 GHz). There are two advantages of using the HWP. First, the modulation of the HWP only rotates the incident polarization angle. In general, when we reconstruct the polarization signal from a pair of bolometers, we have to take a difference between two bolometers. Therefore, if a detector gain difference or beam mismatch is large between two polarization directions, the signal of temperature anisotropy leaks into instrumental polarization. However, when we use a continuously-rotating HWP, we can use each detector independently. Second, as the HWP rotates continuously at the frequency of $f_{\rm HWP} > f_{\rm knee}/4$, the modulated signal appears above the $1/f$ knee of the detector noise. Therefore, we can observe large angular correlations on the sky without the effect of $1/f$ noise, even the scan speed is not high. The achromatic HWP (AHWP) we plan to use has a very high modulation efficiency, close to unity and a large bandwidth that sufficiently covers both 95 and 150 GHz. The AHWP for PB-2 consists of a stack of three HWPs.

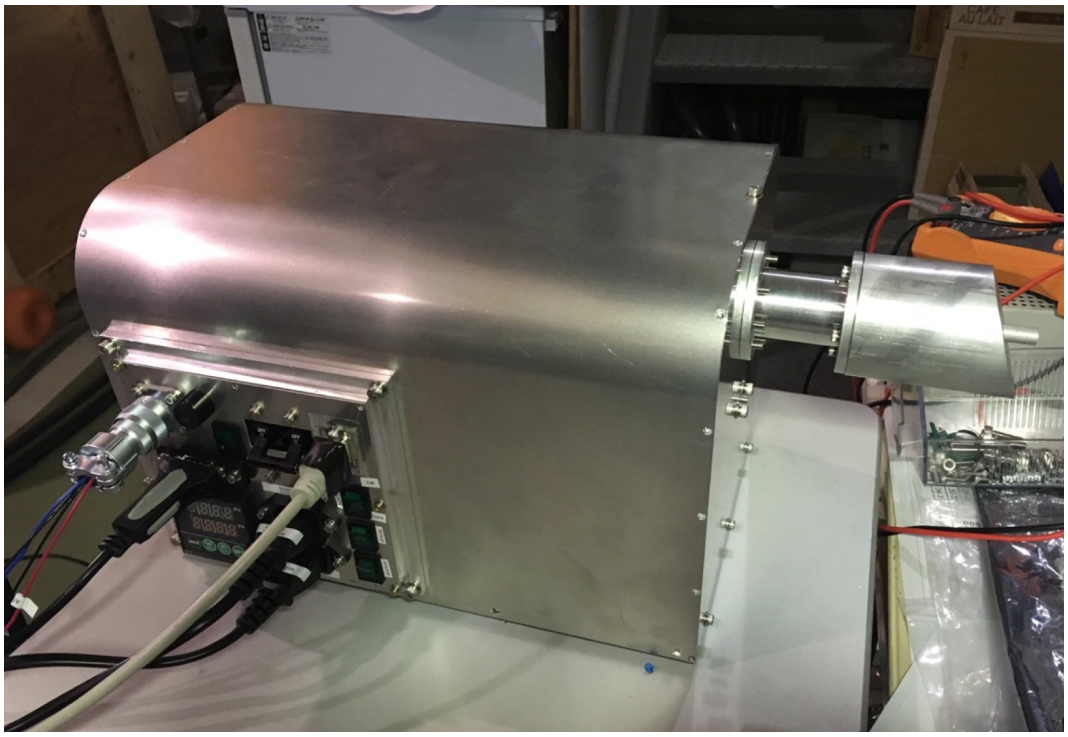

Figure 3.16: Picture of the gain calibrator. The calibration signal is emitted from the light pipe. Private communication with Sayuri Takatori .

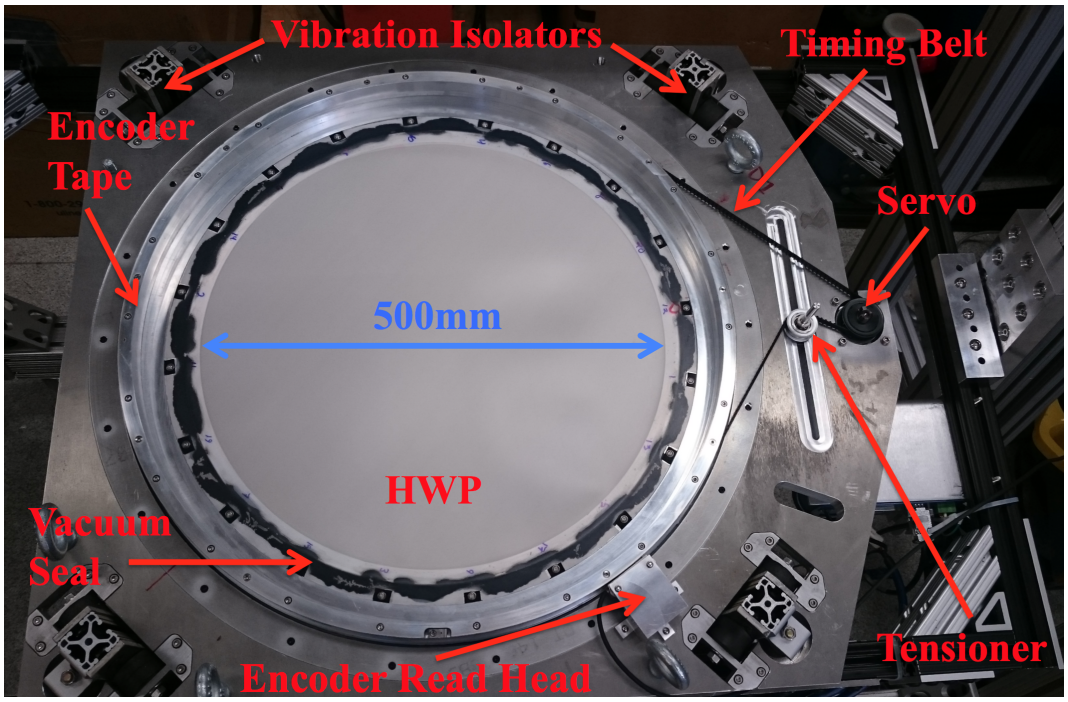

Figure 3.17: Photo of the polarization modulator. Private communication with Charles Hill.

3.8 Technical challenges and system requirements

PB-2 has a large focal plane that mounts 7588 bolometers. To achieve the goals of our measurements, the requirements of the thermal design and optical efficiencies are much harder than previous experiments. According to the science requirements in Sec. 2.7, the PB-2 system has to meet the following requirements.

- **RQ1: Thermal requirements**

  Table 3.2 shows the estimated heat transfer of the PB-2 cryostat, which takes cooling powers from pulse tube coolers and a sorption cooler into account. Among the challenges described in the previous section, we will focus on the thermal design of the PB-2 receiver system, in particular the proper choice of IR filters in this thesis. For this purpose, we need to select IR filter system to satisfy the requirements on the thermal loads.

- **RQ2: Hold time**

  We will measure the CMB patches every day. For the sufficient measurements, the hold time of the sorption cooler is required to be larger than 24 hours.

- **RQ3: NET array**

  We need to satisfy the requirement of total array NET of 4.3 $\mu\mathrm{K}\sqrt{\mathrm{sec}}$. One of the goals of this thesis is to establish and demonstrate thermal design that satisfies this requirement.

- **RQ4: Diffraction limited optics**

  The beam width of the HTT affects the sensitivity of the high multipole measurement [65]. This is because the small scale structure of the polarization pattern beyond the angular resolution is smeared out. When the optics reaches the diffraction limit, the beam width is minimized for a given system. Therefore, we have to achieve the diffraction limited optics for all the pixels at the same time.

Table 3.2: Estimated heat transfer. This table is from Tomaru et.al, with modifications based on measurements in this thesis [16]

Thermal stage	Cooling power	Heat load			
300 K → 50 K (PTC 40 deg.)	30 + 30 = 60 W	radiation cable support optical	8.2 + 9.7 = 17.9 W 3.7 W 0.92 W 17 W	39.5 W (65 %)	20.5 W (35 %)
50 K → 4 K (PTC 40 deg.)	1.4 + 1.4 = 2.8 W	radiation cable support optical	0.06 + 0.07 = 0.13 W 0.14 W 0.09 W 0.5 W	0.86 W (31 %)	1.94 W (69 %)
4 K → 2 K	250 μW	radiation cable support	0.5 μW 8 μW 2 μW	10.5 μW (4.2 %)	239 μW (95.8 %)
2 K → 0.35 K	250 μW	cable support optical	0.74 μW 2 μW 10 μW	12.7 μW (5.1 %)	237.3 μW (94.9 %)
2 K → 0.27 K 0.4 K → 0.27 K	10 μW	radiation cable support optical	32 nW 4 nW 17 nW 5 μW	5 μW (50 %)	5 μW (50 %)

Chapter 4

Development and characterization of optical and thermal elements

Some CMB telescopes employ optical elements such as lenses and filters that are maintained at 4 K to minimize their thermal emission [65]. Typical dielectric materials used to fabricate lenses include polyethylenes, such as high-density polyethylene (HDPE) or ultra high molecular weight polyethylene (UHMWPE) [66, 67, 68]. These materials are ideal because they are relatively economical and have low loss at millimeter wavelengths. This chapter introduces four technologies, alumina lenses, alumina filters, AR coatings with thermally-sprayed mullite and expanded polyimide (Skybond Foam), and black body absorbers for millimeter waves (called KEK black). These optical elements are essential in the POLARBEAR-2 experiment to meet the **RQ 1** $\sim$ **RQ 4**, listed in Section. 3.8. I have played a key role in developing these technologies. The R&Ds of these technologies are described in this chapter.

4.1 Alumina lens

According to the **RQ3** and **RQ4**, the required throughput should increase. Consequently, the optical elements (lenses and filters) must be larger than $\sim$ 30 cm, and the use of a polyethylene lens with such a diameter is problematic for two reasons: the index of refraction (IOR) and diameter. The POLARBEAR-1 experiment uses ultra-high molecular weight polyethylene (UHMWPE) [43]. The IOR of HDPE or UHMWPE is about 1.5. As the lens diameter increases, the lens becomes thicker and highly curved. The resulting steep incident angle of radiation on the lens surface is not ideal for polarimetry. Thus, it is desirable to find another material with a larger IOR and a higher thermal conductivity that still has low loss at millimeter wavelengths. We also have to meet the requirement of diffraction-limited optics. To reduce the aberration of POLARBEAR-2 receiver system, it is required to use material with the large diameter and large IOR The typical values of the desired diameter and IOR are 500 mm and ~ 3.

Such a material may be silicon. The ACTpol experiment employs the silicon lenses [69]. The IOR

of 3.4 in the millimeter wavelength range and thermal conductivity that is a few orders of magnitude greater than that of plastics [70]. Although silicon is a candidate for a lens material, the size of lenses made from silicon is limited by the size of available ingots; the largest ingot is typically about 300 mm in diameter and the price is also very high.

We therefore propose sintered alumina, Al_2O_3, as a candidate material for use in millimeter wave telescopes at cryogenic temperatures. Alumina has already been used in radio frequency applications. The IOR of alumina is 3.1 in the millimeter wavelength range and the thermal conductivity is similar to that of silicon [70]. Moreover, alumina is available in the size up to about 1 m with thicknesses of a few centimeters. Therefore, alumina appears to satisfy the required conditions for millimeter wave applications.

However, the alumina has a high reflectance. Therefore, we have to make the anti-reflection (AR) coating on both surfaces. The technology of the AR coating is described in the next section. In this section, we describe newly-developed alumina lenses for the POLARBEAR-2 experiment. In our R&D, we first characterize the alumina material property, such as IOR, loss tangent and thermal contraction. Second, we actually make the alumina lenses and use the coordinate measuring machine (CMM) for shape measurements and compare the results with the design value. Third, we measure focal points of lenses and compare the results with the prediction. We explain the series of the characterization of the alumina lenses in the following.

4.1.1 Material property

Sintered alumina is fabricated by Nihon Ceratech [71]. Table 4.1 shows the basic properties of three types of alumina, which we call alumina 99.5 % LD, alumina 99.9 %, and alumina AJPF. In this section, we measure the IOR and loss tangent of these samples whose thickness and diameter are 40 mm and 50 mm, respectively. The details of samples are listed in Table.4.1. Figure 4.1 shows photographs of three alumina samples, with purities of 99.5 %, 99.9 %, and 99.99 %, and the corresponding photomicrographs. Each photomicrograph is a montage of 1000 photomicrographs made with a focusing pitch of 0.1 μm. The 99.5 % purity sample underwent an extra process to decrease the loss tangent in the radio frequency range. The alumina 99.5 % LD sample has large voids (diameters of about 30 μm) . The average crystal size is 8 μm and the crystal boundaries were upon the sintering. The average crystal size of alumina 99.9 % is smaller than that of the alumina 99.5 % LD, and the melting point of alumina 99.9 % is below that of the alumina 99.5 % LD. Moreover, the voids of alumina 99.9 %, at about 5 μm are less than those of alumina 99.5 % LD. Finally, the sample of alumina AJPF has sheen, which was obtained using the pow-free method [71], and its crystal size was about 1 μm.

4.1.1.1 Transmittance of alumina

Measurement system The IOR and the loss tangent of AR materials are obtained from transmission measurements. We explain the measurement system shown in Fig. 4.2. The millimeter wave is generated

Table 4.1: Basic properties of three types of alumina. The purity, Young's modulus, Poisson's ratio, and density are obtained from the technical data sheet of Nihon ceratech [71]. The crystal size is calculated from the montage photomicrographs. The group velocity is calculated from Young's modulus and the density.

	Alumina 99.5 LD	Alumina 99.9	Alumina AJPF
Purity [%]	99.5	99.9	99.99
Color	Ivory	Cream	White
Crystal size [μm]	4-10	2-4	1-2
Young's modulus [GPa]	390	400	400
Poisson's ratio	0.24	0.24	0.24
Density [kg/m^3]	3.9×10^3	3.9×10^3	4.0×10^3
Group velocity [m/sec]	1.0×10^4	1.0×10^4	1.0×10^4

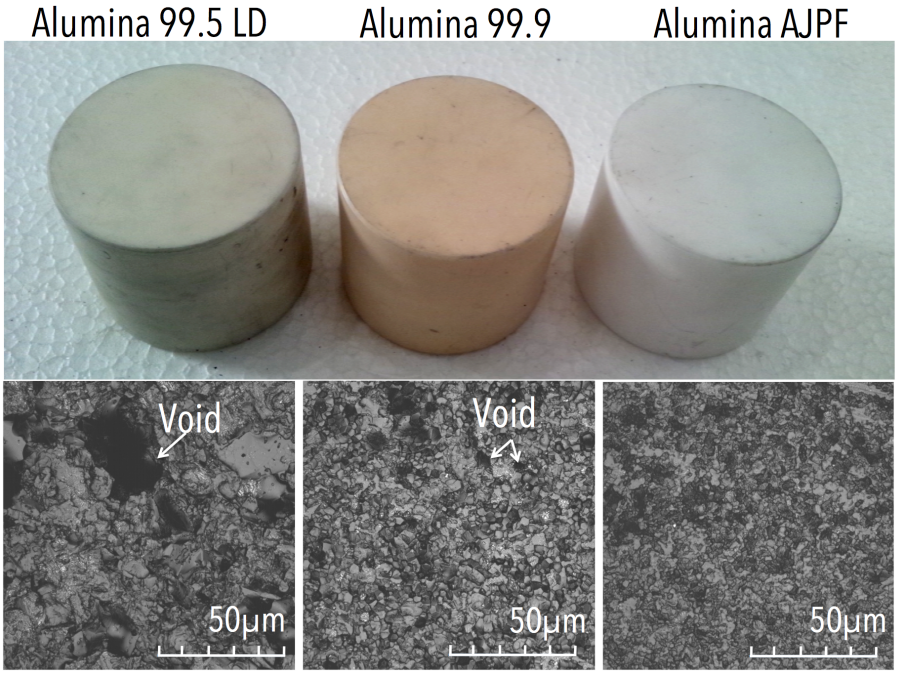

Figure 4.1: Three types of alumina and the corresponding photomicrographs. From left to right, the purities are 99.5 %, 99.9 %, 99.99 %. These samples are referred to alumina 99.5LD, alumina 99.9, and alumina AJPF, respectively. The photomicrographs are montage of 1000 photos, each made with a focusing pitch of 0.1 μm. The structures of an alumina comprise cells of sapphire crystals. Alumina 99.5 LD and alumina 99.9 % contain large and small voids.

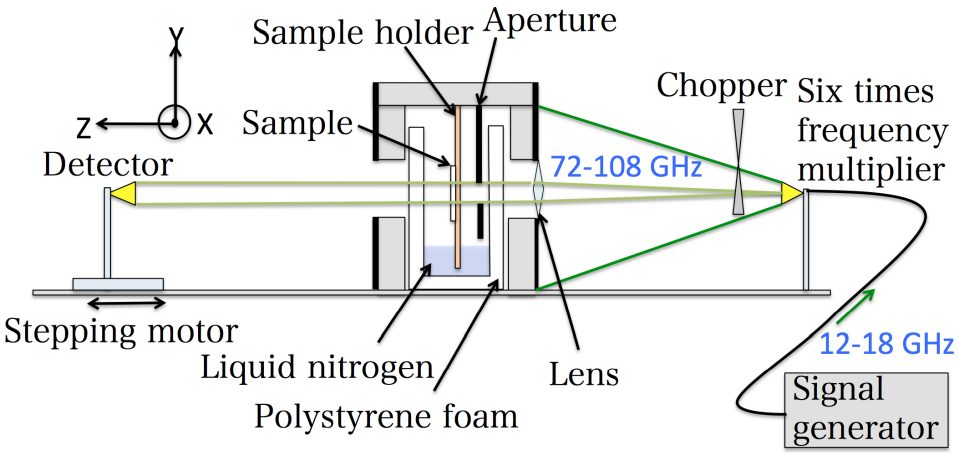

Figure 4.2: Schematic of the millimeter wavelength transmission measurement system. The incident signal is generated by a signal generator operating between 12 and 18 GHz, with multiplied ×6, ×8 and ×9 by a frequency multiplier. The multiplied signal is emitted from the horn and has a 30 degrees beam divergence. The beam is collimated with a rexolite lens and aperture with a hole diameter of 20 mm. The beam is chopped at 20 Hz. A stepping motor scans along the z-direction to measure the standing wave. The sample is placed in the sample holder, which is made of OFHC copper. To measure the transmission at 77 K, the polystyrene foam container is filled with liquid nitrogen and the sample was cooled conductively, as done in previous research [74].

by using a signal generator with a sixfold frequency multiplier. The frequency range of the signal generator is between 12 and 18 GHz [72]. The multiplied frequency is between 72 and 108 GHz. The frequency resolution of our system is 0.12 GHz. The beam is collimated by a lens and the sample is placed immediately after the aperture. The transmitted beam is detected by a diode detector. The signal is chopped at 20 Hz for heterodyne detection at the modulated frequency with a lock-in amplifier, and the signal is recorded by the dedicated data acquisition system (DAQ) [73]. The detector is moved along the optical axis for more than a half wavelength to subtract the effect of a standing wave in the measurement setup. For each material type, we prepare a sample with a diameter of 50 mm. We measure the power with and without the samples and take the ratio to obtain the transmission.

Fit function The transmittance of bulk sample is described as

$$T_s = \frac{T^2\mu^2}{1-2R\mu^2\cos(2\phi)+R^2\mu^4}, \tag{4.1}$$

$$T = \frac{4n}{(1+n)^2}, \tag{4.2}$$

$$R = \frac{(1-n)^2}{(1+n)^2}, \tag{4.3}$$

$$\mu = \exp\left(-k_0 nd\tan\delta\right), \tag{4.4}$$

$$\phi = k_0 nd, \tag{4.5}$$

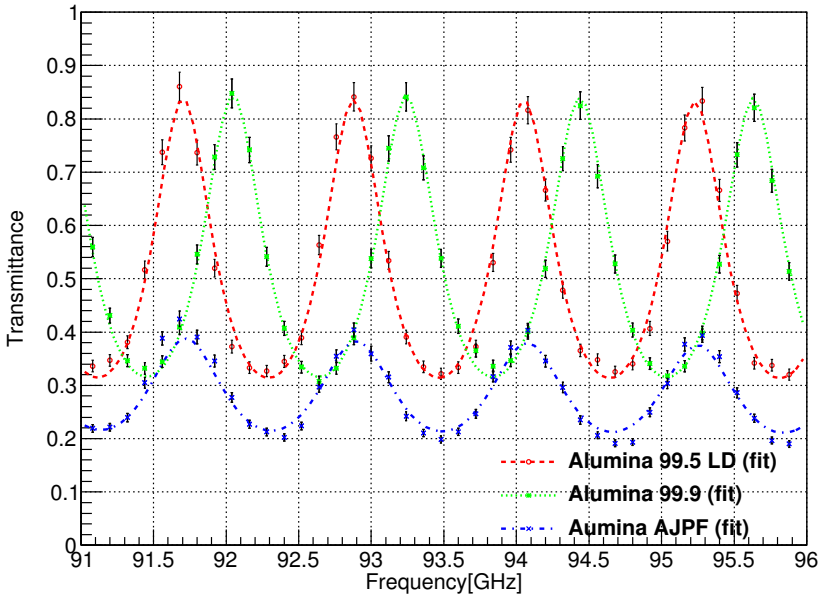

Figure 4.3: The measured transmittance of the alumina at 300 K. The red, green, and blue points are the measured alumina transmittance of 99.5, 99.9 and 99.99 % purities, respectively. The dashed curves are the best fit with Eq. (4.1).

where the n is IOR the loss tangent is tan δ, the thickness of the sample is d, and the wave number is $k = 2\pi\nu/c$. The detail of this equation is shown in Appendix A.

Results We fit the data with Eq. (4.1) to obtain the IORs and loss tangents. Figure. 4.3 shows the example of the measurement. Table 4.2 shows the result of IORs and loss tangents for the three different alumina at 77 and 300 K. We select alumina 99.9 as the lens material.

4.1.1.2 Thermal contraction

A thermal contraction is one of the key properties because the lens curvature radius shrinks with cooling down to 4 K. However, the characterized temperature at 77 K is sufficiently low to estimate the thermal contraction at 4 K because the thermal contraction is saturated below 100K. Then, the curvature between 77 K and 300 K is changed as

$$R_{77K} = \alpha R_{300K}, \tag{4.6}$$

where α is the thermal contraction of the alumina. We define the linear thermal contraction using these values as

$$\alpha = \frac{L_{300K} - L_{77K}}{L_{300K}} \tag{4.7}$$

We measure the thermal contraction using a dial indicator as shown in Fig. 4.4. First, we measure the thicknesses of samples at 300 K (L_{300K}) for 10 times. Second, we measure the thicknesses of the

Table 4.2: Measured optical parameters of alumina. We employ the 99.9 % purity samples for lens material.

Name	Temperature [K]	Thickness [mm]	Index	Loss-tangent [$\times 10^{-4}$]
Alumina 99.5 LD	300	$40.63^{\pm 0.01}$	$3.144^{\pm 0.005}$	3.7 ± 1.7
Alumina 99.9	300	$40.04^{\pm 0.01}$	$3.134^{\pm 0.003}$	3.2 ± 1.0
AJPF	300	$40.05^{\pm 0.01}$	$3.187^{\pm 0.005}$	17 ± 2
Alumina 99.5 LD	77	$40.63^{\pm 0.01}$	$3.117^{\pm 0.005}$	3.0 ± 1.1
Alumina99.9	77	$40.04^{\pm 0.01}$	$3.109^{\pm 0.004}$	1.8 ± 1.0
AJPF	77	$40.05^{\pm 0.01}$	$3.162^{\pm 0.005}$	12 ± 2

Table 4.3: Measured thermal contraction of the alumina between 300 and 77 K. The thicknesses were measured with a micrometer; thus, the thickness errors correspond to the uncertainty of micrometer. The thickness differences were measured with a dial indicator. The errors in the thickness differences correspond to statistical errors. The samples were cooled to 77 K.

Name	Thickness L [mm]	Thickness difference ΔL	CTE α [%]
Alumina 99.5 LD	$40.63^{\pm 0.01}$	0.021 ± 0.002	0.052 ± 0.004
Alumina 99.9	$40.04^{\pm 0.01}$	0.020 ± 0.003	0.051 ± 0.007
Alumina AJPF	$40.05^{\pm 0.01}$	0.021 ± 0.001	0.051 ± 0.003

samples when the samples are submerged in the liquid nitrogen (L_{77K}). For the crosscheck, we measured the aluminum sample, whose thermal contraction efficiency is well measured as the validation of our measurement scheme. The result is

$$\alpha_{Al} = 0.33 \pm 0.01 \ \%, \tag{4.8}$$

where we estimated the error by computing the RMS from the 10 measurements. This result is consistent with a literature value. Table 4.3 shows the results of all the samples. Therefore, we conclude that the thermal expansion of alumina is ~ 0.05 %.

4.1.2 Fabrication and shape measurement

We fabricate the three lenses, field, aperture, and collimator lenses. We chose the alumina with 99.9 % purity as the material of the lenses because of its lowest loss tangent among the samples we tested, for minimizing photon noise in detection bands. All the lenses are fabricated in Nihon Ceratech.

We characterize the shape of alumina lenses using a coordinate measuring machine (CMM) as shown in Fig. 4.5 [75]. The specification of the CMM is listed in Table 4.4. We place the alumina lenses on the stage of CMM for 3 hours to stabilize the temperature. The thickness of lenses are measured on X axis

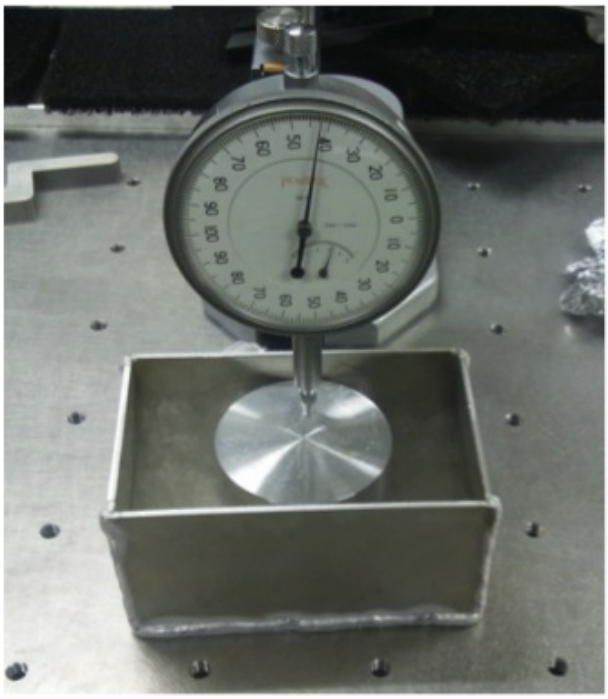

Figure 4.4: The picture of the setup for the thermal contraction measurements. We place the samples in the aluminum box. We measure the thicknesses of samples using a dial indicator. When we perform measurements at cold temperature, we fill liquid nitrogen in the aluminum box.

and Y axis with 5 mm pitches. The measured lens shapes are shown in Fig 4.6 and 4.7. The red and blue points are the measured values. These errors are propagated from the CMM statistical precision. The lens shape is obtained as

$$z = \frac{(1/R_{300K})x^2}{1+\sqrt{1-(1+k)x^2(1/R_{300K})^2}}, \tag{4.9}$$

where R_{300K} and k are the curvature radius and conic constant. Best fit results of these shapes are listed in Table 4.5. These results provide us with important parameters for the alignment of lenses for achieving the diffraction-limited optics. More details are shown in Chap 6.

4.1.3 Focus measurement

The aperture lens is characterized with the system shown in Figure 4.8. We measure X-Y beam maps at 90 GHz with a movable detector. Waist points in the X and Y directions are estimated from measurements of beam widths at various Z positions as shown in Figure 4.8. We plot and fit the measured beam width at each position on the optical axis. The fit model is described as

$$\omega(z) = \omega_0 \left[1 + \left(\frac{\lambda(z_0 - z)}{\pi\omega_0}\right)^2\right]^{\frac{1}{2}}. \tag{4.10}$$

The results of the beam waist measurements are 472 ± 2 (stat.) $\pm$ 12 (sys.) mm on the X-axis and 478 ± 2 (stat.) $\pm$ 12 (sys.) mm on the Y-axis, where the systematic uncertainties are from the uncertainty

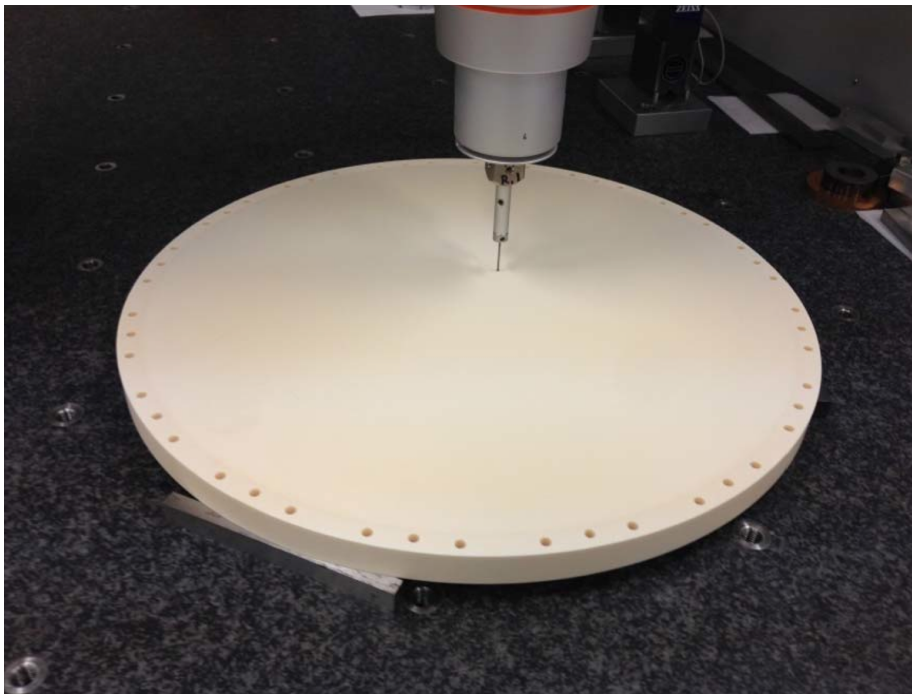

Figure 4.5: Picture of the alumina lens being measured with the CMM.

Table 4.4: Specification of the CMM. The CMM is made by carl-Zeiss company [75]. The measurement size is limited by the available sample size. Accuracy consists of arm uncertainty and sample length, L. Maximum mass is the maximum sample weight.

Type	ZEISS UPMC850 [75]
Measurement size [mm]	$850 \times 1150 \times 600$
Accuracy	$0.6 + L/600$ μm
Optical table size [mm]	$1000 \times 1970 \times 850$
Maximum mass [kg]	1500
Probe diameter	2 mm
Probe weight	0.2 N
Temperature	20 degree Celsius

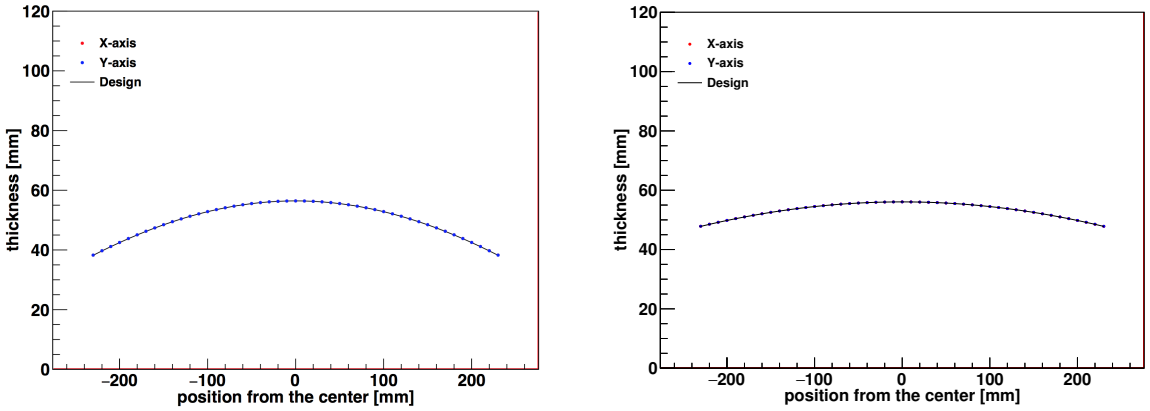

Figure 4.6: The measured shapes of lenses. Left (right) figure is the front (back) side of field lens. The red and blue points are the measured points. The errors are propagated from the accuracy of probe position. For each figure, the black curve is the design value.

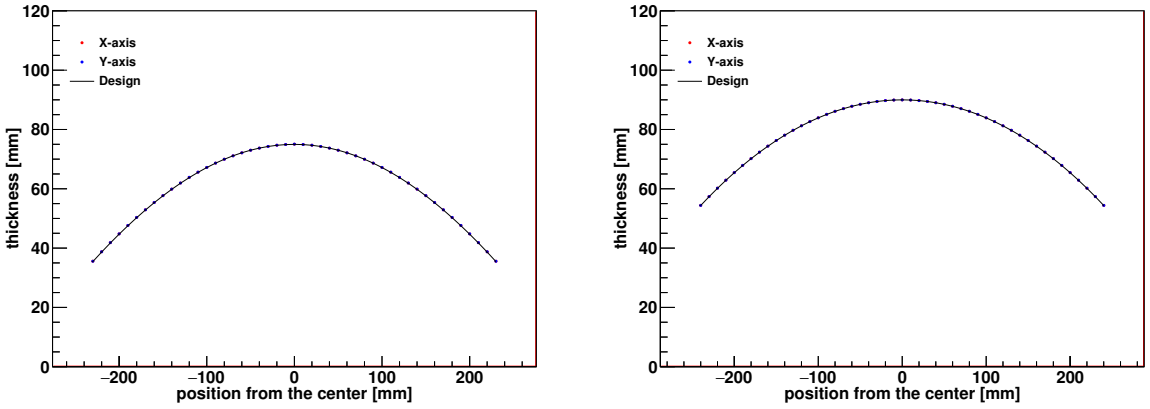

Figure 4.7: The measured shapes of lenses. Left and right plots are aperture and collimator lenses, respectively. The red and blue points are the measured points. The errors are propagated from the accuracy of probe position. The black curve in each figure shows the design value.

Table 4.5: Measured parameters of lenses. We fit the shapes of lenses using Eq.(4.9) as shown in Fig.4.6 and 4.7. The errors are propagated from the uncertainty of the CMM.

	Curvature radius [mm]	conic constant
Field lens (front)	1372.21 ± 0.26	-9.978 ± 0.031
Field lens (back)	3163.41 ± 1.28	-11.58 ± 0.33
Aperture lens	633.73 ± 0.056	-2.846 ± 0.003
Collimator lens	827.21 ± 0.07	0.082 ± 0.004

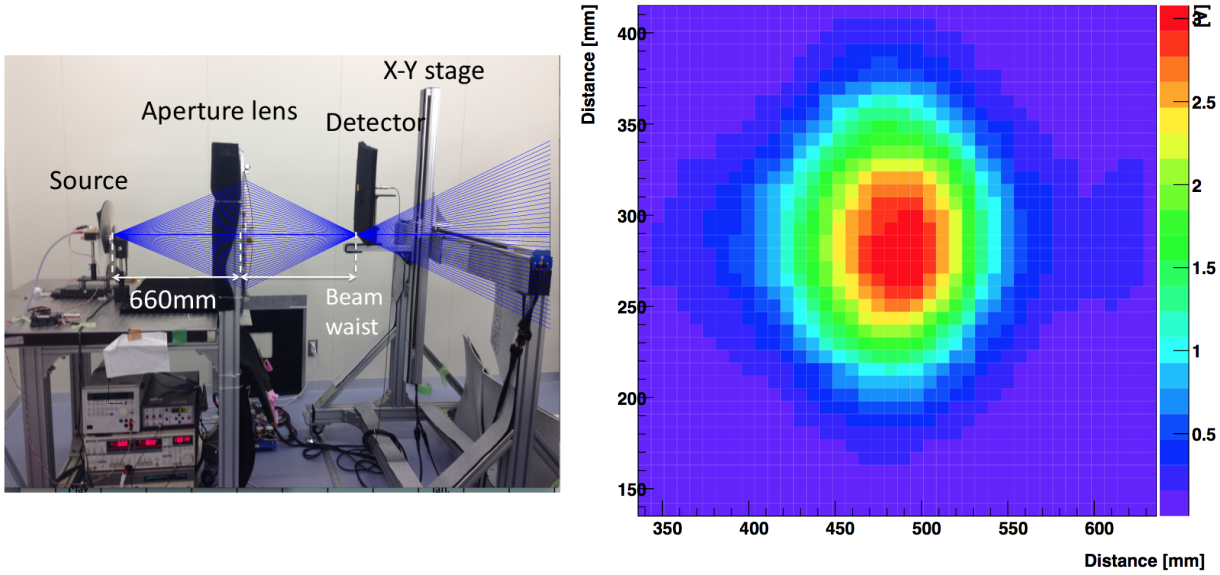

Figure 4.8: Left: Beam measurement system. We mounted a 90 GHz source on the optical bench and a detector on the X-Y stage. We place an alumina lens between the source and detector. The detector moves in a 900 × 900mm square region in the X-Y plane for measuring a beam map. The source moves in the Z direction on the optical bench. Right: Example of the beam width measurements. We fit the data with a 2D Gaussian function to obtain the beam width in X and Y directions.

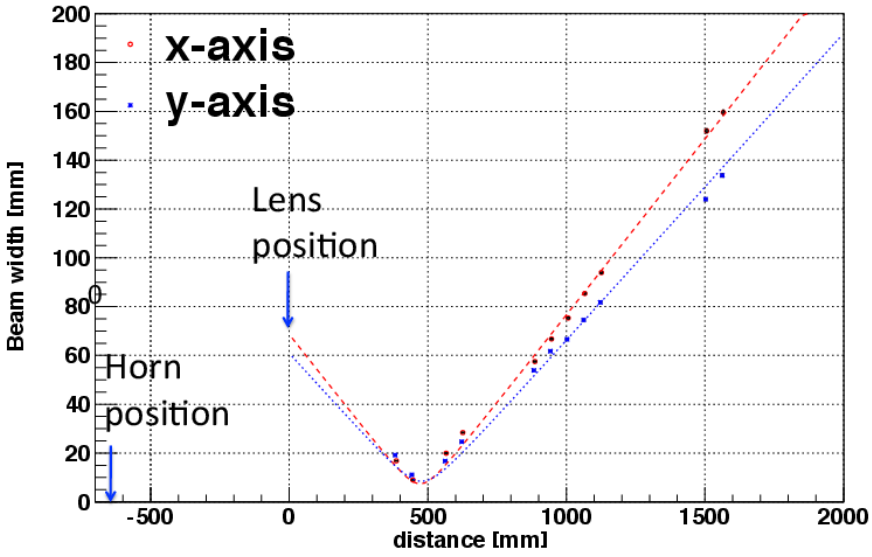

Figure 4.9: The measured beam width in X and Y axes. The distance corresponds to the length of the optical axis from the source and detector. We define the lens position as the origin of the horizontal axis. Then we place the horn at -620 mm. The red and blue curves are best fits with Eq. (4.10).

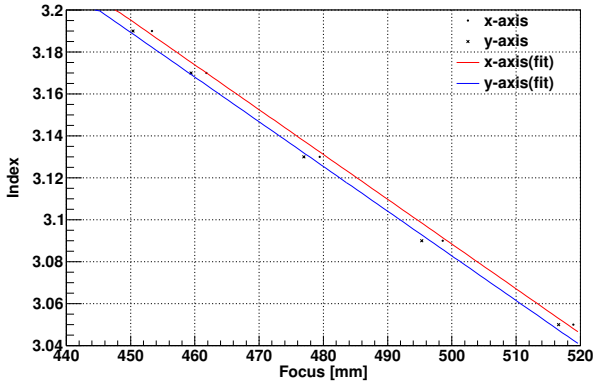

Figure 4.10: The conversion function from the measured focus point to the index of refraction based on ZEMAX simulation. The red and blue lines are the best fit with the simulated beam waist as a function of index of refraction. The offset between two lines arises from the waist position difference between the X and Y axes (w_0 in Fig. 4.11).

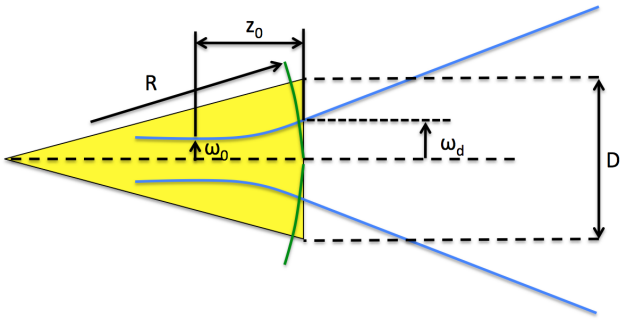

Figure 4.11: The schematic view of the horn model. R is the radius of the horn. z_0 is the distance between the focus and tip of the horn. w_0 and w_d are beam waists at focus and tip. D is length of the side of the horn.

of the curvature radius and the conic constant obtained with a coordinate measuring machine shown in Table. 4.5.

As shown in Fig. 4.10, the focus point and IOR of alumina lens are directly related. Therefore, IOR of the alumina lens is reconstructed from the focus point. We obtain $3.148 \pm 0.004(stat.) \pm 0.026(sys.)$ on the X-axis and $3.128 \pm 0.004(stat.) \pm 0.026(sys.)$ on the Y-axis. These results agree with those in Table 4.2. Systematic uncertainties are small enough to meet the PB-2 optics requirements. Here the offset of beam waist in the horn is corrected as follows.

In this measurement, we estimate IORs using ZEMAX simulation with assuming the parameters of a quadrangular pyramidal horn. The beam waist in the horn is described by the following equation:

$$\omega_0 = \frac{\omega_d}{\sqrt{1 + \left(1 + \frac{\pi\omega_d}{\lambda R}\right)^2}}, \tag{4.11}$$

where ω_d is the beam width at the edge of horn, λ is wavelength, and R is length of the horn. The relation of these parameters is shown in Fig. 4.11. Then, we can describe the beam width at edge of horn, $\omega_d = D/2\Omega$, where Ω and D are the structure constant and the length of the side of the horn. In this study, we assume that $\Omega = 2.857$. Therefore, the position of beam waist in the horn depends on the rectangular shapes with X and Y axis. The offsets of the beam waist can be written by

$$z_0 = \frac{R}{1 + \left(\frac{\lambda R}{\pi\omega_d^2}\right)^2}. \tag{4.12}$$

The estimated z_0 of X axis and Y axis are 6.2 mm and 2.3 mm, respectively.

4.1.4 Short summary of alumina lens development

The PB-2 receiver system housing the large optical system requires to reduce the aberration at each detector. To reduce the aberration, we select the alumina material. We characterize the three types of purity samples at cold temperature. We choose the 99.9 % purity alumina as lens materials because of most least loss tangent of the three sample and meet our requirement. We fabricate the three alumina lenses and measured the shape and IOR. We succeed to develop and characterize the alumina lenses.

4.2 Anti-reflection coating

The anti-reflection (AR) coating is one of the key technologies for the alumina or silicon optics. The three alumina lenses, an alumina IR filter and silicon lenslets are the material of high reflectance due to the large index of refraction, > 3. From a rough calculation, ~ 30 % of the signal is expected to be lost per component in case of no AR coating. To reduce the surface reflection, we place the AR coating on the surface of materials. The PB-1 experiment also used one layer AR coating on lenslets [43]. However, one layer AR coating does not satisfy the band width of POLARBEAR-2 experiment due to the 95 and 150 GHz detectors. We have to develop the broadband transmitted AR coating. Furthermore, the diameter of our optical component is larger than that of other experiment. We require 500 mm in diameter. According to the previous study, ACTpol succeeded in making two- and three-layer AR coatings on silicon lenses, whose diameters were ~ 300 mm [76]. They succeeded using the technology of sub-waves grading (SWG) [77]. It is theoretically possible to apply this technology to an alumina surface; however, it is difficult because the dicing blade is subject to wear and groove pitch and depth are changed. Furthermore, to make a large ingot of silicon and machining the material are very expensive.

SPIDER used a polyimide sheet as an AR coating on sapphire, whose diameter was approximately 250 mm [78]. One reason they chose polyimide is that the thermal expansion of polyimide is similar to sapphire. This method is very easy to perform and less expensive than the method of epoxy and SWG. However, to our knowledge, there have been no recent studies for two-layer AR coating on a large surface.

Recently, the method of thermal spraying has been proposed [79]. This is a state-of-the-art technique for AR coating. We tried to make the mullite surface using this method. There is no cracking with the thermal spraying as an option that enables two-layer AR coating on the large surfaces.

4.2.1 Requirements

Requirements on a AR coating for the PB-2 experiment are as follows;

- 95 % transmittance must be achieved at the detection bands, which are 95 and 150 GHz frequency region with a 30 % fractional bandwidth.
- the alumina diameter must be extendable to 500 mm or larger;

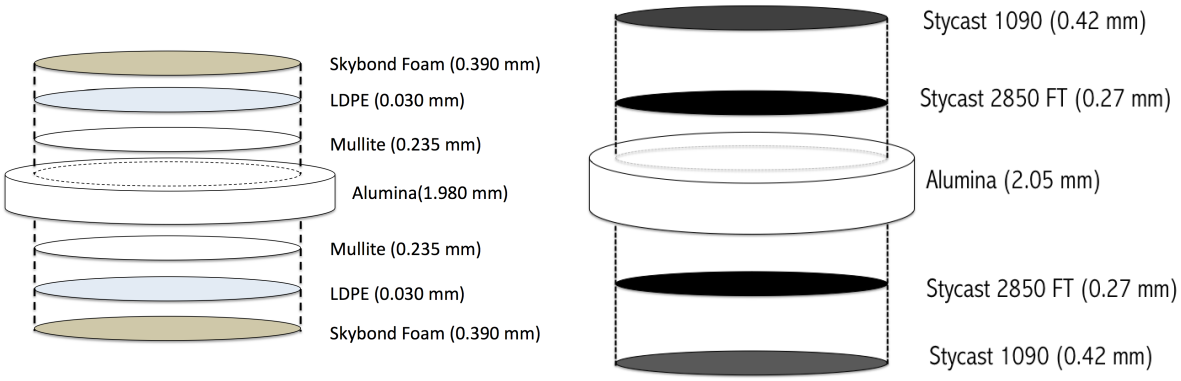

Figure 4.12: Left: A schematic view of the alumina IR filter configuration. The layer of mullite and Skybond Foam are mounted on the alumina disc. Then, we sandwich the LDPE between mullite layer and Skybond Foam layers. Right: Same as that of epoxy coating,

- the fluctuation of the optical path length with AR coating must be less than $\lambda/50$, where λ is the wavelength of the incoming electromagnetic wave.

The sensitivity of the CMB experiment depends on the transmittance of AR coating in the detection band. The thickness of the AR coating is designed to be $\lambda/4$ so that the reflected beam is canceled. The uniformity must be lower than $\lambda/50$, which corresponds to a transmittance uncertainty of 1 %.

4.2.2 Epoxy option and Skybond-Mullite option

We develop two types of two-layer AR coatings, which are epoxy and Skybond-Mullite coating. Both options meet the requirements of the AR coating. The materials of the epoxy option are Stycast 2850 and Stycast 1090, which are specialized for the cryogenic application. On the other hand, the materials of Skybond-Mullite option are the expanded polyimide and mullite. Figure 4.12 shows configuration of two-layer AR coating for two types. Our design consists of alumina that has two-layer anti-reflection (AR) coating on both sides. The AR coating is designed to maximize the transmittance of the normal incident radiation at two detection bands, 95 and 150 GHz, each with 30 % bandwidth.

4.2.3 Material property

We characterize the IORs and loss tangents of the AR materials with transmittance measurements. The measurement system is described in Sec. 4.1.1.1. In the following subsection, we explain the details of AR materials.

4.2.3.1 Mullite

Mullite is one of the ceramic materials; we place the mullite on both alumina surface using the method of thermal spraying made by the Tocalo corporation [80, 79]. The thicknesses of the alumina and mullite

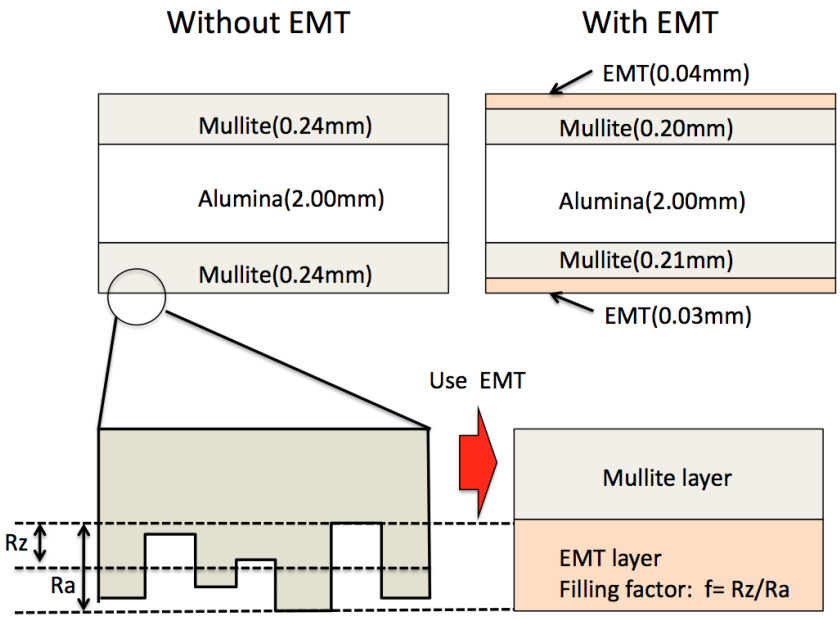

Figure 4.13: The schematic view of the effective medium theory at the mullite surface. The mullite has an asperity surface. We can approximate an asperity surface as the virtual layer based on the EMT. The effective IOR of the virtual layer is described by Equation (4.13). This equation depends on the filling factor which is given by the ratio between $R_{\rm a}$ and $R_{\rm z}$.

are 1.98 mm and 0.235 mm, respectively. These are optimized to obtain the best value for the average transmittance over the 95 and 150 GHz frequency bands.

We measure the transmittance of mullite at 298 and 81 K. The measured frequencies are between 72 and 140 GHz, respectively. This experiment yields a fringe pattern from the interferogram of the alumina and mullite layers. The mullite has asperity structure, with a surface roughness R_a and a ten-point average roughness R_z of 6 μm (6 μm) and 36 μm (34 μm) at one (another) side, respectively. We apply the effective medium theory (EMT) [81] to the surface of mullite as follows:

$$n_{\rm eff} = n_m \sqrt{\frac{2(1-f)(n_0^2 - n_{\rm m}^2) + n_0^2 + 2n_{\rm m}^2}{2n_{\rm m}^2 + n_0^2 + (1-f)(n_{\rm m}^2 - n_0^2)}}, \tag{4.13}$$

where $n_{\rm eff}$, $n_{\rm m}$, and n_0 are the effective IOR, IOR of mullite and vacuum, respectively, and $1-f$ is the filling factor. We can approximate the asperity surface as the virtual layer from the EMT as shown in Fig. 4.13. The f of the EMT layer is equal to $R_{\rm a}/R_{\rm z}$. The estimated IOR and loss tangent with and without EMT are shown in Table 4.6 and Fig. 4.14. The model with EMT is fitted better with measured data, and we employ the model to derive the IOR and loss tangent in the 95 GHz band.

We measured the IOR and loss tangent of mullite within the 95 GHz band. The results of uniformity for IORs and loss tangents are shown in Fig. 4.19. The definitions of the measured points are shown in Fig. 4.19. Each IOR and loss tangent are consistent within the statistical error.

Table 4.6: The basic properties of mullite with and without EMT.

	T[K]	n	$\tan\delta$ $[\times 10^{-3}]$	χ^2/N
without EMT	298	$2.35^{\pm 0.03}$	$36.8^{\pm 3.3}$	163.7/42
	81	$2.34^{\pm 0.04}$	$30.9^{\pm 3.5}$	193.0/42
with EMT	298	$2.53^{\pm 0.03}$	$13.2^{\pm 1.7}$	98.3/42
	81	$2.51^{\pm 0.03}$	$5.4^{\pm 3.4}$	80.4/42

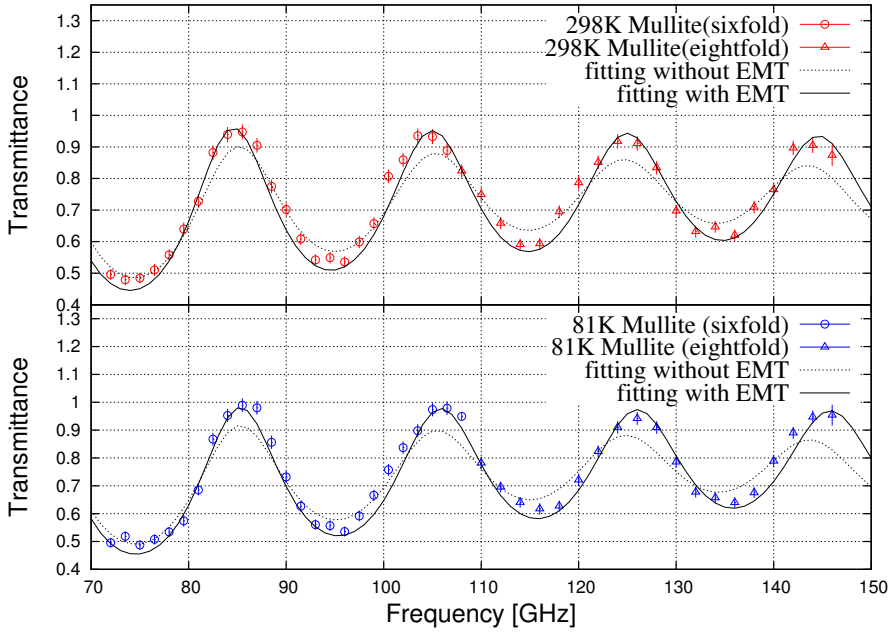

Figure 4.14: The transmittance of alumina with mullite coating at 298 K (top) and 81 K (bottom). The alumina and mullite thicknesses are 2.00 and 0.24 mm. The error bars correspond to systematic errors from fluctuation of the millimeter source.

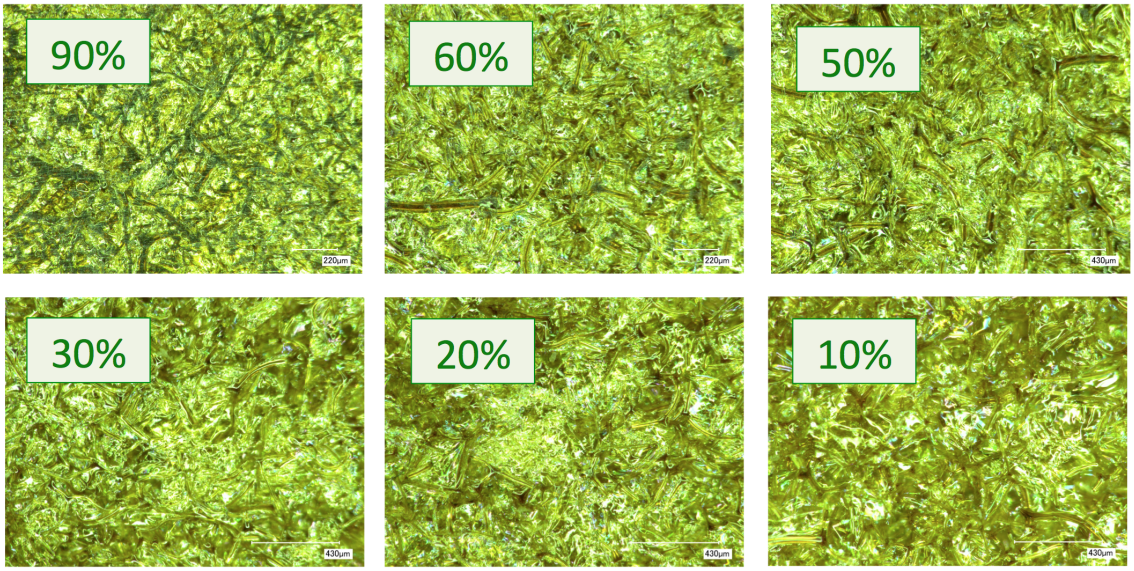

Figure 4.15: Photomicrograph of Skybond Foam. The filling factor is between 10 and 90 %. The bubbles are pressed with a 10 ton weight when the sample is made and the unit cell size is $10 - 20$ μm.

4.2.3.2 Skybond Foam

The Skybond Foam is an expanded-polyimide, which is manufactured by the IST corporation [82]. Figure 4.15 shows a photomicrographs of the Skybond Foam, for which the filling factors are between 10 % and 90 %. The filling factor is the volume-filling fraction of the polyimide in the mixture, which can be controlled from 10 % to 90 %. Each cell of the Skybond Foam has a typical size of 20 μm. In general, the IORs and loss of the material depend on the filling factor [83]. We measure the IOR and loss tangent of Skybond Foam with each filling factor between 10 and 90 % (10, 20, 30, 50, 60, and 90 %). Results are shown in Fig. 4.16. The results of IORs measurement are fitted with Eq.(4.13). The estimated phenomenological parameters of the EMT curves are

$$n_0 = 1.049 \pm 0.005 \tag{4.14}$$

$$n_m = 1.748 \pm 0.006, \tag{4.15}$$

The dimensions of each sample are 100 mm $\times$ 100 mm $\times$ 10 mm.

4.2.3.3 Epoxy

The two-layer AR coating consists of the epoxy glues, Stycast 2850 FT and Stycast 1090, manufactured by Emerson and Cuming [84, 74, 57]. When we use Stycast, we mix catalyst and Stycast. Then we make a thin layer on the alumina surface. We use catalyst 24 LV and 9 M with Stycast 2850 and Stycast 1090. We measure the transmittance of the disc of the Stycast samples as shown in Fig. 4.17. The thickness is measured with the micrometer as listed in Table 4.7. The measured transmittance is shown in Fig. 4.18. We estimate the indices and the losses from the transmittance measurement with Eq. (4.1). The results

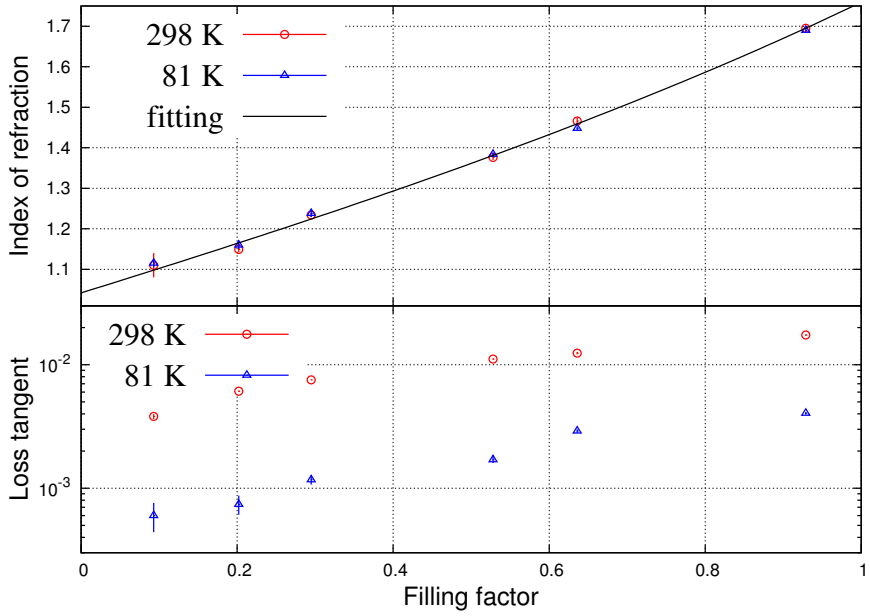

Figure 4.16: Uniformity of IOR (top) and loss tangent (bottom) as a function of filling factor. The sample is measured at 298 K or 81 K. The error bars in the x axis correspond to systematic errors from millimeter source fluctuation. The black curve shows the best fit.

are listed in Table 4.7.

4.2.4 Fabrication

4.2.4.1 Mullite and Skybond AR coating

We describe the fabrication recipe of Mullite and Skybond AR coating. The recipe of the following process is found elsewhere [78].

Table 4.7: Index and loss tangent of epoxy between 72 and 108 GHz for each 1.2 GHz step. We fit the transmission spectrum by using Eq. (4.1). The dominant uncertainty is due to the gain drift of the amplifier in the synthesizer, which arises from the temperature fluctuation.

Name	Temperature [K]	Thickness [mm]	Index	Loss-tangent [$\times 10^{-2}$]
Stycast 2850FT	300	$3.38^{\pm 0.01}$	$2.194^{\pm 0.006}$	1.88 ± 0.04
Stycast 1090	300	$6.85^{\pm 0.01}$	$1.435^{\pm 0.005}$	2.46 ± 0.01
Stycast 2850FT	77	$3.38^{\pm 0.01}$	$2.196^{\pm 0.003}$	0.33 ± 0.02
Stycast 1090	77	$6.85^{\pm 0.01}$	$1.422^{\pm 0.006}$	0.57 ± 0.02

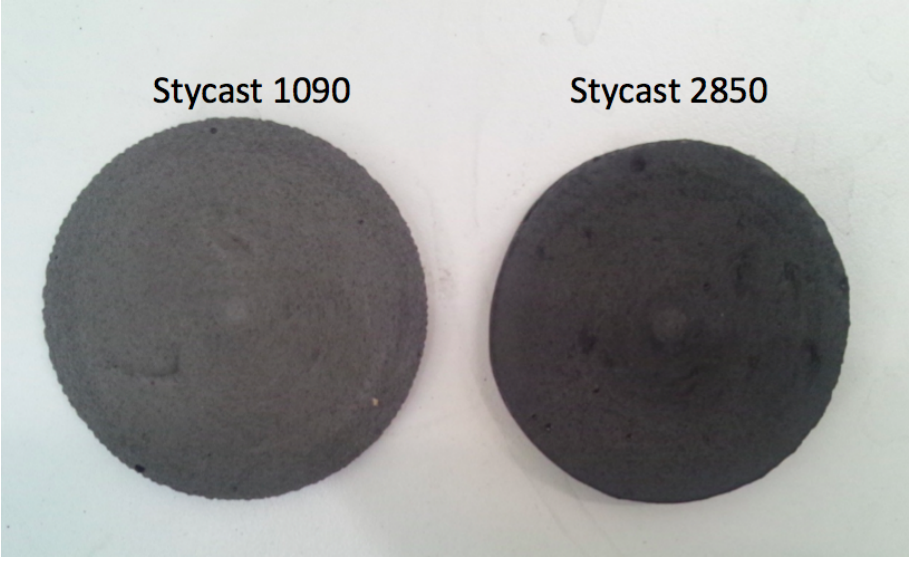

Figure 4.17: Picture of stycast 2850 and 1090.

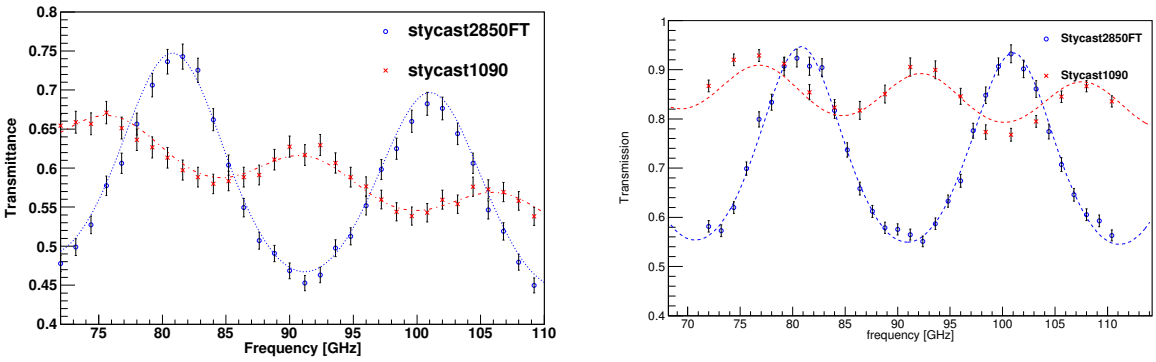

Figure 4.18: Transmittances of the two types of epoxies as a function of the frequency in the millimeter-wavelength range. Sample temperature of the left (right) figure was 300 K (77K). The red and blue points are samples of Stycast 2850FT and Stycast1090, respectively. The dominant error is due to the gain drift of the amplifier in the synthesizer, which arises from the temperature fluctuation. The two curves show the best fits for each sample. The results of the fits are listed in Table 4.7.

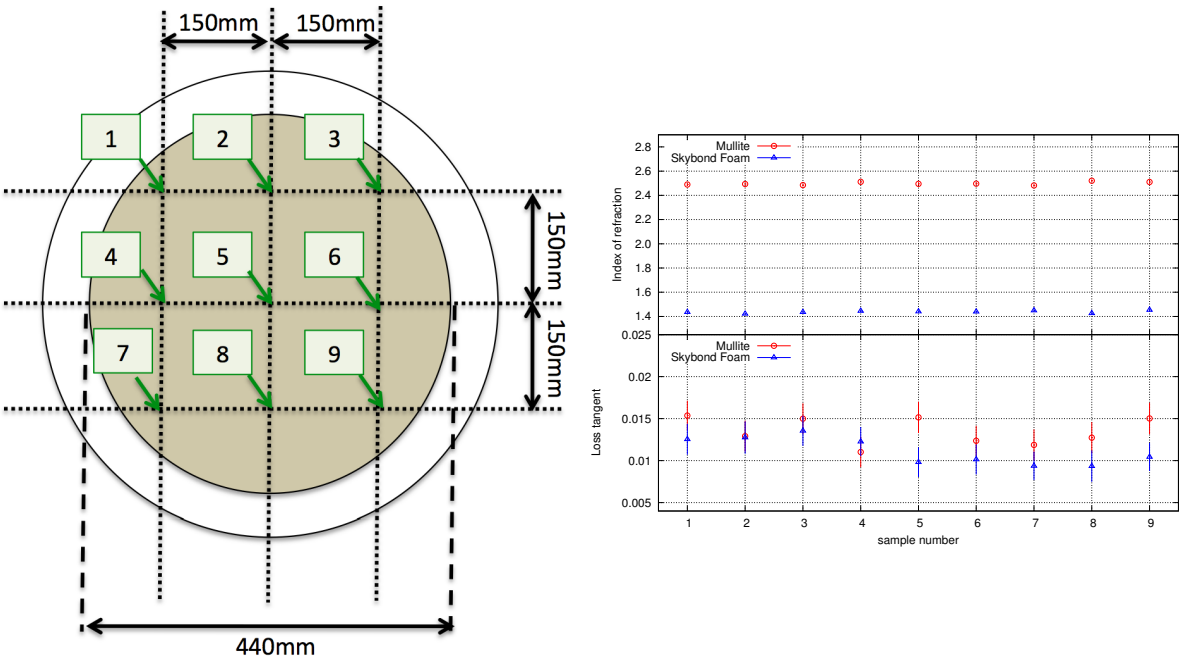

Figure 4.19: Left: Definition of the points for uniformity measurements. We measure transmittances at the 9 points for estimation of the index. Right: Uniformity of IOR (top) and loss tangent (bottom) vs. the measured point number. The mullite and Skybond Foam are measured with a millimeter wave source whose frequency ranges from 72 to 110 GHz. The sample is placed at 298 K. The error bars in the $x-$axis correspond to statistical errors.

Step1 We place the Mullite layer with thermal spraying on both sides of the alumina. The thickness is 0.235 mm as shown in Table 4.8.

Step2 We place the bond layer, which is a sheet consisting of a 30 μm-thick layer of low-density polyethylene (LDPE) at the both sides. Each of the bond layer is sandwiched by the Skybond Foam and mullite layer. We employ the 60 % Skybond Foam as the AR material for the alumina filter. The thickness of the Skybond Foam is 0.39 ± 0.02 mm. Then, the surface of Skybond Foam is machined with a milling machine, whose blade thickness and rotating speed are 4 mm and 6000 rpm, respectively. The uniformity of the thickness is improved by a factor of two through the machining process.

Step3 The stack of Skybond Foam, mullite and alumina is baked in an oven. Then, we sandwich the stack layer with a 10 mm thick aluminum board and press this board using lead blocks with a pressure of $3,000$ N/m^2. We start the bake cycle by slowly ramping up from room temperature to 160 degree Celsius over 6 hours to avoid thermal shock. The oven spends 6 hours at 160 degree Celsius and then another 6 hours ramping back down to room temperature.

Furthermore, we run a thermal cycle test from 300 K to 77 K with conductive cooling. The AR coating passes the thermal cycle test over ten times. None of the results show cracks with thermal contraction.

Table 4.8: Basic properties of alumina and AR materials. The thickness d, the IOR n and the loss tangent $\tan\delta$ are listed. All values are taken from our measurements. Our measurements for n and $\tan\delta$ are taken at the temperature of liquid nitrogen, whereas the thickness values are taken at room temperature. The optical properties of alumina are measured using a variable millimeter wave source between 72 and 140 GHz. We derive the index and loss tangent from the transmittance as a function of the wavelength as described elsewhere [18, 17]. The errors include both statistical and systematic uncertainties. The systematic errors arise from the uncertainty of the AR thicknesses and the fluctuations of the measurement system due to the temperature variation.

Material	Temperature [mm]	d [K]	n	$\tan\delta$ [$\times 10^{-4}$]
Alumina	298	$1.98^{\pm 0.01}$	$3.144^{\pm 0.005}$	$3.7^{\pm 1.7}$
Mullite	298	$0.235^{\pm 0.015}$	$2.517^{\pm 0.02}$	$121^{\pm 16}$
Skybond Foam	298	$0.39^{\pm 0.02}$	$1.436^{\pm 0.025}$	$120^{\pm 2}$
Alumina	81	$1.98^{\pm 0.01}$	$3.117^{\pm 0.005}$	$3.0^{\pm 1.1}$
Mullite	81	$0.235^{\pm 0.015}$	$2.461^{\pm 0.03}$	$53^{\pm 10}$
Skybond Foam	81	$0.39^{\pm 0.02}$	$1.425^{\pm 0.025}$	$25^{\pm 1}$

4.2.4.2 Epoxy AR coating

The Epoxy AR coating consists of two layers, Stycast 2850 and Stycast 1090. We explain the recopy of Epoxy AR coating. The recipe of the following process is found elsewhare[85].

Step1 Before we place the epoxy on the alumina surface, we measure the shape of the lens with the CMM.

Step2 The Stycast2850 is deposited on the surface of alumina. The until-curing epoxy is roughly pressed to1 mm thickness using a aluminum mold.

Step3 We use a milling machine for thinning. The designed thickness is 0.28 mm.

Step4 We measure the AR shape with the CMM and characterize the thickness uniformity.

Step5 The Stycast1090 is deposited on the surface of Stycast2850.

Step6 We use a milling machine for thinning down to 0.42 mm thick.

Step7 We measure the AR shape with the CMM and characterize the thickness uniformity.

Step8 We cut the AR surface with a laser cutter to reduce the curing stress. The groove width and thickness are 0.025 mm and 0.70 mm.

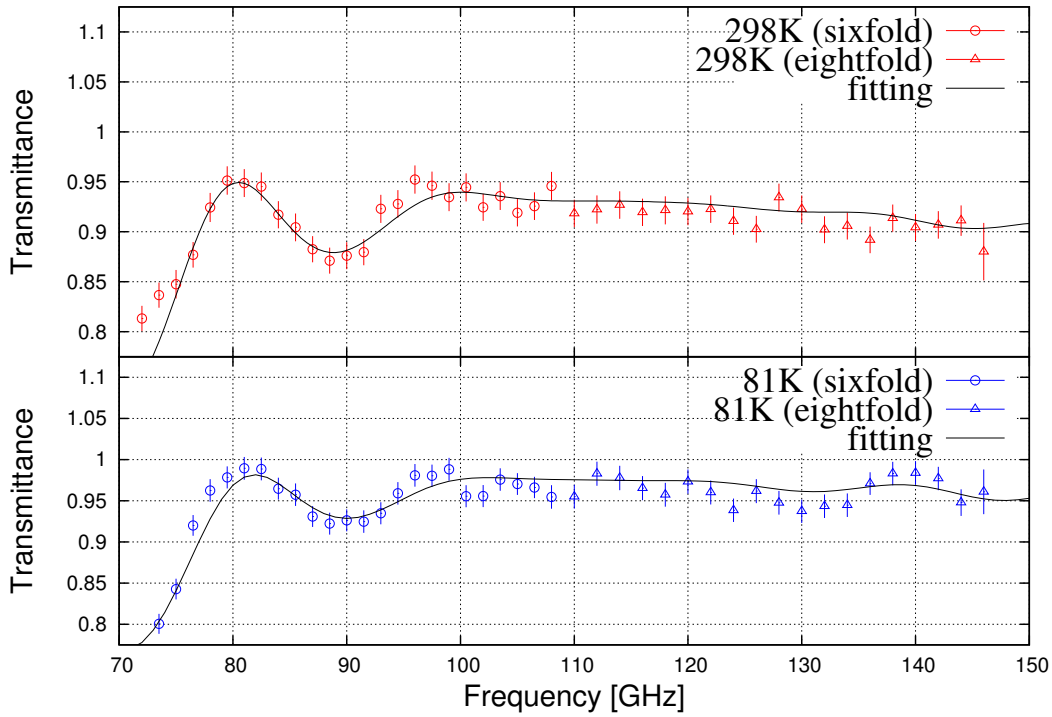

Figure 4.20: The transmittances of the IR filter as a function of the frequency. The sample is kept at 298 K (top) and 81 K (bottom). The dashed line is the prediction with 1-σ error, which includes the errors in the construction parameters given in Table 4.8.

4.2.5 Transmittance

We measure the transmittance of the AR coating with the same setup described in Sec. 4.1.1.1 at room temperature and at 81K cooled with liquid nitrogen. The diameter and thickness of the sample is 50 mm and 2 mm. The thicknesses of the alumina and AR layers are listed in Table 4.8 . Figure 4.20 shows the result. The dashed line is the prediction with EMT, which is obtained from the parameters and errors listed in Table 4.8. The estimated transmittances are 95.9 % and 95.8 % in the 95 GHz and 150 GHz bands, respectively. Because this alumina is very thin, we can neglect the loss of alumina. Therefore, the measured transmittance of AR coating meets our requirement of 95 %.

Table 4.9: Measured uniformities of Skybond Foam and mullite. These values are the mean and rms of the uniformity of thickness, d, and index, n, as shown in Figs. 4.22 and 4.19.

	d [mm]	d rms[mm]	n	n rms	Optical path length [mm]
Mullite	0.251	0.010	2.461	0.063	0.016
Skybond Foam	0.391	0.008	1.425	0.020	0.009

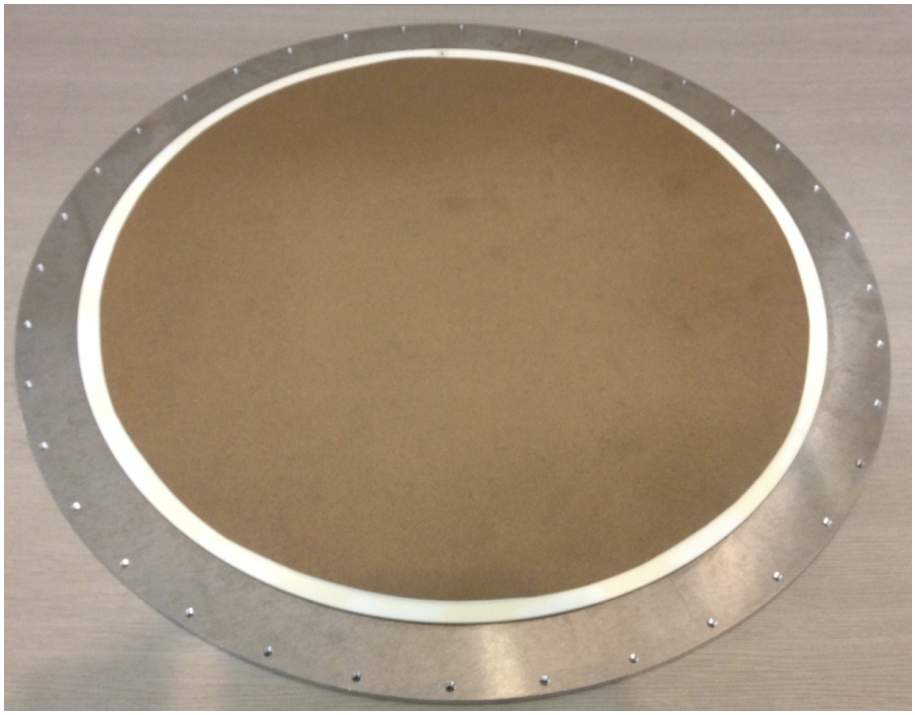

Figure 4.21: An alumina filter with a two-layer AR coating at both surfaces. The sample diameter is 460 mm and the AR layers are extended to a disc with a diameter of 440 mm. This means that the a 10 mm thick ring from the edge of the filter is without IR layers, and is used as the mount region to cool the alumina filter directly.

4.2.6 Uniformity of the coating

We place the Skybond foam and mullite AR coating on both surfaces of the alumina disc. The diameter of AR coating is 460 mm. We require that the uniformity in the optical path length is better than $\lambda/50$.

We characterize the uniformity of the thicknesses of mullite and Skybond Foamusing a coordinate measuring machine (CMM). The results are shown in Fig. 4.22. We calculate the optical path length in both mullite and Skybond Foam with the measured IOR and thickness. These fluctuations are less than $\lambda/50$ as shown in Table 4.9. We characterize the uniformity of the IOR using four samples independently. All IORs and loss tangents agree within statistical uncertainties. The IOR and loss tangent of the thick Skybond Foam and sheet are also consistent within one sigma error.

4.2.7 Short summary of AR coating development

We develop the new two-layer AR coating to reduce the refraction of high IOR materials, such as Alumina, Silicon, and Sapphire. We employ the Mullite and Skybond Form 60 % as AR materials. The maximum diameter of coating is 530 mm corresponding to that of the collimator lens. The measured uncertainty of optical path length ($\delta(nd)$) meets our requirement, less than $\lambda/50$. We also develop the Epoxy two layer AR coating. We avoid the thermal contraction mismatch using stress relief grooves [18, 85]. Both

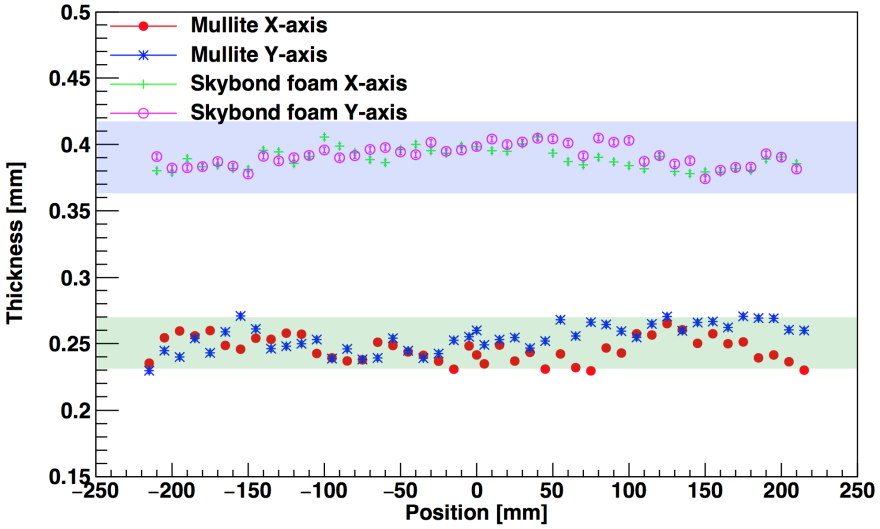

Figure 4.22: Thicknesses of the mullite and Skybond Foam layers which are characterized by CMM to an accuracy of 2 μm – uncertainty. The red and blue points are the characteristic directions of the X and Y-axes, respectively, where the position is the distance from the filter center. The acceptable thickness uncertainties of mullite and Skybond Foam are 0.022 and 0.037 mm, respectively. The error bars correspond to systematic errors of the thickness rms of alumina. These results meet our requirements.

of coatings are employed to PB-2 AR coating.

4.3 Alumina filter

We address the scalability in diameter based on our results and discuss the cryogenic compatibility. Some of the next generation CMB experiments need a window diameter of 500 mm or larger. The cooling power of the PB-2 receiver and expected optical heat load are summarized in Table 3.2 [16].

PB-2 requires the filter size of 460 mm in diameter that is mounted at the 50 K stage. This filter absorbs the emission from the window. The PB-2 window is assumed to be made of Zotefoam, which absorbs the IR radiation efficiently. Thus, the dominant heat source to the 50 K and 4 K stages is the thermal emission from the room temperature window that is radiatively cooled to around 200 K at the inner surface. The estimated power from the window is about 17 W. We need to remove this heat at the 50 K stage before it reaches the 4 K stage by using the cooling power.

The temperature of the filter with a given diameter is determined by the thermal conductivity and the thickness. Although the thicker filter conducts the heat away from the filter more efficiently, the absorption of the incident radiation at the detection band increases with a thicker filter. Therefore, thickness is not a free parameter we can choose for a better thermal performance. When the thickness of the filter is determined, the temperature of the filter equilibrates based on the conductance and the emissivity of the filter. When the temperature of the filter is significantly higher than the edge temperature, the filter itself becomes an emissive element that contributes significantly to the 4 K stage.

4.3.1 Requirements

We develop an alumina filter with a diameter of 460 mm and characterize its thermal and optical properties. The goals are to meet the following requirements for the PB-2 experiment.

- 3 dB cutoff frequency below 1 THz to cut IR radiation effectively;
- the filter diameter must be extendable to 450 mm or larger;
- the temperature rise less than 10 K.

4.3.2 3 dB cutoff

We measure the 3 dB cutoff of the alumina filter using a Martin-Puplett Fourier transform spectrometer (FTS). A detailed description of this FTS is available elsewhere [86]. We measured the transmittance from 250 GHz to 1500 GHz at 300 K and 19 K. We placed the disc-shaped sample in the FTS system with a crossing beam. Then, we measure the interferogram with the test sample. As a reference, we also took data without the test sample. We Fourier-transformed interferogram of the data with the sample and the reference data. The transmission spectra are calculated from the ratio between them. We measured samples of mullite and Skybond whose parameter is shown in Table. 4.8. Figure 4.23 shows the measured spectra. The estimated 3 dB cutoffs are 450 and 700 GHz at 298 and 19 K. Both the results show that the transmittances at the cold temperature are higher than that of the room temperature. This is because the losses from alumina and AR coating materials become lower at the lower temperature.

4.3.3 Thermal conductivity

4.3.3.1 Experiment

The thermal conductivity was measured over a temperature range from 4 to 100 K. Figure 4.24 shows a schematic view of the experimental setup. The samples were 2 mm × 30mm × 100 mm. For each given sample, one end was mounted on a cold plate directly connected to a cryogen tank that was filled either with liquid nitrogen or liquid helium to cover the temperature ranges. A silicon-diode thermometer and a resistance heater were mounted on one end of each sample via OFHC copper plates. Resistances of 100 Ω or 20 kΩ were used for the measurements at $LN_2 (T > 77\ \mathrm{K})$ and LHe_2 ($4\ \mathrm{K} < T < 77\ \mathrm{K}$) temperatures, respectively. A second silicon-diode thermometer was mounted on the cold plate. We apply the heated one end of each sample via the resistor and recorded the temperatures given by the two thermometers.

We extracted the thermal conductivity κ by using

$$P_{el} = \frac{A}{L}\int \kappa(T)dT \sim \frac{A}{L}\bar{\kappa}(T)\Delta T \tag{4.16}$$

$$\kappa = \frac{L}{A}\frac{P_{el}}{\Delta T}, \tag{4.17}$$

where P_{el} is the electrical power dissipated by the heater resistor.

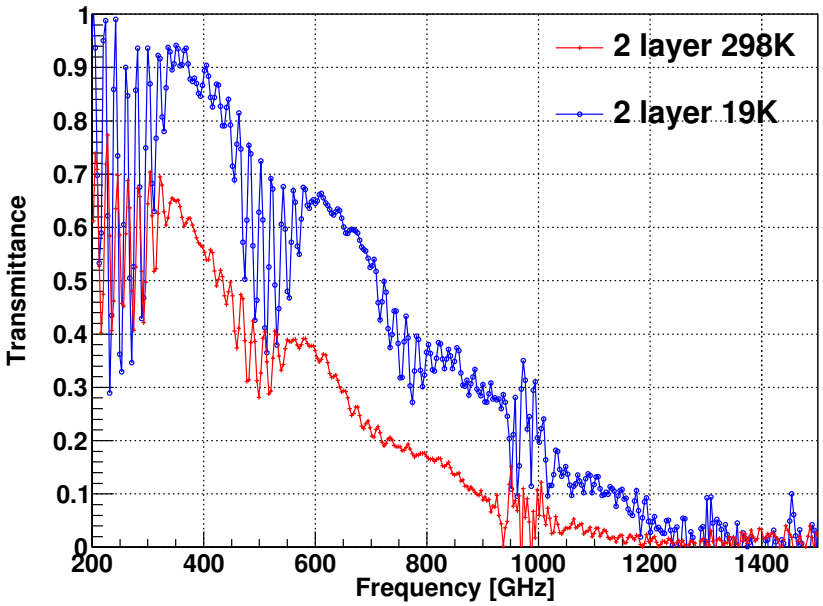

Figure 4.23: The transmittance of the IR filter at the THz band. The crosses represent the sample temperature of 295 K and the open circles represent 19 K. This sample has two layers of AR coating: mullite and Skybond Foam.

To verify the apparatus, we used it to measure thermal conductivity of a stainless-steel sample (SUS304). The result agrees with the published value within one-sigma, which confirms that the measured thermal conductivity is not dominated by the contact resistance [87]. The measured thermal conductivities are shown in Fig. 4.25. The measured and literature values are inconsistent because the grain size of the alumina is different. The detail of this discussion is shown in Appendix C.

4.3.4 Thermal gradient of filter

We measure the temperature distribution of the alumina filters when they are used as IR filters in a cryostat. The diameters of two samples are 460 mm and 100 mm. The thickness is 2 mm for both samples. Figure 4.26 shows the measurement configuration. The prototype filter is mounted on a 77 K shell that is located just below the Zotefoam window. We mount the four silicon diode thermometers on the filter as shown in Figure 4.26. The size of thermometers is 1 mm $\times$ 2 mm $\times$ 3 mm. The absorption of the thermometer is less than that of the filter, so that the temperature of the thermometer only depends on the filter temperature. Figure 4.27 shows the radial temperature profile of the filter. The measured temperature rise from the edge to the center is 0.26 ± 0.13 K (2.30 ± 0.13 K) for the filter with 100 mm (460 mm) in diameter. Here each error is from calibration accuracies of the thermometers.

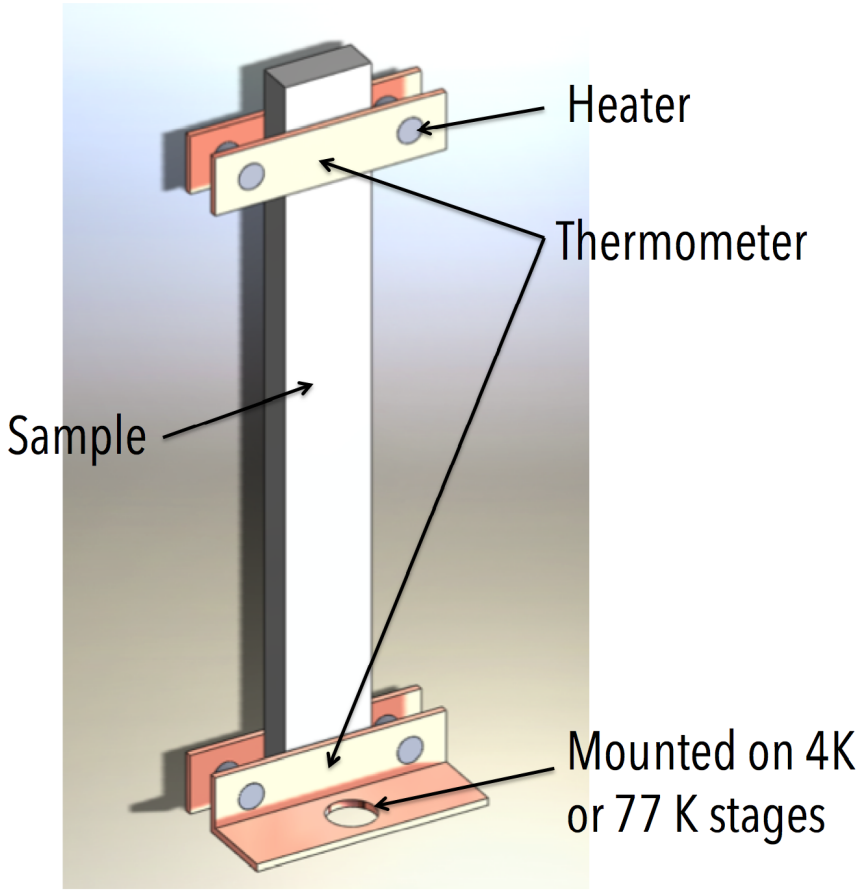

Figure 4.24: Schematic view of apparatus used to measure thermal conductivity. The sample was sandwiched between two copper plates and mounted on a plate held at 4 or 77 K.

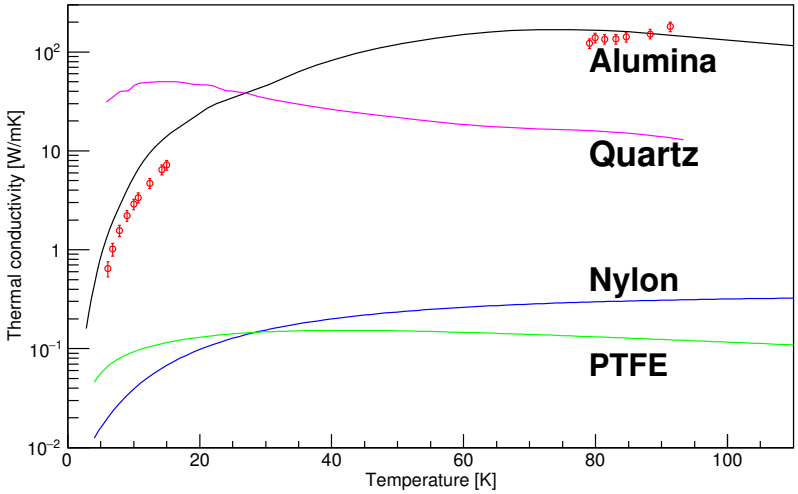

Figure 4.25: The red points are the measured thermal conductivities. The each solid curve represents literature values.

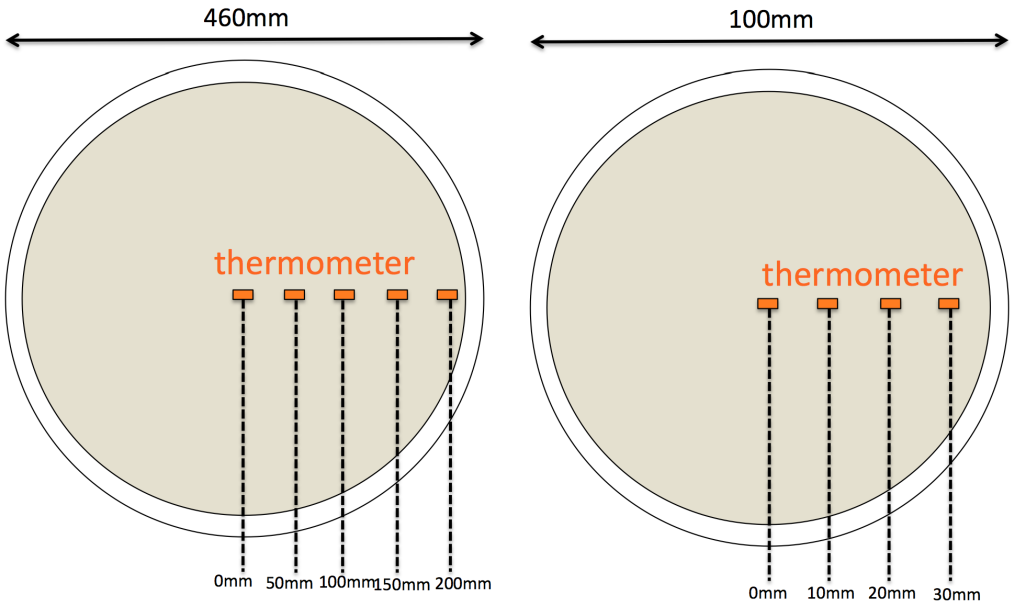

Figure 4.26: The schematic view of the temperature distribution measurement.

4.3.4.1 The model of temperature distribution

We construct the thermal model for the temperature profile in order to make a comparison between the measured results and the expected temperature distribution. The difference of the temperature between the center and the edge can be written analytically as

$$\Delta T(r) = T(r) - T_{edge} = P_{con}\frac{R^2 - r^2}{4\pi t\kappa R^2}, \tag{4.18}$$

where T_{edge} is the edge temperature, t is the filter thickness, and κ is the thermal conductivity of alumina, R and r are the radius of the filter and the radial distance from the center [88]. While the filter has two-layers of AR coating, we neglect them in our thermal model because they do not contribute due to the significantly lower thermal conductivities and thicknesses than those of alumina. The conducted power, P_{con}, from the filter to the thermal bath is assumed as

$$P_{con} = P_{in} - P_{rad} \sim P_{in}, \tag{4.19}$$

where P_{in} is the incident absorbed radiative power from the window, and P_{rad} is the emissive power from the filter surface. The modeled temperature distributions are over-plotted in Fig. 4.27. The results of temperature rises meet our requirement. For comparison, we also measure the temperature of a filter made of PTFE that has the same geometry as the prototype alumina filter. The PTFE filter is 2 mm thick. The temperature difference with the PTFE filter is over 100 K which is significantly larger than that of the alumina filter.

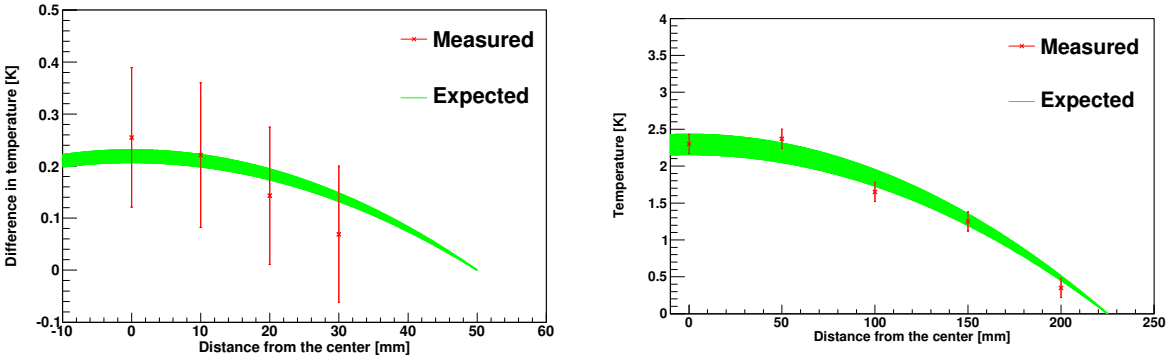

Figure 4.27: The temperature distribution across the 100 mm alumina filter is plotted as a function of the radial distance from the center of the filter. The offset of the temperature is removed and the offset is the edge temperature of 90.3 K and 50.3 K. The crossed points are the measured values with the error bars estimated from the calibration accuracy. The expected region is also shown in the plot, which is not a fit but is based on the thermal model with the basic parameters.

4.3.5 Short summary of Alumina filter development

The large optical system of PB-2 needs the large optical window. The large optical window allows the large emission to the cold optical system. To reduce this emission, we newly developed the alumina IR filter, whose cutoff is 700 GHz at 19 K. The thermal conductivity of the developed filter is three orders of magnitude larger than that of conventional filter. Thanks to the high thermal conductivity, we achieve to suppress the temperature rise between edge and center of thefilter. The temperature rise is only 2.3 $\pm$ 0.1 K. This number is much less than that of conventional filters.

4.4 Millimeter absorber

Almost all the CMB experiments employ the absorber to block the stray light and define beam edge. Typical materials of absorber fall into two types. One is a foam type, such as HR-10 or AN 72. Another is solid type, such as bock black or CR-112.

The foam absorber has an advantage of the low reflection and high absorption. However, the thermal conductivity of the foam absorber is very low. It implies that the temperature of the absorber rises even with very faint radiation. In contrast, solid absorbers in general have much higher thermal conductivity than foam ones. However, they have high reflectance in millimeter wavelength regions due to their high index of refraction (IOR).

In this thesis, we explain a new type of the absorber that has high absorption, low reflectance and is easily shaped in any form. We call the new absorber “KEK black”. The KEK black consists of carbon black base containing powder beads made of expanded Polystyrene foam. Powder beads are provided by MOGU company. Their typical diameter of the powder beads is 0.5 mm, which is similar to the typical size of Mie scattering. When light rays enter the absorber, they are Mie-scattered multiple times. The

Table 4.10: The recipe of measured samples.

Sample name	Stycast1090[g]	Catalyst9[g]	Carbon black[g]	Powder beads[g]
A	10	0.9	2	0.0
B	10	0.9	2	0.1
C	10	0.9	2	0.5
D	10	0.9	2	0.7
E	10	0.9	4	0.0
F	10	0.9	4	0.1
G	10	0.9	4	0.5
H	10	0.9	4	0.7
I	10	0.9	6	0.0
J	10	0.9	6	0.1
K	10	0.9	6	0.5
L	10	0.9	6	0.7

optical path length gets longer as a result. Since the carbon black is an efficient absorber for millimeter waves, KEK black works as a very good absorber.

4.4.1 Fabrication and measured sample

In this section, we explain the fabrication method of the KEK black as follows.

Step1 The Stycast 1090 is mixed with catalyst 9.

Step2 We add the carbon black to the until-cured Stycast and mix until clay-like.

Step3 We add the powder beads and mix until the powder beads are distributed uniformly.

Step4 The mixed clay is cured for 1 day.

The recipe of measured sample are listed in Table 4.10. We make 12 types of KEK black with different compositions of the carbon black and powder beads. Additionally, we measure the Bock black [89] and CR112 [57] as conventional absorbers.

4.4.2 Transmittance in millimeter wave length

We measure the transmittance of KEK black in the millimeter wavelength. The measured frequencies are between 72 to 146 GHz, where the optical sources we used are $\times 9$ and $\times 6$ frequency multipliers. The setup of the measurement system is shown in Fig. 4.2. The measured transmittance is shown in Fig. 4.28. The thickness of all the samples is 2 mm.

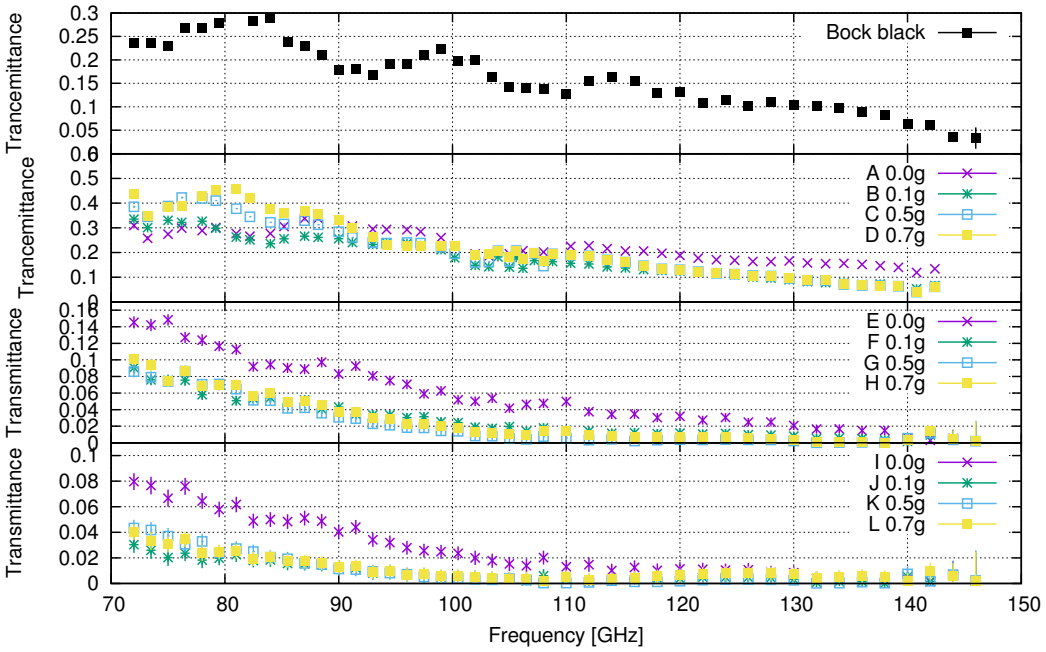

Figure 4.28: The measured transmittance of the KEK black. The measured frequencies are between 72 to 146 GHz. Each error is statistical due to gain fluctuations. The first panel shows the transmittance of Bock black, where error bars show $\pm 1\sigma$ uncertainty. From second to fourth panels are results of KEK black. The details of the sample are listed in Table. 4.10.

Figure 4.29: The pictures of black bodies.

4.4.3 Transmittance at the sub-millimeter wavelength

The transmittance spectra of 2 mm thick samples of G are shown in Figure 4.30. We measured the transmittance from 250 GHz to 1500 GHz at 300 K and 19 K. We placed the disc-shaped sample in the FTS system with a crossing beam. Then, we measure the interferogram with the test sample. As a reference, we also took data without the test sample. We Fourier-transformed interferogram of the data with the sample and the reference data. The transmission spectra are calculated from the ratio between them. The measured samples are KEK black, bock black and CR112 as shown in Fig. 4.29

.

4.4.4 Reflectance

Measurement system We explain the measurement system for reflectance measurement as shown in Fig. 4.31. The millimeter wave is generated by using a signal generator with a sixfold frequency multiplier. The frequency range of the signal generator is between 12 and 18 GHz. The multiplied frequency is between 72 and 108 GHz. The frequency resolution of our system is 0.12 GHz. The beam was collimated by lenses. The reflected beam is detected by a diode detector. The signal was chopped at 13 Hz for heterodyne detection at the modulated frequency with a lock-in amplifier, and the signal was recorded by a DAQ. The detector was moved along the optical axis for more than a half wavelength to subtract the effect of a standing wave in the measurement setup. For each material type, we prepared a sample with a diameter of 50 mm and thickness of 2 mm. The sample is mounted on the aluminum plate. We measured the power with and without the samples and took the ratio to obtain the reflection.

Measurements and results We measure the reflectance of 8 samples and a conventional absorber. The setup for the measurement is shown in Fig. 4.31. The incident signal is generated by a signal generator between 12 and 18 GHz, multiplied sixfold by a frequency multiplier. The multiplied signal is emitted from the scalar horn that has 10 degree beam divergence. The beam is collimated with a UHMWPE lens and an aperture with a hole size of 4 cm. The beam is chopped at 16 Hz. The sample is placed in the sample holder made of aluminum. The beam is refracted on the samples or aluminum

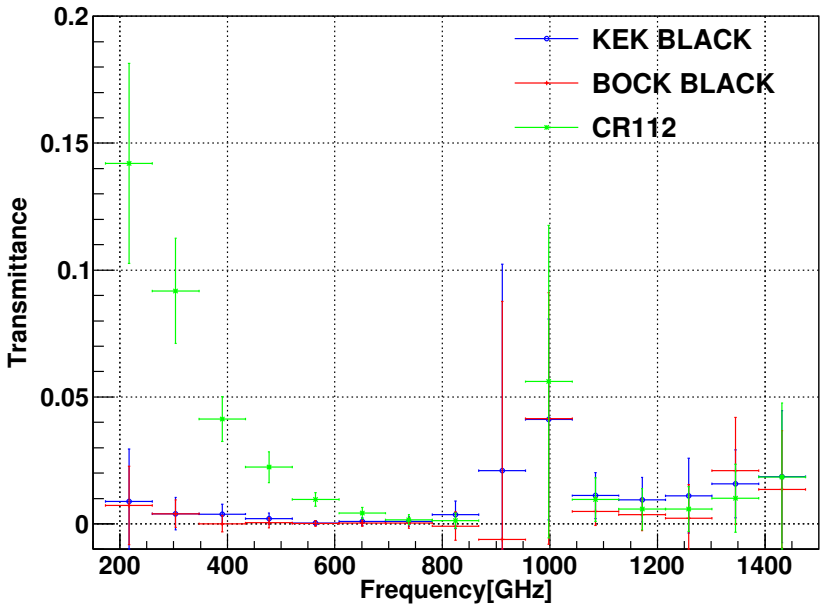

Figure 4.30: The measured transmittance of absorber. The measured samples are KEK black, Bock black and CR112. The sample thickness and diameter are 2mm and 20 mm. Measurements are carried out at 300 K.

surfaces. The reflectance of aluminum is assumed unity. The refracted beam is also collimated with a UHMWPE lens and detected. The rejected signal interferes with the sample surface and the other side of the surface, which is in contact with the aluminum plate snugly. The measured reflectance is shown in Fig. 4.32 and 4.33 .

4.4.5 Short summary of millimeter absorber development

We newly invent the absorber, 'KEK black'. We compare it with conventional ones, where we tried various recipes for producing the KEK black. The performance with any recipe we tried is better than that of the conventional absorber. The reflectance of many power beads sample tend to be less than that of others. However, the sample of C(G) and D(H) are not different significantly. The reflectance with a high carbon concentration tends to be higher. Therefore, we conclude that sample G has better performance in millimeter wavelengths. The transmittance of sample G is less than 10 % when we use a 2 mm thick sample. The transmittance in sub millimeter wavelengths is less than 1 %. The averaged reflectance of sample G is less than 20 %, which is sufficiently less than that of the conventional absorber. We have decided to place a 4mm thick KEK black at the inner surface of 4 K shell.

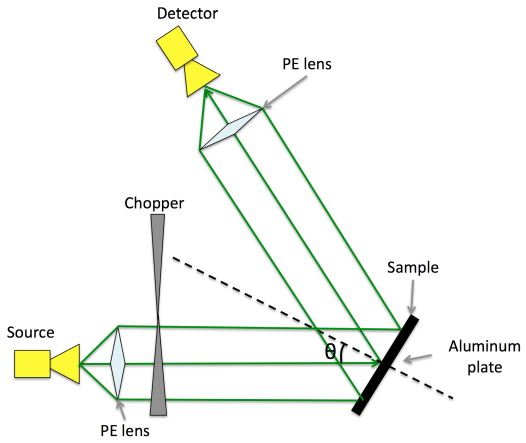

Figure 4.31: The system overview of reflectance measurement. The source and detector are mounted on the optical table with angle of 60 degrees. The beam is collimated with the UHMWPE lenses. The beam is reflected by the surface of the measured sample which is placed on the aluminum plate. The signal is modulated by a chopper whose frequency is 13 Hz.

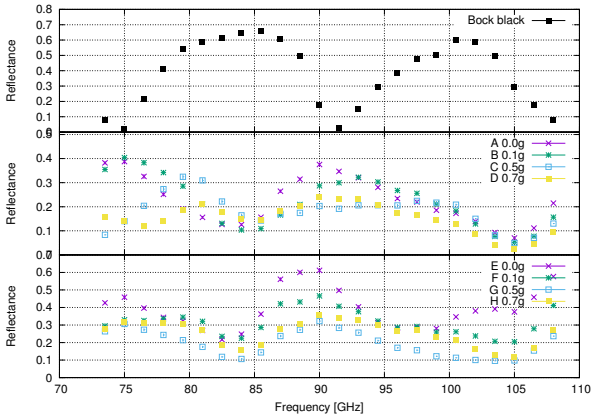

Figure 4.32: Reflectance with 75 degrees for the Bock black and KEK blacks as a function of the frequency in the millimeter-wavelength range. Sample temperature was 300 K. The samples are listed in Table 4.10. The dominant error is due to the gain drift of the amplifier in the synthesizer, which arises from the temperature fluctuation.

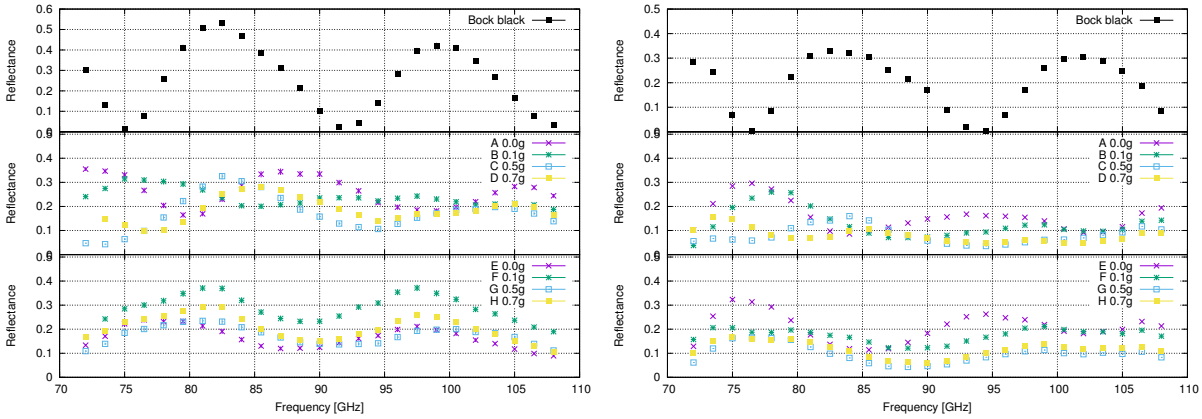

Figure 4.33: Left and right are the measured reflectance with 60 and 45 degrees for the Bock black and KEK blacks as a function of the frequency in the millimeter-wavelength range. Sample temperature was 300 K. The samples are listed in Table 4.10. The dominant error is due to the gain drift of the amplifier in the synthesizer, which arises from the temperature fluctuation.

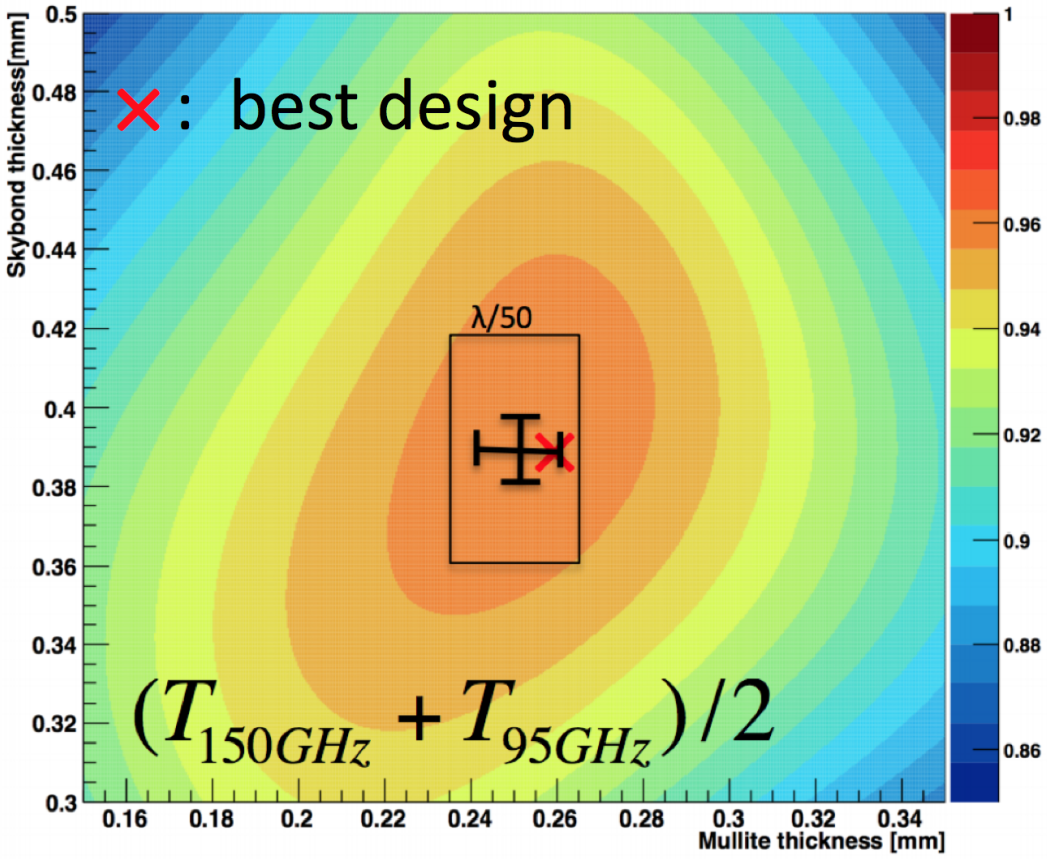

Figure 4.34: Contour plot for thickness optimization of mullite and Skybond foam AR coating. The color chart shows the average transmittance of 150 and 95 GHz with fractional bands. The rectangular box and red point are $\lambda/50$ requirement and best design. The black points represent measurements and error bars as listed in Table 4.9.

4.5 Discussion

4.5.1 Optimization of AR parameters

The thickness of two-layer AR coatings for alumina lenses and alumina filter should be optimal when we assume to fix the IOR. We calculate the average transmittance with 95 and 150 GHz bands for each thickness combination. Figure 4.34 is the contour plot in the parameter space. Our design requirement on the thickness uncertainty is $\lambda/50$ which is corresponding to square on Fig. 4.34. As you see, the transmittance uncertainty is less than 1 % in the square, which is satisfactory. Furthermore, error bars in Fig. 4.34 are less than the area of square. Therefore, we conclude that transmittance uncertainty is less than 1 %.

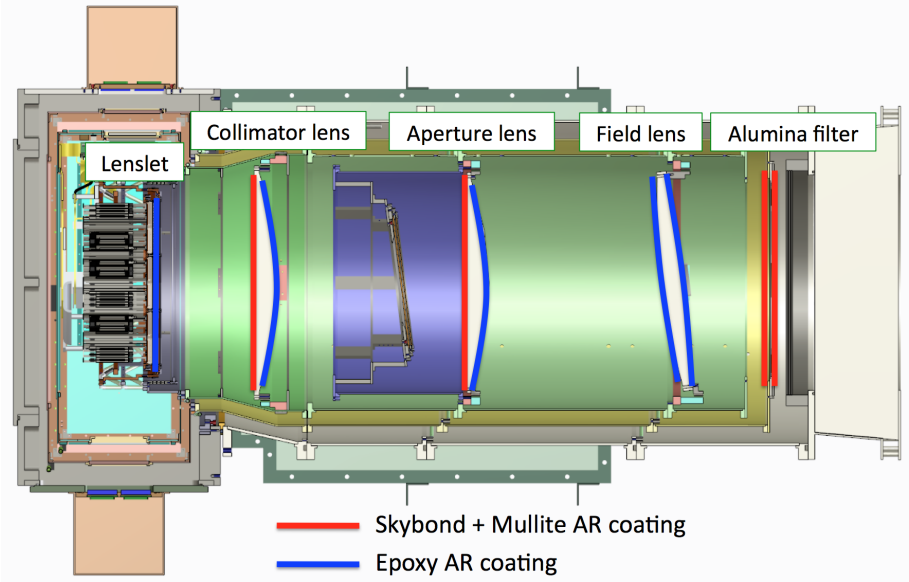

Figure 4.35: Combination of AR coating in POLARBEAR-2 optics.

4.5.2 Emissivity of AR coating

We estimate the emissivity of the alumina filter using the construction parameters given in Table 4.8 . The estimated reflectances are 2.2 % and 1.1 % at 95 GHz and 150 GHz bands. The emissivity, ϵ, is estimated by the following equation:

$$\epsilon = A = 1 - R(d, n, \tan\delta, \nu) - T(d, n, \tan\delta, \nu), \tag{4.20}$$

where A, R and T are the absorption, the power reflectance, and the transmittance of the filter, respectively. The estimated emissivities of the alumina filter are 2.0 % and 3.1 % in the 95 GHz and 150 GHz bands, respectively. This values will be used in Chap. 7.

4.5.3 Application of two-layer AR coating

We apply the technologies of AR coating to the PB-2 optics. We place the two-layer AR coating on the silicon lenslet, alumina lenses and alumina filter. Figure 4.35 shows the configuration of AR coating in the PB-2 receiver system. We place the Skybond foam and mullite AR coating on the flat surfaces. The epoxy AR coating is placed on the curved surfaces. Figure 4.36 shows the pictures of AR coating of collimator and aperture lenses.

4.5.4 Incident angle

We study the AR transmission by incident angles. The component of the electric field parallel to this plane is defined as transverse-magnetic (TM) wave and the perpendicular to this plane is defined as transverse-electric (TE) wave. The transmittances of TM and TE waves are different although it becomes the same

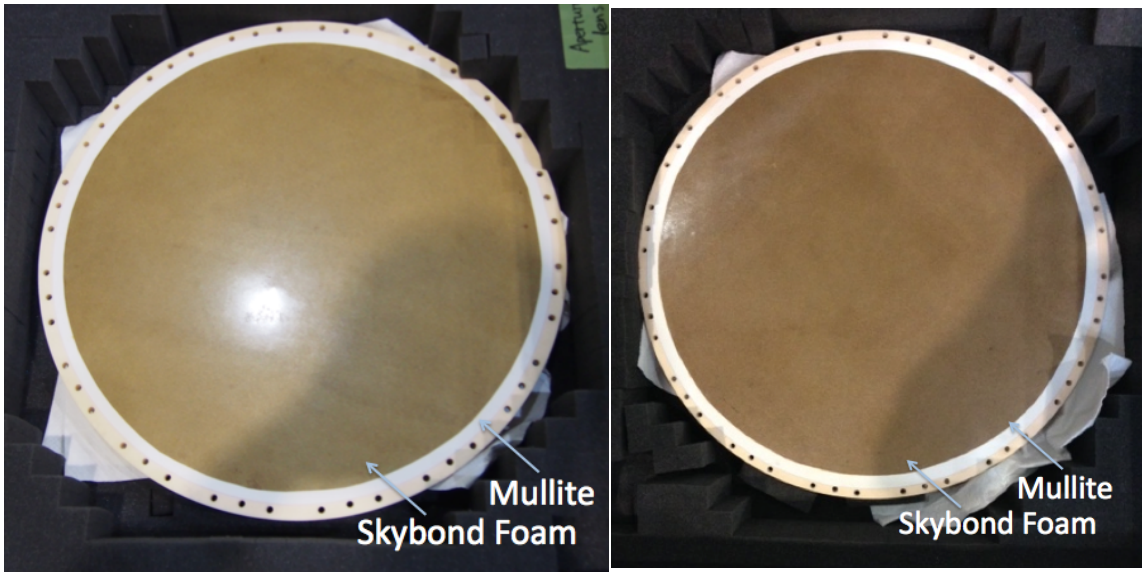

Figure 4.36: Left (right): two-layer AR coated aperture (collimator) lens. The mullite and Skybond form is placed on the first and the second layers.

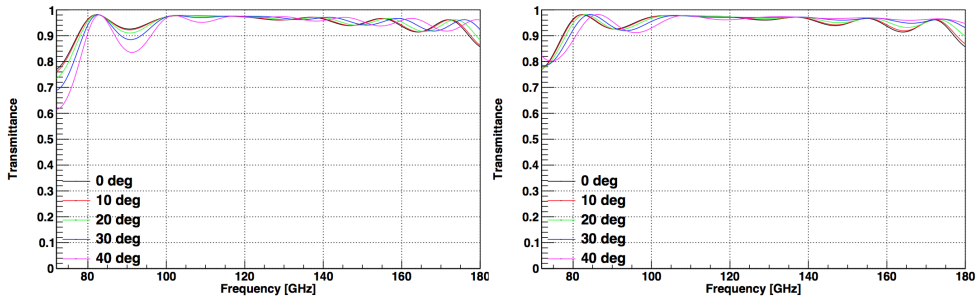

Figure 4.37: Calculation of the transmittance curves when we change the incident beam angle. The left and right figures are transmittances of TE and TM waves.

number at an incident angle of 0 degrees. Figure 4.37 shows TE and TM transmittances. In our case, the incident angle of AR coating is less than 20 degrees. Therefore, the difference of two transmittance is ignorable.

4.5.5 Temperature rise of the filter

We construct the thermal model based on the thickness and thermal conductivity of the filter. The incident power from the window is absorbed by the alumina filter, whose power conducts to filter edge and re-emits from the filter surface, respectively. The emissivity of the filter is assumed to be unity in the IR band. Figure 4.38 shows the radial temperature profile of the filter for various materials, including alumina, when the filter diameter is 500 mm and the edge temperature is anchored at 50 K. We compute for various values of κt in Eq.(4.18). The IR filter using alumina with the thickness of 2 mm corresponds to $\kappa t = 244$ mW/K. When the alumina filter is used for PB-2, the expected excess temperature at the

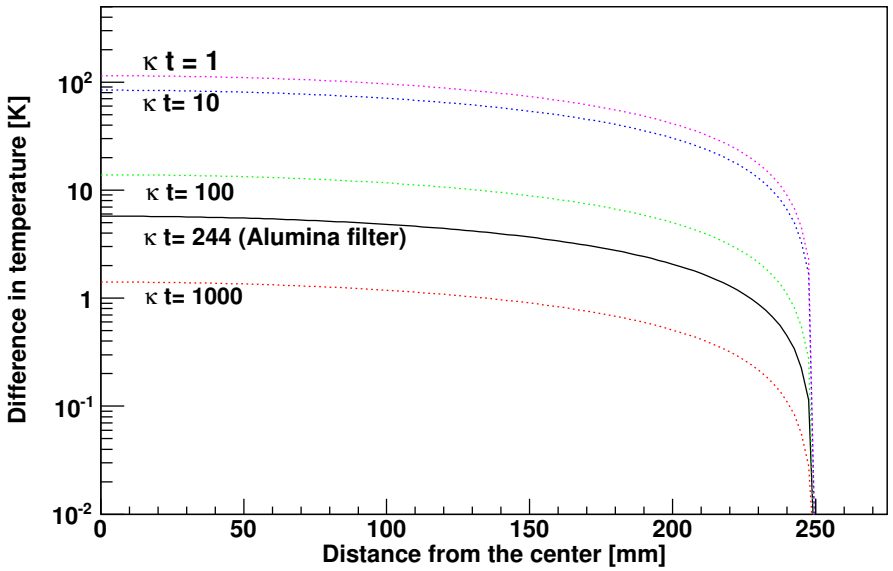

Figure 4.38: The temperature difference of the alumina filter is shown as a function of the radial distance of the filter. In our model, we assume that the edge temperature is 50 K, the temperature of a Zotefoam window is 200 K, the emissivity of the filter is 1, and the emission from the filter is uniform. Each curve corresponds to $\kappa t = 1, 10, 100, 1000$ in the unit of [mW/K]. A 2 mm-thick alumina and 20 mm-thick PTFE yield $\kappa t = 244$ mW/K and 2 mW/K, respectively [18].

center of the filter is less than 6 K from the edge temperature. By contrast, the temperature difference of conventional filters such as polyethylene, Nylon, and PTFE is $\sim$ 120 K and the corresponding re-emission from the filter itself is about 2 W that is significant amount to the available cooling power at the 4 K stage. On the other hand, the expected transmitted radiative power and the re-emitted power from the alumina filter are 20 mW and 45 mW, respectively. These are small enough compared to the cooling power at the 4 K.

We also explore the filter temperature as a function of the filter diameter up to 1000 mm as shown in Fig. 4.39. The lower the value of κt is, the steeper the temperature rise is due to the limited thermal conductance of the filter. For the case of low κt, it is seen that the temperature approaches asymptotically to the value determined purely by the radiative heat exchange. The IR filter made of alumina is on the other hand still effective for a diameter beyond 500 mm.

4.6 Summary

In this section, we explain the development and characterization of the key technologies for PB-2 experiments. These technologies play a critical role to achieve the **Rq1**$\sim$**Rq4**.

The PB-2 system with the large optical system has to reduce the aberration at each detector. To reduce the aberration, the alumina material is selected. We employ the 99.9 % purity alumina that meets

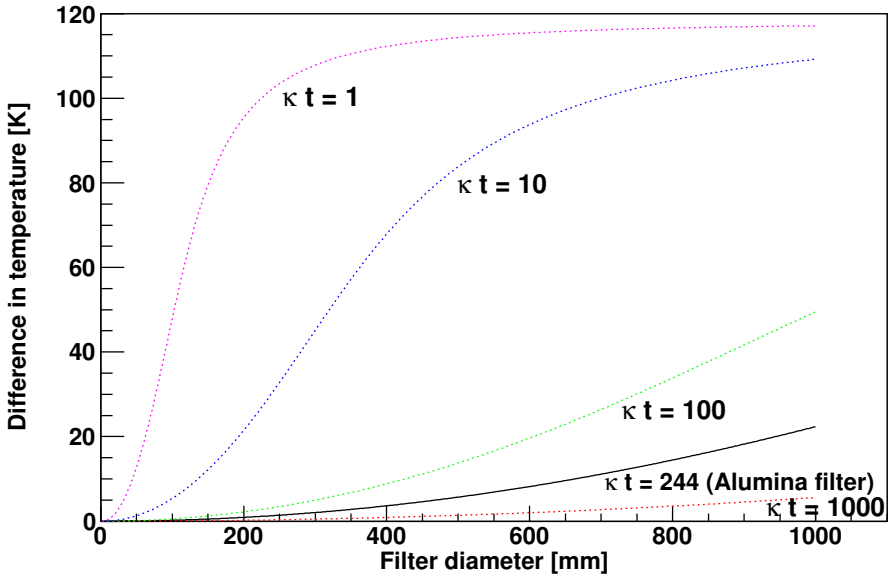

Figure 4.39: The temperature of the alumina filter is shown as a function of the filter diameter. We assume that the edge temperature is 50 K, and temperature of a Zotefoam window is 200 K [18].

our requirements on loss, IOR, and the ingot size. We fabricate the three alumina lenses and measured the shape and IOR. We succeed to develop and characterize the alumina lenses using a CMM and a millimeter source.

We develop the two-layer AR coating for high IOR materials, such as alumina, silicon, and sapphire. We employ the combination of mullite and Skybond Foam with a filling factor of 60 % as the AR coating on flat alumina surfaces. The 2-layer epoxy coating technique has been adopted on curved alumina surfaces. The maximum diameters of AR coatings are 530 mm corresponding to that of the collimator lens. The measured uncertainty of the optical path length ($\delta(nd)$) meets our requirement, i.e. less than $\lambda/50$.

The PB-2 experiment needs the large optical window. The large optical window allows the large emission to any other cold optical system. To reduce this emission, we newly developed alumina IR filters. We have confirmed with measurements that the transmittance, the 3 db cutoff (700 GHz) and temperature rise (2.3 ± 0.1 K) all satisfy our requirements.

We newly invent the absorber, 'KEK black'. We compare it with a conventional absorber, where twelve different recipes for KEK black have been tried. The performance with any recipe we tried is better than that of the conventional absorber. In particular, the performance of sample G is better than that of other samples. We have thus decided to place the 4mm thick absorber at the inner surface of 4 K shell of the PB-2 receiver system.

Chapter 5

Beam simulation

In this chapter, we describe the optical design and simulation of the PB-2 system. The PB-2 optical system consists of the off-axis Gregorian telescope and the alumina optical system. The focal plane of the Gregorian focus is not telecentric. To achieve the telecentric focal plane, the alumina lenses are used as re-imaging lenses. These optical systems are employed in some CMB experiments, such as SPT-3G [90] and ACT [91]. The optical system should be able to achieve the diffraction limit. When the diffraction limit ibreaks, the aberration becomes large. The large aberration of the optical system causes the serious degradation of the angular resolution. In particular, the worse angular resolution results in the sensitivity loss in the high multipole (i.e. small angular scale) regions.

All the detectors must satisfy the diffraction limit. The sensitivity of the PB-2 is shown in the Eq.(2.99), which is assumed to employ a diffraction limited Gaussian beam. Our requirements for the beam width are

- 3.5 arcmin (for 150 GHz),
- 6.0 arcmin (for 95 GHz).

In this chapter, we discuss the beam width projected on the sky with a simi-analytical approach. In Section 5.1, we explain the calculation of the beam with the aberration. In Section 5.2, we describe the simulation method of PB-2 optical system. In Section 5.3, we discuss the aberration with the convoluted beams. In Section 5.4, we calculate the beam effect on the CMB observation.

5.1 Aberration and beam width

We discuss the beam calculation with aberration. In general, the beam with aberration is expressed as

$$w = \int\int_d \exp\left(-ikW(\xi,\eta)\right) d\xi d\eta, \tag{5.1}$$

where $W(\xi,\eta)$ is wavefront aberration and d is an iris diameter. ξ and η are arbitrary position on the iris coordinate. The Strehl ratio is defined as a ratio of beam peaks between the diffraction-limited beam

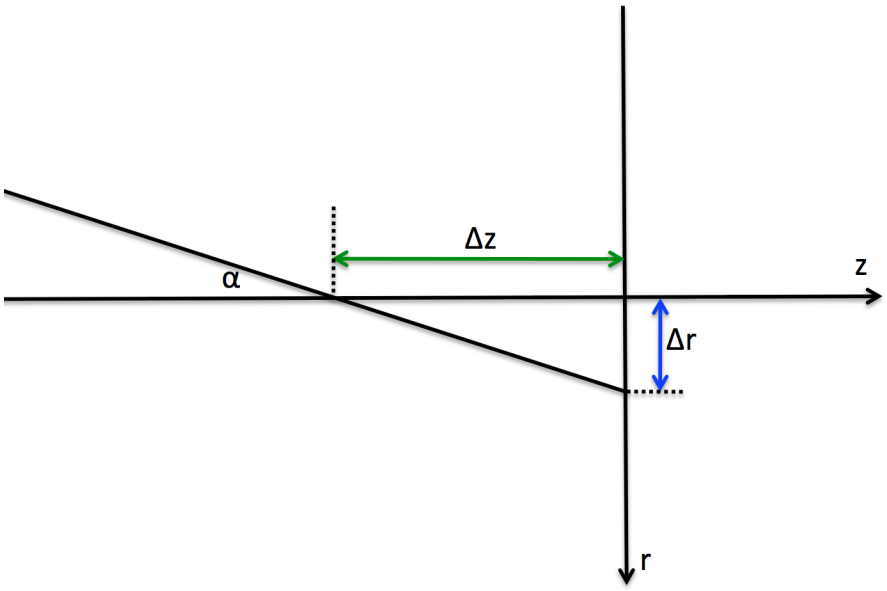

Figure 5.1: Configuration of coordinate for defocus aberration.

and aberration beam:

$$SR = \frac{1}{\left(\int\int_d d\xi d\eta\right)^2}|w|^2. \tag{5.2}$$

In this section, we assume that all the aberration is defocus, which is generated by miss alignment. In a real system, the major miss alignment is caused by the thermal shrinking through the optical axis. Therefore, this calculation is regarded as a good approximation. We define parameters as shown in Fig. 5.1.

ρ is a radius of iris coordinate defined by $\rho^2 = \xi^2 + \eta^2$. To define the aberration, we place the $x - y$ coordinate as $r^2 = x^2 + y^2$. When the focus moves to Δz by the aberration, the lateral aberration is seen as

$$\Delta r = \Delta z \tan\alpha = \Delta z \frac{\rho}{1-\rho^2} = -\Delta z \frac{\partial}{\partial \rho}\sqrt{1-\rho}. \tag{5.3}$$

Therefore, the defocus aberrations are described as

$$\Delta x(\xi,\eta) = -\frac{\partial W(\xi,\eta)}{\partial \xi}, \tag{5.4}$$

$$\Delta y(\xi,\eta) = -\frac{\partial W(\xi,\eta)}{\partial \eta}. \tag{5.5}$$

We obtain the following equation:

$$W(\xi,\eta) = \Delta z\sqrt{1-\xi^2-\eta^2}. \tag{5.6}$$

Redefining the focus as the origin, the above equation becomes

$$W(\xi,\eta) = -\Delta z\left(1-\sqrt{1-\xi^2-\eta^2}\right). \tag{5.7}$$

To generalize the lens model with the index of reflection, n, we yield

$$W(\xi,\eta) = -n\Delta z\left(1-\sqrt{1-\frac{\xi^2+\eta^2}{n^2}}\right) \tag{5.8}$$

The wavefront is described as

$$SR = \exp\left(-\frac{\pi a^2}{\sqrt{12}n\lambda}|\Delta z|\right), \tag{5.9}$$

where a is the numerical aperture, λ is the wavelength. We use Eq.(5.1), Eq.(5.8) and Eq.(5.9) to express beams with aberration. Figure 5.2 and 5.3 show the calculated beam as a function of Strehl ratio.

5.2 GRASP Simulation

We simulate the far field beam with GRASP. [19] The GRASP is a widely-accepted simulation tools for physical optics. The GRASP can simulate the polarized electric field. The GRASP generates the Gaussian beam from the feed horn. The beam excites free electrons on the mirror and generates the current density distribution. The current density distribution generates the secondary electric field. The secondary electric waves then generate the current density on the primary mirror. Finally, we can calculate the re-emitted beams on the primary mirror.

In the simulation, we discuss the Gregorian optical system, which obeys the Mizuguchi-Dragone condition. We assumed to place the feed horn at the Gregorian focus. To be exact, we should include the alumina optical system for the calculation of the cross polarization. For exact simulation of the cross polarization, we usually use the QUAST [53] option, which is an add-on software for the GRASP package.

The main goal of our study is the estimation of the beam width with aberration. The resolution depends on the shape of the main beams. The initial parameter of GRASP is estimated with combination of HFSS and ZEMAX simulation. We simulate the beam pattern of the sinuous antenna with a lenslet at 95 and 150 GHz using the HFSS simulation as shown in Fig. 5.4. The antenna and lenslet model is developed by Aritoki Suzuki.

The beam pattern of the focal plane is projected to the Gregorian focus with ZEMAX simulation. We calculate the transfer function from the ZEMAX simulation. We estimated the initial condition of GRASP simulation with HFSS simulation at 94 and 148 GHz. The assumed parameters are shown in Table. 5.1. The constructed mirror position is shown in Fig. 5.5. We simulate the far field electric wave distribution as shown in Fig. 5.6

The intensities of the beams in Fig. 5.6 are calculated with

$$I = E_x E_x^* + E_y E_y^*. \tag{5.10}$$

We also estimate the Q,U components using Eqs. (2.63) and (2.64).

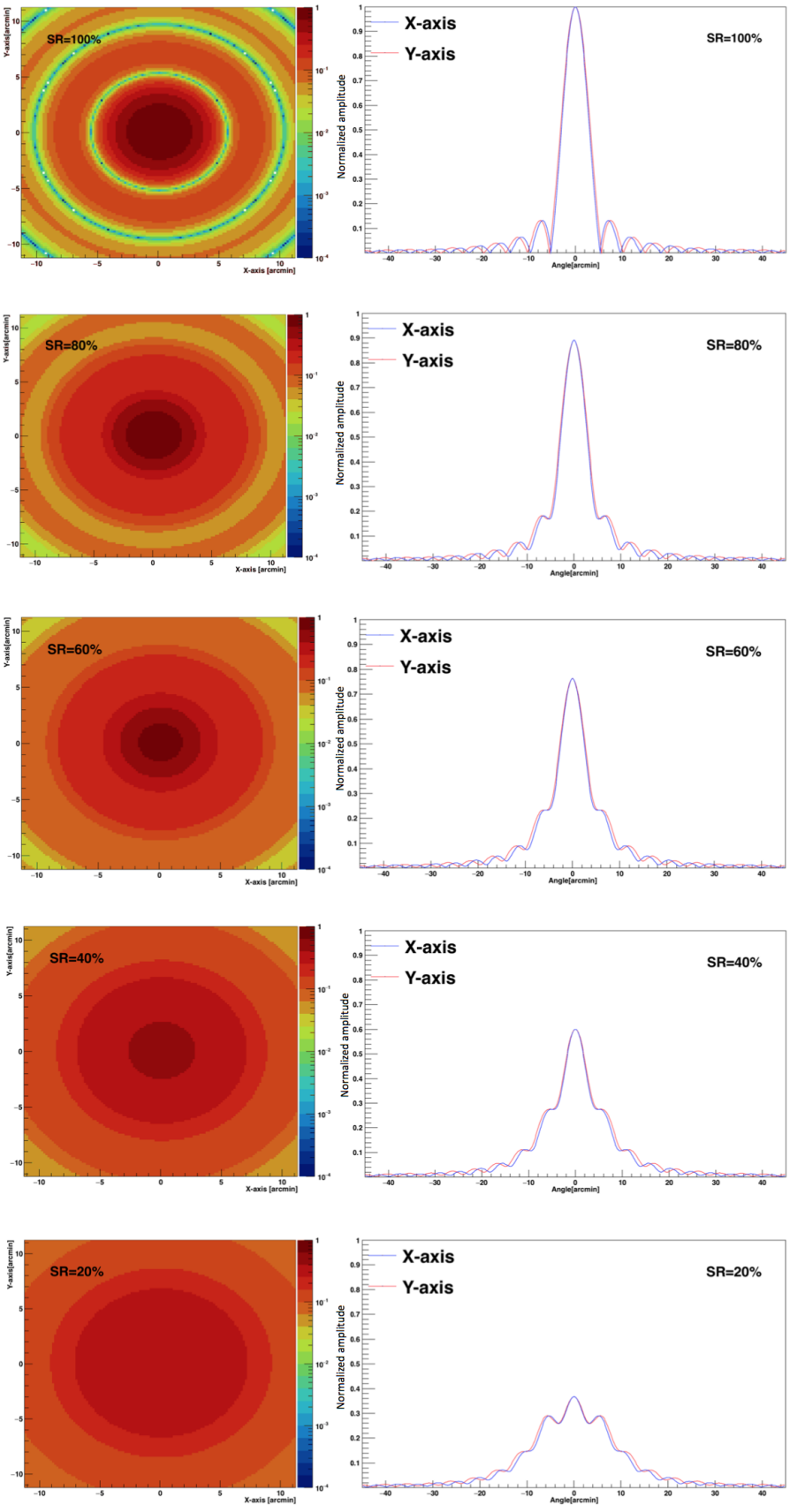

Figure 5.2: The beam at 95 GHz is calculated with the analytical method. All the beams are with aberration. Low SR maps are suppressed due to the aberration.

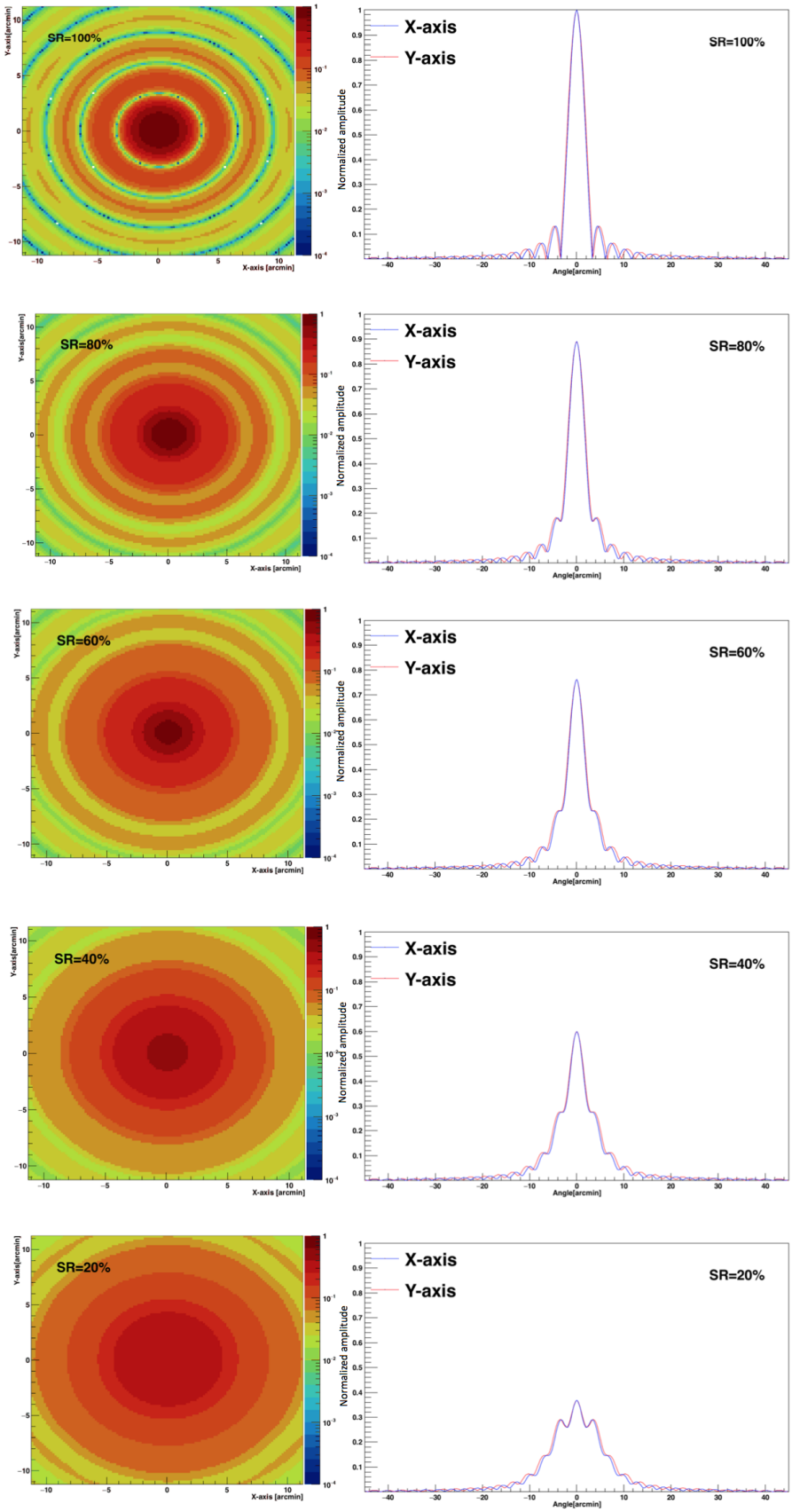

Figure 5.3: The beam at 150 GHz is calculated with the analytical method. All the beams are with aberration. Low SR maps are suppressed due to the aberration.

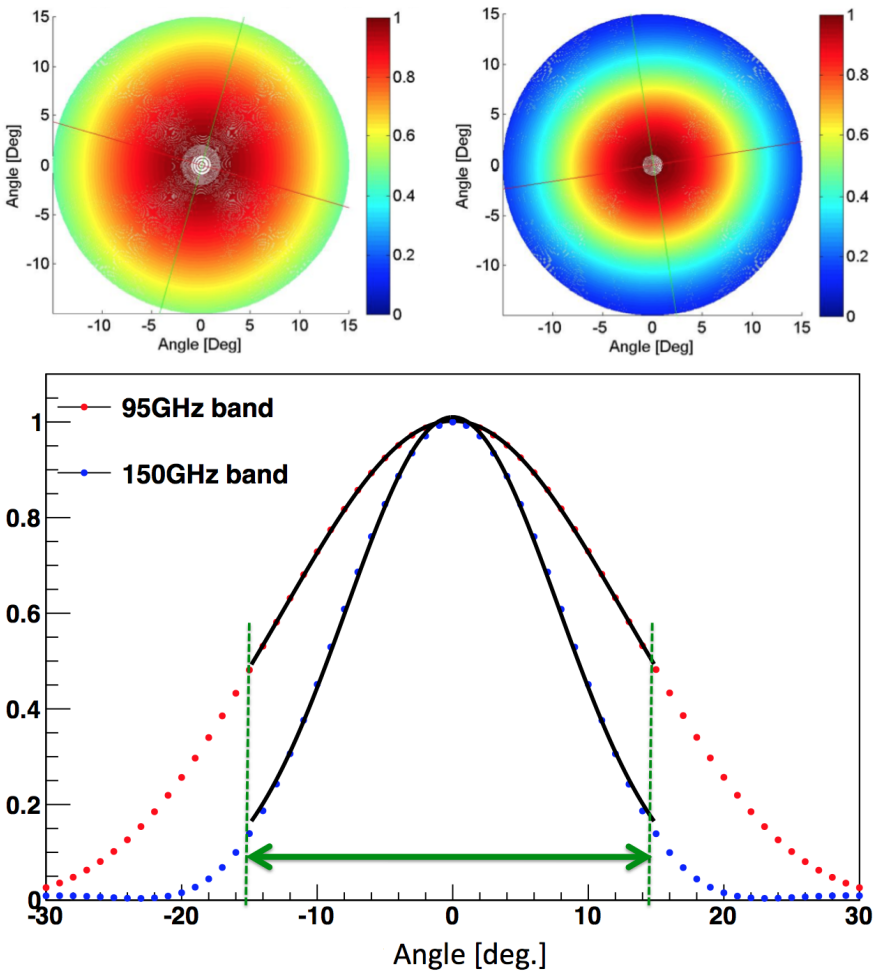

Figure 5.4: The simulation of beams of detectors at 95 and 150 GHz. Both maps can be modeled as Gaussian beams. These maps are calculated by HFSS.

Table 5.1: The assumed parameters of GRASP simulation.

Reflector System	Dual Reflector System
Main reflector aperture diameter	2.5m
Focal Length	2.2m
Angle between main reflector axis and sub reflector axis	19.526259
Distance	0.999999 m
Subreflector eccentricity	0.39338149
Satisfy Mizuguchi condition	Yes
Use absolute or relative values	Absolute

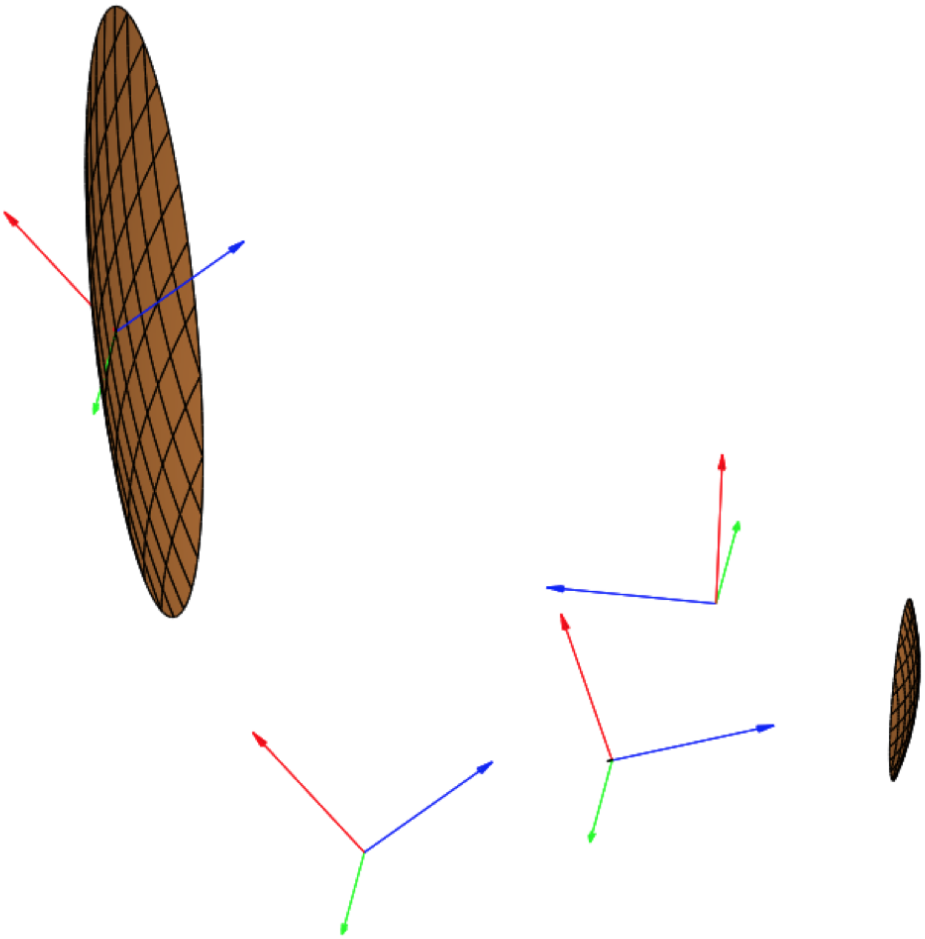

Figure 5.5: Setup of GRASP simulation.

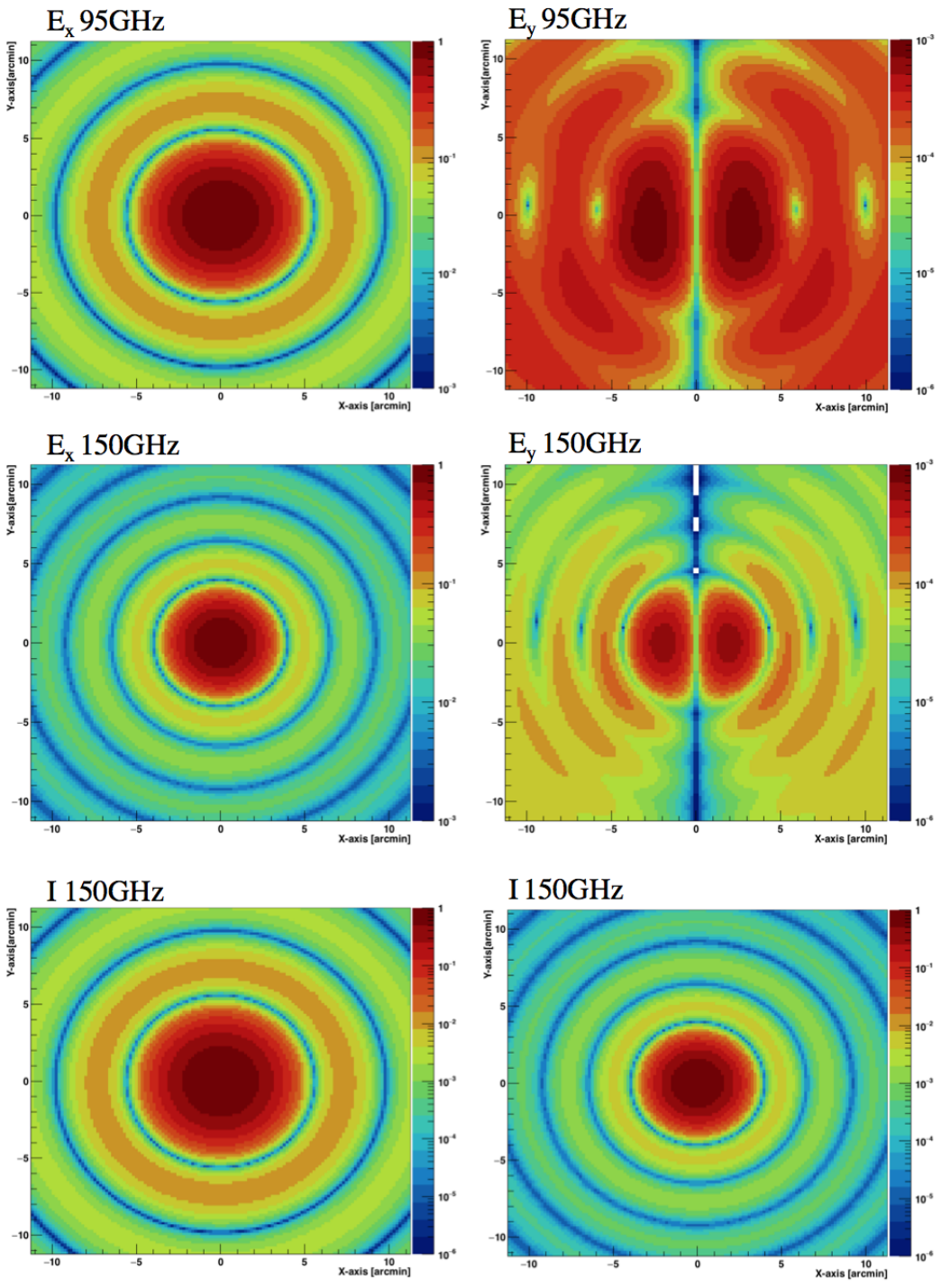

Figure 5.6: Results of GRASP simulation. Aberration effects are not included. Amplitudes are normalized with E_x peaks.

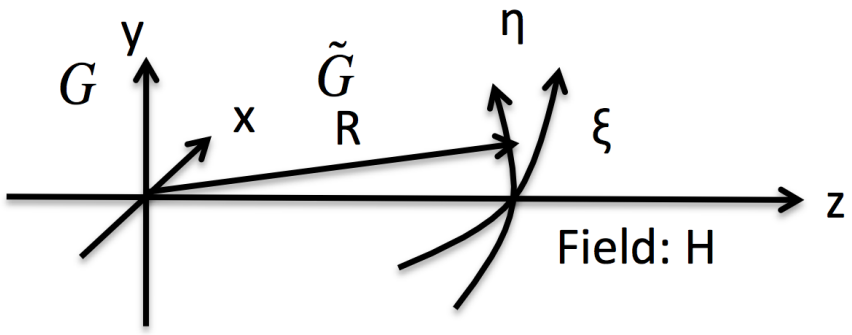

Figure 5.7: Coordinate of the real space and Fourier space.

5.3 Convolution of the beam

We explain the method of the beam simulation with the aberration. In section 5.1 and 5.2, we calculate the aberration effect of the beams and simulate the beams on the sky. In this section, we convolute two beams. We can regard the aberration beam as window function of the simulated GRASP beams. Therefore, we first discuss the far field beam propagation with the window function.

Figure 5.7 shows the propagation of electric waves from G to G' coordinate, where the distance between the origin of G and G' is described as the following equation:

$$\tilde{g}(\xi,\eta) = A\int\int g(x,y)\frac{e^{ikr}}{r}dxdy, \tag{5.11}$$

where $g(x,y)$ is a field on the G space, A is a normalization factor, e^{irk}/r is a spherical field at (x,y) position. Therefore, the projected field can describe the sum of elementary waves on G. Here, we expand the distance of r as follows:

$$\begin{aligned} r &= \sqrt{(x-\xi)^2+(y-\eta)^2+z^2} \\ &= z\sqrt{1+\frac{(x-\xi)^2}{z^2}+\frac{(y-\eta)^2}{z^2}} \\ &= z\left(1+\frac{1}{2}\frac{(x-\xi)^2}{z^2}+\frac{1}{2}\frac{(y-\eta)^2}{z^2}+\cdots\right) \\ &= z+\frac{1}{2}\frac{(x-\xi)^2}{z}+\frac{1}{2}\frac{(y-\eta)^2}{z}+\cdots \\ &= z+\frac{\xi^2+\eta^2}{2z}-\frac{x\xi+y\eta}{z}+\frac{x^2+y^2}{2z}+\cdots \end{aligned} \tag{5.12}$$

We take the far field approximation. We can neglect the higher order terms. Therefore, we can describe

the distance as $r = z + \frac{\xi^2+\eta^2}{2z} - \frac{x\xi+y\eta}{z}$. Then, $\tilde{g}(\xi,\eta)$ is written by

$$\begin{aligned}
\tilde{g}(\xi,\eta) &= \frac{e^{ik\left(R+\frac{\xi^2+\eta^2}{2R}\right)}}{R} A \int\int g(x,y) e^{i\frac{k}{R}(x\xi+y\eta)} dxdy \\
&= \frac{e^{ik\left(R+\frac{\xi^2+\eta^2}{2R}\right)}}{R} A \int\int g(x,y) e^{ik(\theta_x x+\theta_y y)} dxdy \\
&= \frac{e^{ik\left(R+\frac{\xi^2+\eta^2}{2R}\right)}}{R} A \int\int g(x,y) e^{i(k_x x+k_y y)} dxdy. \qquad (5.13)
\end{aligned}$$

We conclude that the far field pattern on G' corresponds to the Fourier transformed pattern on G. The representation of the Fourier transform can also be written as the convolution.

$$\begin{aligned}
H(k_x,k_y) &= \frac{e^{ik\left(R+\frac{\xi^2+\eta^2}{2R}\right)}}{R} A \int\int f(x,y) w(x,y) e^{i(k_x x+k_y y)} dxdy \\
&= \frac{e^{ik\left(R+\frac{\xi^2+\eta^2}{2R}\right)}}{R} A \int\int \left(\int\int F(k'_x,k'_y) e^{i(k'_x x+k'_y y)} dk'_x dk'_y \right) w(x,y) e^{i(k_x x+k_y y)} dxdy \\
&= \frac{e^{ik\left(R+\frac{\xi^2+\eta^2}{2R}\right)}}{R} A \int\int F(k'_x,k'_y) \left(\int\int w(x,y) e^{-i((k_x-k'_x)x+(k_y-k'_y)y)} dxdy \right) dk'_x dk'_y \\
&= \frac{e^{ik\left(R+\frac{\xi^2+\eta^2}{2R}\right)}}{R} A \int\int F(k'_x,k'_y) W(k_x-k'_x,k_y-k'_y) dk'_x dk'_y \\
&= \frac{e^{ik\left(R+\frac{\xi^2+\eta^2}{2R}\right)}}{R} AF * W(k_x,k_y) \qquad (5.14)
\end{aligned}$$

Therefore, the far field pattern of G' corresponds to the convolution of $F(\xi,\eta)$ and $W(\xi,\eta)$, which are the Fourier transformed field, $f(x,y)$, and window function, $w(x,y)$. We simulate the intensity map with aberration, which convolutes with GRASP and aberration beams as shown in Fig. 5.8.

5.4 Sensitivity and beams

Finally, we discuss the beam effect of the power spectrum. When we analyse the CMB data, we have to calculate the power spectra on the measured sky area. The calculated B-mode pattern is averaged with the weight of the beam of the telescope, so that the small structure is smeared by the beam resolution. The relation is presented in the exponential factor of Knox formula as shown in Eq.(2.99). In this case, we assumed the diffraction limited Gaussian beam, the sensitivity becomes worse because the beam with large aberration can not be modeled as a Gaussian beam. Thus, we estimate the exponential factor in the Knox formula using arbitrary beams, $B(\vec{\boldsymbol{x}})$. The exponential factor can describe two-step processes. At first, we calculate the two-dimensional Fourier transform of the beam pattern:

$$\hat{B}(\vec{\boldsymbol{l}}) = \int d^2x B(\vec{\boldsymbol{x}}) e^{-i\vec{\boldsymbol{l}}\cdot\vec{\boldsymbol{x}}} \qquad (5.15)$$

The power spectrum is defined in Fourier space as a function of multipole, l. Second, we find the angular average of square of Fourier transformed beam pattern:

$$W_l = \frac{1}{2\pi} \int_0^{2\pi} d\phi \left| \hat{B}(\vec{\boldsymbol{l}}) \right|^2. \qquad (5.16)$$

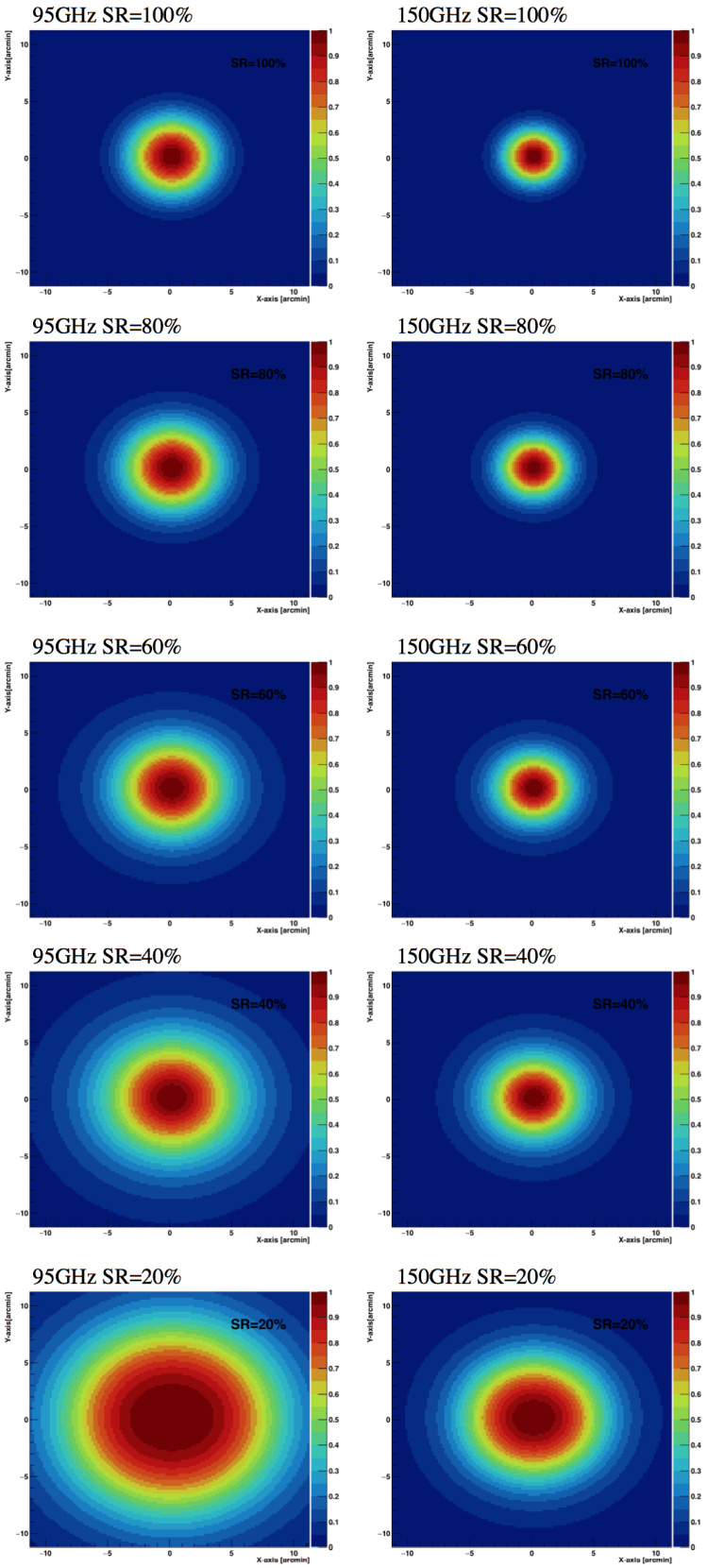

Figure 5.8: The convoluted beams of GRASP and aberration beams. Beam widths are increased by aberration.

In the case of Gaussian beam, W_l is corresponding to $e^{-l^2\sigma^2}$. We calculate the W_l with any Strehl ratio as shown in Fig. 5.9. Fig. 5.10 shows the calculation of the FWHM by changing the Strehl ratio.

5.5 Summary

We discuss the beam pattern with aberration in this chapter. When we design the large cold optical system, the alignment is one of the most important studies because the size of the lenses shrinks at the cold temperature. The shrinking may cause the misalignment of optical system and deform the beam shapes by aberration. The beam with aberration smears the small structure, so that the sensitivity of high multipole moment becomes worse. In this section, we assumed the defocus aberration. We conclude that the beam size increases if the the Strehl ratio is less than 0.8. We calculate the effective beam width as a function of Strehl ratio. This relation can be compared with the real measurements. In the next section, we actually try the alignment and simulate the Strehl ratio based on real measurements.

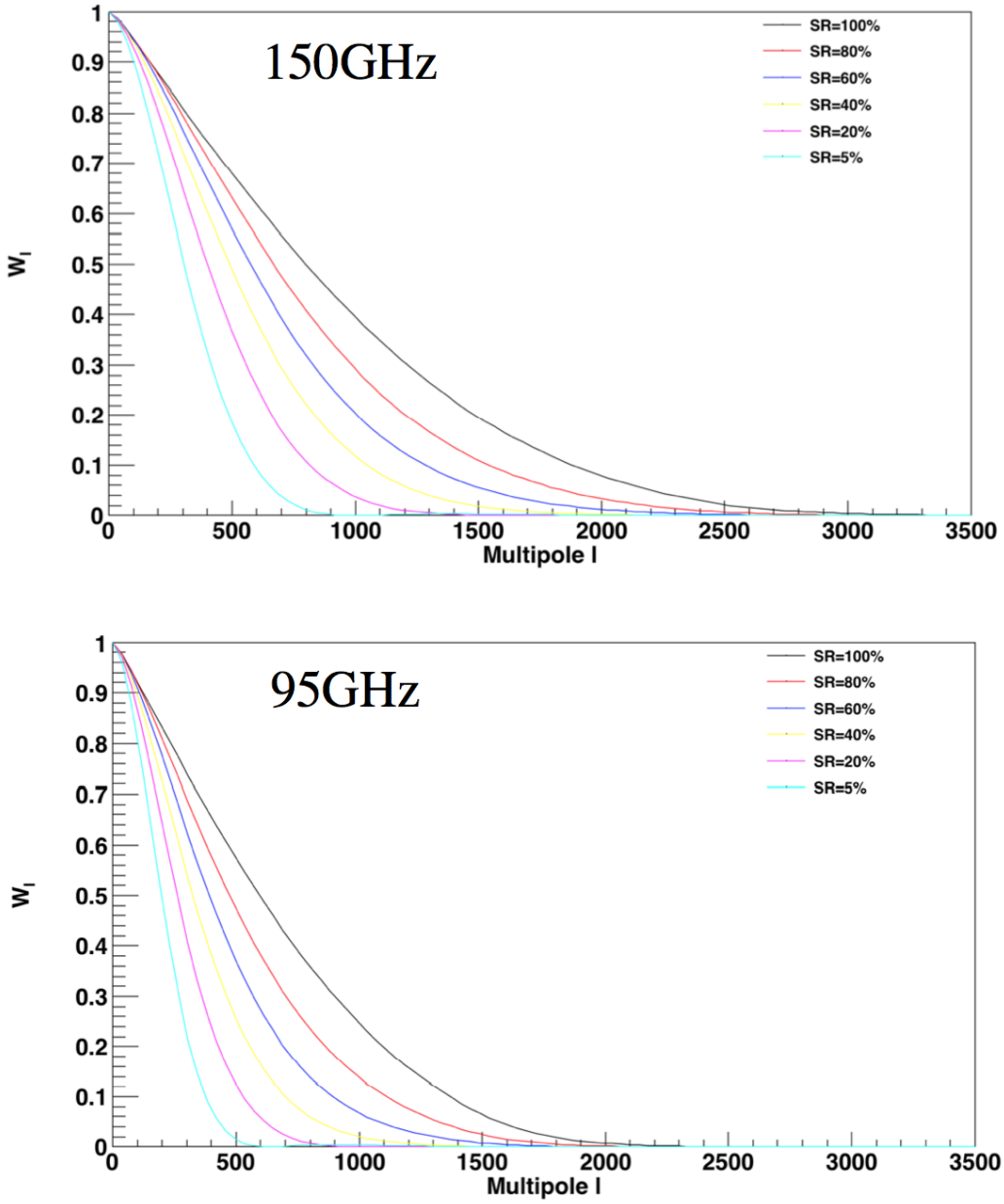

Figure 5.9: The window function as a function of multipole moment. The inverse of window function, W_l^{-1}, is proportional to sensitivity as shown in Eq. (2.99).

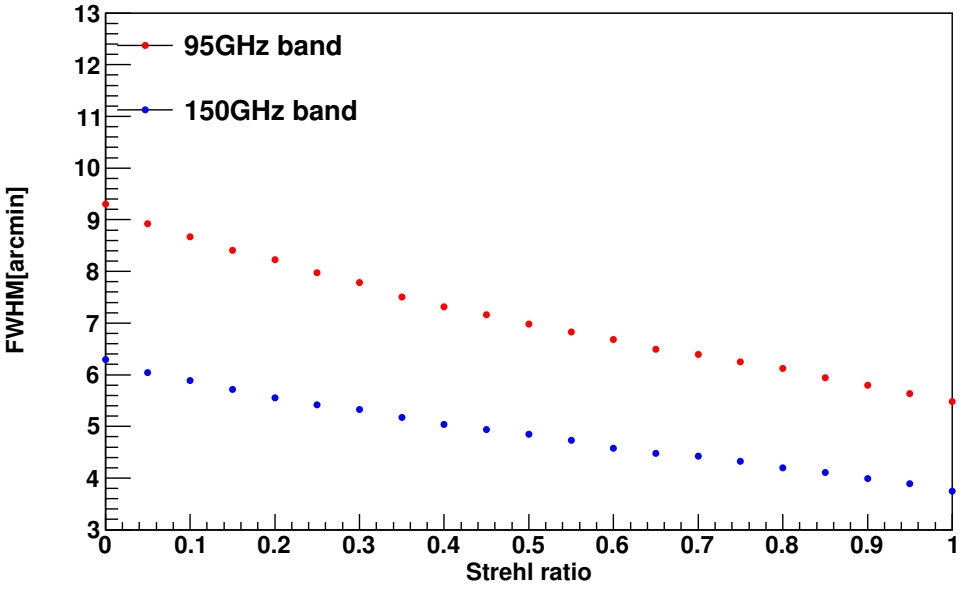

Figure 5.10: The estimated FWHM of beam with abberation.

Chapter 6

Alignment of optical elements

The characterization of an alumina optics is one of the key tasks to achieve the large optics with a large focal plane. All the pixels should meet the requirements of diffraction limited optics at each detection frequency. We employ the alumina optics for the PB-2 system as re-imaging lenses. The purity of an alumina is 99.9 % because of the lowest loss tangent for minimizing the photon noise in a detection band. In this chapter, we summarize the alignment method and results.

6.1 Optical design with ZEMAX simulation

We designed the optics which is based on the ray trace simulation, ZEMAX. The requirements of the optical design are listed as follows:

(i) PB-1 mirrors The HTT is designed to accommodate a large diameter of the focal plane. However, the diameter of the PB-1 focal plane is less than the design diameter. PB-2 uses the maximum size of focal plane with the same mirrors.

(ii) Focal plane with the 365 mm in diameter According to science requirements, we need to make a large detector array with 7588 detectors. To meet our requirements, we should place the 365 mm focal plane.

(iii) Diffraction-limited optics at each pixel To meet the requirements of diffraction limited optics, we must reduce the aberration and pseudo-polarization through the photon transmission with optical component. We have used the UHMWPE lenses in the PB-1 experiment. The UHMWPE optics cannot be used for the PB-2 optical system. This is because it generates the large aberrations and pseudo polarization at each lens.

(vi) The lenses diameter To reduce the aberration sufficiently, we should make a small aberration optics. We require the high IOR material and large diameter of lenses. From the simulation, the

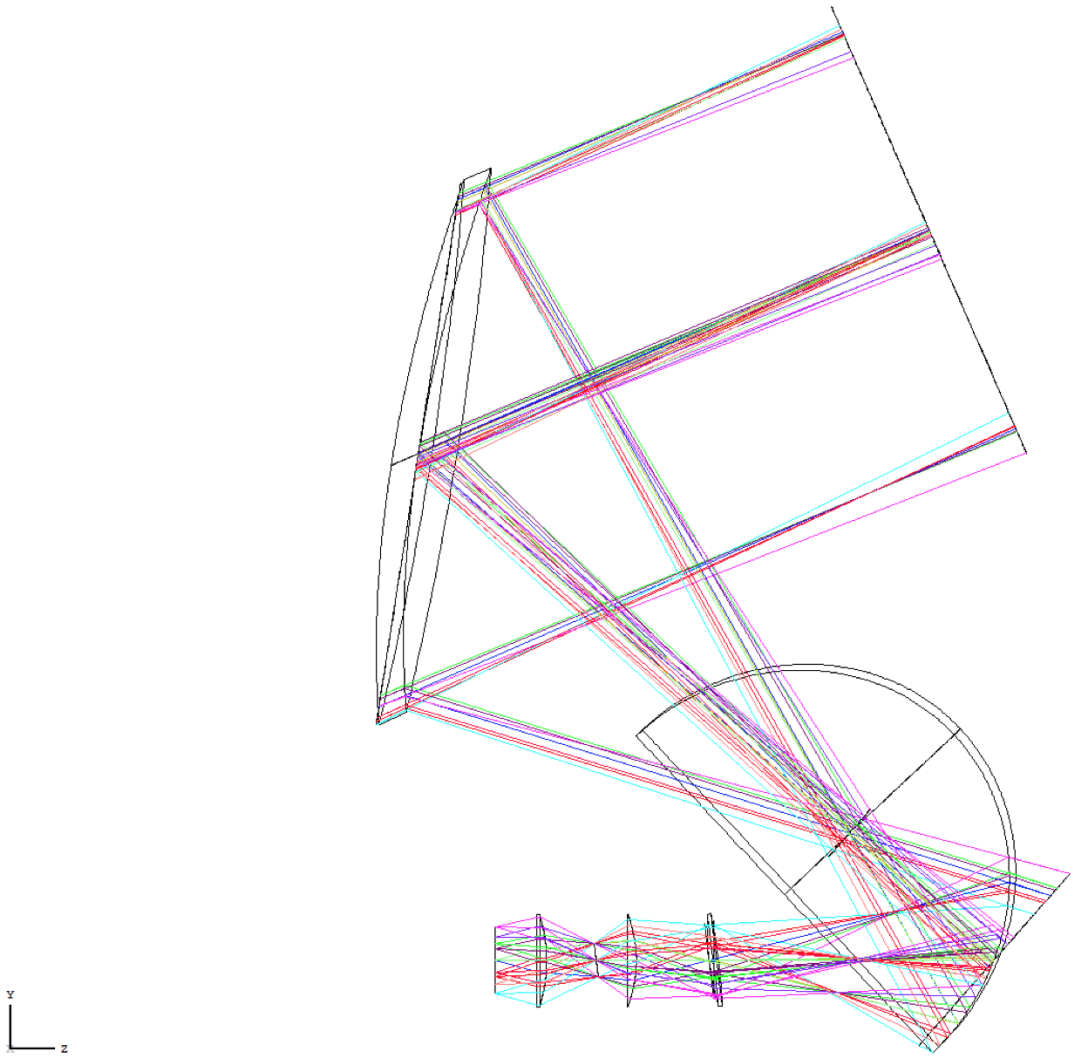

Figure 6.1: The simulated optical design with ZEMAX.

requirement on the lens diameter is 500 mm.

We design the optical system to meet these criteria. Fig. 6.1 shows the designed optics with ZEMAX.

6.2 Strehl ratio

The throughput of alumina optics is an overall measure of the amount of ray that can be collected by the optical system. However, the performance of optical system is more usefully measured in"diffraction limited field of view" (DLFOV). That is the size of focal plane in which the optical performance is diffraction limited [65]. The Strehl ratio and rms wavefront error are commonly used to determine

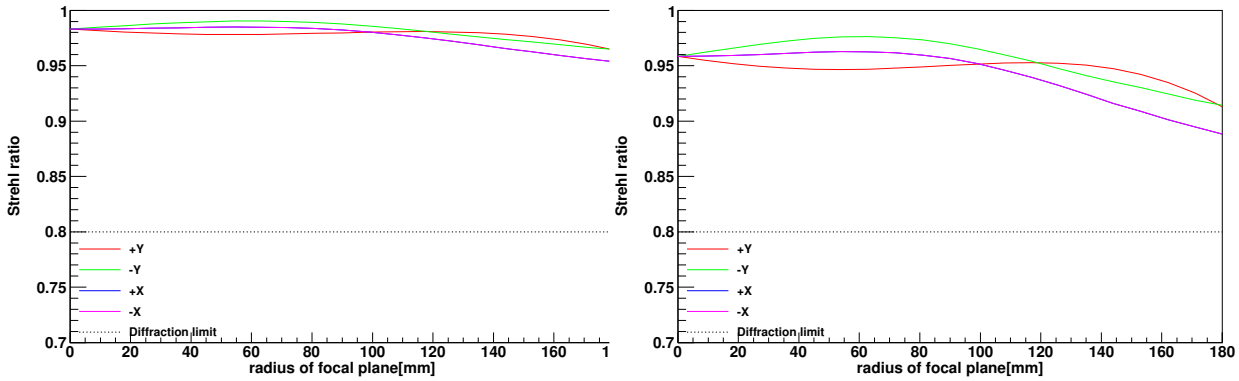

Figure 6.2: The Simulated Strehl ratio of PB-2 optical system with the optimized position. Left (Right) plot shows results of 95 GHz (150 GHz). Definitions of axes are shown in Fig. 6.4.

whether the optical performance is diffraction limited. The Strehl ratio is defined by

$$SR = |e^{i\phi}|^2 = |e^{i2\pi\delta/\lambda}|^2, \tag{6.1}$$

where ϕ is a phase error. According to Mahajan formula, the Strehl ratio can be written by

$$SR \sim e^{-\sigma^2}, \tag{6.2}$$

where σ is the rms wavefront error, $\sigma = \sqrt{\phi - \bar{\phi}}$. Our system that provides a Strehl ratio larger than 0.8 at a particular field point is generally considered diffraction limited at the field point. The minimum DLFOV is the area on the focal plane with Strehl ratio larger than 0.8. Therefore, our optical systems have to be optimized for a higher Strehl ratio.

6.2.1 Tolerance analysis

The tolerance analysis is one of the powerful methods to estimate the aberration and Strehl ratio with any optical systems. We place the mirrors of HTT, three alumina lenses, three metal mesh filters, and an alumina filter in the optical system. The flat disc of optical elements, such as alumina filter and HWP, changes the relative position of lenses and mirrors through the optical axis. This is because the optical path length in the material is extended by $(n-1)d$, where n is an index of refraction and d is thickness of the bulk sample. This effect may lead to miss-alignment of the lenses.

We calculate the Strehl ratio with Monte Carlo simulation based on the measured values and errors of the lens shapes, IOR and thermal contraction as shown in Fig. 6.2 and 6.3. We list parameters that are assumed in the simulation in Table 6.1. We also estimate the requirements for the alignment positions of lenses. The definitions for the alignment, tilt, XY-plane, and Z-axis are shown in Fig 6.4. The requirements of lenses alignment are shown in Table 6.2.

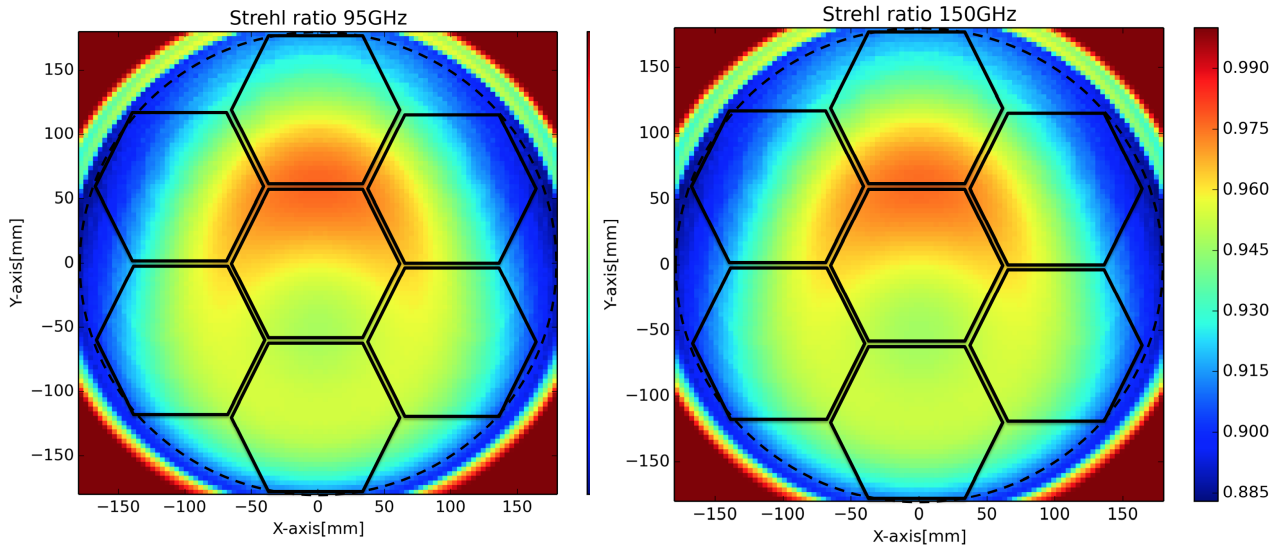

Figure 6.3: The Simulated Strehl ratio of PB-2 optical system. Left (Right) plot shows results of 95 GHz (150 GHz). Definitions of axes are shown in Fig. 6.4.

Table 6.1: Inputs of the ZEMAX simulation. We assumed the measured curvature radius at 77 K, conic constant, thickness, index of refraction, lateral tolerance, and surface irregularity.

	Curvature radius [mm]	Conic constant	Thickness [mm]	IOR	Lateral terrance [mm]	Surface irregularity [μm]
Half wave plate	∞	-	11.10	3.06	-	-
Alumina filter	∞	-	2.00	3.117	-	-
Field lens (front)	1372.08 ± 0.3	-9.978 ± 0.031	50.0 ± 0.5	-	± 0.006	15
Field lens (back)	3164.20 ± 1.3	-11.58 ± 0.033	-	3.109 ± 0.004	± 0.003	7
Aperture lens (front)	633.74 ± 0.6	-2.846 ± 0.003	50.0 ± 0.5	3.109 ± 0.004	± 0.002	30
Aperture lens (back)	∞	-	–	-	-	11
Metal mesh filter	∞	-	4.50	1.5017	-	-
Metal mesh filter	∞	-	4.50	1.5017	-	-
Collimator lens (front)	827.19 ± 0.7	0.082 ± 0.004	50.0 ± 0.5	3.109 ± 0.004	± 0.001	6
Collimator lens (back)	∞	-	-	-	-	5
Metal mesh filter	∞	-	4.50	1.5017	-	-

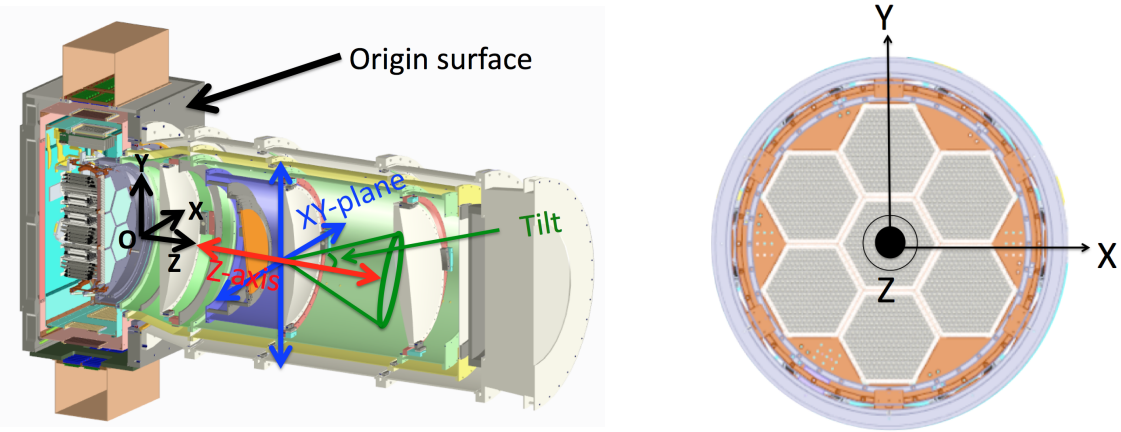

Figure 6.4: Left: Definition of alignment parameters. We selected the front panel of receiver cryostat as the origin of coordinate. The blue plane represents the position tolerance for the XY-axis. The red arrow points the lens position in Z-axis. The green cone indicates a tilt of lens position. Right: Definitions of coordinates for the Srtahl ratio simulation.

Table 6.2: Requirements on lens alignments. Definitions of components are shown in Fig 6.4

	X-axis [mm]	Y-axis [mm]	Z-axis [mm]	Tilt [deg.]	Tilt(x)[deg.]	Tilt(y)[deg.]
Field lens	0.00 ± 6.00	0.00 ± 6.00	1192.10 ± 9.00	7.00 ± 0.5	7.00 ± 0.5	0.0 ± 0.5
Aperture lens	0.00 ± 6.00	0.00 ± 6.00	$718.53 \pm .009$	0.00 ± 0.5	0.0 ± 0.5	0.0 ± 0.5
Collimator lens	0.00 ± 6.00	0.00 ± 6.00	283.84 ± 9.00	0.00 ± 0.5	0.0 ± 0.5	0.0 ± 0.5

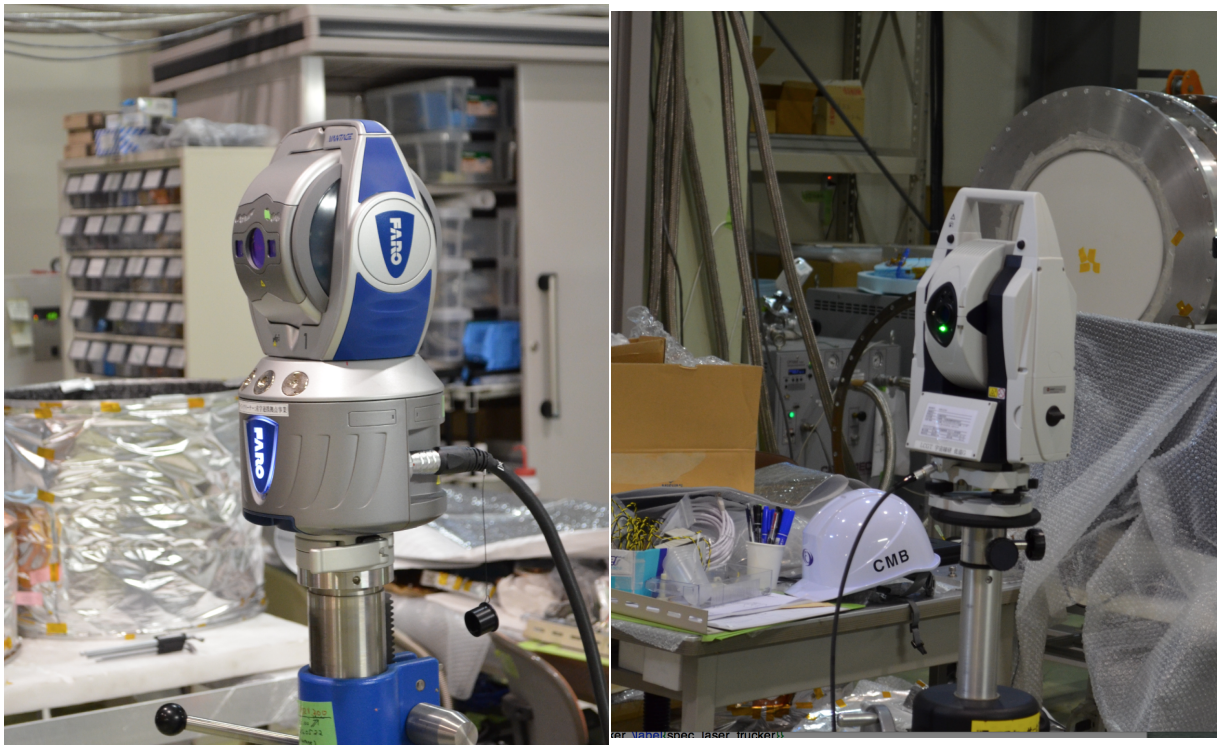

Figure 6.5: Laser trackers. (Left) FARO Laser Tracker Vantage. (Right) Leica AT401.

6.3 Alignment of optical components

We align and measure the alumina lenses and the focal plane. The laser trucker is one of the alignment tools. We used laser trackers for alignment of the lenses.

6.3.1 Laser tracker

Figure 6.5 shows the picture of two laser trackers. One is FARO Laser Tracker Vantage. Another is Leica AT401. The measurement principle of laser tracker is to measure the angle and distance of the two axes. The laser tracker points the target, which is placed in the corner cube reflector as shown in Fig 6.6 and 6.7. The corner cube mirror reflects the laser back in the same optical path. The reflected laser returns to the emitting point of the laser tracker. When the laser light is returned to the tracker, two angle encoders measure the elevation and rotation angle. Furthermore, it measures the absolute distance from the phase of light and calculates the three-dimensional position of the corner cube mirror. The distance between the laser tracker and the measured points is 8 m. The uncertainty of the FARO laser tracker vantage and Leica AT 401 are 0.016 mm/m + 0.0008 mm/m $\times$ 8 m = 0.022 mm and 0.015 mm/m + 0.006 mm/m $\times$ 8 m = 0.063 mm.

We define the origin of the z axis using the front surface of the receiver cryostat. We measured 7 points as shown in Fig 6.8. The rms of flatness and angle with these 7 points are 0.06 mm and 0.012 deg, which are much less than the tolerance shown in Table 6.2.

We then define the origin of XY position using the front surface. We fit measured 12 points to

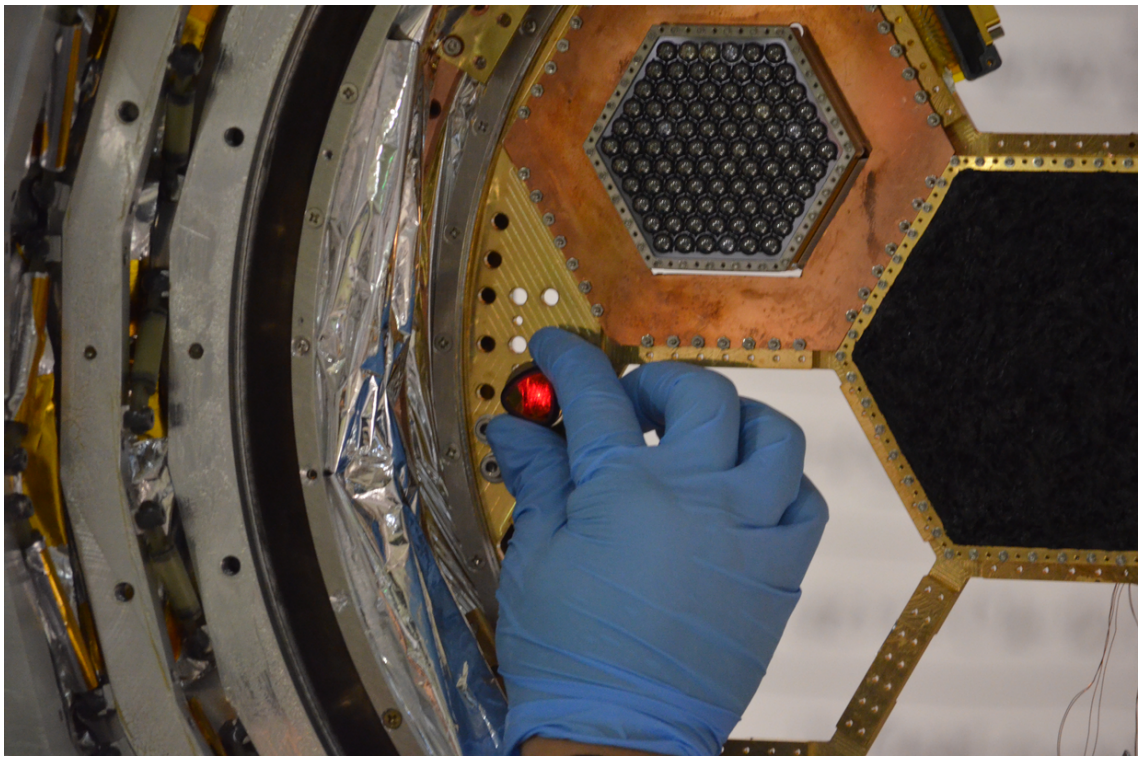

Figure 6.6: Picture of the laster tracker measurement.

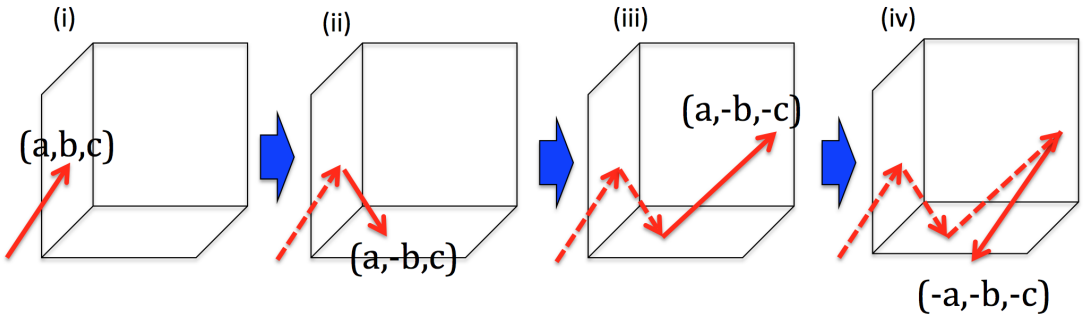

Figure 6.7: Principle of comer cube mirror. (i) The incident ray is reflected on the left side of mirror corresponding to conversion matrix of $diag(1,-1,0)$. (ii) The reflected ray is reflected on the bottom mirror corresponding to $diag(1,1,-1)$. (iii) The ray is reflected on the right mirror corresponding to $diag(-1,1,1)$. (iv) The ray comes back in the same way to the backside corresponding to $diag(-1,-1,-1) = diag(1,-1,1)diag(1,1,-1)diag(-1,1,1)$.

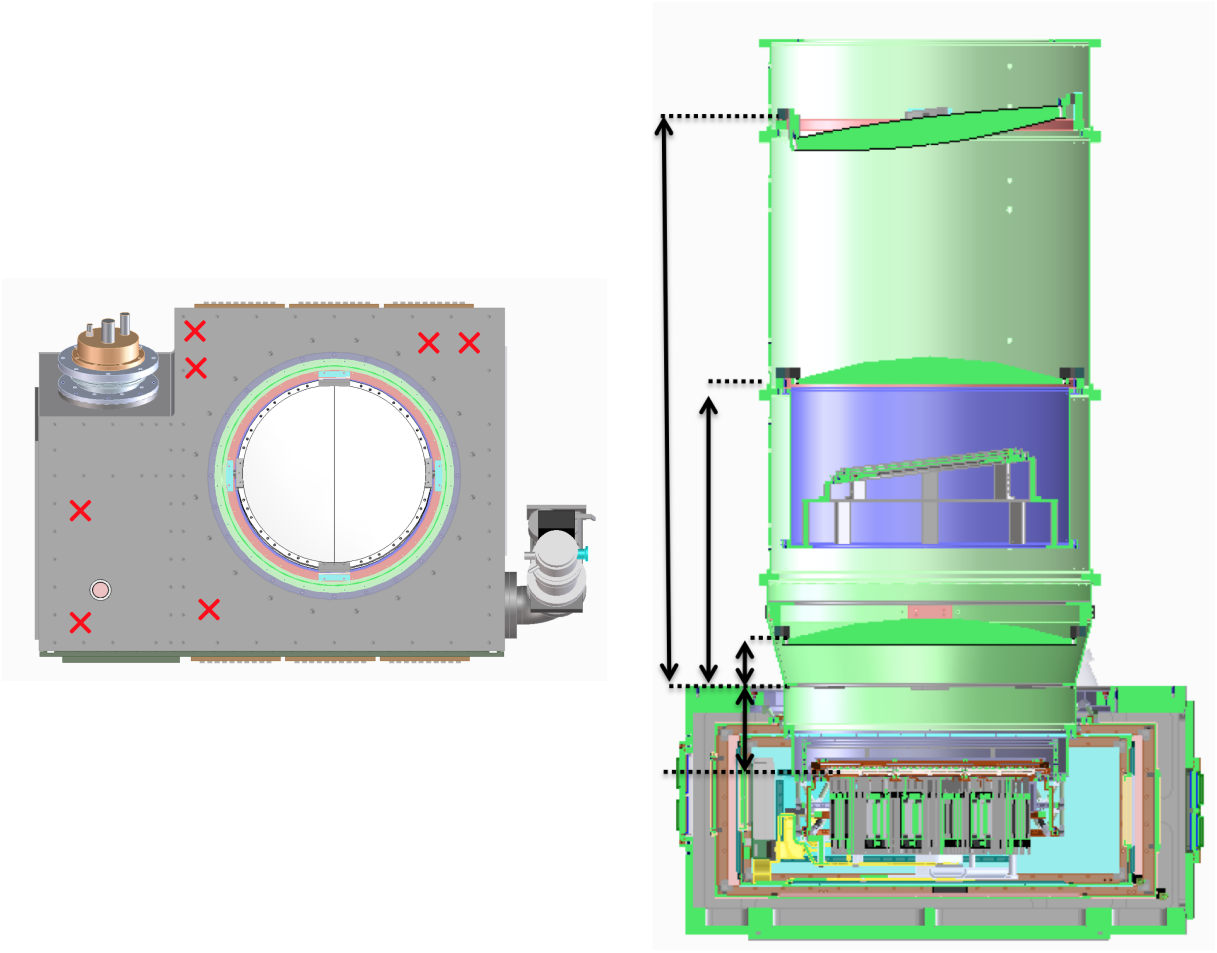

Figure 6.8: Left: the measured position of the Z-direction. Right: definition of lenses positions and focal plane of z-axis.

Table 6.3: Specification of laser tracker.

Type	FARO Laser Tracker Vantage	Leica AT401
Size	224×416 mm	351×221 mm
Weight	12.6 kg	7.3 kg
Maximum measurement length	80 m	80 m
Laser	$632 - 663$ nm (1 mW cw) class II	635 nm (0.5 mW) class II
Resolution	0.5 μm	0.1 μm
Uncertainty	16 μm + 0.8 μm/m	15 μm + 6 μm/m

estimate the center position. Y direction corresponds to the gravity axis.

We measure the position of the focal plane. To be exact, we measured the distance between the origin and the 250 mK plate. The origin of the Z axis simulation is the tip of the lenslet as shown in Fig. 6.9. The distance from the 250 mKplate and the tip of lenslet is measured with a caliper. The measured position to the tip of lenslet from the 250 mK plate is 10.28 mm. We measure the positions of three lenses. When we estimate the XY-plane, we use screw holes around the edges of lenses. To estimate the z position, we measure the lens edge. The lens edge provides the flat surface for the alignment. Finally, we can get the origin coordinate of lenses and normal vector, where bases correspond to the normal vector of origin. The results of normal vector and position coordinate with focal plane and lenses are listed in Table. 6.5. From this table, we estimate the measured distance of XY-plane, Z-axis, and tilt. $\xi_{250mK}, \xi_{FL}, \xi_{AL}$,and ξ_{CL} are coordinates of the focal plane, field lens, aperture lens and collimator lens. The origin of Z-axis corresponds to the 250 mK plate as $\xi_{FP} = \xi_{250mK} + (0.0, 0.0, 10.28)$. The distances from the focal plane to each lens are obtained as

$$\Delta\xi_{FL} = \xi_{FL} - \xi_{FP}, \tag{6.3}$$

$$\Delta\xi_{AL} = \xi_{AL} - \xi_{FP}, \tag{6.4}$$

$$\Delta\xi_{CL} = \xi_{CL} - \xi_{FP}, \tag{6.5}$$

where $\Delta\xi_{FL}, \Delta\xi_{AL}, \Delta\xi_{CL}$ are differences in the distance of field lens, aperture lens and collimator lens. The measured positions are shown in Fig. 6.10.

n_{FP}, n_{FL}, n_{AL}, and n_{CL} are normal vectors of focal plane, field, aperture and collimator lens. Then, the tilt angles of the lenses are obtained as

$$n_{FP} \cdot n_{FL} = \cos\theta_{FL}, \tag{6.6}$$

$$n_{FP} \cdot n_{AL} = \cos\theta_{AL}, \tag{6.7}$$

$$n_{FP} \cdot n_{CL} = \cos\theta_{CL}. \tag{6.8}$$

The measured angles are shown in Fig. 6.11. The results for the collimator and aperture lenses meet our requirements.

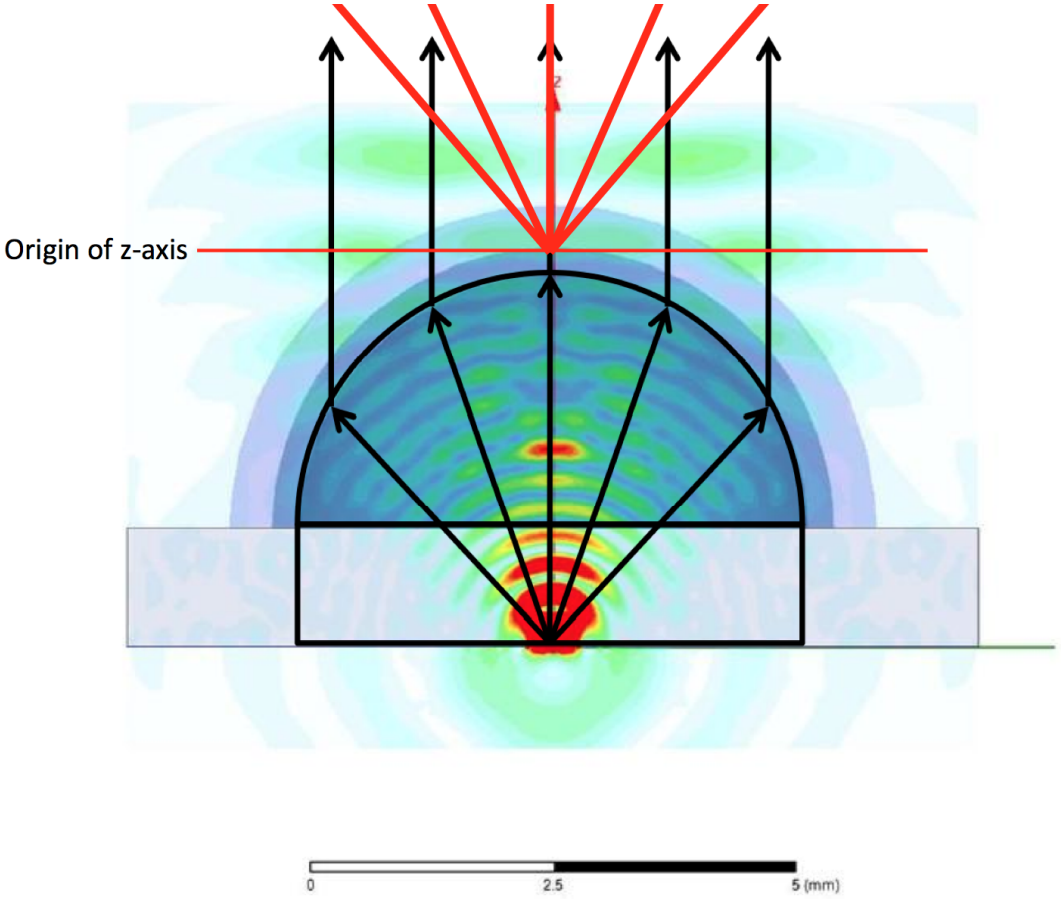

Figure 6.9: The origin of z-axis simulated by HFSS simulation. Private communication with A.Suzuki.

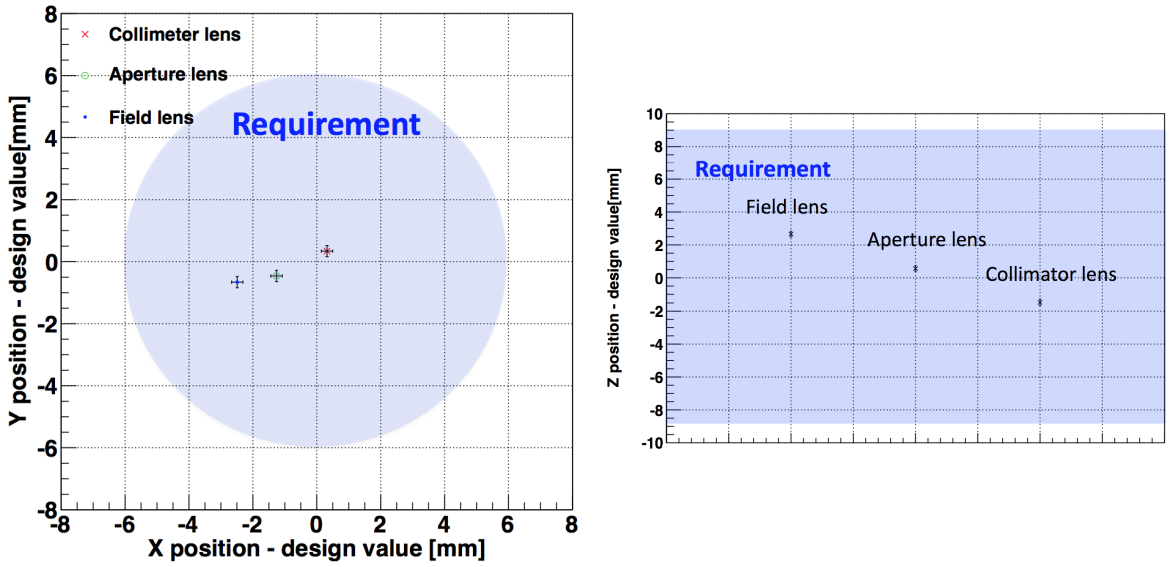

Figure 6.10: The measured lenses position. Left: The X and Y positions from the design value. Right: The measured Z positions.

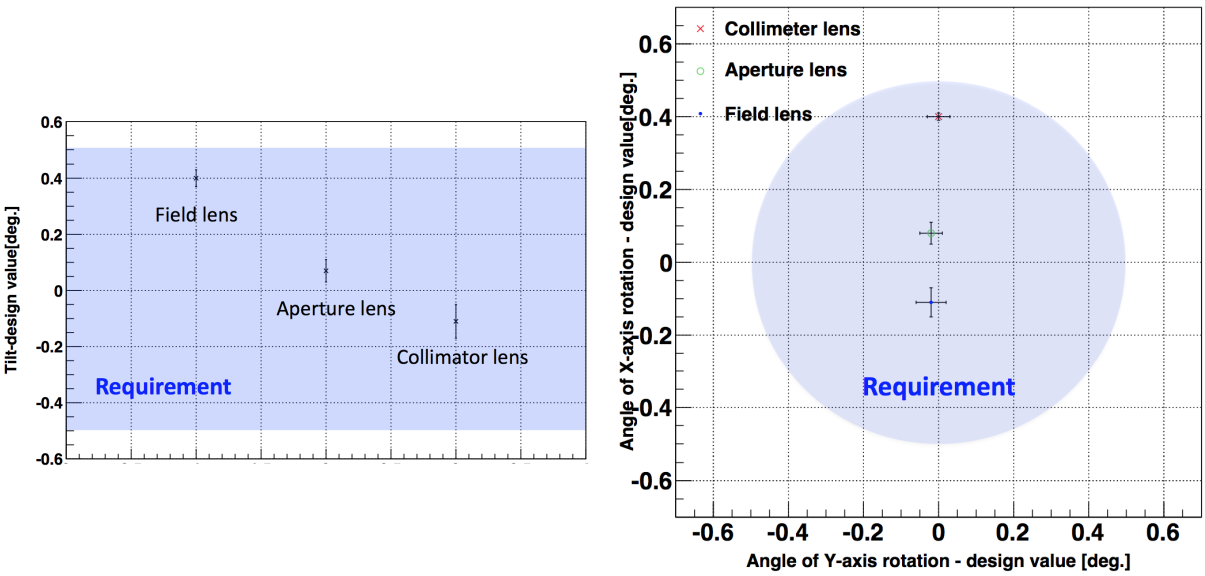

Figure 6.11: Measured lenses angle from the design value.

Table 6.4: Result of lenses alignments.

	ξ	Position vector [mm]	Normal vector	Angle [Degree]	
250mK plate	X	-0.03 ± 0.13	-0.0006	θ	0.04 ± 0.04
	Y	-0.80 ± 0.13	0.0003	θ_x	0.02 ± 0.03
	Z	-166.01 ± 0.13	1.0000	θ_y	-0.04 ± 0.03
Collimator lens	X	0.313 ± 0.13	-0.0006	θ	0.39 ± 0.03
	Y	-0.464 ± 0.13	-0.0068	θ_x	-0.39 ± 0.02
	Z	84.581 ± 0.13	0.9999770	θ_y	-0.03 ± 0.02
Aperture lens	X	-1.29 ± 0.13	-0.0010	θ	-0.09 ± 0.02
	Y	-1.26 ± 0.13	0.0016	θ_x	0.06 ± 0.02
	Z	565.26 ± 0.13	0.9999981	θ_y	0.09 ± 0.02
Field lens	X	-2.52 ± 0.13	-0.000279	θ	6.91 ± 0.02
	Y	3.58 ± 0.13	0.120273	θ_x	6.91 ± 0.02
	Z	1038.58 ± 0.13	0.992741	θ_y	-0.02 ± 0.01

Table 6.5: The estimated lenses positions from the focal plane.

	X-axis [mm]	Y-axis [mm]	Z-axis [mm]	tilt[degree]	tilt (x) [degree]	tilt (y) [degree]
Field lens	-2.49 ± 0.18	4.38 ± 0.18	1194.31 ± 0.18	6.89 ± 0.06	6.89 ± 0.04	0.02 ± 0.04
Aperture lens	-1.26 ± 0.18	-0.46 ± 0.18	720.99 ± 0.18	0.07 ± 0.04	0.08 ± 0.03	-0.02 ± 0.03
Collimator lens	0.32 ± 0.18	0.34 ± 0.18	240.31 ± 0.18	0.40 ± 0.03	-0.40 ± 0.01	0.00 ± 0.03

6.4 Discussion

6.4.1 The method of lens alignment with laser tracker

In Chap. 2, we calculate the significance level for accurate measurements of the B-mode. Then, we assumed that our optical system meets the diffraction limit. However, it is not straightforward to achieve the diffraction-limited optics for the large-diameter focal plane. We have achieved this goal with the large alumina-based optical system. The main advantages to use alumina are low aberration and high thermal conductivity. To realize the alumina optical system, we need to place each alumina component with sufficient accuracy, for which requirements are listed in Table. 6.2. We should characterize the lenses position and angles, respectively. Then, we compare these with design values. In our study, we employ the laser tracker to measure the lenses positions. The laser tracker is a popular measurement system in the accelerator alignment. The laser tracker tracks the corner cube mirror. It measures the three-dimensional position of the center of the corner cube mirror. The lenses are placed into the optics tube, so that the compact object of corner cube mirror has advantage to measure the lenses position.

6.4.2 Design of lens holder and lens position

We contrived the method for mounting lenses. In the observation of CMB on the ground, we consider the motion stability of the elevation scan. We mount the pin type lens holder corresponding to the horizontal axis as shown in Fig. 6.12. This pin can limit the degree of freedom against the rotation motion of the lens. We fix the rotation motion with the spring type holder. The accuracy of the lenses angle of the pin type is better than that of spring type. This difference of accuracy leads to the longitudinal shape as shown in Fig. 6.11. Although the spring accuracy is worse, we choose this method to reduce the difference of thermal contraction between the alumina lens and 4 K shells. The material of 4 K and 50 K shells are A1100 and A5083 whose thermal contraction is 99.58 %. The relative positions of each lens are designed assuming thermal shrink. The lenses holders are mounted at inner surfaces of 4 K shells. Each shell is supported with the truss structure made of vespel pipes. The thickness and diameter of the vespel pipe, VESPEL SP1, is 0.35 mm 9.5 mm.

6.4.3 Strehl ratio with the measured map

We simulate the Strehl ratio based on the measured lens positions as shown in Table 6.5. The simulated Strehl ratios at 95 and 150 GHz are shown in Fig. 6.13. We also calculated the two-dimensional SR maps at 95 and 150 GHz corresponding to the focal plane coordinate as shown in Fig. 6.14. All the regions meet our requirements, i.e. $SR > 0.8$. Therefore, our optical system meets the condition of diffraction-limited optics.

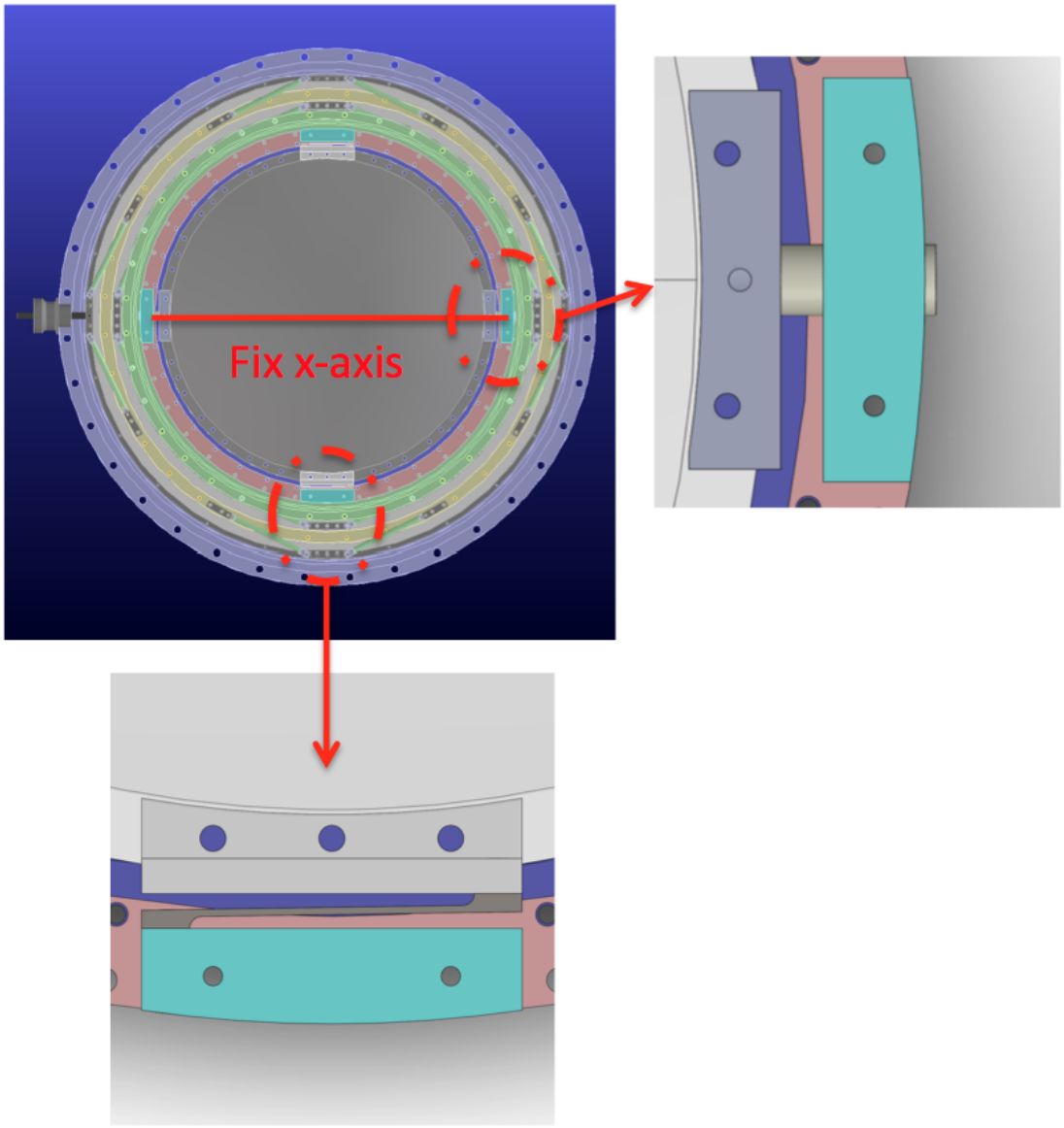

Figure 6.12: The design of the lens holder. The alumina lenses hold the pin and spring type holders.

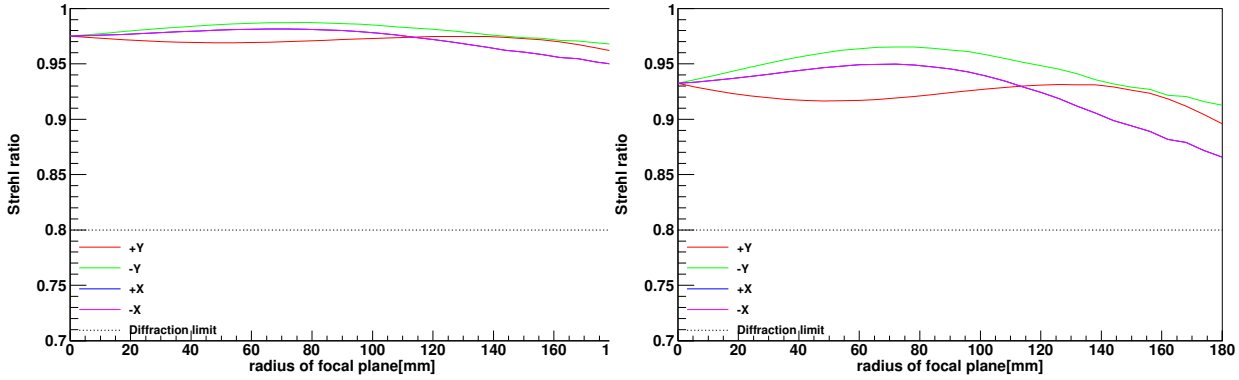

Figure 6.13: The simulated Strehl ratio of PB-2 optical system based on the measured lens positions. Left (Right) plot shows results of 95 GHz (150 GHz). Definitions of axes are shown in Fig. 6.4.

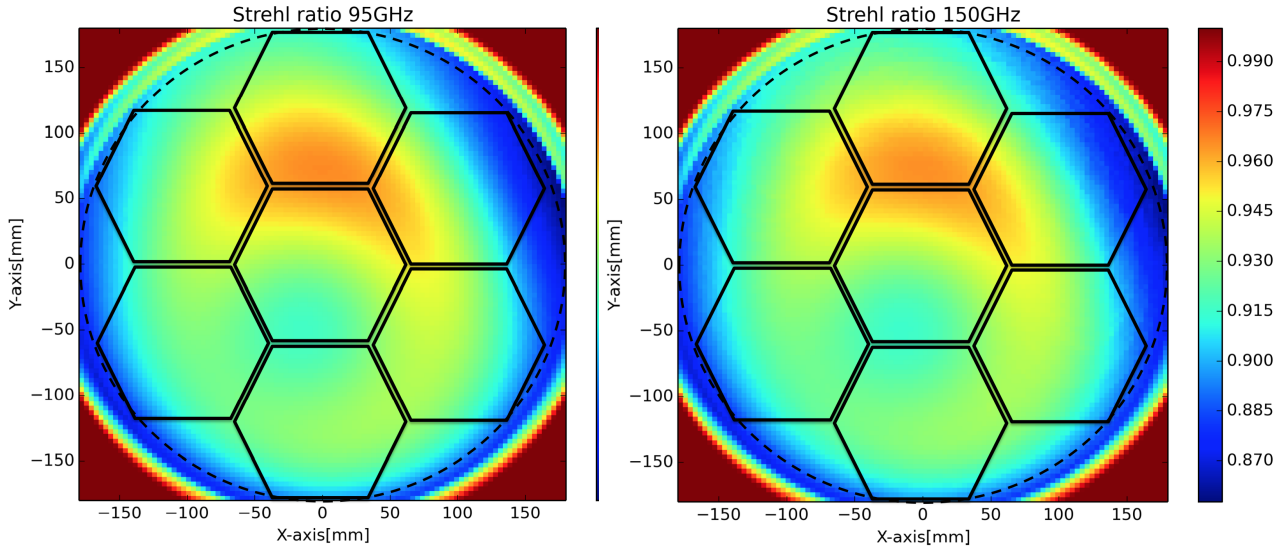

Figure 6.14: The simulated Strehl ratio of PB-2 optical system based on the measured lenses positions. Left (Right) plot shows results of 95 GHz (150 GHz). Definitions of axes are shown in Fig. 6.4.

6.5 Conclusion

We have measured the position vector and normal vector of each lens and focal plane. All the results meet our requirements. Therefore, our optical system satisfies the condition of diffraction-limited optics.

Chapter 7

Sensitivity analysis based on the measurement

Any CMB experiment has various types of the instrumental noise. In the case of the POLARBEAR-2 (PB-2) project, we consider three possible sources of noise; statistical signal noise, thermal carrier noise of TES bolometers, and the readout noise. In this chapter, we discuss the optical loading of the POLARBEAR-2 receiver system. We express noise theory in terms of the noise equivalent power (NEP). The total noise is given by

$$\mathrm{NEP}^2_{\mathrm{tot}} = \mathrm{NEP}^2_{\mathrm{photon}} + \mathrm{NEP}^2_{\mathrm{thermal}} + \mathrm{NEP}^2_{\mathrm{readout}}. \tag{7.1}$$

It is important that each term depends on the instrumental specification. In Sec. 2.7, we defined the statistical error of the B-mode measurement.

7.1 Noise

7.1.1 Photon noise

The power from the i-th element, counting from the bolometer-mounted focal plane to CMB is expressed as

$$P_i = \int \frac{\epsilon_i \eta_i^{\mathrm{cum}} h\nu}{\exp\left(\frac{h\nu}{k_B T_i}\right) - 1} d\nu, \tag{7.2}$$

where ϵ_i is the emissivity of i-th element and η_i^{cum} is the cumulative efficiency, defined as

$$\eta_i^{\mathrm{cum}} = \Pi_{j=1}^{i-1} \eta_j, \tag{7.3}$$

where η_i is efficiency of the i-th optical element. The photon noise can be written as follows:

$$\mathrm{NEP}_{\mathrm{photon}} = \sqrt{2 \int P h\nu d\nu + 2 \int P^2 d\nu}, \tag{7.4}$$

where

$$P = \Sigma P_i. \tag{7.5}$$

We can neglect the second term in Eq.(7.4). This term is known as a photon bunching term. Then, we define the thermal load as Rayleigh-Jeans temperature:

$$T_{\rm load} = 300 \times \frac{P}{\int P_{\rm BB(300K)} d\nu}, \tag{7.6}$$

where $P_{\rm BB(300K)}$ is a black body spectrum at 300 K.

7.1.2 Thermal noise

The thermal noise [92] is described as

$$NEP^2_{\rm thermal} = 4\gamma k_B g T^2_{\rm bolo}, \tag{7.7}$$

where γ is a numerical factor

$$\gamma = \frac{n+1}{2n+3} \frac{1-(T_0/T_{\rm bolo})^{2n+3}}{1-(T_0/T_{\rm bolo})^{n+1}}, \tag{7.8}$$

and g is the instantaneous conductance ($g = dP/dT$). The thermal conductivity is known as $\kappa(T) \cong T^n$ ($n = 3$ for super conductor, n=1 for metal). The PB-2 uses $n = 1$ for thermal conductance to the bolometer leg.

We assume the temperature of the focal plane as $T_0 = 250$ mK and the nominal bolometer temperature as $T_{\rm bolo} = 300$ mK. The instantaneous and integrated thermal conductance are

$$G = nG_{\rm ave} \frac{1 - T_0/T_{\rm bolo}}{1 - T_0^n/T_{\rm bolo}^n}. \tag{7.9}$$

The choice of the average thermal conductance depends on the maximum signal that appears during the observation at the operation point, the transition edge. We take the safety factor of 3 of the maximum loading as

$$G_{\rm ave} = \frac{3P}{T_{\rm bolo} - T_0}. \tag{7.10}$$

7.1.3 Readout noise

We consider the SQUID noise and its end-to-end readout noise. We use the current noise as $I_{\rm rms}$. We assume $I_{\rm rms} = 7$ pA $\cdot \sqrt{\rm s}$ from the PB-1 result. Then, NET is

$$NEP_{\rm readout} = I_{\rm rms} V_{\rm bias}, \tag{7.11}$$

where $V_{\rm bias}$ is the bias voltage. To estimate the electric power, P_e, we assume that the operational resistance of TES bolometer is 1 Ω. Then, we obtain

$$P_e = 2P = \frac{V^2_{\rm bias}}{R}. \tag{7.12}$$

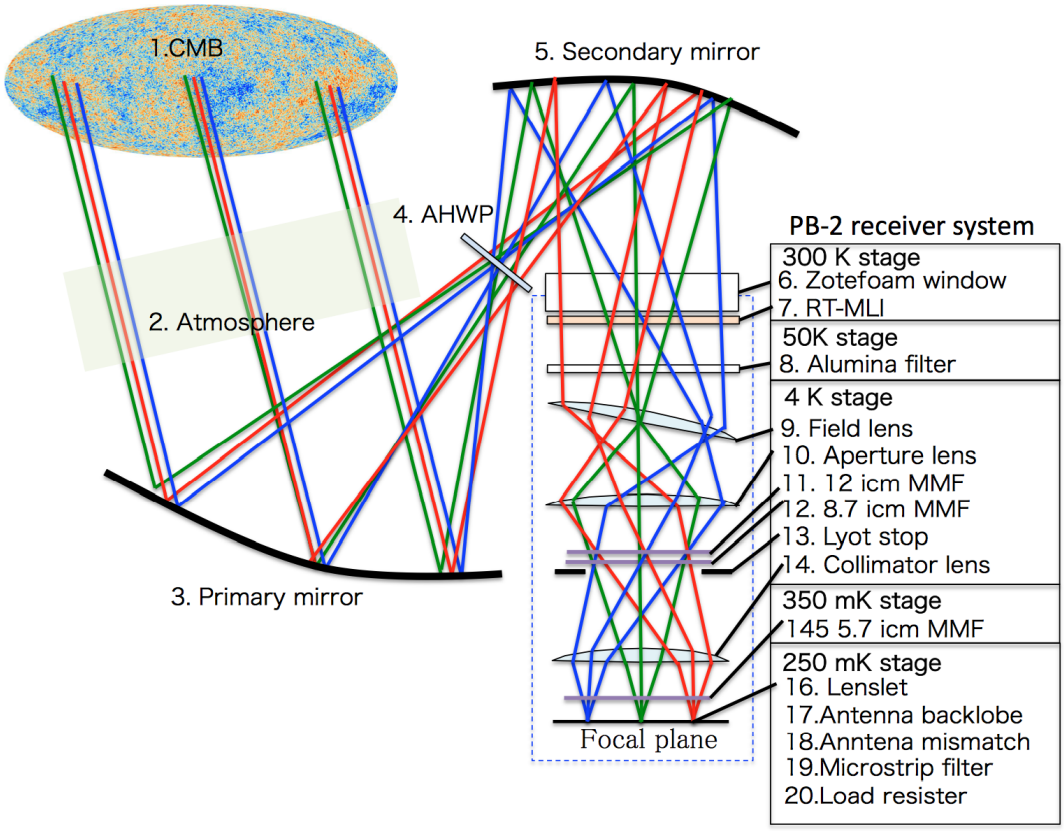

Figure 7.1: Optical elements of the PB-2 system.

7.2 Assumption of the sensitivity calculation

7.2.1 Specifications of PB-2 optical elements

As shown in Chapter 3, the PB-2 receiver consists of the optical cryostat housing the reimaging lenses and the infrared filters, and the detector cryostat housing TES bolometers. The large focal plane imposes the substantial requirements on the thermal design of the optical elements at each of 4 K, 50 K, and 300 K stages. The assumed optical elements are shown in Fig. 7.1. The specification of the receiver system is shown in Table 7.1.

7.2.2 Temperature of optical elements

We measure the temperatures of the optical elements as shown in Fig. 7.2. We use these values as inputs for the sensitivity analysis.

7.2.3 Cosmic microwave background

The CMB temperature is measured by COBE and other projects. We use the measured temperature of 2.72548 ± 0.00057 K.

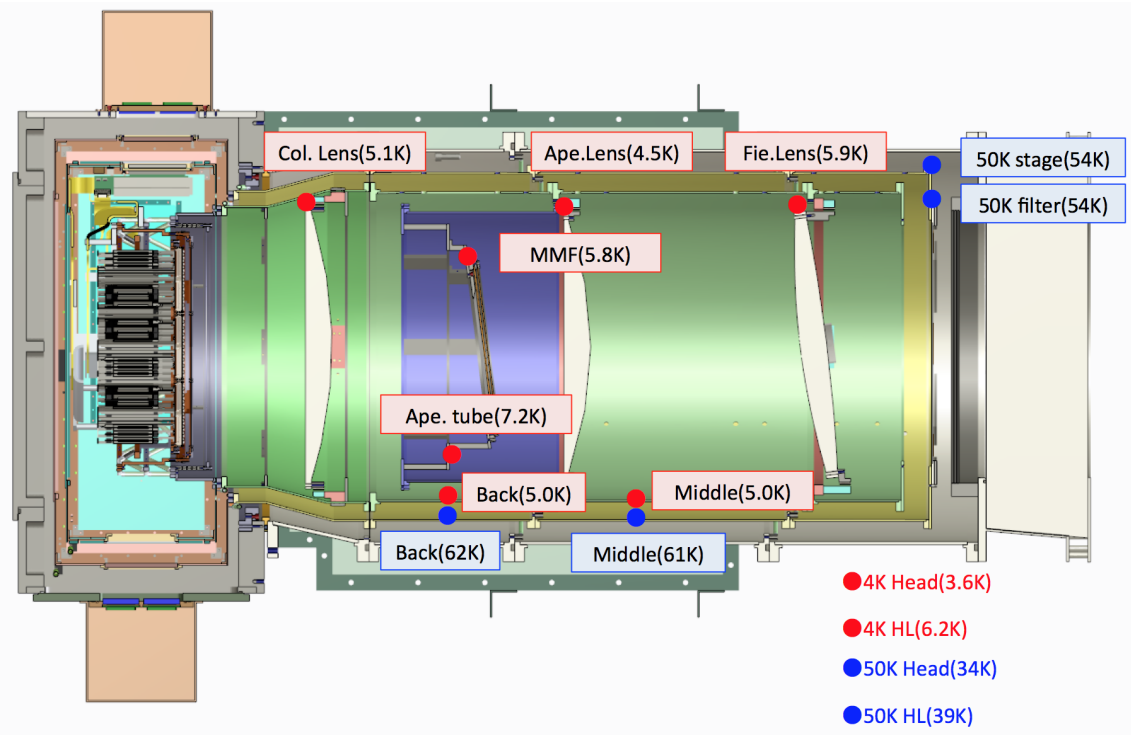

Figure 7.2: Results of the cooling test for the optical cryostat.

Table 7.1: PB-2 receiver specifications.

	W-band	D-band
Frequency center	94.3 GHz	147.8 GHz
Band width	30.6 %	26.0 %
Number of bolometers	3794	3794
F/#	1.92	1.92
Diameter of lenslet	5.346 mm	5.346 mm
NET requirement	$< 360\ \mu\mathrm{K}\sqrt{\mathrm{sec}}$	$< 360\ \mu\mathrm{K}\sqrt{\mathrm{sec}}$
$\mathrm{NET}_{\mathrm{array}}$ requirement	$< 5.6\ \mu\mathrm{K}\sqrt{\mathrm{sec}}$	$< 5.6\ \mu\mathrm{K}\sqrt{\mathrm{sec}}$

Table 7.2: Basic properties of our HWP. The thickness, d, the index of reflection, n, and the loss tangent, $\tan\delta$ are listed. n and $\tan\delta$ are measured at the liquid nitrogen temperature, while the thickness values are measured at the room temperature.

Material	d [mm]	n	$\tan\delta$ [$\times 10^{-4}$]
Sapphire(e)	3.6	3.400	$0.5^{\pm 0.7}$
Sapphire(o)	3.6	3.060	$1.4^{\pm 0.8}$
RT3006	0.23	2.60	1.5
HDPE	0.383	1.52	2.0

Table 7.3: Estimated transmittance, reflectance, and emissivity of AHWP with AR coating.

Material	Frequency [GHz]	AR coating	Transmittance [%]	Reflectance [%]	Emissivity [%]
AHWP	95	RT3006+HDPE	98.9	1.1	1.5
	150	RT3006+HDPE	98.3	1.7	2.0

7.2.4 Atmosphere

One of the largest contributions as the noise source comes from the atmospheric emission. The atmospheric emission is described as a gray body radiation at $T = 273$ K. We assume that the emissivity is 3 %, which corresponds to PWV of 1 mm, at the telescope elevation of 60 degrees in both bands. Thus, the effective temperature is about 8 K. The assumed efficacy of atmosphere is 97 %.

7.2.5 Half-wave plate

The material properties of AR coated HWP are listed in Table 7.2. The transmittances of the AHWP with AR coating are 0.989 and 0.983 at 95 and 150 GHz as shown in Table 7.3, respectively.

7.2.6 Zotefoam window

We calculated the effective temperature of the Zotefoam in detection bands. First, we separate the Zotefoam into N layers along the optical axis. We simulated the temperature distribution inside the Zotefoam window as shown in Fig. 7.3. We define the simulated temperature distribution at i-th layer as T_i. The emissivity at the i-th layer is

$$\epsilon_i = 1 - (1 - \epsilon)^{1/N}, \tag{7.13}$$

where ϵ is an emissivity of 200 mm Zotefoam. Then, we define the effective temperature of Zotefoam as:

$$T_{\rm eff} = \frac{\Sigma \epsilon_i T_i}{\epsilon}. \tag{7.14}$$

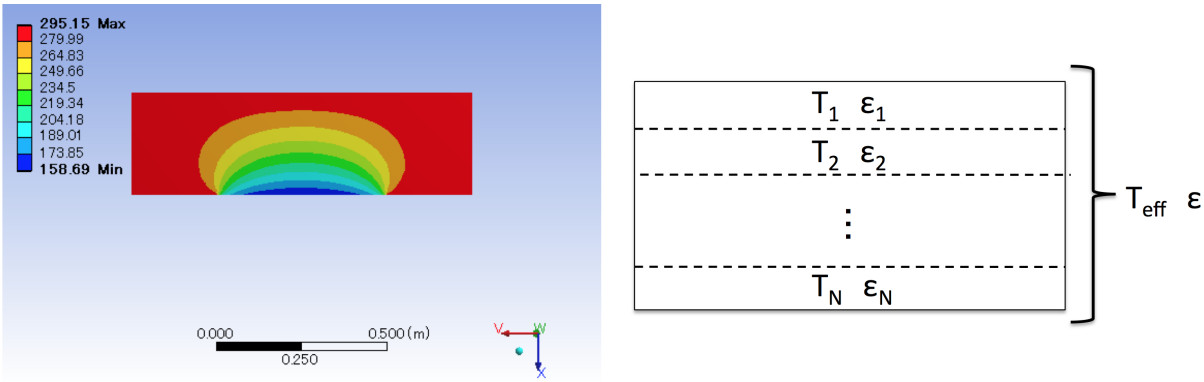

Figure 7.3: Left: One of the simulation results for temperature distribution. Right: Assumption of the layer for the effective temperature calculation.

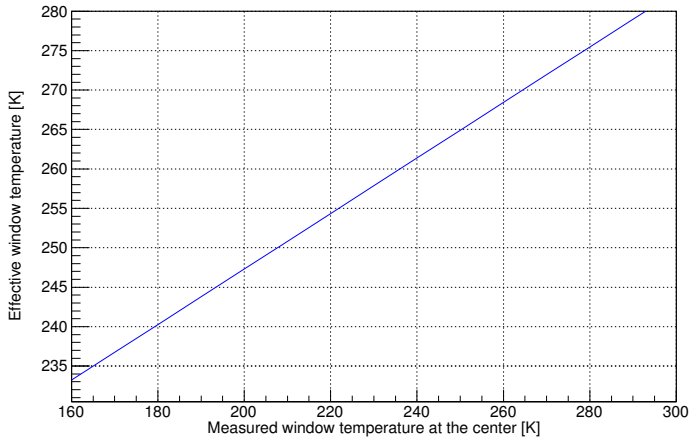

Figure 7.4: Calculation of the effective temperature as a function of the measured Zotefoam window temperature on the vacuum side for 20 cm thickness. The x-axis is the measured temperature of window at center on the vacuum side. The y-axis is the calculated temperature from the simulation of temperature distribution between both surfaces of the window.

The result of the calculation is shown in Fig. 7.4, where we assume the emissivity of 2.0 %. Using the result, the effective temperature is estimated to be 265 K.

7.2.7 RT-MLI

The transmittance of RT-MLI [55] at detection band is measured as shown in Fig. 7.6, where the thickness is 174 mm . We employ the six-stacked RT-MLI, which has low thermal conductivity and transmission over the THz region as shown in Fig. 7.5. While being transparent for the millimeter waves, it thermally behaves similarly to the usual MLI layers for the passive cooling. According to Fig. 7.5, the surface scattering is negligible. The blue solid and dashed curves show results for the six-stacked RT-MLI with each layer having the same thickness. If the effect of the surface scattering is not negligible, the

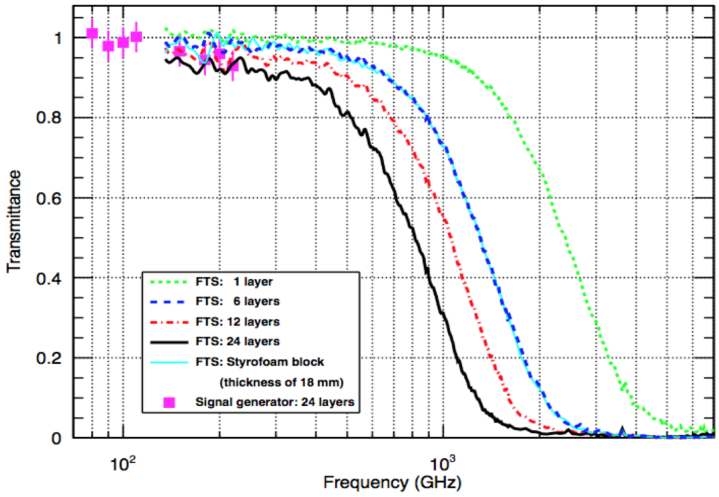

Figure 7.5: Transmittance of RT-MLI at room temperature measured with FTS. The transmittances for four different configurations distinguished by the number of layers (1, 6, 12, and 24 layers) are shown in the figure. The transmittance of a Styrofoam block is shown for comparison. Below the 220 GHz region, the transmittance of the 24-layer sample was also measured using signal generators. This result is from J.Choi et al [55].

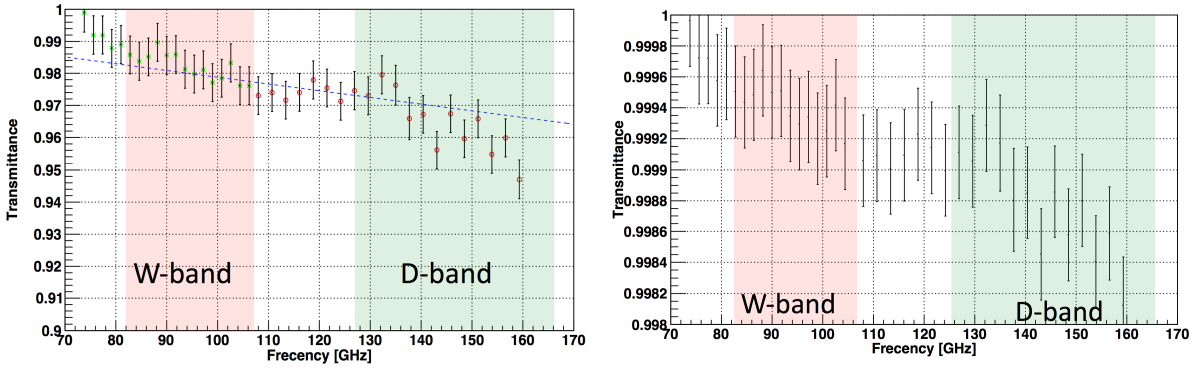

Figure 7.6: Left: The measured transmittance of Styrofoam. The thickness of Styrofoam is 174 mm. Right: Estimated transmittance of 6 stacked RT-MLI using the left plot. The average efficiencies are 0.9994 and 0.9986 at 95 and 150 GHz, respectively.

transmittance should decrease by the surface scattering at the high frequency. From the measurement, we estimate the transmittance of the six-stacked RT-MLI (6 mm). The averaged efficiencies are 0.9994 and 0.9986 at 95 and 150 GHz, respectively. The measured temperatures of the six-stacked RT-MLI are 168 K and 247 K at the side of the alumina filter and Zotefoam window. The average temperature is 208 K. The emissivities of the RT-MLI are 0.0006 and 0.001 at 95 and 150 GHz when we assume that the surface refraction is negligible.

Table 7.4: Estimated transmittance, reflectance, and emissivity.

Material	Frequency [GHz]	AR coating	Transmittance [%]	Reflectance [%]	Emissivity [%]
Alumina filter	95	Mullite and Skybond	95.8	2.2	2.0
	150	Mullite and Skybond	95.8	1.1	3.1
Alumina lens	95	Epoxy	90.5	2.6	7.9
(field lens)	150	Epoxy	88.9	1.0	10.1
Alumina lens	95	Hyblid	91.8	0.6	7.6
(aperture and collimator lens)	150	Hyblid	87.3	1.2	11.5

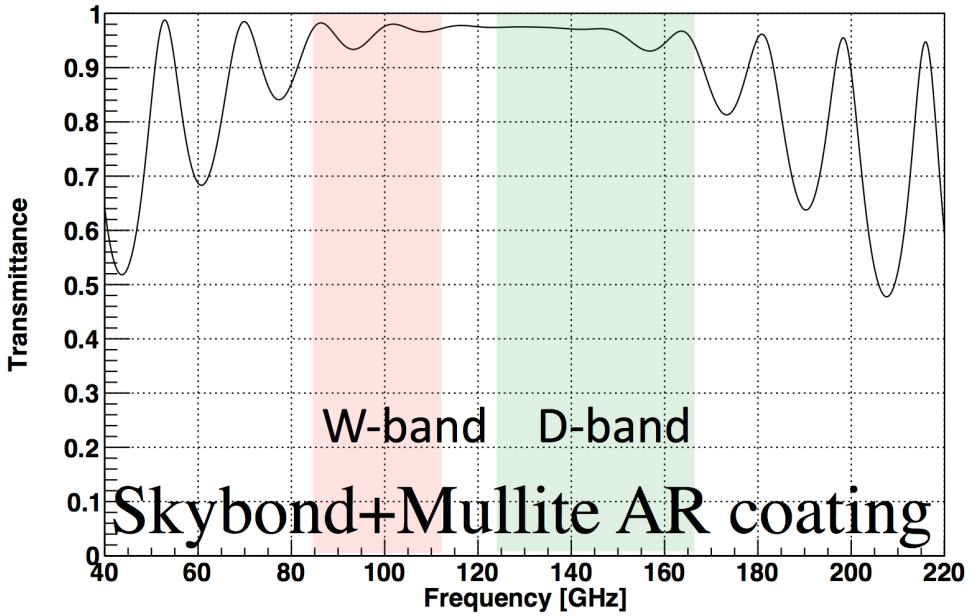

Figure 7.7: Transmittance of alumina filter with Skybond+Mullite AR coating. The parameter used for the calculation is shown in Table 4.8. The band averages of transmittances are 96.1 % and 96.0 % in 95 and 150 GHz band, respectively.

7.2.8 Alumina filter

We calculated the expected fringes as shown in Fig. 7.7, where parameters shown in Table 4.8 are used for calculation. The emissivity is assumed to be 0.04 in each detection band as shown in Fig. 7.4 .

7.2.9 Alumina lenses

We placed the epoxy and Mullite+Skybond AR coating on the curved and flat surface, respectively. The size of three alumina lenses is assumed to be ϕ 500 mm $\times$ t50 mm. Fig. 7.8 shows the expected

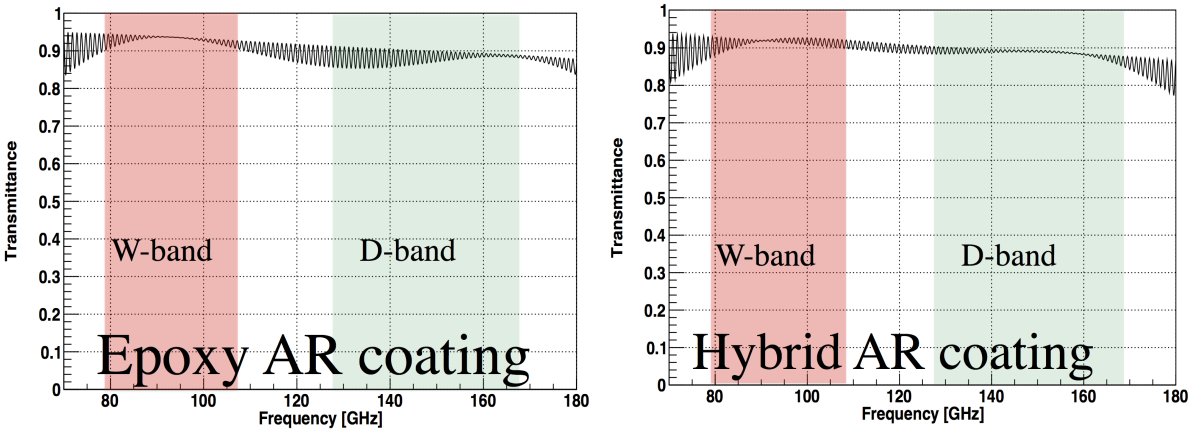

Figure 7.8: Left: Transmittance of alumina lenses with epoxy AR coating. The parameters of the lenses are shown in Table 4.2. The band averages of transmittances are 91.8 % and 87.3 % at 95 and 150 GHz band, respectively. Right: Transmittance of alumina lens with hybrid AR coating. The parameters of the lens are shown in Table 4.2. The band averages of the transmittance are 90.0 % and 88.9 % in 95 and 150 GHz band, respectively.

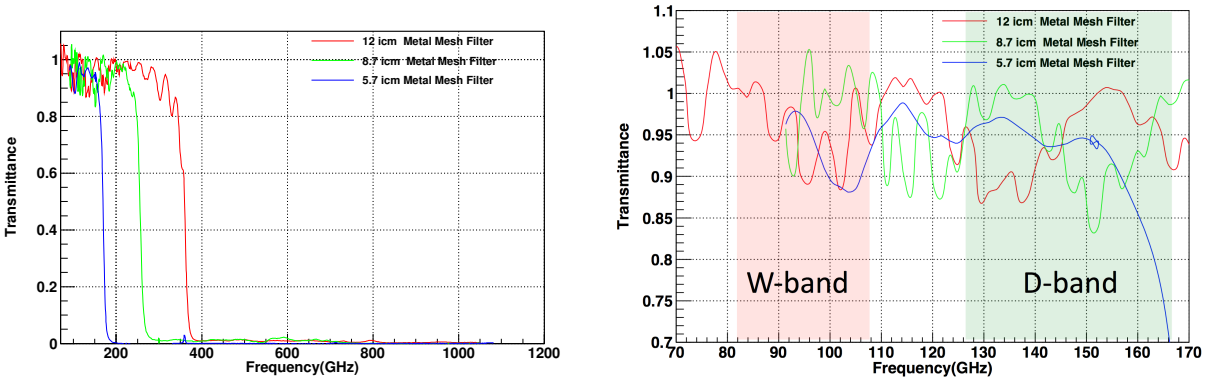

Figure 7.9: Left: Transmittance of metal mesh filters. The spectra are measured by the Cardiff group. Right: Enlarged view of the detection band of left figure.

transmittance of alumina lenses with each AR coating. The average efficiency is calculated as 91.9 % and 87.2 % at 95 and 150 GHz.

7.2.10 Metal mesh filters (MMF)

The measured transmittance of metal mesh filter by Cardiff group is shown in Fig. 7.9. The measured temperature of 5.7 icm MMF is 0.496 K. We calculated the emissivity and efficiency in the detection bands as shown in Tables 7.5-7.6.

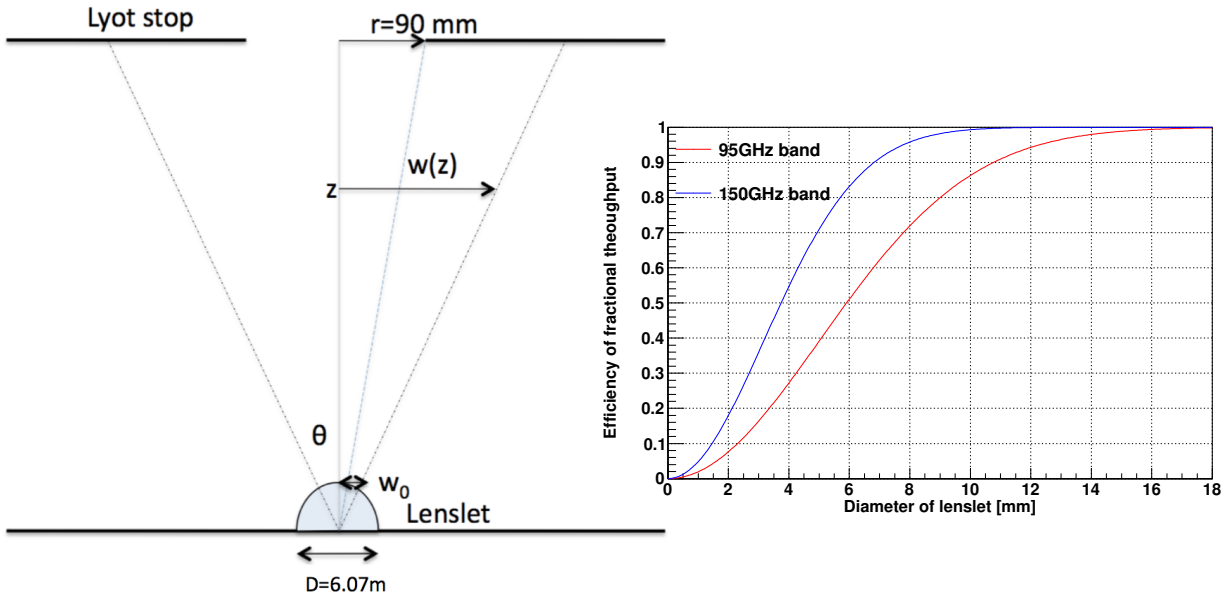

Figure 7.10: Left: Schematic view of lenslet and Lyot stop geometry. Right: Fractional throughput of the Lyot stop. The blue and red curves are throughputs at 150 and 95 GHz. Since the diameter of lenslet is 6.07 mm, the efficiencies are 51.6 % and 83.6 % in 95 and 150 GHz, respectively.

7.2.11 Lyot stop and black body

The Lyot stop defines the beam size for each lenslet. The optimal size of lenslet is chosen from the following calculation as shown in Fig. 7.10. The gaussian beam with waist is produced by ellipse lenslet as

$$w_0 = \frac{D}{2.6}, \tag{7.15}$$

where D is a diameter of lenslet. We assume the diffraction limited optics. Then, the angle of Gaussian beam is given by

$$\theta = \frac{\lambda}{\pi w_0} = \frac{2.6\lambda}{\pi D} \sim \frac{w(z)}{z}, \tag{7.16}$$

where $w(z)$ is the size of beam at height z above lenslet. The bean angle is corresponding to the diameter of the Lyot stop. The power through the aperture is expected as

$$\eta_{\rm Lyot} = \frac{P}{P_0} = \left(1 - exp\left(-\frac{2r^2}{w(z)^2}\right)\right) \tag{7.17}$$

$$= \left(1 - exp\left(-\frac{2\pi^2 D^2 r^2}{2.6^2 \lambda^2 z^2}\right)\right) \tag{7.18}$$

$$= \left(1 - exp\left(-\frac{\pi^2}{13.52}\left(\frac{D}{F\lambda}\right)^2\right)\right), \tag{7.19}$$

where r is the radius of the aperture and F is the ratio of the focal length to the diameter of the entrance pupil. The measured temperature of the black body is less than 5.4 ± 0.5 K. The emissivity is assumed to be1.0. We use these assumptions for the sensitivity analysis.

Table 7.5: Parameter table in W band

Optical elements	Temperature [K]	Emissivity	Efficiency	Total efficiency	Power [pW]	Load [K]	NEP [aW/$\sqrt{\text{Hz}}$]
Load resister	0.25	0.0	1.00	1.0	0.0	0.0	0.0
Microstrip filter	0.25	0.00	0.87	0.87	0.0	0.0	0.0
Antenna mismatch	0.25	1.00	0.988	0.86	2.73×10^{-8}	2.9×10^{-7}	0.0018
Antenna backlobe	0.25	1.00	0.91	0.78	2.70×10^{-8}	2.9×10^{-7}	0.0017
Silicon lenslet	0.25	0.05	0.95	0.74	1.22×10^{-9}	1.3×10^{-8}	0.00037
5.7icm MMF	0.496	0.01	0.94	0.70	9.2×10^{-7}	9.8×10^{-6}	0.010
Collimator lens	5.1	0.068	0.90	0.64	0.035	0.37	2.1
Lyot stop	5.8	1.0	0.54	0.34	0.25	2.7	3.6
8.7icm MMF	5.8	0.01	0.976	0.33	0.0026	0.028	0.57
12icm MMF	5.8	0.01	0.96	0.32	0.0026	0.028	0.57
Aperture lens	4.5	0.068	0.90	0.29	0.013	0.14	1.29
Field lens	5.9	0.064	0.92	0.27	0.018	0.19	1.5
Alumina filter	54.0	0.02	0.96	0.26	0.055	0.60	2.67
RT-MLI	177	0.00060	0.99940	0.26	0.0055	0.058	0.82
Zotefoam window	265	0.02	0.98	0.26	0.27	2.9	6.2
Secondary mirror	273	0.01	0.99	0.25	0.14	1.5	4.3
WHWP	273	0.015	0.989	0.25	0.20	2.2	5.3
Primary mirror	273	0.01	0.99	0.25	0.13	1.4	4.2
Atmosphere	273	0.030	0.97	0.24	0.40	4.3	7.8
CMB	2.73	1.0	1.0	0.24	0.05	0.53	2.5
Total				0.237	1.58	16.8	14.1

7.3 PB-2 sensitivity

We calculated the PB-2 sensitivity with epoxy AR coating as shown in Table. 7.5 and 7.6 . We also calculated the PB-2 sensitivity with the Mullite and Skybond foam AR coating as shown in Table. 7.5 and 7.6 . The list of the optical elements is consistent with Fig. 7.1. Then, we employ the temperatures, emissivities and efficiencies in the tables. We calculated the optical power and load to the detector with Eqs.(7.2) and (7.6). Finally, we estimate the photon NEP using Eq.(7.4). We summarized the results of the sensitivity analysis in Table 7.7. We discuss the sensitive components from these calculations in the next section.

Table 7.6: Parameter table in D band

Optical elements	Temperature [K]	Emissivity	Efficiency	Total efficiency	Power [pW]	Load [K]	NEP [aW/$\sqrt{\text{Hz}}$]
Load resister	0.25	0.00	1.00	1.00	0.0	0.0	0.0
Microstrip filter	0.25	0.00	0.87	0.87	0.0	0.0	0.0
Antenna mismatch	0.25	1.00	0.988	0.86	3.7×10^{-12}	2.3×10^{-11}	2.6×10^{-5}
Antenna backlobe	0.25	1.00	0.91	0.78	3.7×10^{-12}	2.3×10^{-5}	2.6×10^{-5}
Silicon lenslet	0.25	0.05	0.95	0.74	1.7×10^{-13}	1.0×10^{-12}	5.4×10^{-6}
5.7icm MMF	0.496	0.01	0.92	0.68	1.3×10^{-8}	8.0×10^{-8}	0.002
Collimator lens	5.1	0.104	0.89	0.060	0.043	0.27	2.9
Lyot stop	5.8	1.0	0.85	0.51	0.081	0.51	2.2
8.7icm MMF	5.8	0.01	0.94	0.48	0.0040	0.025	0.88
12icm MMF	5.8	0.01	0.94	0.46	0.0037	0.023	0.85
Aperture lens	4.5	0.1046	0.89	0.404	0.022	0.14	2.1
Field lens	5.9	0.098	0.87	0.358	0.036	0.22	2.7
Alumina filter	54.0	0.031	0.958	0.34	0.14	0.90	5.4
RT-MLI	177	0.0012	0.9988	0.34	0.019	0.12	1.9
Zotefoam window	265	0.02	0.98	0.34	0.46	2.9	10.1
Secondary mirror	273	0.01	0.99	0.33	0.23	1.4	6.9
WHWP	273	0.0199	0.983	0.33	0.46	2.8	10.0
Primary mirror	273	0.01	0.99	0.32	0.23	1.4	6.8
Atmosphere	273	0.031	0.97	0.31	0.7	4.5	12.9
CMB	2.73	1.0	1.0	0.31	0.046	0.29	3.0
Total				0.304	2.49	15.6	22.8

Table 7.7: Summary of POLARBEAR-2 sensitivity

	W-band	D-band
Science requirement of NET [μK$\sqrt{\text{sec}}$]	360	360
Science requirement of $\text{NET}_{\text{array}}$ [μK$\sqrt{\text{sec}}$]	5.6	5.6
Band width [%]	30.6	26.0
Number of bolometer	3794	3794
Total efficiency[%]	23.7	30.4
Total power [pW]	1.58	2.49
Total load [K]	16.8	15.6
$\text{NEP}_{\text{photon}}$ [aW/$\sqrt{\text{Hz}}$]	14.9	23.0
$\text{NEP}_{\text{thermal}}$ [aW/$\sqrt{\text{Hz}}$]	8.7	11.1
$\text{NEP}_{\text{readout}}$ [aW/$\sqrt{\text{Hz}}$]	12.0	15.0
NEP[aW/$\sqrt{\text{Hz}}$]	21.1	29.7
NET[μK$\sqrt{\text{sec}}$]	280	313
$\text{NET}_{\text{array}}$[$\mu$K$\sqrt{\text{sec}}$]	4.54	5.08
combined $\text{NET}_{\text{array}}$	3.39	

7.4 Discussion

We estimate the NET array sensitivity and the optical efficiency based on the measurements. The requirement of the NET array is 4.3 μK$\sqrt{\text{sec}}$ as discussed in Sec. 2.10. The estimated NET array of 3.39 μK$\sqrt{\text{sec}}$ is much better than that of the requirement. We try to calculate the dependence of the Lyot stop and the alumina filter temperatures. Figure 7.11 and 7.12 are the power and the NET array from the filter. The power increases from 45 K and 80 K. As the measured temperature of the alumina filter is 54 K, the estimated power at 95 and 150 GHz are 0.058 pW and 0.14 pW, respectively. If we calculate the alumina filter power equivalent to the estimated power at 95 and 150 GHz, we obtain 3.7 % and 5.6 % with respect to the total power, respectively. The array NET between 45 K and 80 K meets our requirement of 4.3 μK$\sqrt{\text{sec}}$ and goal of 4.0 μK$\sqrt{\text{sec}}$.

We also calculated the power and the array NET as a function of Lyot stop temperature as shown in Fig. 7.13 and 7.14. The temperature of the Lyot stop depends on the power and array NET sensitivity strongly because the solid angle of the detector sees the Lyot stop directly. The emissivity of the Lyot stop is approximately 1 in millimeter wavelength. Therefore, the temperature dependence of the Lyot stop is larger than that of the alumina filter.

The slope of 95 GHz is larger than that of 150 GHz. This is because the solid angle of 95 GHz band is larger than that of 150 GHz due to the diffraction angle of the lenslet-coupled detectors. The power of the atmosphere at 95 and 150 GHz is 0.4 and 0.7 pW. If the temperature of the Lyot stop becomes

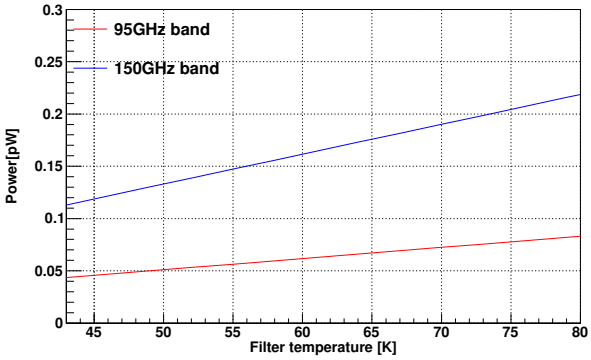

Figure 7.11: Loading power from the alumina filter as a function of filter temperature.

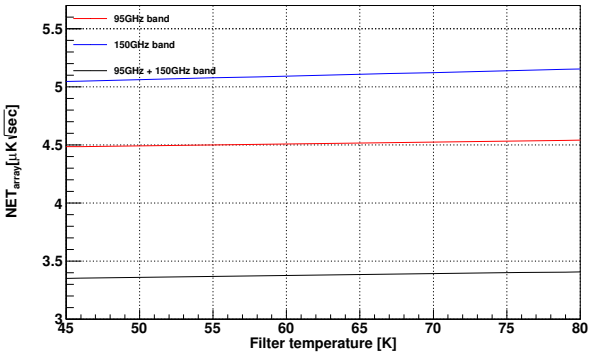

Figure 7.12: Array NET from the alumina filter as a function of filter temperature.

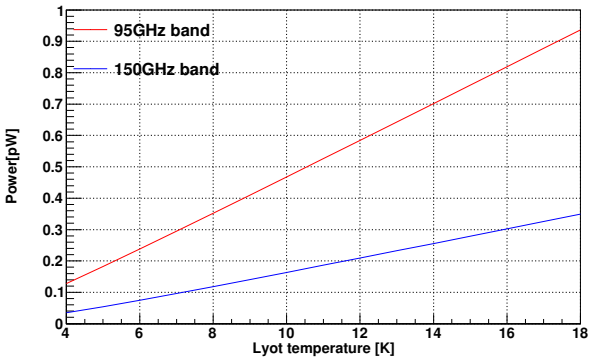

Figure 7.13: Loading power from the Lyot stop as a function of Lyot stop temperature.

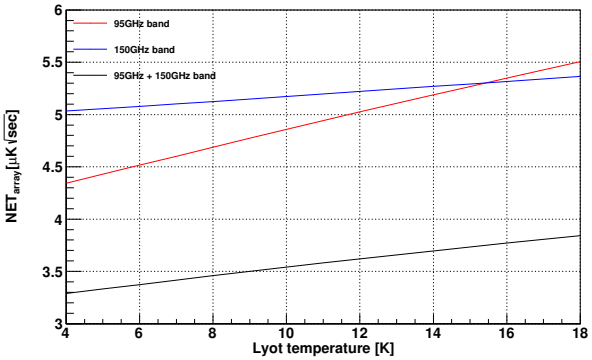

Figure 7.14: Array NET from the alumina filter as a function of filter temperature.

larger than 9 K, the Lyot stop emits the largest power among the components as listed in Table 7.5 and 7.6. Therefore, we should keep the temperature of the Lyot stop below 9K. The measured temperature of the Lyot stop is 5.8 K, which meets our requirement sufficiently. The estimated power at 95 and 150 GHz are 0.25 pW and 0.081 pW, respectively. The powers correspond to alumina filter power to total power ratio of 15.8 % and 3.3 %. The NET arrays between 45 K and 80 K meet our requirement of 4.3 μK$\sqrt{\text{sec}}$ and goal of 4.0 μK$\sqrt{\text{sec}}$.

7.5 Conclusion

We have calculated the sensitivity based on the measurement. The estimated optical efficiencies are 0.237 and 0.304, respectively. We have also calculated the array NET and obtained 4.54 μK$\sqrt{\text{sec}}$ for 95 GHz and 4.54 μK$\sqrt{\text{sec}}$ for 150 GHz. The combined array NET is 3.39 μK$\sqrt{\text{sec}}$.These results meet our requirements from Sec. 2.10.

Chapter 8

Basic optical characterization of the POLARBEAR-2 receiver system

8.1 Introduction

In this chapter, we characterize the optical performance of the POLARBEAR-2 receiver system, using prototype bolometers with saturation power higher than the observation-quality bolometers, which are useful for laboratory testing. Since the final (observation-quality) characterization on beams and polarization properties will be done with HTT at the site, we focus on the evaluation of optical efficiency, the polarization responsivity, and briefly describe results of the beam measurements.

8.2 Setup

We place the optical components into the POLARBEAR-2 receiver system as shown in Fig. 8.1. These optical components are explained in Chap. 3. In particular, the fabrications of alumina lenses, alumina filter and KEK Black are described in Chap. 4. In this system, we laminated the Skybond and mullite AR coating on flat surfaces. The epoxy AR layer, which is to be used for curved surfaces, is not coated. The detector modules are placed on the focal plane as shown in Fig. 8.2.

8.2.1 Test wafer (ver.4 wafer)

We place a test wafer (called the ver.4 wafer) at 250 mK stage which is the prototype detector wafer for the optical characterization. The lenslets mount on the ver.4 wafer with two-layer Epoxy AR coating. The design of the ver.4 wafer is basically the same as the observation-grade wafers that are in preparation. There are four TES bolometers connected to a sinuous antenna through microstrip lines for dual-band polarization measurements. Each TES is biased at the middle point between the superconducting and normal conducting. If we observe temperature change, the resistance of the TES increases. Therefore,

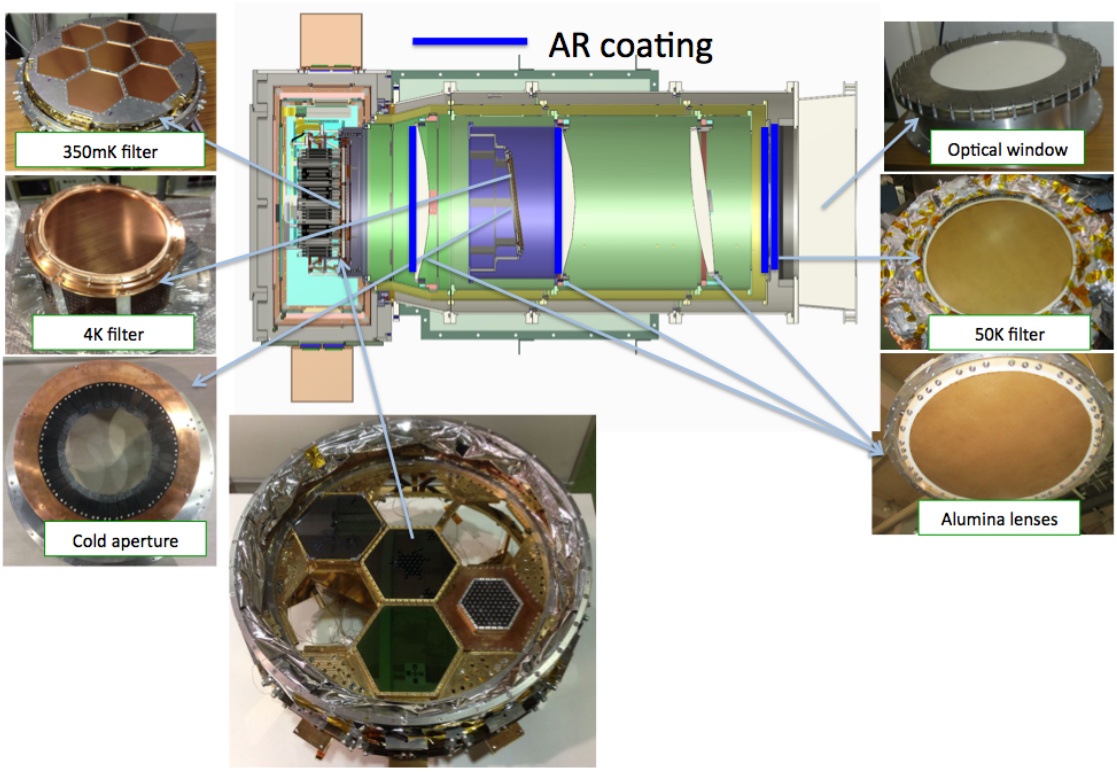

Figure 8.1: Configuration of the optics system for the characterization. In this test, AR coating is partially (2 out of 6 surfaces) applied.

it operates as a thermometer of high sensitivity. We should keep the temperature stability sufficiently. Each TES is placed away from the thermal bath for this purpose. In other words, each TES and thermal bath is weakly linked. The temperature of the thermal bath should be kept at much lower temperature than that of the TES. The TES operation point is controlled with biasing and generating the power of the Joule heat. We keep a constant voltage to the TES. The advantage of the constant voltage bias is the stable operation of temperature. If the temperature of the TES rises, the resistance is increased and the current is reduced. Therefore, the power of Joule heat is decreased and a negative feedback is applied to the TES operation.

The power from the antenna is detected by the TES. When the TES is in a stable operation, the sum of the detected power, P_{opt}, and power of the Joule heat, P_{bias}, from the antenna is equal to the thermal bath, P_{sat}. If the heat bath is constant, we are able to estimate the P_{opt} from the bias power.

The saturation power of the ver.4 wafer is designed to be 50-100 pW. This power is much larger than the expected loading at the observation site. When we perform the optical test in the laboratory, we usually use the thermal source whose power is higher than the expected loading at the site. Therefore, the detector with higher saturation power is convenient for the optical measurement.

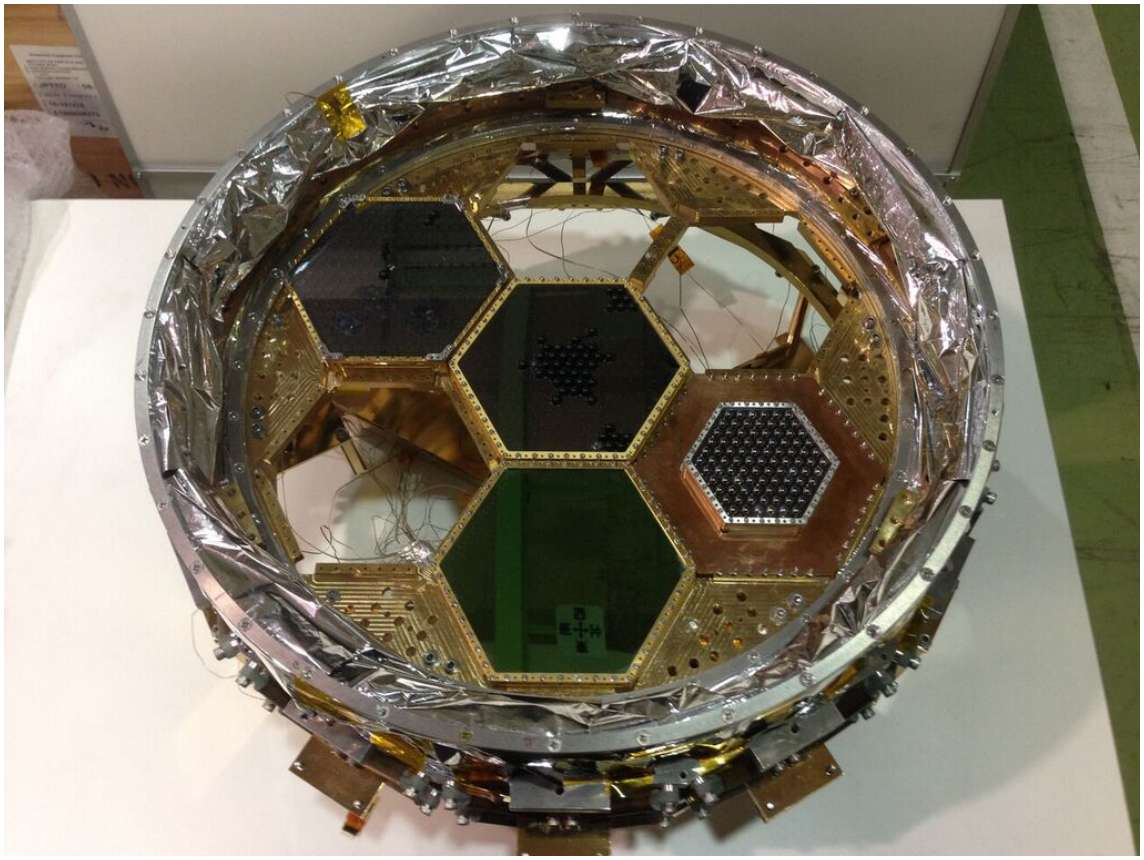

Figure 8.2: The focal plane and detector modules. The test wafer (called the ver.4 wafer) is installed at the center. Other two larger wafers are dummy wafers for cooling tests, and smaller one is the same type of wafer used in POLARBEAR-1.

Table 8.1: Parameters of the LC board.

Channel	Capacitance[μF]	Inductance [μH]	Frequency [kHz]
Ch 1	6.94	16	430
Ch 2	1.22	16	1039
Ch 3	3.24	16	633
Ch 4	1.89	16	836
Ch 5	11.73	16	330
Ch 6	1.50	16	942
Ch 7	4.74	16	526
Ch 8	2.66	16	701

8.2.2 LC resonance filter

We mount the inductor and capacitor chips on the readout board as shown in Fig. 8.3. All the inductances of the inductor chips are 16 μH. The capacitances of condensers are listed in Table 8.1. We employ a readout system with a multiplexing factor of 8 in the frequency domain in the test cryostat. The operation of 8 multiplexing factor board is sufficiently stable because it is already used in the POLARBEAR-1 experiment. The resonant frequencies are between 200 kHz and 1200 kHz, which are also the same as those used at POLARBEAR-1.

8.2.3 SQUID board

The signal of voltage-biased TES detectors are read with a superconducting quantum interference device (SQUID). We mount the SQUID board on the 4 K stage. The SQUID converts the magnetic flux in the coil produced at the input coil to a voltage across its junctions. The SQUID voltage is read out at room temperature. The linearity of the SQUID response is accomplished over a large bandwidth by the digital active nulling (DAN). [64]

8.2.4 RF box and SQUID controller

To control the SQUID board, we mount the SQUID controller board as shown in Fig. 8.5. This board is sensitive to RF noise and extra magnetic field. We place the SQUID controller board into the RF box. The conductive tape is sandwiched with the connection of the RF box to shield the RF noise.

8.2.5 DfMUX

The DfMUX is the readout board at room temperature, which is used in PB-1 system. Figure 8.6 shows the mounted DfMUX board. The DfMUX provides access to time streams of the detector. The motherboard reads all the channels to a port on the network multicast. The DFMUX can obtain the

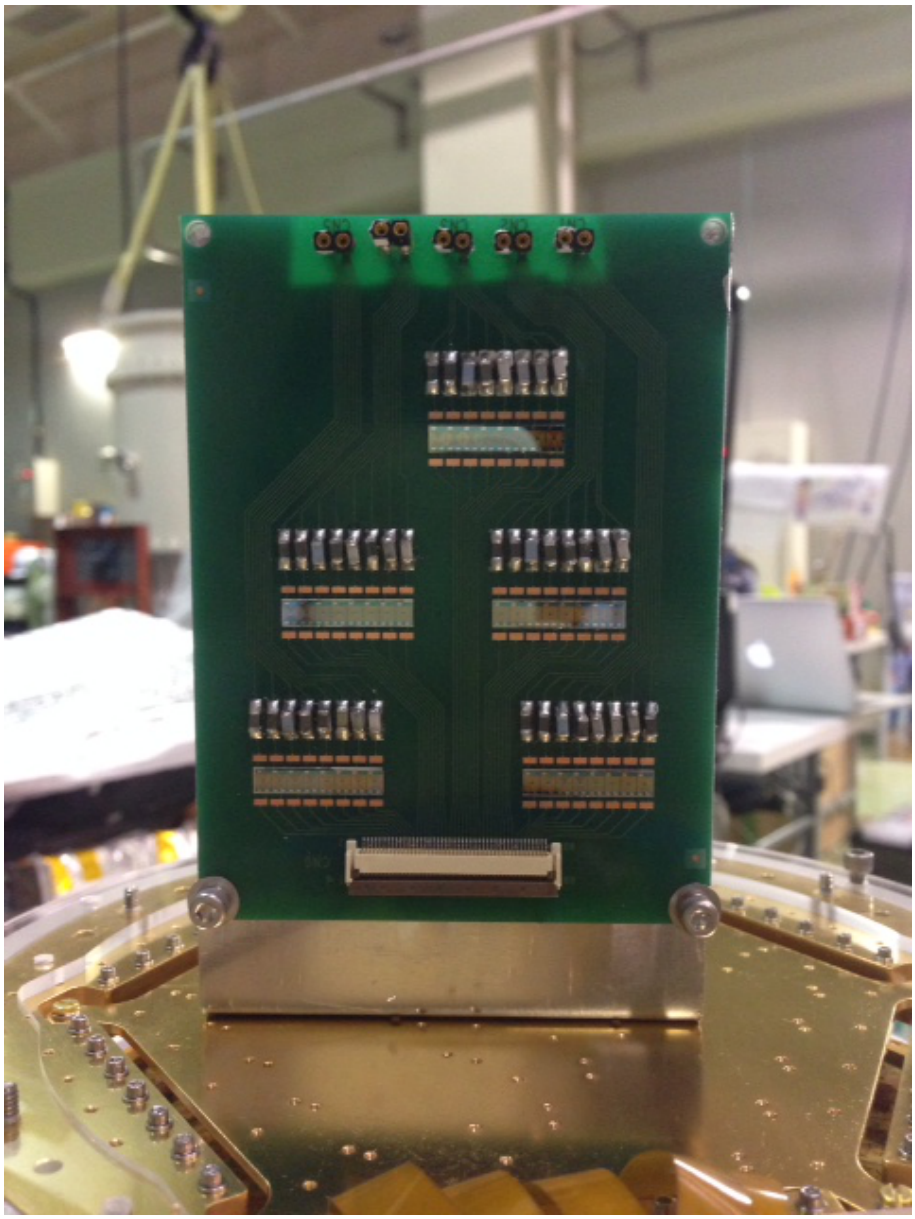

Figure 8.3: The LC resonance board. The capacitors and inductors, forming the resonance circuits with the TES bolometer, are placed on the board. Five resonance circuits are put on the board, and 40 bolometers are read out with 8-MUX readout system.

Figure 8.4: SQUID mounting board. We place eight SQUID chips on the board.

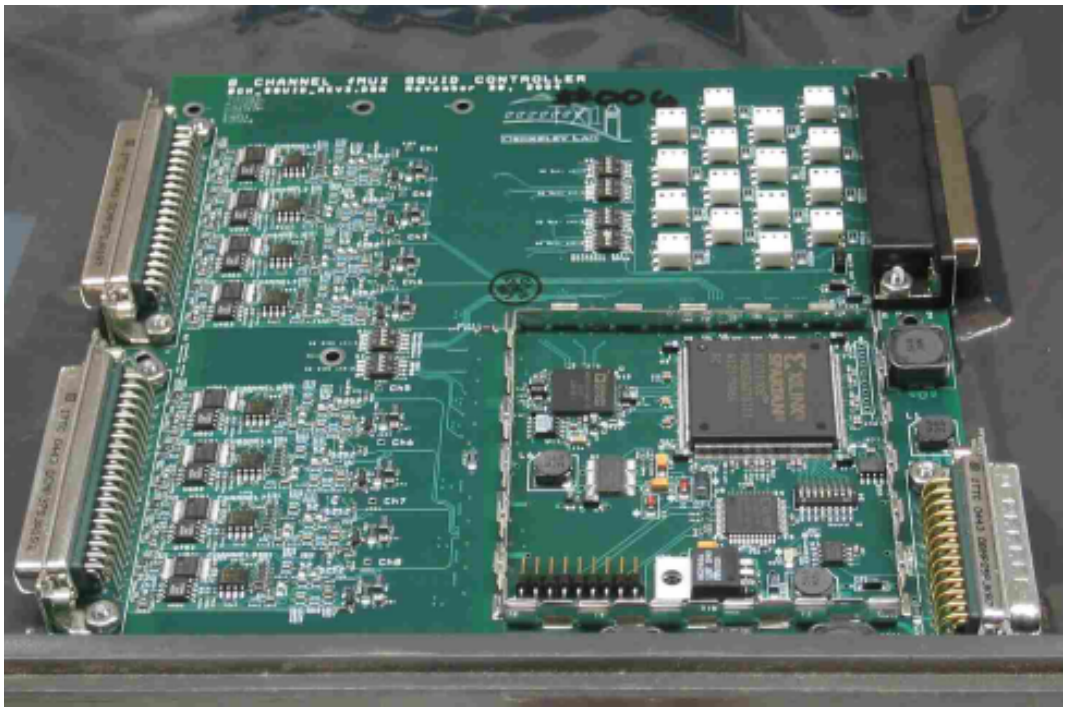

Figure 8.5: Picture of SQUID controller board. Private communication with Y. Akiba.

housekeeping information. This operation can be done through the CGI call to a Web server running on the motherboard.

8.3 Readout characterization

8.3.1 System overview

We place the test wafer on the 250 mK stage, which is connected to the LC board. Flex cables are used for the connector between the wafer and the LC board. One LC board can read 40 bolometers. The LC board is mounted at the back side of the wafer plate. We use 2 SQUID cards for each resonance filter on LC boards. SQUID boards and LC boards are connected with NbTi microstrip cables. The system configuration is shown in Fig. 8.7.

8.3.2 Characterization of SQUID board

When we use the SQUID as a magnetic flux sensor, we usually measure the V-Φ curve. The response of SQUID is obtained by

$$V(\Phi) = RI\sqrt{1 - \left(\frac{2I_c}{I}\right)^2 \cos^2\left(\frac{\pi\Phi}{\Phi_0}\right)}, \tag{8.1}$$

where $\Phi_0 = h/2e$ is the magnetic flux quanta, I is bias current of the SQUID. I determines the amplitude of voltage, while Φ is driven by the feedback current. The operation point of V-Φ curve is defined as $1/2(V_{\max} - V_{\min})$. According to this equation, when $I/I_c = 1$, response of SQUID will be the most sensitive to magnetic flux. Thus, we need to tune the current to be $I/I_c = 1$. However, SQUID response is non-linear with the magnetic flux. Thus, it is necessary to linearize the SQUID signal with feedback mechanism. We call the case with this feedback (without the feedback) a close (open) loop configuration. The measured V-Φ curve is shown in Fig. 8.8.

8.3.3 Network analysis

The signals of the TES bolometers are multiplexed by using the LCR resonance filter with AC bias, so that we should measure the points of the LCR resonance frequency. The resonance points of the LCR resonance frequencies are shown in Table. 8.1. The LCR peaks are corresponding to

$$T(\omega) = \Sigma_{i=1}^{8} \frac{A}{0.03 + R_{\rm TES} + i\omega L_i + \frac{1}{i\omega C_i}}, \tag{8.2}$$

where T is the spectrum of network analysis, A is the amplitude, $R_{\rm TES}$ is the bolometer resistance. In the simple system, each peak is described as

$$\omega_i = \frac{1}{\sqrt{L_i C_i}}. \tag{8.3}$$

Figure 8.9 shows the measured spectrum. Each amplitude of the peak corresponds to the LCR resonance peak. We fit the peaks and estimate the center frequency and amplitude. The fitted peaks are shown in Table. 8.2.

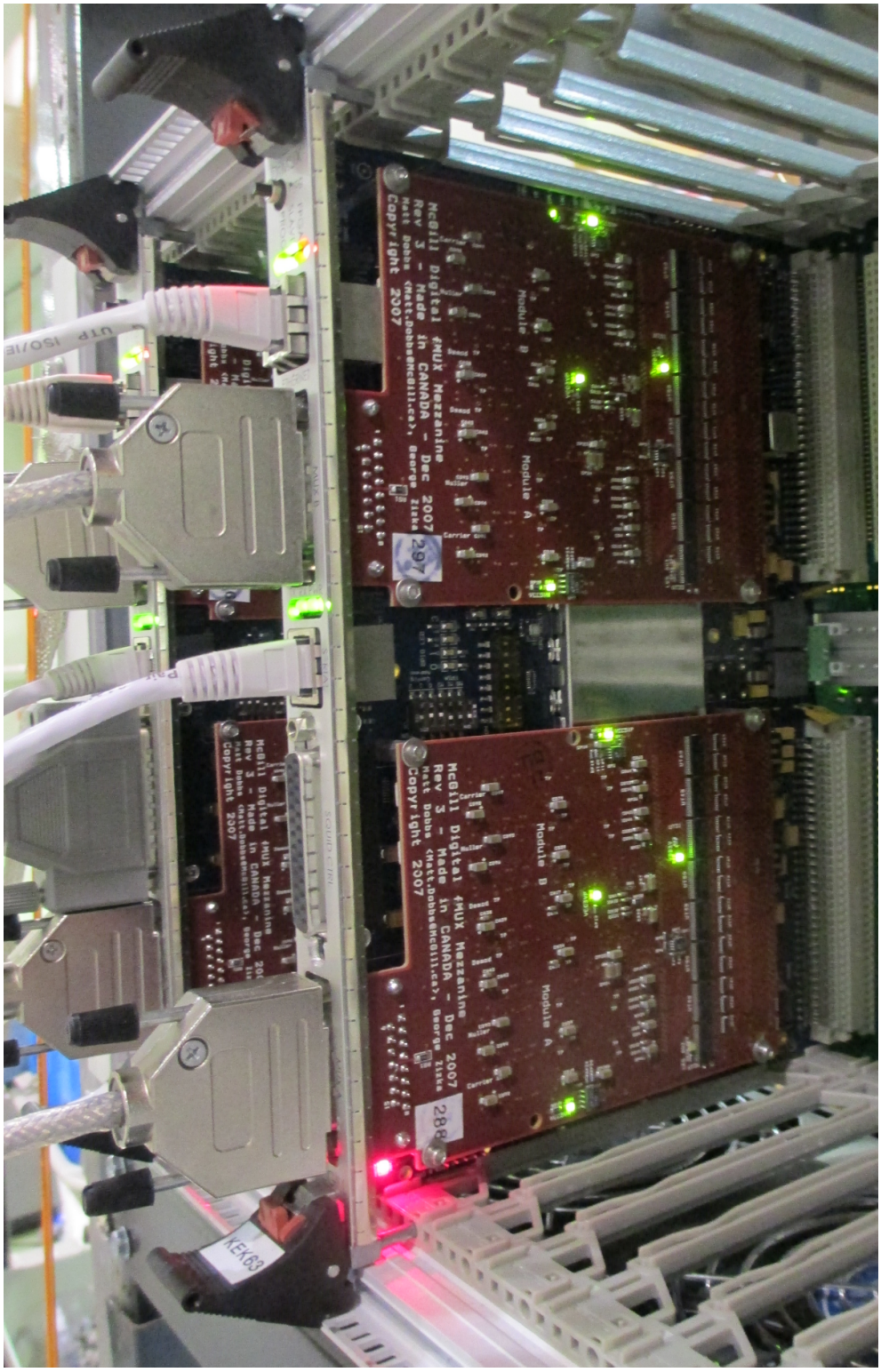

Figure 8.6: Picture of DfMUX board. Private communication with Y. Akiba.

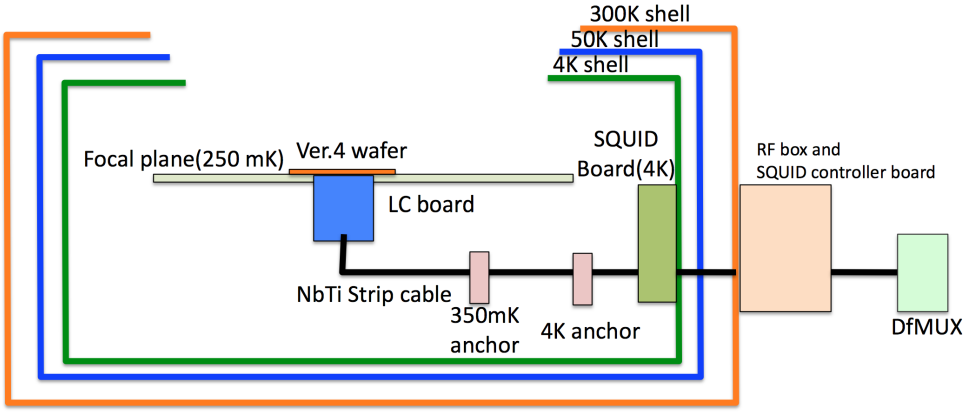

Figure 8.7: Schematic view of readout system.

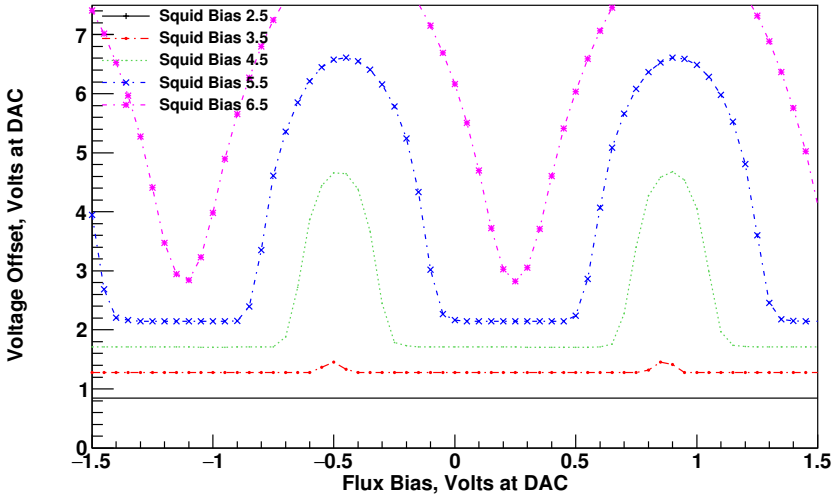

Figure 8.8: The measured V-ϕ curves under the different biasing conditions.

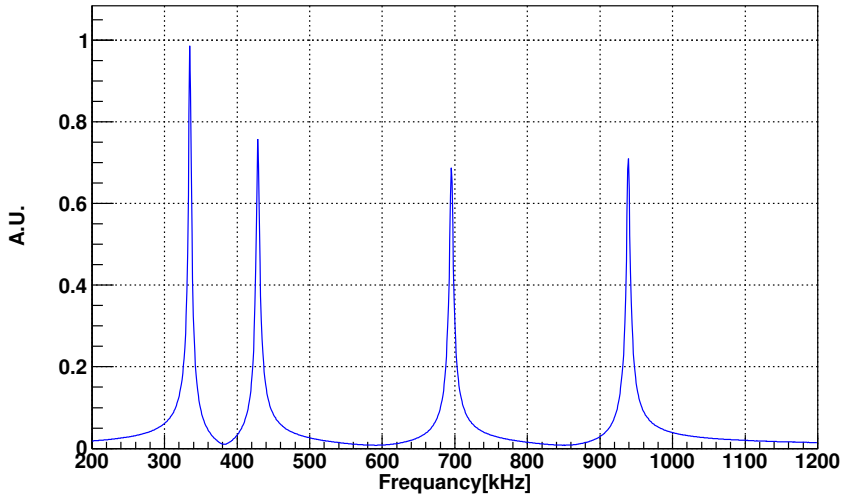

Figure 8.9: The measured resonant peaks from the network analyses. The hight and position of each peak correspond to the $R_{\rm TES}$ and LCR resonance point.

Table 8.2: List of usable bolometers for the measurement.

Channel	LCR peak[kHz]	NEP [aW/$\sqrt{\rm Hz}$]	Optical/dark
1	334.765	-	no lenslet
2	428.571	342	no lenslet
3	695.331	204	Optical(95 GHz)
4	939.042	141	Optical(150 GHz)

8.3.4 Noise level

We take the time-ordered data (TOD), $x_i(t)$. The noise of the measurement is calculated with Fourier transformation of the TOD. The Fourier-transformed TOD is

$$F(f) = \Sigma_{n=0}^{N-1} x(t) e^{\left(-i\frac{f}{f_{\rm DAQ}}n\right)}, \tag{8.4}$$

where N is the number of sampled data, $f_{\rm DAQ}$ is a sampling frequency. The noise equivalent power is defined as

$$NEP = \sqrt{\frac{F(f)F^*(f)}{N f_{\rm DAQ}}}. \tag{8.5}$$

We measure the TOD and NEP as shown in Fig 8.10. The integration time of measurement is 3666 sec. The estimated NEPs of 95 and 150 GHz detectors are 204 and 141 aW/$\sqrt{\rm Hz}$, where we averaged the FFT spectrum between 1 and 50 Hz.

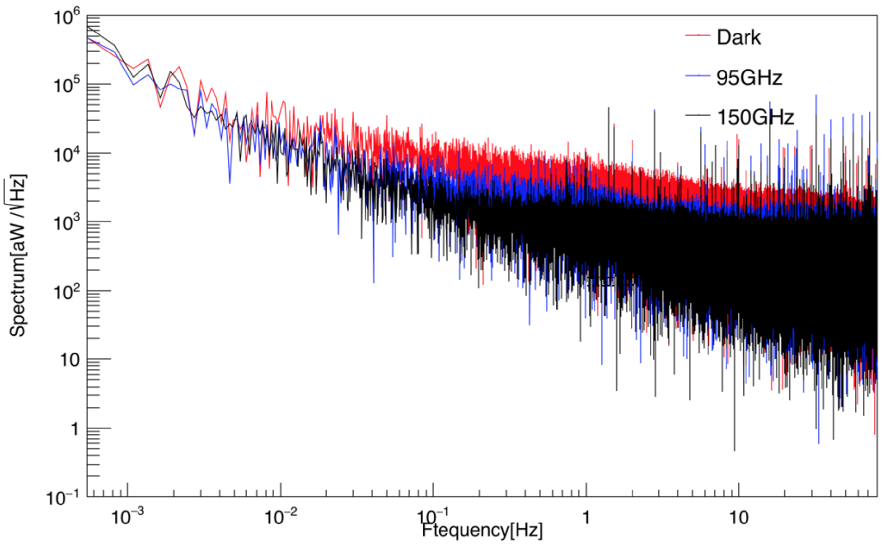

Figure 8.10: The measured noise equivalent power and noise power spectra. The fit parameters of NEP are summarized in Table. 8.2

8.4 Knife edge method

The beam shape is characterized as

$$I(x,y) = \exp\left(-\frac{2(x-\mu_x)^2}{w_x^2} - \frac{2(y-\mu_y)^2}{w_y^2}\right) \propto I_x(x)I_y(y), \tag{8.6}$$

where the beam is described with only four parameters, μ_x, μ_y, w_x, and w_y. Here, we use the rotation matrix,

$$R: \begin{bmatrix} x-\mu_x \\ y-\mu_y \end{bmatrix} \rightarrow \begin{bmatrix} \cos\theta & -\sin\theta \\ \sin\theta & \cos\theta \end{bmatrix} \begin{bmatrix} x-\mu_x \\ y-\mu_y \end{bmatrix}, \tag{8.7}$$

where θ is a rotation angle of the beam axis. Thus, the beam shape can be written by

$$I(x,y;\theta) = \exp\left(-\frac{2((x-\mu_x)\cos\theta - (y-\mu_y)\sin\theta)^2}{w_x^2} - \frac{2((x-\mu_x)\sin\theta + (y-\mu_y)\cos\theta)^2}{w_y^2}\right) \tag{8.8}$$

We use the knife-edge method to obtain these parameters. The method is commonly used in visible laser optics [93]. The beam is covered by a knife edge and the transmitted power is measured.

First, we consider the x-axis. When we intercept the beams with black body absorbers in the $x < x_{bb}$ region, the transmitted beam amplitude is written by

$$P(x_{bb}) = \int_{x_{bb}}^{\infty}\int_{-\infty}^{\infty} I(x,y;\theta)dxdy \tag{8.9}$$

$$\propto \int_{x_{bb}}^{\infty}\left(-\frac{2(x-\mu_x)^2}{\frac{w_x^2w_y^2(w_x^2\sin^2\theta+x_y^2\cos^2\theta)}{w_x^2w_y^2+(5w_x^4-2w_x^2w_y^2+5w_y^2)\sin^4 2\theta/16}}\right)dx \tag{8.10}$$

$$= \mathrm{erf}(\infty) - \mathrm{erf}\left(\frac{\sqrt{2}(x_{bb}-\mu_x)}{\sqrt{\frac{w_x^2w_y^2(w_x^2\sin^2\theta+x_y^2\cos^2\theta)}{w_x^2w_y^2+(5w_x^4-2w_x^2w_y^2+5w_y^2)\sin^4 2\theta/16}}}\right) \tag{8.11}$$

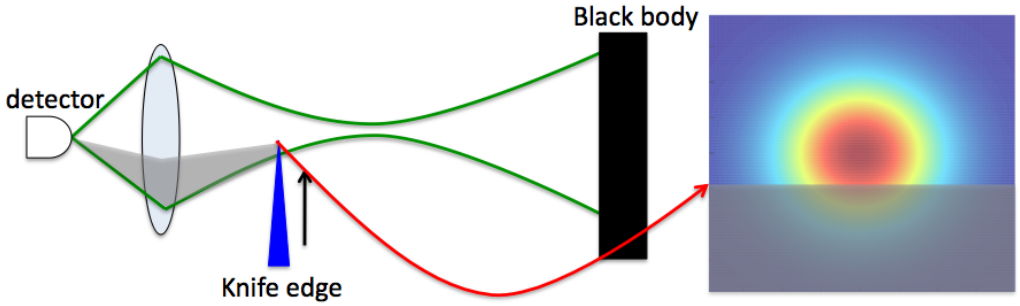

Figure 8.11: Schematic view of the knife-edge measurement. The black body source covers the entire beam. The knife edge makes a shadow. We measure the integrated power at each knife edge position.

where erf(ξ) is a Gaussian error function. The Gaussian error function is defined as

$$\mathrm{erf}(\xi) = \int_0^{\xi} \exp\left(-\xi^2\right) d\xi. \tag{8.12}$$

When we generalize the model to any axis, we can use

$$P(R) = \mathrm{erf}(\infty) - \mathrm{erf}\left(\frac{\sqrt{2}(R - (\mu_x \cos\phi + \mu_y \sin\phi))}{\sqrt{\frac{w_x^2 w_y^2 (w_x^2 \sin^2(\theta+\phi) + x_y^2 \cos^2(\theta+\phi))}{w_x^2 w_y^2 + (5w_x^4 - 2w_x^2 w_y^2 + 5w_y^2)\sin^4 2(\theta+\phi)/16}}} \right), \tag{8.13}$$

where R is an integral axis and ϕ is the integral direction.

8.4.1 Experimental setup

We place a mirror and a chopped cold load (i.e. a 77 K black body). The chopper frequency is 10 Hz. We place the black body strip, one by one, at the front of the window as shown in Fig. 8.12 and 8.13. The width of the black body strip is 23 ± 2 mm. We measure the difference between 77 K and 300 K signals with taking 10 second data for each strip. We estimate the power with Eq. (8.16).

8.4.2 Results

The measured error function curves for each detector at each axis are shown in Fig. 8.14. The error bars correspond to statistical uncertainties.

We estimate the μ_x, μ_y, w_x, w_y, and θ using the simultaneous fitting with $\phi = \{0, \pi/4, \pi/2, 3\pi/4\}$ with the following equation:

$$P(R) = A - B \times \mathrm{erf}\left(\frac{\sqrt{2}(R - (\mu_x \cos\phi + \mu_y \sin\phi))}{\sqrt{\frac{w_x^2 w_y^2 (w_x^2 \sin^2(\theta+\phi) + x_y^2 \cos^2(\theta+\phi))}{w_x^2 w_y^2 + (5w_x^4 - 2w_x^2 w_y^2 + 5w_y^2)\sin^4 2(\theta+\phi)/16}}} \right) \tag{8.14}$$

The results of the fit are summarized in Table 8.3. The calculated χ^2/N is 103/73, where we assume that the uncertainty of the angle and the strip width are 5 degrees and 2 mm, respectively. We compare

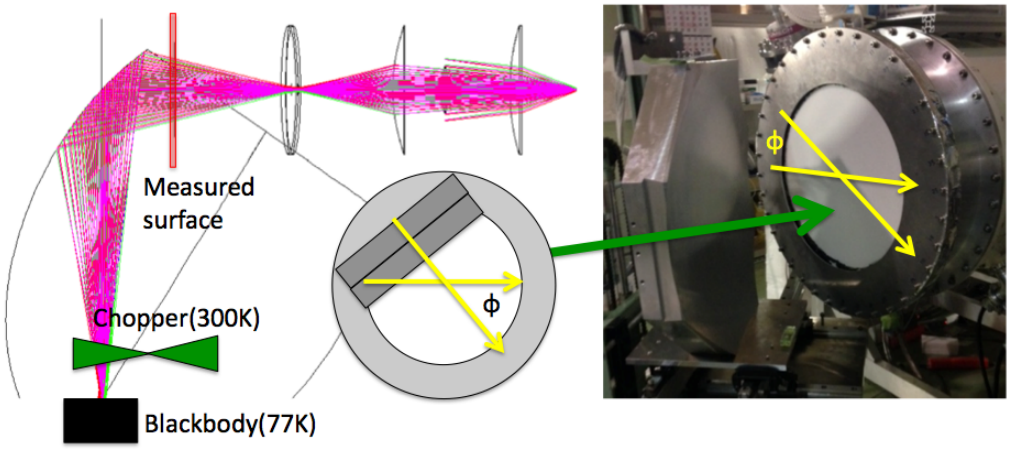

Figure 8.12: The experimental setup of the knife edge method. We place the strip of black body at the window in the ϕ direction. We place the chopped cold load. The measured powers correspond to the erf function.

Table 8.3: Results of the beam map measurement with the knife edge method, and comparison with the simulation. The simulation errors correspond to the uncertainties of black body strip positions.

	Detector	X center[mm]	Y center[mm]	X beam width[mm]	Y beam width[mm]	angle[deg]
Measured	95 GHz	5.7 ± 0.9	8.2 ± 1.0	125.3 ± 3.2	123 ± 2.5	17.8 ± 1.7
Simulation	95 GHz	6.40 ± 0.01	8.1 ± 0.4	128 ± 3	120 ± 2	0

the results with simulation. We simulate the footprint diagram at the window surface using ZEMAX as shown in Fig. 8.15. The simulated center points and beam widths are summarized in Table. 8.3. The reconstructed beam is shown in Fig. 8.16 (left). All the measured center points agree within one sigma errors. The beam widths in x and y axes in both detectors are also consistent within one sigma errors. We also convert the x axis from the position to the angle. Here, we assume that the beams are emitted from the Gregorian focus. The calculated plots are shown in Fig. 8.17. The reconstructed beam is also shown in Fig. 8.16 (right). The beam parameters are summarized in Table 8.4.

Since all the results satisfy our requirements without angle. The angle of elliptical beams may make a beam systematic if the origin of angle is from the optical system. However, the angle of 17.8 degrees are acceptable because the angle uncertainty of detector are also same order. So, we can explain detector uncertainty. When we regard 17.8 degrees degrees as detector uncertainty, the systematic error is mitigated by $1/\sqrt{3794}$. We conclude that the basic beam characterization is finished and the alumina optical system is validated.

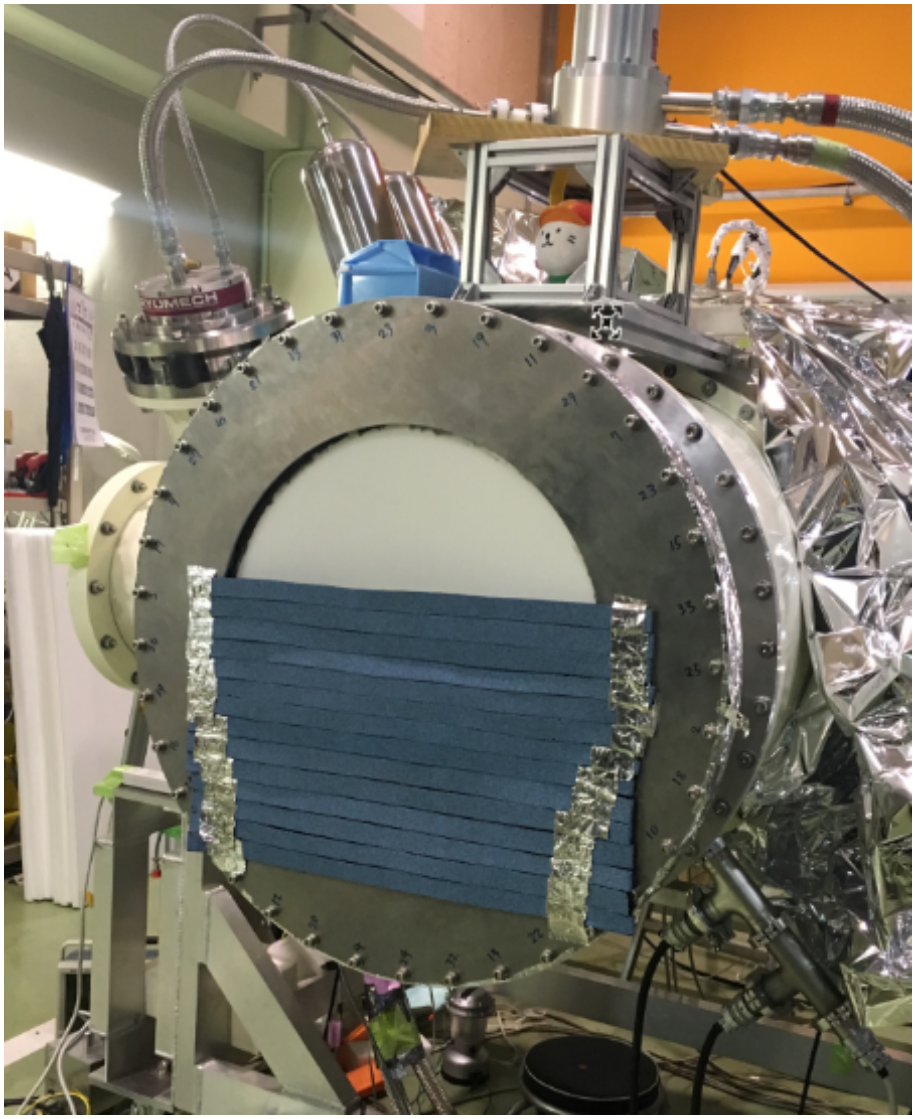

Figure 8.13: The picture of the black body strips at the window. The strips are added one by one. The width of the black body strips is 23 ± 2 mm.

Table 8.4: Same as Table 8.3 but the x axis is converted to the angle assuming that the beams are emitted from the Gregorian focus.

	Detector	X center[deg]	Y center[deg]	X beam width[deg]	Y beam width[deg]	angle[deg]
Measured	95 GHz	0.65 ± 0.11	0.95 ± 0.12	14.5 ± 0.4	14.2 ± 0.3	18.3 ± 1.7

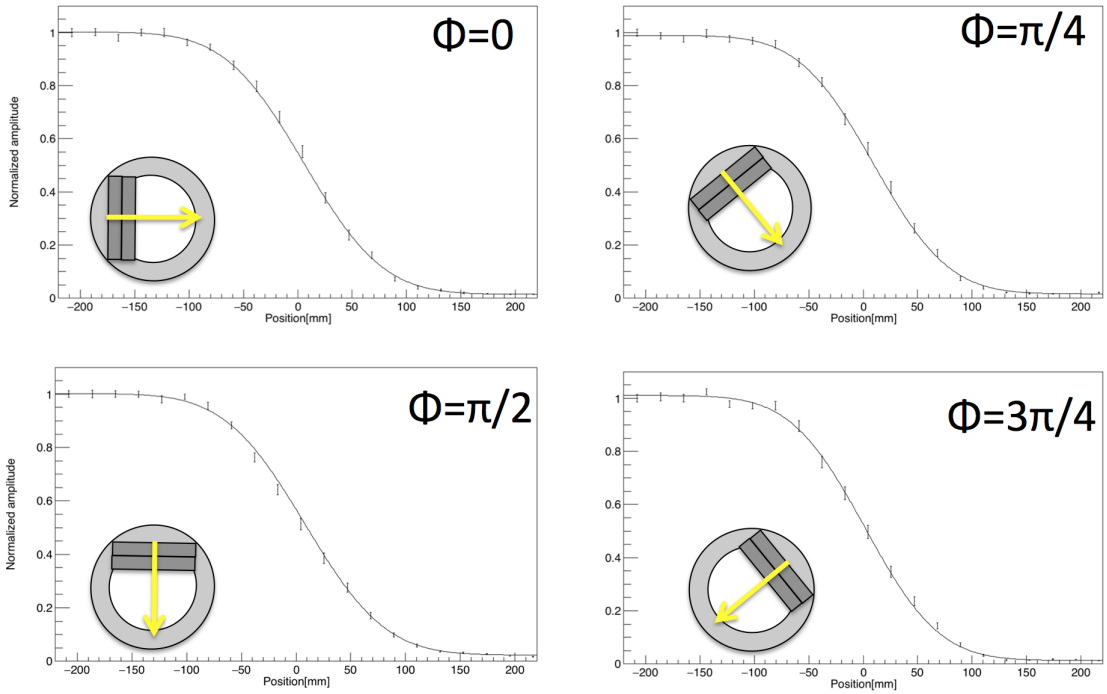

Figure 8.14: The measured intensities with fits to the Gaussian error function for different integration angles of $\{0, \pi/4, \pi/2, 3\pi/4\}$ with the knife edge method. The horizontal axis of each figure is the edge position. The black curves are the best fits. The estimated fitting parameters are listed in Table. 8.3

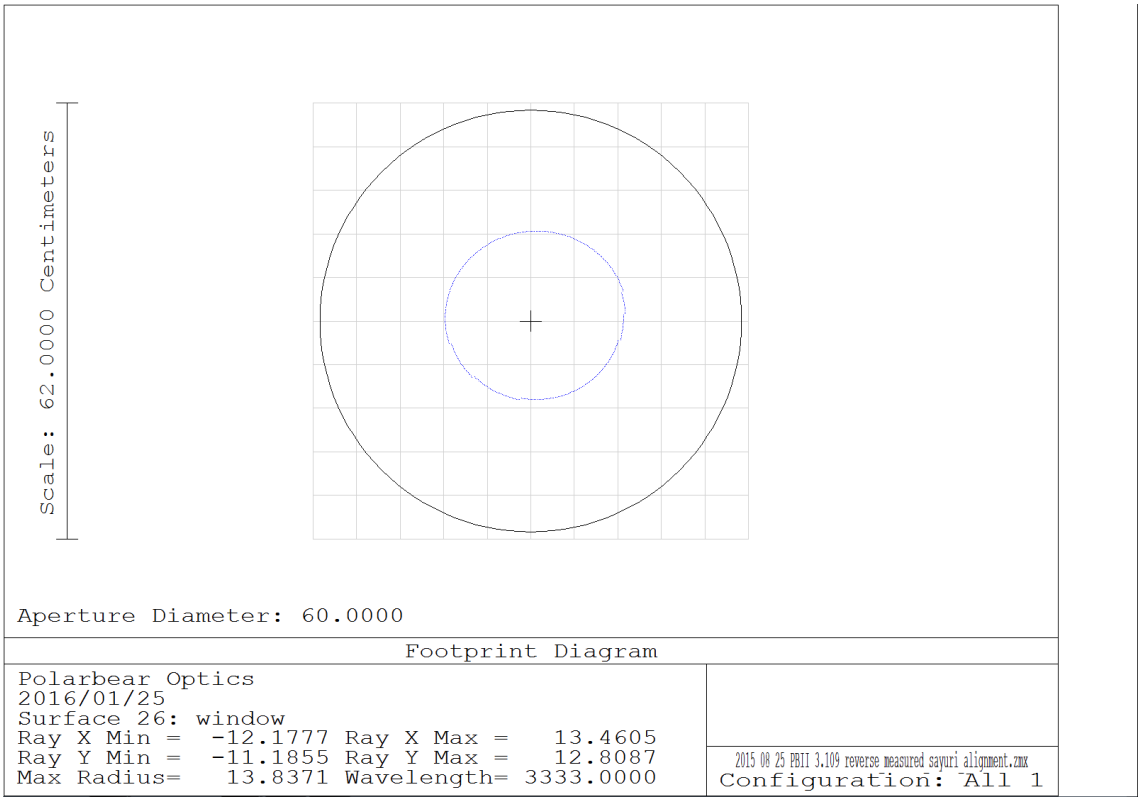

Figure 8.15: The simulated footprint diagram at the receiver window. In the plot, the circle corresponds to the 1/e point.

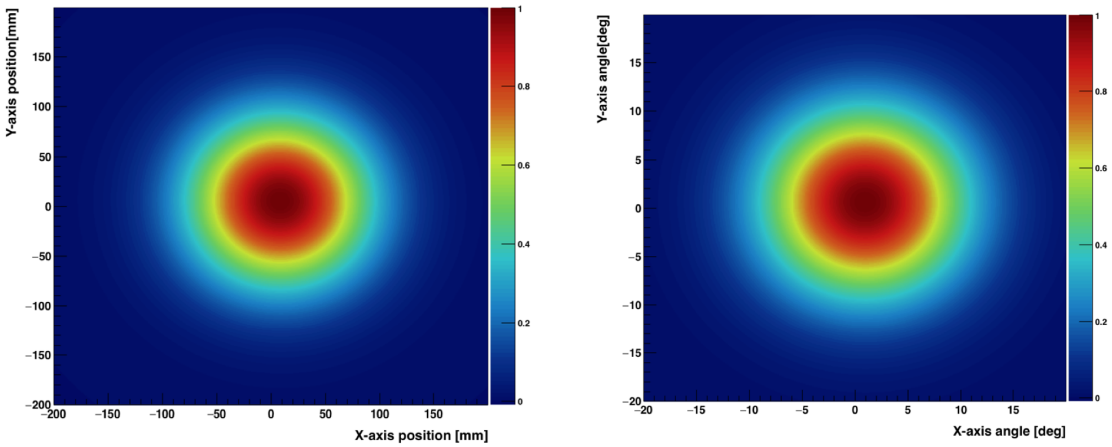

Figure 8.16: Reconstructed beam maps with the knife edge method for the 95 GHz band. Left: as a function of the positions. Right: as a function of the angles assuming that the beam is emitted at the Gregorian focus.

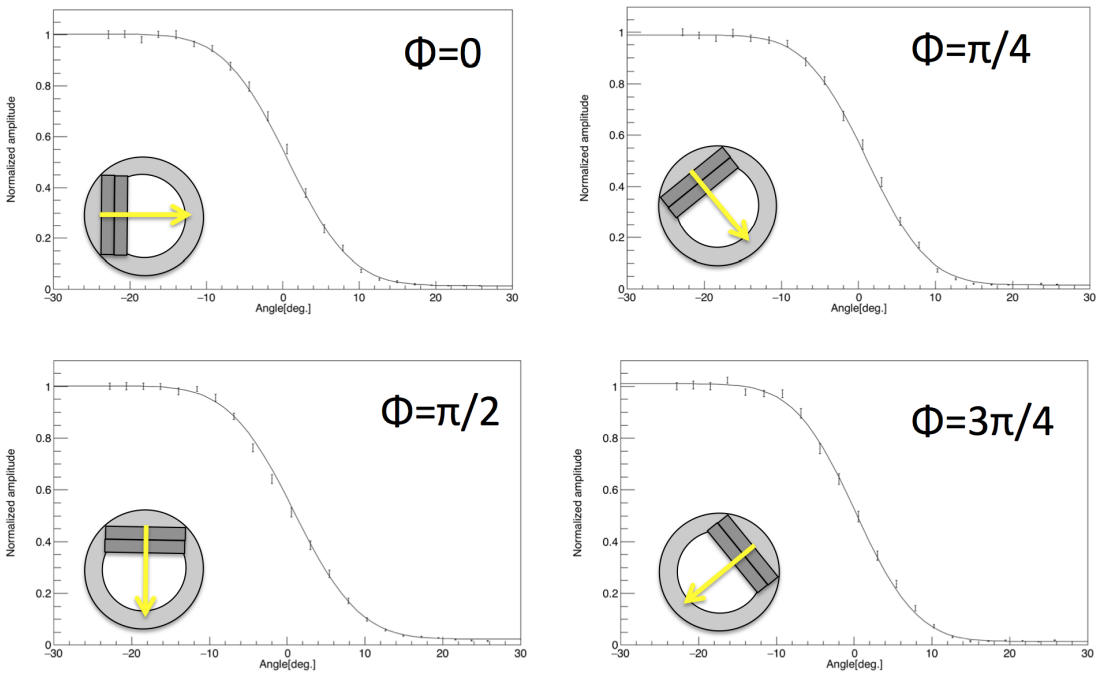

Figure 8.17: The same results as Fig. 8.14 but with the calculated angle from the Gregorian focus as the horizontal axis. The estimated fitting parameters are listed in Table 8.4.

8.5 Polarization

We measure the polarization response of the detector. We use the top and bottom detectors at 95 GHz. The measurement setup is shown in Fig. 8.18. A mirror and a wire grid are placed on the optical axis. The wire grid is tilted by 30 degrees to avoid standing waves. The polarized signal is modulated with an optical chopper whose frequency is 15 Hz. The wire grid is rotated at 0.16 GHz. The angle of the wire grid is monitored with and encoder. Figure 8.19 shows the raw data of measurement, where the phase of the top detector delays by 180 degrees with respect to the bottom detector. We estimate the modulated amplitude of the chopper with Eq. (8.16). We sort the data with the encoder data as shown in Fig. 8.20. We estimate the error bar from Fig. 8.20. The measured signal is shown in Fig. 8.21. We fit the data using the following model:

$$A + B\sin(2\theta + \phi) + C\sin(4\theta + \phi), \tag{8.15}$$

where θ and ϕ are the angle and phase of the wire grid. The 4f term is introduced empirically. The χ^2/N of the top and bottom pixels are 70/54 and 102/54, respectively. The offset factors are 4.76 ± 0.01 % and 3.51 ± 0.01 %, which are corresponding to the cross polarization loss. These factors are called the polarization efficiencies. The origins of the cross polarization is the mirror. We estimate the cross polarization of the mirror using QUAST simulation. The simulated factor is 3-5 %, which is consistent with our measurement.

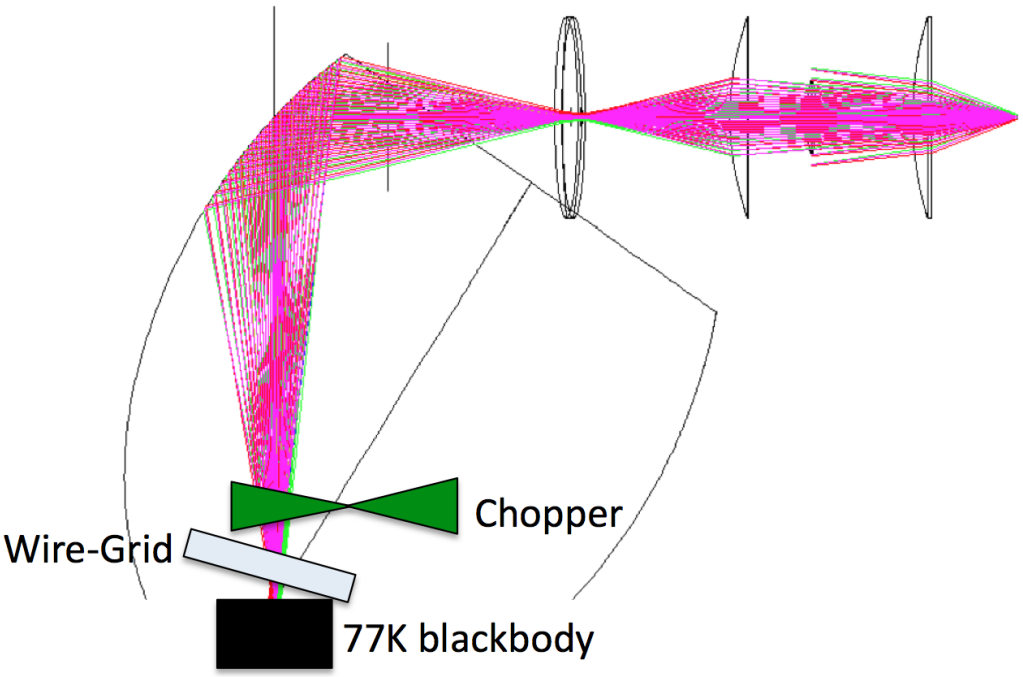

Figure 8.18: Experimental setup of the polarization measurement.

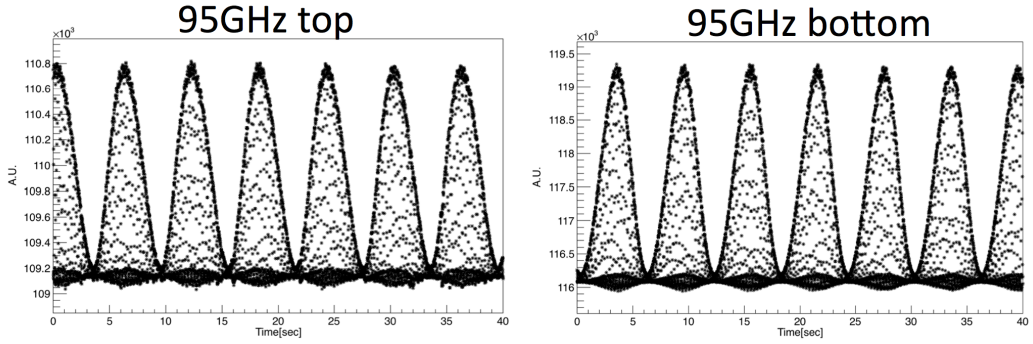

Figure 8.19: The raw data of the polarization measurement.

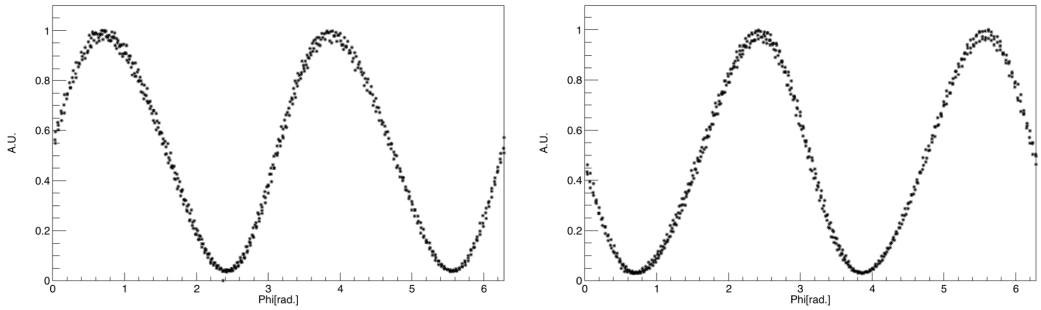

Figure 8.20: The sorted data with the optical encoder signal.

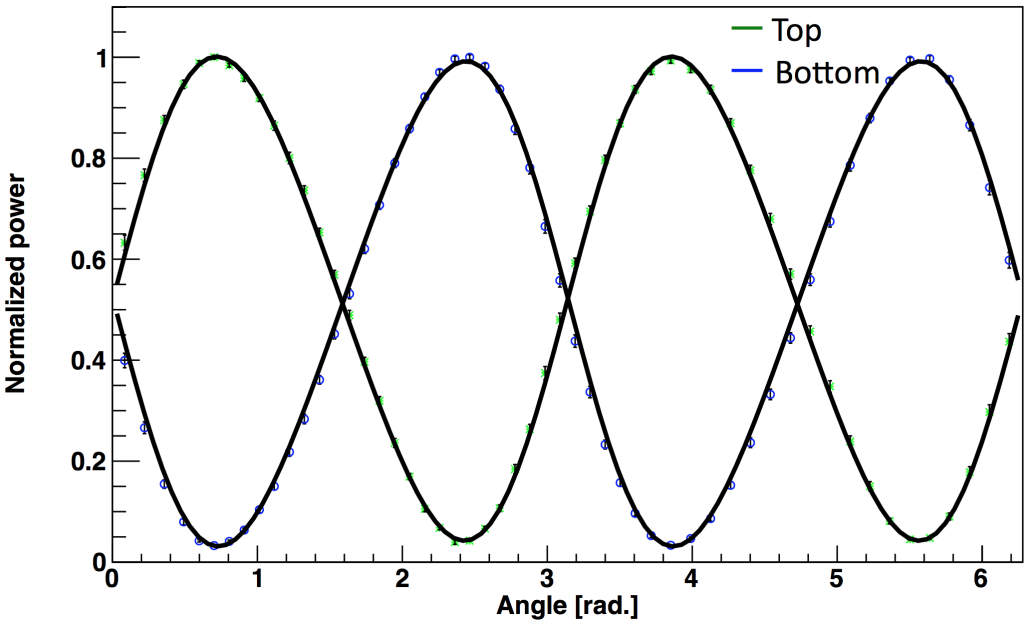

Figure 8.21: The results of the polarization measurement. The errors are statistical.

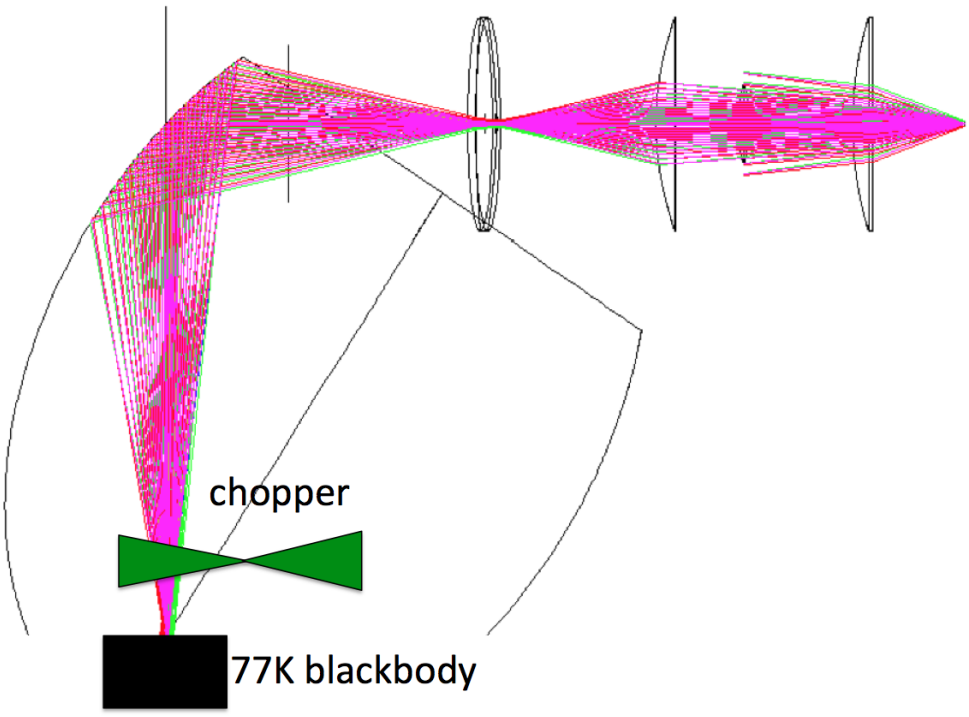

Figure 8.22: Schematic view of the optical power measurement.

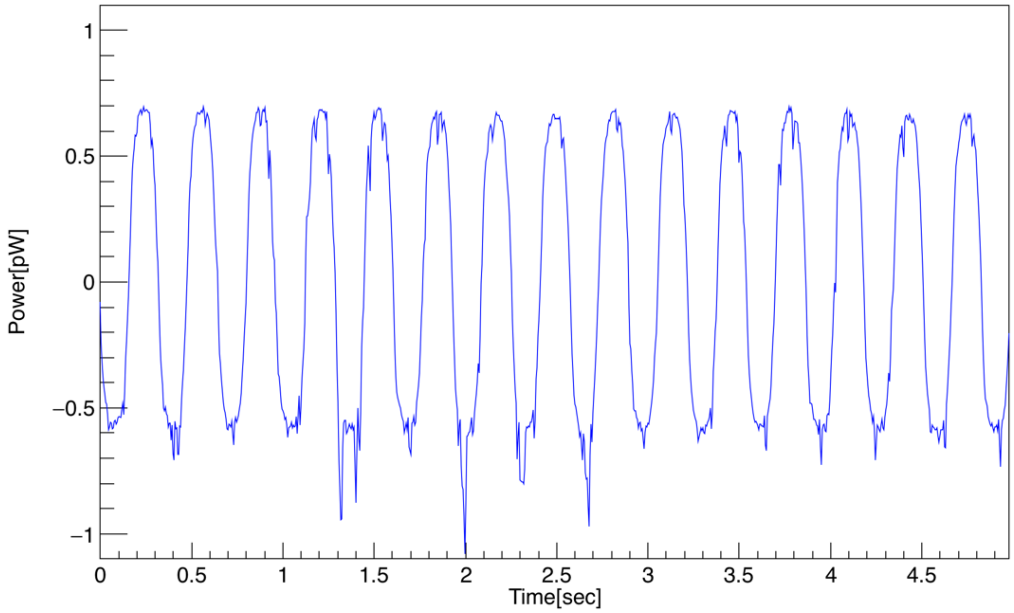

Figure 8.23: Time-ordered-data (TOD) . Clear liquid nitrogen signal is seen at the chopper frequency. This curve is an example of the measured data with chopping at 3.2 Hz.

8.6 Optical power

In this measurement, we used the chopped cold load source as the reference signal, which is the black body made of HR25. We use it in the liquid nitrogen. The beam is collimated with the mirror. The ray diagram and collimated beam width are simulated with ZEMAX. The simulated ray diagram with the mirror and beam width are shown in Fig. 8.22. We designed the diameter of cold load source larger than that of beams for covering the beam sufficiently. The chopper frequency is changed between 5 Hz and 11 Hz. Figure 8.23 shows the example of TODs. We can model this signal with the following function,

$$P_0 + \Delta P \sin(2\pi\omega t + \phi), \tag{8.16}$$

where P_0, ΔP, f and ϕ are the offset, amplitude, frequency and phase. The TODs of 5 Hz and 11 Hz are fitted separately for every $2/f$ seconds. We calculate and fit the histograms of ΔP, and f, where we subtract the offset of these parameters. The estimated ΔP, and f are shown in Table 8.5.

8.6.1 Optical efficiency

The amplitude of the power is modeled as

$$P(f) = \frac{\Delta P_0}{\sqrt{1+\tau^2 f^2}}, \tag{8.17}$$

where f is the frequency of the chopper, τ is a time constant of the bolometer, and ΔP_0 is the modulated power between 77 K and 300 K source. Figure 8.24 shows the measured optical power and best fit curve

Table 8.5: Modulated amplitude of 95 GHz and 150 GHz detector for chopped liquid nitrogen signal at various chopper frequencies. Using this data, the time constant and optical efficiency are evaluated.

frequency	95 GHz [pW]	150 GHz [pW]
5.00 ± 0.01	1.396 ± 0.005	2.088 ± 0.012
7.00 ± 0.01	1.399 ± 0.005	1.922 ± 0.014
9.00 ± 0.01	1.4005 ± 0.005	1.782 ± 0.011
10.98 ± 0.01	1.390 ± 0.005	1.669 ± 0.011

Table 8.6: Results of optical efficiency measurement

Detector	$\Delta\nu$[GHz]	Time constant [msec]	Power[pW]
95	18.0	1.8 ± 0.5	$1.402 \pm 0.005 \pm 0.001$
150	21.1	13.4 ± 0.4	$2.250 \pm 0.002 \pm 0.0001$

of the time constant.

We estimate the optical efficiency using Fig. 8.24. The band shapes of each pixel are shown in Fig. 8.25. The estimated band width at 95 and 150 GHz are 18.0 and 21.1 GHz, respectively. The detected power consists of three parts as follows:

$$P_{sat} = P_{load} + P_{dewar} + P_{bias}(T_{load}), \tag{8.18}$$

where P_{sat}, P_{load}, P_{dewar}, and P_{bias} are saturation power, optical loading, dewar loading and bias power. The optical loading can be described as follows:

$$P_{load} = \eta \Delta\nu k T_{load}, \tag{8.19}$$

where η, $\Delta\nu$, k are the optical efficiency, band width, and Boltzmann constant, respectively.

We modulate the optical loading between T_{300K} and T_{77K}. Then, we assume that P_{dewer} and P_{sat} are not changed with the temperature modulation. The measured amplitude of the modulated power, ΔP_0, is corresponding to

$$\Delta P_0 = \eta \Delta\nu k (T_{300K} - T_{77K}). \tag{8.20}$$

We can obtain the optical efficiency as follows:

$$\eta_{95\ \mathrm{GHz}} = 2.53 \pm 0.04\ \%, \tag{8.21}$$

$$\eta_{150\ \mathrm{GHz}} = 3.54 \pm 0.002\ \%, \tag{8.22}$$

The largest systematic error in our measurement is the estimation of power. When we estimate the power, we usually use the following equation:

$$P = I^2 R, \tag{8.23}$$

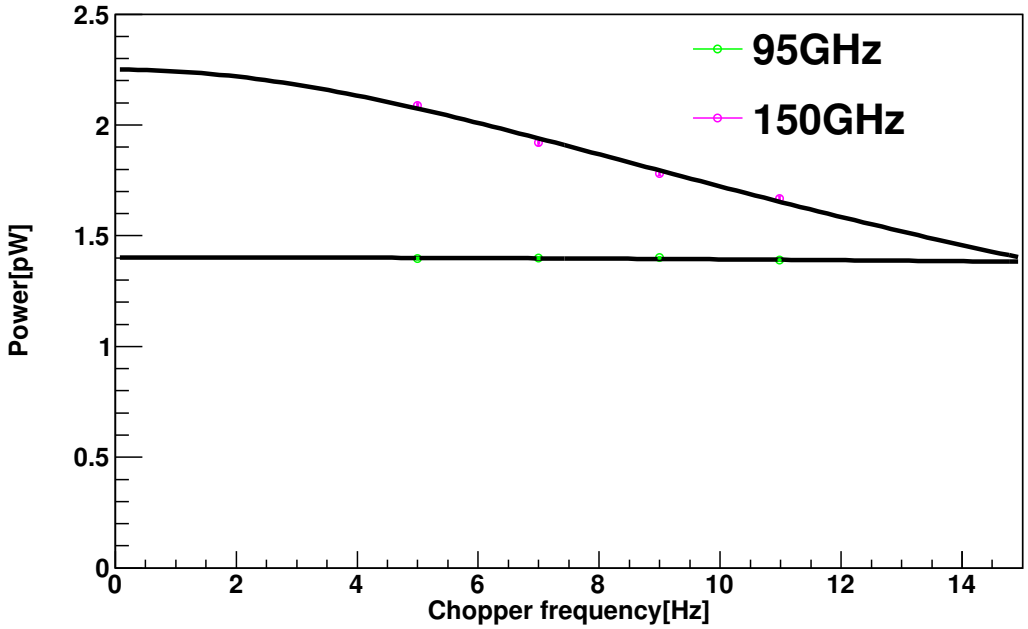

Figure 8.24: The measured optical power with each chopper frequency. Black curves are best fits. The fit parameters are shown in Table 8.6.

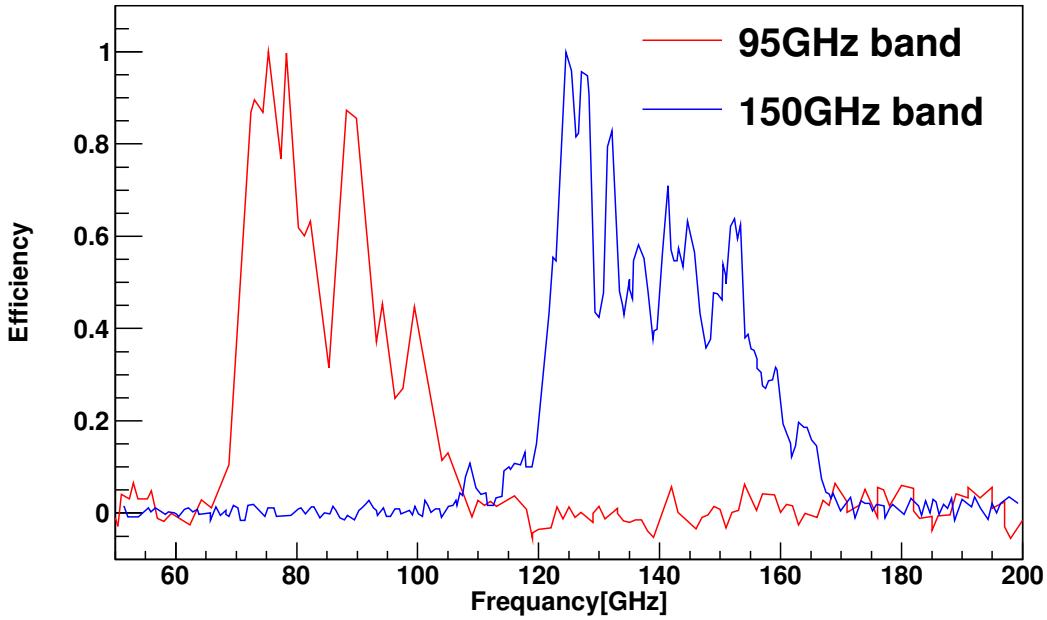

Figure 8.25: Measured band efficiencies of 95 and 150 GHz bands. Private communication with Yasuto Hori.

where I is the current of the nuller and R is resistance of the bolometer. R is measured as a ratio of carrier voltage and nuller current. However, we should subtract the effect of the parasitic resistance, r, as follows:

$$\bar{R} = R - r = \frac{V}{I} - r. \tag{8.24}$$

The typical value of r is 0.1 ± 0.1. We add this uncertainty as a systematic error.

The expected values of optical efficiency in PB-2 were discussed in Chap. 7. In this measurement, we install the different configuration from Chap. 7, so that the expected optical efficiency and optical power are less than that in Chap. 7. The assumed values are listed as follows.

Uncertainty of wafer optical efficiency Optical efficiencies of several ver.4 wafers are reported elsewhere [79]. We take the optical efficiency uncertainty, 6.84 %, in both bands in our study.

RMS of the optical efficiency in ver.4 wafer The measured antenna efficiencies of another ver 4 wafer are 36.06 ± 4.87 % and 31.50 ± 5.38 % at 95 and 150 GHz band. We take these as the typical values of ver.4 wafers when we estimate the power and optical efficiency.

AR coating of filter and lenses In this system, we do not employ the epoxy AR coating. The predicted transmittance of alumina lenses are shown in Fig. 8.26, where we assume the thickness of the lenses is 50 mm. The average transmittances in 95 and 150 GHz bands of the aperture and collimator lenses are 54.8 and 52.8 %. The average transmittances in band of the field lens are 0.686 and 0.662 %. The bandwidths of 95 and 150 GHz band are also different. We also estimate the band uncertainty when we assume the measured alumina property and AR materials.

Metal mesh filter The uncertainty of transmittance for the measured metal mesh filter is assumed to be 1 %. This value is obtained from the private communication with Hiroshi Yamaguchi and Tomotake Matsumura.

The systematic error budget is summarized in Table. 8.7. The expected powers and optical efficiencies are summarized in Table 8.8. These values are consistent with the measured values. We conclude that our system is understood sufficiently and thus we have demonstrated the high sensitivity receiver system.

8.7 Discussion

8.7.1 Beam profile using knife edge method

We characterize the beam profile using the knife edge method for 95 GHz. The knife edge offers advantages. First, this method can be easily compared with optical simulation. In the usual method with a beam mapper, the measured beam map using an X-Y stage is convolved with the beam pattern of the source and detector, so that we need to deconvolute the two beams. However, in the knife edge

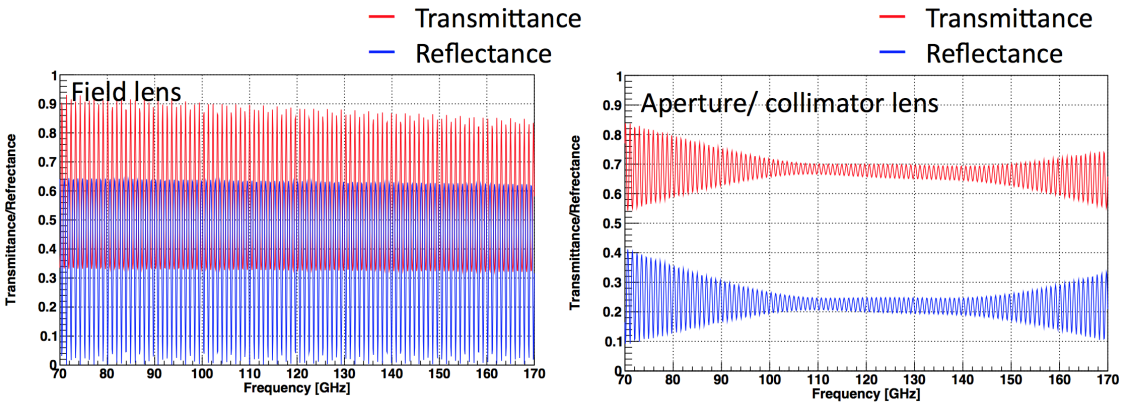

Figure 8.26: The calculated transmittance of the field lens (left) and aperture/collimator lenses (right).

Table 8.7: Error budget of optical efficiency

Error list	95 GHz power[pW]	150 GHz power [pW]	95 GHz optical efficiency	150 GHz optical efficiency
Wafer	0.11 (6.86 %)	0.15 (6.86 %)	0.16	0.24
Detector	0.08 (4.87 %)	0.12 (5.38 %)	0.11	0.19
Alumina lens + filter	0.03 (2.13 %)	0.07 (3.02 %)	0.05	0.11
MMF	0.02 (1.00 %)	0.02 (1.00 %)	0.02	0.03
Total	0.193 (8.74%)	0.146 (9.28%)	0.20	0.32

Table 8.8: Comparison for the powers and optical efficiencies. The expected values are scaled with the optical efficiency in Chap.7.

	Detector [GHz]	Power [pW]	optical efficiency[%]
Expected	95	1.56 ± 0.19	2.29 ± 0.20
Expected	150	2.21 ± 0.15	3.48 ± 0.32
Measured	95	$1.402 \pm 0.005 \pm 0.001$	$2.53 \pm 0.04 \pm 0.01$
Measured	150	$2.25 \pm 0.02 \pm 0.0001$	$3.54 \pm 0.002 \pm 0.0002$

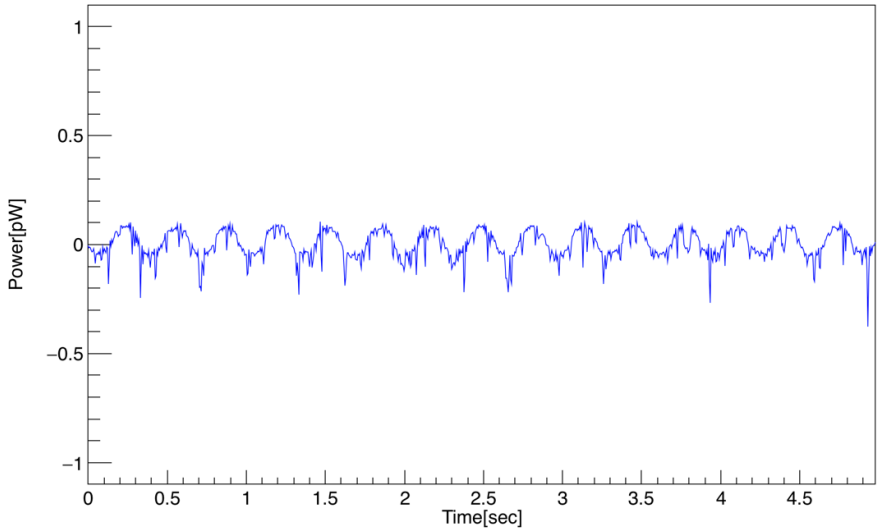

Figure 8.27: The measured signal with a detector with no lenslet.

method one can compare the model with the measured map directly through the erf(ξ) curve. Second, this method allows rapid scanning. In the case of a X-Y beam mapper, the number of the measurement points is N^2 when we measure $N \times N$ resolution beam maps. However, the knife edge method requires only $4N$ points, assuming that we measure with 4 directions. These advantages are expected to be helpful for us to perform quick laboratory tests.

8.7.2 Direct stimulation

The TES bolometer usually receives the signal from an antenna with a lenslet through a microstrip filter. However, the detector without a lenslet in some cases is also stimulated directly. The 95 and 150 GHz detectors we have characterized have lenslets. Figure 8.27 shows a comparison of the 95 GHz detector and another detector without a lenslet. The observed signals with the detector without the lenslet are an order of magnitude smaller. Furthermore, since the case of direct stimulation is not through a microstrip filter, band characteristics can not be seen. However, Fig. 8.25 shows the observed band characteristics. Therefore the signal we observe is not from direct stimulation.

8.8 Summary

In this chapter, we have characterized the optical system of the PB-2 receiver system. The measured beam agrees with the simulated foot print diagram. Therefore, we conclude that we have demonstrated and crosschecked the beam shape as expected from the measured positions of the lenses. The measured powers are consistent with the expected power within 1 sigma error. Therefore we conclude that the

optical and thermal design of the POLARBEAR-2 cryostat and optical system satisfactory for precision B-mode observations.

Chapter 9

Discussion

In this chapter we focus on two things. In the next section, we discuss remaining laboratory tests we need to carry out before shipping the PB-2 receiver system to Chile. In Section 9.2 we discuss the possible applications of the AR coating technology, which has been a key to the successfull development of the PB-2 receiver system, to future experiments.

9.1 Preparation for the deployment

A series of laboratory experiments need to be performed before the deployment of the POLARBEAR-2 receiver system. The basic steps of the testing in the laboratory are as follows:

Installation of the lenses with AR coating and the observation-quality detector modules The efficiency loss on each surface of alumina without AR coating is about 25 %. The losses due to the antenna efficiency and bandwidth with the bolometers used in the laboratory tests described in the previous chapter are also 30 % and 60 %. Therefore, the total efficiency in the test measurements was only 5 %. With the epoxy AR coating and observation-quality detectors, we should check that the total efficiency is larger by an order of magnitude.

More accurate measurements of optical efficiencies, cross polarization, spectra, and beam with the total system with observation-quality detector modules We should perform a series of measurements with better accuracy to characterize the system as a whole. Optical efficiencies, cross polarization, spectra and beam profile need to be measured.

Characterization of the noise equivalent temperature We should characterize the noise equivalent temperature directly. In our measurements described in the previous chapter, we estimate the NET from the optical efficiency. However, this measurement did not include the loading from the dewer. What is the most important is to examine the NET directly. One of the most powerful methods is a sky emulator. The sky emulator can make the radiation corresponding to the sky temperature in Chile.

In laboratory measurements, the power from the window is larger than that of the saturation power. Therefore, we usually attenuate the power even if we use a 77 K load. However, since the attenuator is placed inside the cryogenic stage, the estimation of the exact power is very difficult. On the other hand, the sky emulator can make the cold load whose effective temperature is between 10 K and 30 K.

When we complete all the tests above and confirm that the performance is satisfactory, we will ship our system to Chile for deployment.

9.2 Application of AR coating technology to future experiments

9.2.1 Simons array

The Simons Array employs the copies of two more PB-2 systems to achieve the high sensitivity measurements with three telescopes as shown in Fig. 9.2. Table 9.1 shows the specification of three telescopes, which are denoted as system A, B and C.

We note that the AR coating for the system C needs careful considerations. The optimized thicknesses of the AR layers are proportional to the quarter-wavelength. Therefore, the thicknesses of AR layers of the system C will be less than those of the system A and B. The thiner layers yield the less loss of the AR coating. However, the loss tangent of the 280 GHz region are higher than that of 150 GHz region. We need to make the trade-off between the thickness and loss effect when we make a design of PB-2C AR coating. Figure 9.1 shows the calculated the PB-2C transmittances of the alumina filter when we assumed the parameter in Fig. 4.8. Then, the optimized thicknesses at 220 and 280 GHz bands are 0.14 and 0.17 mm, respectively. Here factor k is multiplied to each loss tangents of AR materials, $k \tan \delta$. $k = 2.0$ is the worst case. Therefore, the average transmittance at system C will not be change or high even if loss tangent of AR materials are twice.

The metal mesh filter is placed on the 350 mK stage. Its cut-off frequency is 172 GHz. However, the detection band of the system C is larger than that of the system A and B. Therefore, we have to place a metal mesh filter with a larger cut-off frequency. When we assume the Lyot stop temperature of 5 K and the focal plane diameter of 365 mm, the expected loading would be 3.6 and 3.0 μW with the metal mesh filter cut-off frequency of 360 and 320 GHz. These thermal emission are acceptable.

Therefore, we can conclude that the technologies of PB-2C enable to use the extended our technology.

9.2.2 LiteBIRD

LiteBIRD (Lite (Light) satellite for the studies of B-mode polarization and Inflation from cosmic background Radiation Detection) is a satellite to map the polarization of the CMB radiation over the full sky at large angular scales [33, 94]. Figure 9.3 shows the executive summary of the LiteBIRD misson.

One of the technical challenges of LiteBIRD is a broadband AR coating on large AHWPs made of sapphire. There will be two telescopes. The low-frequency telescope will cover 40 - 235 GHz, while the high-frequency telescope will be for 280 - 402 GHz. Each telescope adopts an AHWP. Solutions listed

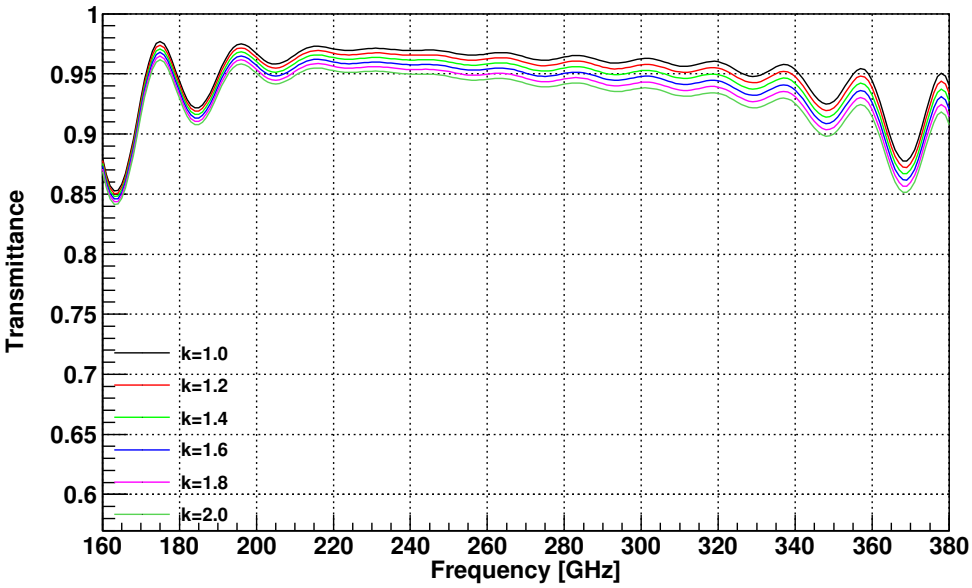

Figure 9.1: The calculated transmittance of the alumina filter when we optimize the PB-2C detection bands.

Figure 9.2: Conceptual picture of Simons Array.

Table 9.1: The specification of the Simons Array experiment.

System	Frequency [GHz]	Number of detectors
A	95	3794
	150	3794
B	95	3794
	150	3794
C	220	3794
	280	3794

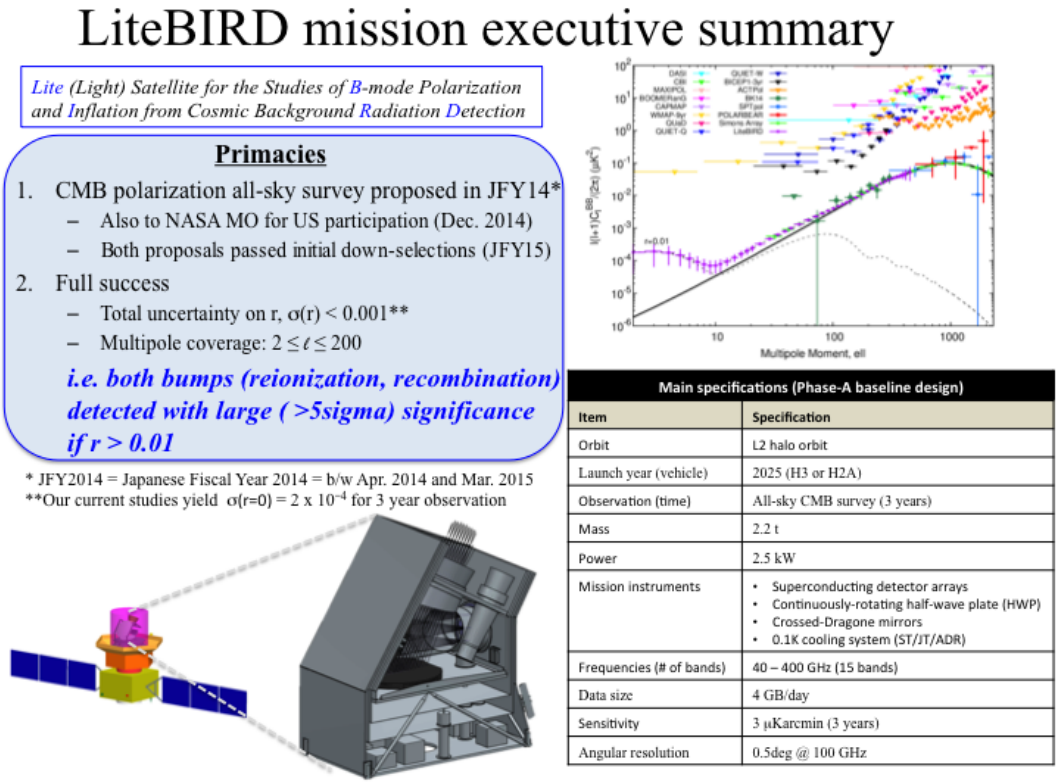

Figure 9.3: The executive summary of the LiteBIRD mission. Private communication with Masashi Hazumi.

so far include sub-waves grading (SWG) AR coating and multilayer AR coating. There are advantages and disadvantages with each method. The SWG method is tried on sapphire of 50 mm in diameter. However, It is difficult to apply this method to the larger size of sapphire that is required for the LiteBIRD experiment. We have developed the Skybond-mullite AR coating. The Skybond provides a potential to multilayer coating because the available indices of refraction are between 1.1 and 1.7 due to the filling factor. Therefore, we expect to achieve the multilayer AR coating with the same material. The advantage of the same material is to avoid the crack with cooling thanks to the same thermal expansion at each layer. Furthermore, polyimide is quite robust against damages from cosmic rays. In contract, almost all the materials of plastic will be deteriorated by the cosmic rays. Therefore, the technology with expanded polyimide is a good fit to LiteBIRD.

Chapter 10

Conclusion

I have developed and characterized the optical system of POLARBEAR-2 in order to perform precision measurements of the CMB B-mode. POLARBEAR-2 is an experiment for performing high-sensitivity observations by placing 7,588 detectors on the focal plane of 365 mm in diameter. We plan to start scientific observations in 2017. I have succeeded in developing essential key technologies to satisfy requirements for achieving the goals of the observation. The first among them is lenses made of alumina that sufficiently suppress aberration for the large focal plane of POLARBEAR-2. We have performed measurements of optical and thermal properties of alumina. The developed lenses have been aligned in the laboratory using the laser tracker. The lenses are arranged with sufficient accuracy to achive the diffraction-limited optics. We have also developed a new method for two-layer anti-reflection (AR) coating on the optical components made of alumina. Development of AR coating is essential in order to suppress the reflection in the alumina optics for wide-band observations. The new anti-reflection coating is realized with using the thermally-sprayed mullite and expanded polyimide (Skybond Foam) for the large flat surface.

To achieve the large focal plane, we need a large window. However, it imposes a challenge in the thermal design. Initial studies came to the conclusion that conventional IR filters are not sufficient for the case with such a large window. The surface temperature rises by about 100 K at the center of a filter compared with the edge of the filter in case of conventional filters, such as PTFE. I have developed a new type of IR filter made of alumina. The thermal conductivity of the alumina filter is three orders of magnitude as large as that of the conventional filter. We find that the temperature rise at the center is only 2.3 K with the alumina filter.

Another challenge is unexpected stray light entering through the window that might also result in more thermal load on the focal plane. A standard method for reducing such stray light is to cover the inner surface of the 4 K stage with blackbody absorbers. We have invented a new black absorber named "KEK Black" for this purpose. The KEK black is optimized for millimeter-wave observations. Thanks to the use of the KEK black and the alumina filter, we achieved a holding time of 38 hours, which meets our requirement.

We have calculated the experimental sensitivity using the measured temperatures and transmittances of the optical elements. The calculated sensitivity is 3.39 $\mu\mathrm{K}\sqrt{\mathrm{sec}}$, which implies that our system has a sufficient margin to the required value of 4.30 $\mu\mathrm{K}\sqrt{\mathrm{sec}}$.

We have prepared an end-to-end system for validation of beam and sensitivity. All the optical components are housed in the optics cryostat and cooled down successfully. Prototype dual-color TES bolometers are mounted on the focal plane and read out with the DfMUX system. We have confirmed signals from a cold load. The cross section of the beam is measured with the knife edge method. The results are consistent with the simulation within 1 σ. The optical efficiency and power at each band are also estimated from the measurements. The measured powers are consistent with the expected values.

To conclude, we have developed the POLARBEAR-2 receiver system. We have overcome several challenges that mainly arise from the fact that we are to employ a very large focal plane for precision measurements of CMB B-mode polarization. Validation of beam and sensitivity has been done successfully, satisfying requirements imposed from the observational needs. New key technologies such as the alumina IR filter developed and described in this thesis are already being applied in other CMB projects including SPT3G and BICEP3. Our pioneering work can also play an important role in the optical system of next-generation and future CMB observations.

Appendix A

Analytical calculation of transmittance

We discuss the transmittance and reflectance model here [31]. We now study the flat balk material through the linear polarized electromagnetic waves. First, we consider the boundary condition. The electric or magnetic field should be continuous across the each boundary surface. Here, we define the incident electric field, E_I, as shown in Fig. A.1. Then, the boundary condition at the surface I is given by

$$E_I = E_{iI} + E_{rI} = E_{tI} + E'_{rII}, \tag{A.1}$$

and

$$H_I = \sqrt{\frac{\epsilon_0}{\mu_0}}(E_{iI} - E_{rI})\hat{n}_0 \cos\theta_{iI} = \sqrt{\frac{\epsilon_0}{\mu_0}}(E_{iI} - E'_{rII})\hat{n}_1 \cos\theta_{iII}, \tag{A.2}$$

where

$$\mathbf{H} = \sqrt{\frac{\epsilon_0}{mu_0}}\hat{n}\mathbf{k} \times \mathbf{E}. \tag{A.3}$$

Here $\mathbf{k}$ is the wave number, $\hat{n}_i$ is the complex IOR on the i-th surface. The complex IOR is defined as

$$\hat{n} = n^{(r)} - in^{(i)}. \tag{A.4}$$

Here we define the non-complex IOR and loss tangent as follows,

$$n = n^{(r)}, \tag{A.5}$$

$$\tan\delta = \frac{n^{(i)}}{n^{(r)}}. \tag{A.6}$$

The boundary condition of the surface II is also described by

$$E_{II} = E_{iII} + E_{rII} = E_{tII}, \tag{A.7}$$

and

$$H_{II} = \sqrt{\frac{\epsilon_0}{\mu_0}}(E_{iII} - E_{rII})\hat{n}_1 \cos\theta_{iII} = \sqrt{\frac{\epsilon_0}{\mu_0}}E_{tII}\hat{n}_3 \cos\theta_{iII}. \tag{A.8}$$

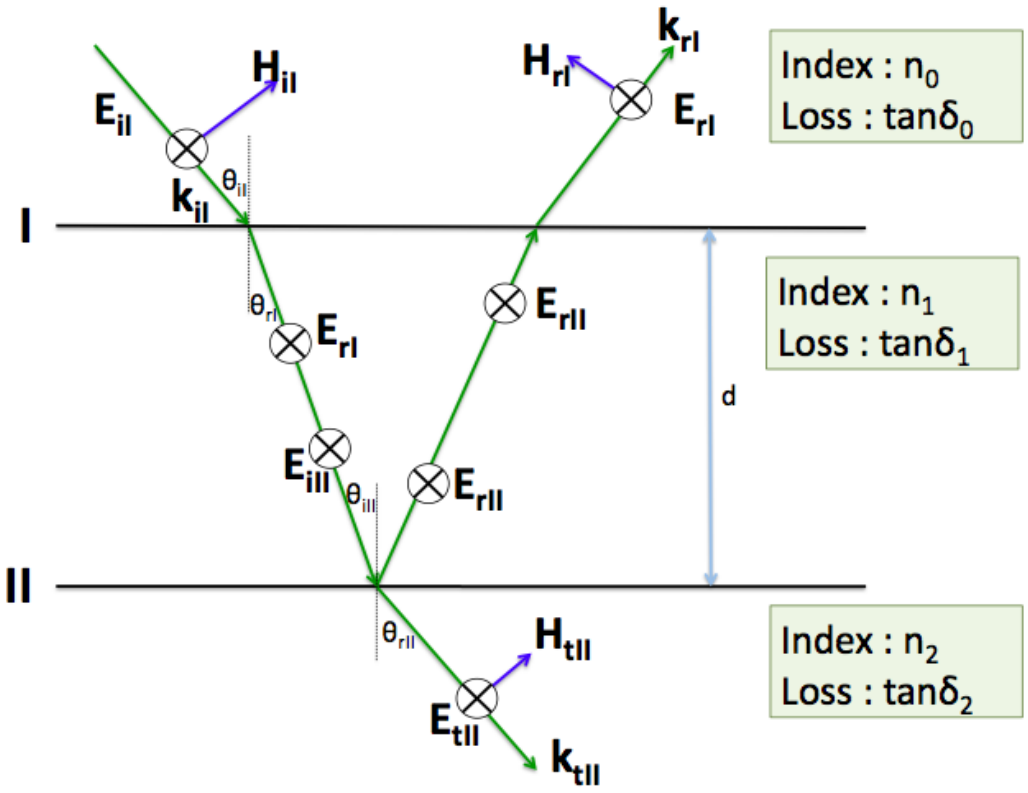

Figure A.1: Configuration of the transmittance model.

Now, define the thickness of the material as d. Then, the phase shift through the material can be written by

$$h = 2\hat{n}_1 d \cos\theta_{iII}/2, \tag{A.9}$$

so that we obtain

$$E_{iII} = E_t e^{-k_0 h}, \tag{A.10}$$

$$E_{rII} = E'_r e^{k_0 h}. \tag{A.11}$$

Using these equations, Eq. (A.7) and Eq. (A.8) become

$$E_{II} = E_t e^{-k_0 h} + E'_r e^{k_0 h}, \tag{A.12}$$

$$H_{II} = \sqrt{\frac{\epsilon_0}{\mu_0}}(E_t e^{-k_0 h} - E'_r e^{k_0 h})\hat{n}_1 \cos\theta_{iII}. \tag{A.13}$$

These equations can be solved as

$$E_I = E_{II}\cos k_0 h + H_{II}(i\sin k_0 h)/\Upsilon_1, \tag{A.14}$$

$$H_I = E_{II}\Upsilon_1 i\sin k_0 h + H_{II}\cos k_0 h, \tag{A.15}$$

where

$$\Upsilon_1 = \sqrt{\frac{\epsilon_0}{\mu_0}} n_1 \cos\theta_{iII}. \tag{A.16}$$

When the incident wave is a TM wave,

$$\Upsilon_1 = \sqrt{\frac{\epsilon_0}{\mu_0}} n_1 / \cos\theta_{iII}. \tag{A.17}$$

We now adopt a matrix notation:

$$\begin{bmatrix} E_I \\ H_I \end{bmatrix} = M_I \begin{bmatrix} E_{II} \\ H_{II} \end{bmatrix}, \tag{A.18}$$

where

$$M_I = \begin{bmatrix} \cos k_0 h & (i\sin k_0 h)/\Upsilon_I \\ \Upsilon_I i\sin k_0 h & \cos k_0 h \end{bmatrix}. \tag{A.19}$$

Here $M_I$is called the characteristic matrix. The information of the material property is present in the characteristic matrix perfectly. Generally, we can extend it to the multilayer model as follows:

$$\begin{bmatrix} E_I \\ H_I \end{bmatrix} = M_I M_{II} \cdots M_i \begin{bmatrix} E_{i+1} \\ H_{i+1} \end{bmatrix}, \tag{A.20}$$

where we can describe the 2×2 characteristic matrix of the system as

$$M = M_I M_{II} \cdots M_i = \begin{bmatrix} m_{11} & m_{12} \\ m_{21} & m_{22} \end{bmatrix}. \tag{A.21}$$

We now substitute Eq. (A.1) and Eq. (A.7) into this equation

$$\begin{bmatrix} E_{iI} + E_{rI} \\ (E_{iI} - E_{rI})\Upsilon_0 \end{bmatrix} = M \begin{bmatrix} E_{tII} \\ E_{tII}\Upsilon_s \end{bmatrix}, \tag{A.22}$$

where

$$\Upsilon_0 = \sqrt{\frac{\epsilon_0}{\mu_0}}\hat{n}_0 \cos\theta_{iI}, \tag{A.23}$$

and

$$\Upsilon_s = \sqrt{\frac{\epsilon_0}{\mu_0}}\hat{n}_N \cos\theta_{iI}. \tag{A.24}$$

We define the reflectance and transmittance of electrical waves as

$$a_r = \frac{E_{rI}}{E_{iI}}, \tag{A.25}$$

and

$$a_t = \frac{E_{tII}}{E_{iI}}. \tag{A.26}$$

Then, the matrices can be replaced as

$$\begin{bmatrix} 1 + a_r \\ (1 - a_r)\Upsilon_0 \end{bmatrix} = M \begin{bmatrix} a_t \\ a_t\Upsilon_s s \end{bmatrix}. \tag{A.27}$$

Then, we get the rerations of

$$a_r = \frac{\Upsilon_0 m_{11} + \Upsilon_0\Upsilon_s m_{12} - m_{21} - \Upsilon_s m_{22}}{\Upsilon_0 m_{11} + \Upsilon_0\Upsilon_s m_{12} + m_{21} + \Upsilon_s m_{22}}, \tag{A.28}$$

and

$$a_t = \frac{2\Upsilon_s}{\Upsilon_0 m_{11} + \Upsilon_0\Upsilon_s m_{12} + m_{21} + \Upsilon_s m_{22}}. \tag{A.29}$$

Multiplying a_r and a_t by its complex conjugate, the reflectance and transmittance are written as

$$R_s = a_r a_r^*, \tag{A.30}$$

$$T_s = a_t a_t^*. \tag{A.31}$$

Simple case: bulk transmission Let's consider the simple case of a bulk transmission. For a single layer, we assume $i = I$. Then, we can describe a_r and a_t as

$$\begin{aligned} a_r &= \frac{i\sin(k_0 h)(1-n^2)}{2n\cos(k_0 h) + i\sin(k_0 h)(1+n^2)} && \text{(A.32)} \\ &= \frac{i\frac{e^{ik_0h} - e^{-ik_0h}}{2i}(1-n^2)}{2n\frac{e^{ik_0h} + e^{-ik_0h}}{2} + i\frac{e^{ik_0h} - e^{-ik_0h}}{2i}(1+n^2)} && \text{(A.33)} \\ &= \frac{(e^{ik_0h} - e^{-ik_0h})(n+1)(n-1)}{e^{ik_0h}(n+1)^2 - e^{-ik_0h}(n-1)^2} && \text{(A.34)} \\ &= \frac{(1 - e^{-i2k_0h})\frac{n-1}{n+1}}{1 - \frac{(n-1)^2}{(n+1)^2}e^{-i2k_0h}} && \text{(A.35)} \\ & && \text{(A.36)} \end{aligned}$$

and

$$
\begin{aligned}
a_t &= \frac{2n}{2n\cos k_0 h + i\sin k_0 h(1+n^2)} && \text{(A.37)}\\
&= \frac{2n}{2n\frac{e^{ik_0h}+e^{-ik_0h}}{2} + i\frac{e^{ik_0h}-e^{-ik_0h}}{2i}(1+n^2)} && \text{(A.38)}\\
&= \frac{4n}{e^{ik_0h}(n+1)^2 - e^{-ik_0h}(n-1)^2} && \text{(A.39)}\\
&= \frac{\frac{4n}{(n+1)^2}e^{-ik_0h}}{1-\frac{(n-1)^2}{(n+1)^2}e^{-i2k_0h}}. && \text{(A.40)}\\
& && \text{(A.41)}
\end{aligned}
$$

Now we define transmittance, T, reflectance, R, with the surface (not bulk) absorption coefficient, μ, and phase, ϕ, as

$$
\begin{aligned}
R &= \frac{(1-n)^2}{(1+n)^2}, && \text{(A.42)}\\
T &= \frac{4n}{(1+n)^2}, && \text{(A.43)}\\
\mu &= e^{-k_0 n d tan\delta/\cos\theta_{iI}}, && \text{(A.44)}\\
\phi &= knd/\cos\theta_{iI}. && \text{(A.45)}
\end{aligned}
$$

a_r and a_t are written as

$$
\begin{aligned}
a_r &= \frac{(1-\mu^2 e^{-i2\phi})\sqrt{R}}{1-R\mu^2 e^{-i2\phi}} && \text{(A.46)}\\
a_t &= \frac{T\mu e^{i\phi}}{1-R\mu^2 e^{-i2\phi}}. && \text{(A.47)}
\end{aligned}
$$

We calculate R_s and T_s:

$$
\begin{aligned}
R_s &= a_r a_r^* && \text{(A.48)}\\
&= \frac{(1-\mu^2 e^{-i2\phi})\sqrt{R}}{1-R\mu^2 e^{-i2\phi}}\frac{(1-\mu^2 e^{i2\phi})\sqrt{R}}{1-R\mu^2 e^{i2\phi}} && \text{(A.49)}\\
&= \frac{(1-2\mu^2\cos(2\phi)+\mu^4)R}{1-2R\mu^2\cos 2\phi + R^2\mu^4} && \text{(A.50)}
\end{aligned}
$$

and

$$
\begin{aligned}
T_s &= a_t a_t^* && \text{(A.51)}\\
&= \frac{T\mu e^{i\phi}}{1-R\mu^2 e^{-i2\phi}}\frac{T\mu e^{-i\phi}}{1-R\mu^2 e^{i2\phi}} && \text{(A.52)}\\
&= \frac{T^2\mu^2}{1-2R\mu^2\cos 2\phi + R^2\mu^4}. && \text{(A.53)}
\end{aligned}
$$

Finally, we define the absorptance:

$$
\begin{aligned}
A_s &= 1 - T_s - R_s && \text{(A.54)}\\
&= T\frac{1-T\mu^2-R\mu^4}{1-2R\mu^2\cos 2\phi + R^2\mu^4}. && \text{(A.55)}
\end{aligned}
$$

If we place lossless material, i.e. $\mu = 1$, $A_s = 0$, that implies the energy conservation low, i.e. $R_s + T_s = 1$. If we place perfect black body, i.e. $\mu = 0$, $R = 1 - T = 0$, we see $A_s = 1$.

Interestingly, even if we place high absorption material, $\mu = 1$, the absorptance dose not become unity, $A_s = T = 1 - R$. Therefore, although high absorptance material is used, we can not realize the perfect black body without anti-refection of black body, $R = 0$.

Appendix B

Emissivity at IR band

We measured the emissivity of the samples at 300 K by using a TSS-5X radiative thermometer made by Japan Sensor Corporation [95]. The frequency range of the radiative thermometer is from 14 to 150 THz. The emissivity was measured by using refraction at the sample surface. IR radiation is emitted from a hemispherical blackbody furnace attached to the sample, as shown in Figure B.2. This radiation is refracted at the sample surface in a manner that depends on the emissivity. This radiative thermometer is calibrated by using standard materials, with emissivities $\epsilon_h = 0.94$ and $\epsilon_l = 0.06$. The unknown emissivity ϵ_s is estimated by using the following equations:

$$P_h = (1 - \epsilon_h)F_0P_0 + \epsilon_h F_1 f(T_h), \tag{B.1}$$

$$P_l = (1 - \epsilon_l)F_0P_0 + \epsilon_l F_1 f(T_l), \tag{B.2}$$

$$P_s = (1 - \epsilon_s)F_0P_0 + \epsilon_s F_1 f(T_s), \tag{B.3}$$

where P_h, P_l, and P_s are the powers detected by the radiative thermometer. In each equation, the first term is the refracted power generated in the hemispherical blackbody furnace. This power is represented by the black solid arrow in Figure B.2. The second term is the gray body radiation from the sample surface. This power is represented by the dashed blue arrow in Figure B.2. The quantities F_0 and F_1 are constant geometrical factors. The samples were held at the same temperature, $T_h = T_l = T_s = 292$ K, and on an aluminum plate with emissivity of 0.14. Therefore, we can solve Equations (B.2-B.3) and estimate the unknown emissivity, ϵ_s. The results of these measurements are given in Table B.1.

Table B.1: Optical materials and emissivities. All measurements are at 300K.

Material	Emissivity	Material	Emissivity
Zotefoam	0.68	Expanded polystyrene	0.75
Alumina 99.5 %	0.78	Alumina 99.9 %	0.77
Alumina AJPF	0.79	Stiro form	0.58
Silicon	0.63	Amorphas Silicon	0.77
DP190	0.92	Stycast 2850 FTJ	0.93
PTFE	0.92	Metal mesh filter	0.68
Expanded UHMWPE	0.82	UHMWPE	0.95
Stycast2850FT	0.90	Stycast1090	0.91
Stycast2850GT	0.90	Cu	0.07
Aluminum	0.10	MLI	0.06
CR110	0.88	CR112	0.88
CR114	0.84	CR116	0.80
MLI with mesh	0.34	Eccosobe (AN72)	0.98
Eccosobe (HR10)	0.97	G-10	0.99
KEK black	0.98	Bock black	0.98
Kapton	0.83	Diamond like carbon	0.39
Phosblack	0.64	Rexolite	0.92
BSR-1	0.74	HR25	0.60
GDS	0.82	MCS	0.73
FGM-40	0.71	QR-13	0.89
LS-26	0.86	Nickel phosphorus	0.94
PM2020	0.90	PM23D	0.90
PM131	0.90	PM58P	0.90
PM15X	0.90	PM1010	0.90

Figure B.1: Measurement system and calibration samples.

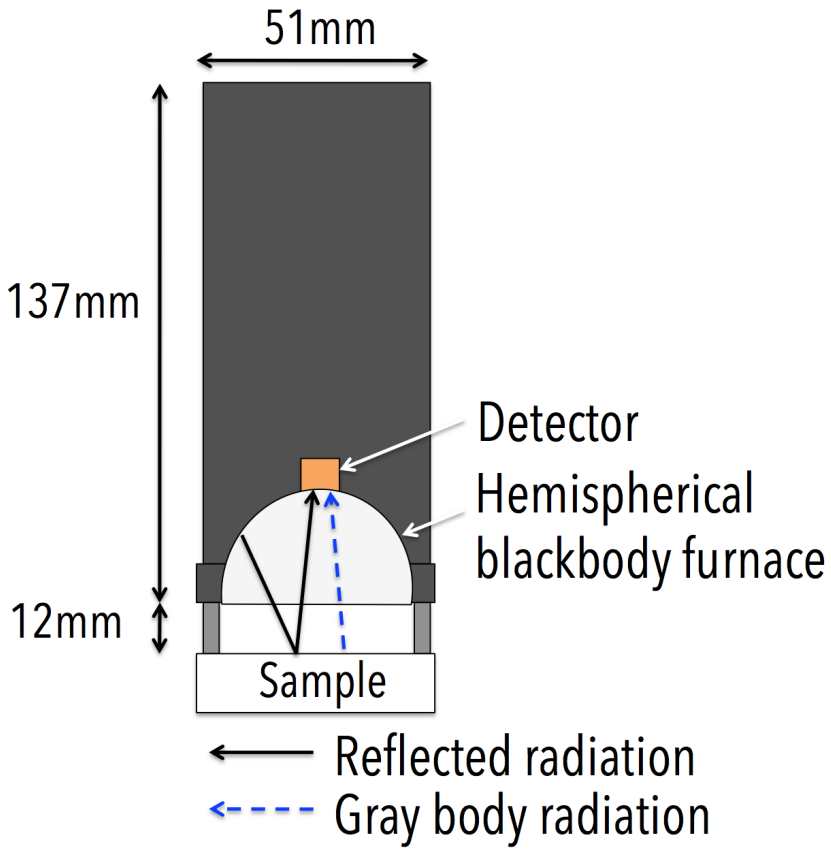

Figure B.2: Schematic of radiative thermometer. A hemispherical blackbody furnace is placed on the sample. The detector is mounted at the center of the blackbody furnace to measure the sum of the refracted power and the gray body radiation. The refracted radiation is emitted from the hemispherical blackbody furnace and refracted at the alumina surface. The gray body radiation is emitted at the sample surface. The detector was calibrated by using standard materials.

Appendix C

Alumina property

To facilitate the design of alumina optical elements, we discuss the thermal and optical properties of alumina.

C.1 Optical properties

C.1.1 Experiment

The IOR and the loss tangent in the sub-millimeter wavelength range were measured by using a Martin-Puplett Fourier transform spectrometer (FTS). A detailed description of this FTS is available elsewhere [86]. We measure the transmittance from 250 GHz to 1500 GHz at two different temperatures of 30 K and 300 K. We place the disc-shaped sample in the FTS system with crossing beam. Then, we measure the interferogram with the sample and reference, which is in this case atmosphere. The disk-shaped samples were 20 mm in diameter and either 2 mm and 5 mm in thickness.

C.1.1.1 Results

We Fourier-transformed interferograms of the sample and reference. The transmission spectra are calculated from the ratio between the Fourier-transformed interferogram of the sample and reference. The transmission spectra of 2 mm thick samples are shown in Figure C.1. We fit the IOR and the loss tangent using the spectral data with Equation (4.1) and determine the thickness d from the measured transmittance and the frequency ν. First, we estimate the IOR by using transmittance of 2 mm-thick sample. Secondly, the loss tangent was calculated by using transmittance of 5mm-thick samples with fixing the measured IOR. The corresponding IOR and the loss tangent are given in Figures C.2 and C.3.

C.1.2 Discussion

We measured the optical properties of alumina; i.e. the IOR and loss tangent between 70 GHz and 1.6 THz and emissivity between 14 and 150 THz . The IOR of the three samples is about 3.1-3.2 over

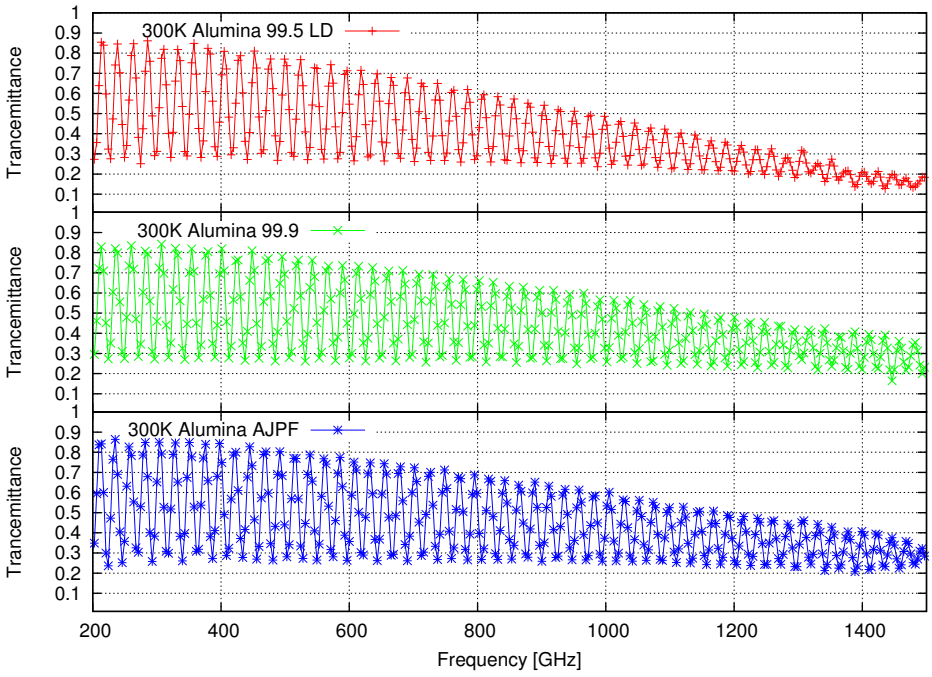

Figure C.1: Transmittances of the three types of alumina samples as a function of the frequency in a sub-millimeter range [17]. The 2-mm-thick sample is at 300 K for the measurement. The red, green and blue points correspond to alumina 99.5 LD, alumina 99.9 and alumina AJPF, respectively.

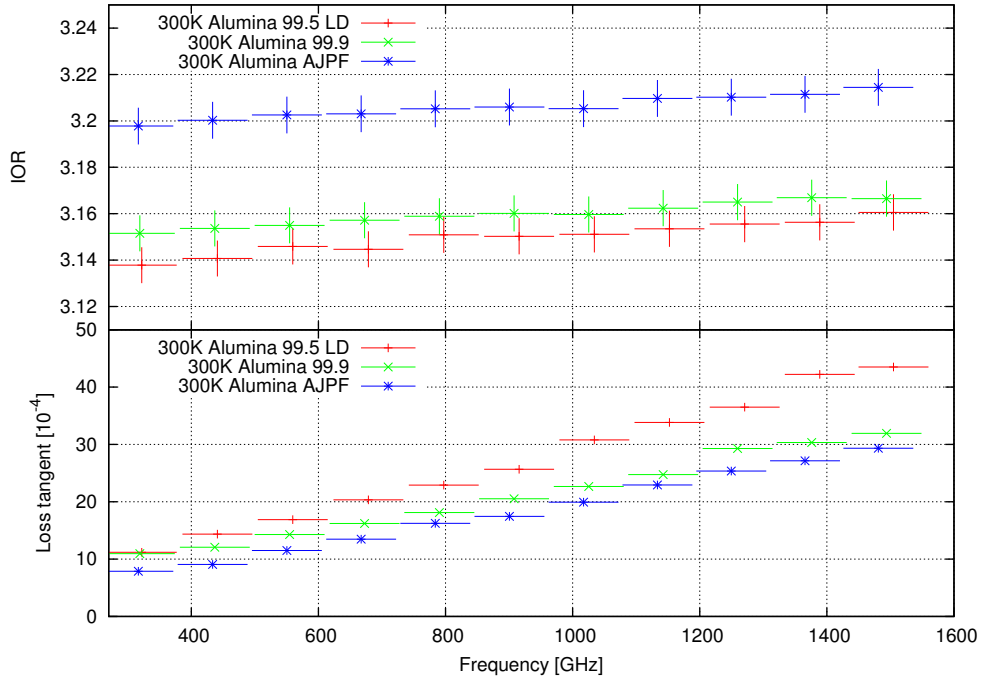

Figure C.2: IOR's (top) and loss tangents (bottom) as a function of the frequency in a sub-millimeter wave length range [17]. The samples are at 300 K for the measurements. The red, green and blue points correspond to alumina 99.5 LD, alumina 99.9, and alumina AJPF, respectively. The x and y error bars correspond to the binning width and statistical errors, respectively.

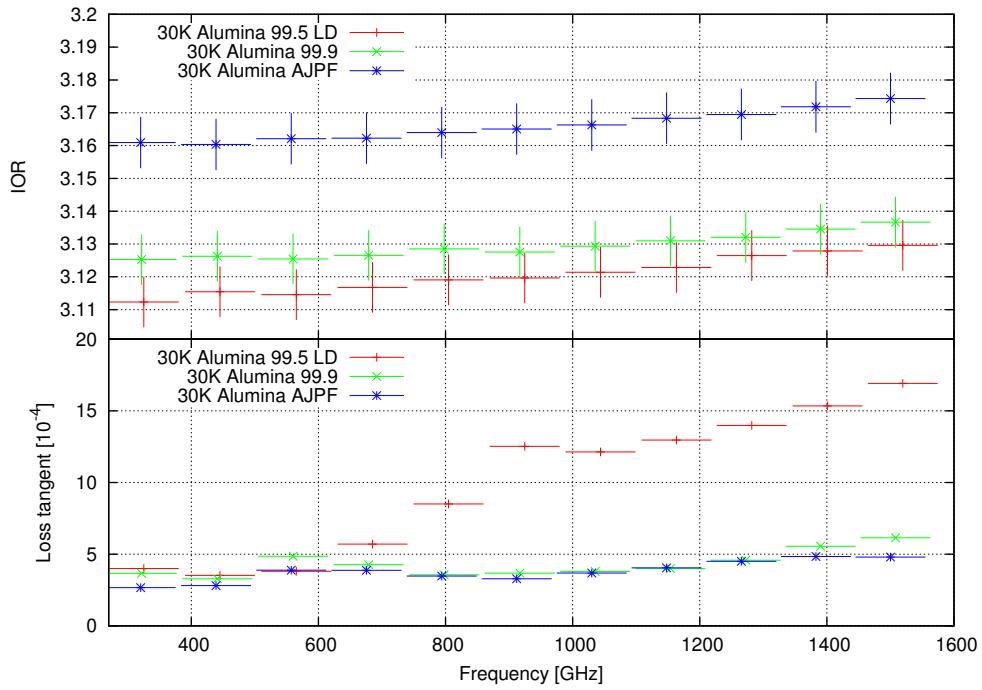

Figure C.3: Same as Figure 7 expect that the measurements are performed at 30 K [17].

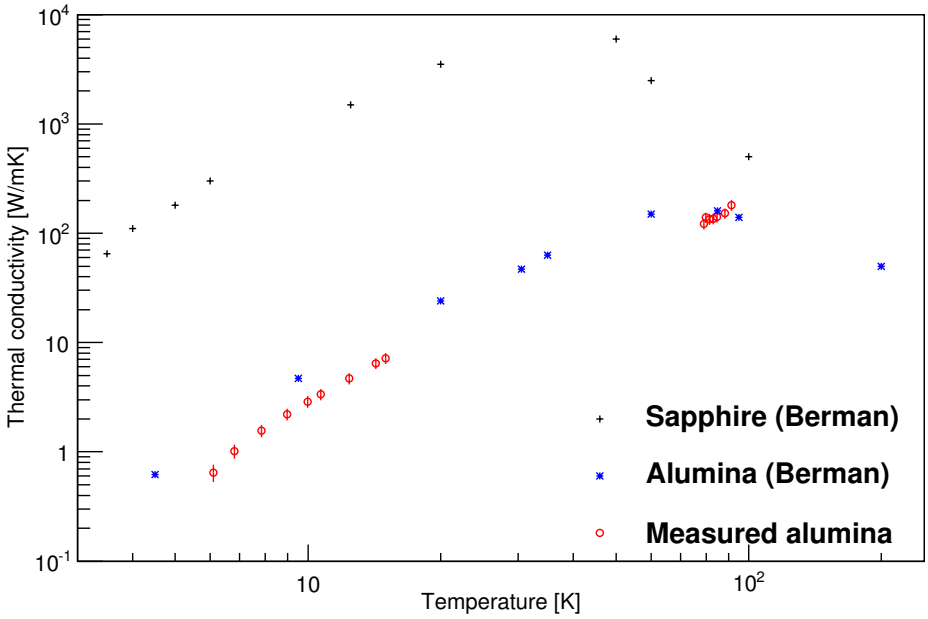

Figure C.4: Measured thermal conductivity of alumina 99.5 LD (red points) as a function of temperature. The error is the systematic error associated with the uncertainty in the length of the sample. The black and blue points are published results for thermal conductivity for sapphire crystals and alumina [97, 98]. The sapphire sample was a 3 mm single crystal, whereas the alumina used for the present study was polycrystalline.

the entire millimeter wavelength range. It is seen that the loss tangent of alumina AJPF is greater than those of alumina 99.5 LD and alumina 99.9. The optical properties of alumina do not depend on the sample direction. Alumina is polycrystalline, and is composed of small cells of sapphire with a typical size of a few μm. Since the crystal axis of each sapphire cell is random, bulk alumina has no crystal axis. The loss tangents at room temperature are less than those at cold temperatures in both the millimeter and sub-millimeter wavelength ranges.

The IoR increases as a function of frequency in the sub-millimeter wavelength range. Thus, this range is within the regime of normal dispersion. The loss tangent of alumina 99.5 becomes large as it approaches the sub-millimeter wavelength range, which we attribute to scattering from voids at the alumina surface because this length scale agrees with the scattering length in the sub-millimeter wavelength range. The IORs of alumina agree within the millimeter and sub-millimeter ranges. The IORs and loss tangents found in this study are consistent with published values [70].

The measured emissivities at 292 K are independent of purity and thickness. We estimated reflectance using 4-mm-thick samples of alumina 99.5 LD, alumina 99.9 and alumina AJPF at 14 and 150 THz. We obtain reflectance values of 0.22, 0.22 and 0.24, respectively. These values are consistent with published values [96].

C.2 Thermal properties

Alumina is known to be a polycrystalline, i.e. an alumina is a collection of small sapphire. The properties of alumina depend on its purity, crystal size and sintering conditions. In this section, we discuss the thermal conductivity of alumina at low temperature. Generally, the thermal conductivity depends on the mean free path in the material as follows:

$$\kappa = \frac{1}{3} c_v v l, \tag{C.1}$$

where c_v is the specific heat, v is the group velocity, and l is the mean free path. The specific heat is described by Debye's T^3 law ($c_v \sim T^3$). Therefore, the thermal conductivity of alumina is proportional to T^3. The thermal conductivity depends on the size effect and the Umklapp effect. the thermal conductivity of alumina at higher temperatures, (about 80 to 300 K) also depends on the Umklapp effect, which depends on the phonon scatterings [97, 99, 98]. The purity of alumina and its voids are one reason for such scattering. The measured thermal conductivity at 15 to 100 K therefore results from contributions of the size effect and the Umkapp effect.

However, at lower temperatures, $\sim$ 4 to 20 K, the Umklapp effect is suppressed and the thermal conductivity of alumina depends on the mean free path. When the size of sapphire crystal is larger than that of the mean free path, l become the mean free path of phonon in the crystal. The typical size of mean free path of the sapphire is about 1 mm. However, if the size of sapphire crystal is less than than that of the mean free path of phonon, the mean free path length is corresponding to crystal size. Since the alumina consists the small sapphires, the amplitude of thermal conductivity of an alumina is proportional to grain diameter of alumina [97, 99, 98].

Here,we measured the thermal conductivity of alumina between 4 K and 100 K as shown in Figure C.4. We over-plot the literature value of thermal conductivity of the sapphire and alumina sample [97, 99, 98]. Figure C.4 fits to the thermal conductivities between 4 K and 15 K. The fitting function is as follows:

$$\kappa = pT^q, \tag{C.2}$$

where T is temperature. The results are shown in Table C.1, where q is restricted within 2.7 ± 0.1. The published crystal size for sapphire is 3 mm, which is significantly larger than the mean free path of about 1 mm. Therefore, we can assume that the thermal conductivity of the sapphire is explained as the mean free path of the phonos perfectly. From the ratio between amplitude of sapphire and alumina thermal conductivity, the estimated crystal sizes of published alumina and measured alumina are 6.4 ± 0.2 μm and 3.2 ± 0.1 μm, which is at the same order of the value in Table 4.1 as well as in the literature. [98]

C.3 Conclusion

We measured the thermal and optical properties of aluminas. The thermal conductivity and IoR of alumina are greater than those of conventional millimeter wavelength optical elements. However, the

Table C.1: Best fits of thermal conductivity by assuming Debye model. We fitted the thermal conductivity as a function of temperature by using equation (C.2). The parameter q is restricted as $q = 2.7 \pm 0.1$. The mean free path of sample with a diameter of 3 mm is about 1 mm. We estimate the mean free path from the size effect.

Name	p	Mean free path [mm]
Sapphire (Berman)	$1.88^{+0.64}_{-0.42}$	1
Alumina (Berman)	$0.012^{+0.003}_{-0.0024}$	0.0064 ± 0.0002
Measured	$0.0060^{+0.0016}_{-0.0013}$	0.0032 ± 0.0001

thermal contraction and loss tangent are less than those of conventional optical elements. These properties mean that alumina may offer significant advantages for use as optical elements in future millimeter wavelength measurements.

Appendix D

Development of mirror

We developed and off-axis elliptical mirror for laboratory measurements as shown in Fig. D.1. The elliptical mirror can change the focus from the Gregorian focus point to out of the receiver as shown in Fig. 8.12. The requirement of the mirror diameter is larger than 700 mm for covering beams sufficiently. We designed the mirror shape using ZEMAX. The material of the mirror is Al5083 because of the high durability. Of course, the return loss of high purity material is less than that of low purity material. However, we decide the high durability material. The surface of the mirror is machined with a ball end mill. Figure D.2 shows the milling machine. In order to reduce the deformation due to the cutting heat, the mirror is cooled with water during the machining.

We measure the surface shape using CMM. The result of the measurement is shown in Fig. D.3. Figure D.4 shows the difference between the designed and measured value. The measured roughness is 0.125 mm. Since the requirement of roughness is 0.6 mm, the measured value meets our requirement.

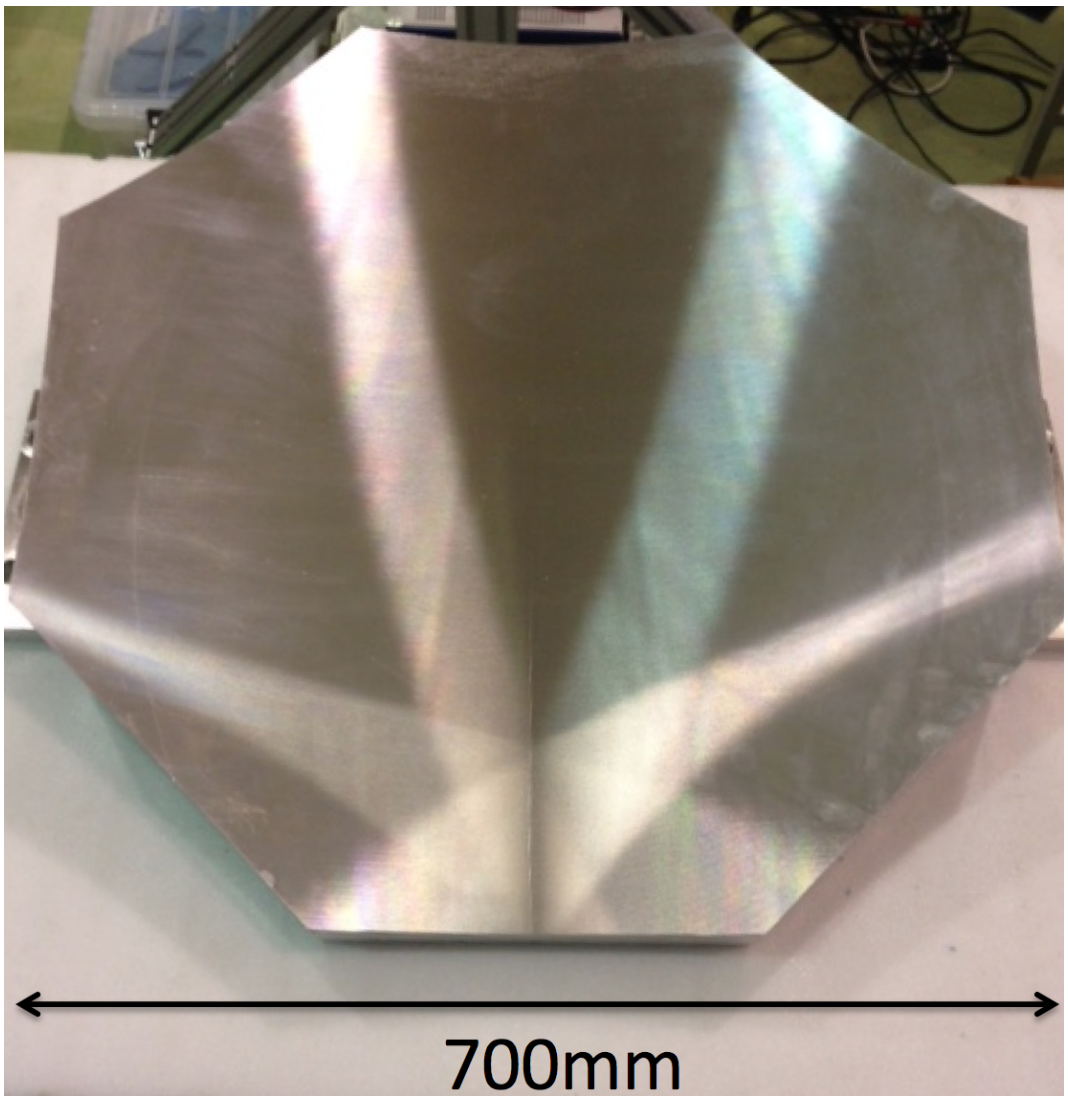

Figure D.1: The designed mirror for laboratory tests .The diameter of the mirror is corresponding to the beam size.

Figure D.2: The milling machine with a ball end mill.

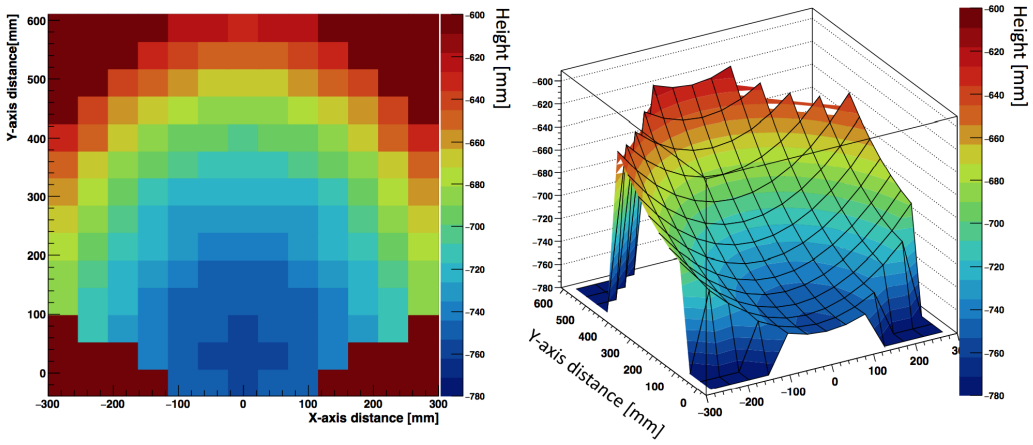

Figure D.3: The results of surface measurement with CMM.

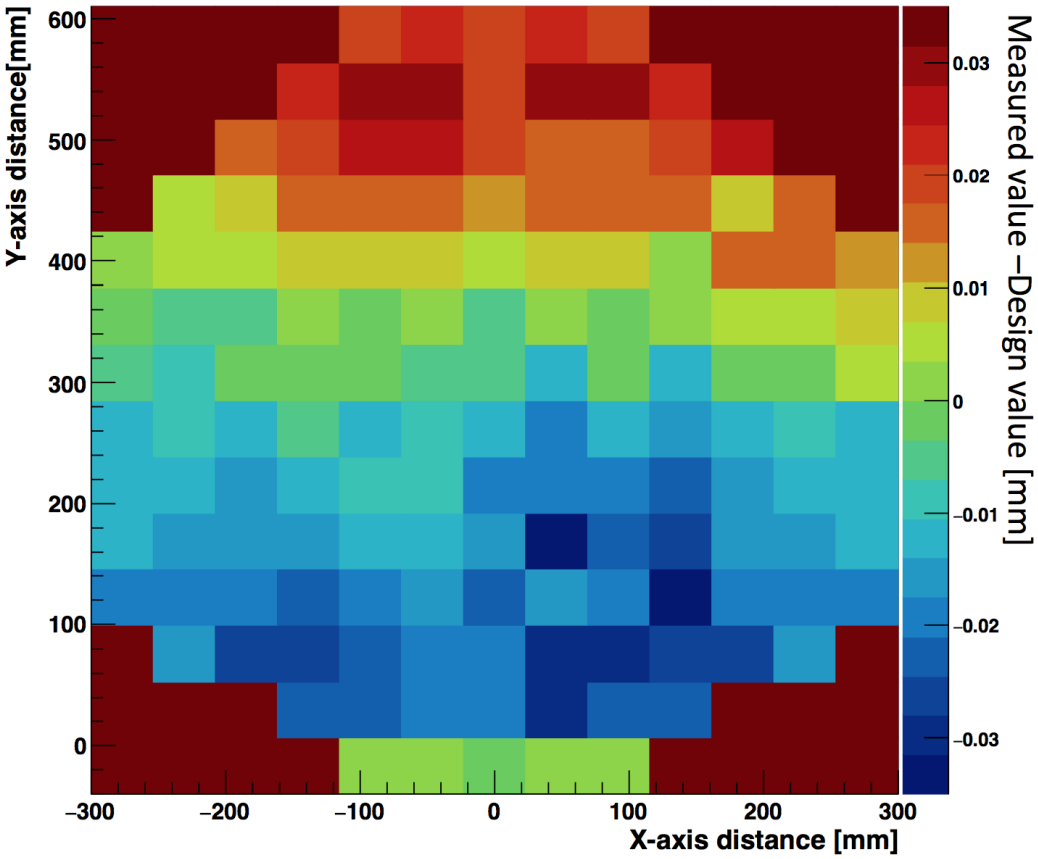

Figure D.4: The thickness difference between the designed and measured value.

Bibliography

[1] C.L. Bennett, D. Larson, J.L. Weiland, N. Jarosik, G. Hinshaw, et al. Nine-Year Wilkinson Microwave Anisotropy Probe (WMAP) Observations: Final Maps and Results. 2012.

[2] E.S. Walker, I.M. Hook, M. Sullivan, D.A. Howell, P. Astier, et al. Supernova Legacy Survey: Using Spectral Signatures To Improve Type Ia Supernovae As Distance Indicators. 2010.

[3] G. Hinshaw, D. Larson, E. Komatsu, D.N. Spergel, C.L. Bennett, et al. Nine-Year Wilkinson Microwave Anisotropy Probe (WMAP) Observations: Cosmological Parameter Results. 2012.

[4] K. Sato. First Order Phase Transition of a Vacuum and Expansion of the Universe. *Mon.Not.Roy.Astron.Soc.*, 195:467–479, 1981.

[5] Alan H. Guth. The Inflationary Universe: A Possible Solution to the Horizon and Flatness Problems. *Phys.Rev.*, D23:347–356, 1981.

[6] Andrei D. Linde. CHAOTIC INFLATION. 1988.

[7] K. N. Abazajian et al. Inflation Physics from the Cosmic Microwave Background and Large Scale Structure. *Astropart. Phys.*, 63:55–65, 2015.

[8] Timothe Delubac et al. Baryon acoustic oscillations in the Ly alpha forest of BOSS DR11 quasars. *Astron. Astrophys.*, 574:A59, 2015.

[9] P. A. R. Ade, Y. Akiba, A. E. Anthony, K. Arnold, M. Atlas, D. Barron, D. Boettger, J. Borrill, C. Borys, S. Chapman, Y. Chinone, M. Dobbs, T. Elleflot, J. Errard, G. Fabbian, C. Feng, D. Flanigan, A. Gilbert, W. Grainger, N. W. Halverson, M. Hasegawa, K. Hattori, M. Hazumi, W. L. Holzapfel, Y. Hori, J. Howard, P. Hyland, Y. Inoue, G. C. Jaehnig, A. Jaffe, B. Keating, Z. Kermish, R. Keskitalo, T. Kisner, M. Le Jeune, A. T. Lee, E. M. Leitch, E. Linder, M. Lungu, F. Matsuda, T. Matsumura, X. Meng, N. J. Miller, H. Morii, S. Moyerman, M. J. Myers, M. Navaroli, H. Nishino, H. Paar, J. Peloton, D. Poletti, E. Quealy, G. Rebeiz, C. L. Reichardt, P. L. Richards, C. Ross, K. Rotermund, I. Schanning, D. E. Schenck, B. D. Sherwin, A. Shimizu, C. Shimmin, M. Shimon, P. Siritanasak, G. Smecher, H. Spieler, N. Stebor, B. Steinbach, R. Stompor, A. Suzuki,

S. Takakura, A. Tikhomirov, T. Tomaru, B. Wilson, A. Yadav, and O. Zahn. Evidence for gravitational lensing of the cosmic microwave background polarization from cross-correlation with the cosmic infrared background. *Phys. Rev. Lett.*, 112:131302, Apr 2014.

[10] Antony Lewis and Anthony Challinor. Weak gravitational lensing of the cmb. *Phys.Rept.*, 429:1–65, 2006.

[11] K. N. Abazajian et al. Neutrino Physics from the Cosmic Microwave Background and Large Scale Structure. *Astropart. Phys.*, 63:66–80, 2015.

[12] Wayne Hu and Martin J. White. A CMB polarization primer. *New Astron.*, 2:323, 1997.

[13] Wayne Hu. CMB temperature and polarization anisotropy fundamentals. *Annals Phys.*, 303:203–225, 2003.

[14] Uros ˘ Seljak and Matias Zaldarriaga. Signature of gravity waves in the polarization of the microwave background. *Phys. Rev. Lett.*, 78:2054–2057, Mar 1997.

[15] P. A. R. Ade et al. BICEP2 / Keck Array VI: Improved Constraints On Cosmology and Foregrounds When Adding 95 GHz Data From Keck Array. 2015.

[16] Takayuki Tomaru et al. POLARBEAR-2 Experiment. *Proc.SPIE*, 2012.

[17] Y. Inoue, N. Stebor, P. A. R. Ade, Y. Akiba, K. Arnold, A. E. Anthony, M. Atlas, D. Barron, A. Bender, D. Boettger, J. Borrilll, S. Chapman, Y. Chinone, A. Cukierman, M. Dobbs, T. Elleflot, J. Errard, G. Fabbian, C. Feng, A. Gilbert, N. W. Halverson, M. Hasegawa, K. Hattori, M. Hazumi, W. L. Holzapfel, Y. Hori, G. C. Jaehnig, A. H. Jaffe, N. Katayama, B. Keating, Z. Kermish, Reijo Keskitalo, T. Kisner, M. Le Jeune, A. T. Lee, E. M. Leitch, E. Linder, F. Matsuda, T. Matsumura, X. Meng, H. Morii, M. J. Myers, M. Navaroli, H. Nishino, T. Okamura, H. Paar, J. Peloton, D. Poletti, G. Rebeiz, C. L. Reichardt, P. L. Richards, C. Ross, D. E. Schenck, B. D. Sherwin, P. Siritanasak, G. Smecher, M. Sholl, B. Steinbach, R. Stompor, A. Suzuki, J. Suzuki, S. Takada, S. Takakura, T. Tomaru, B. Wilson, A. Yadav, H. Yamaguchi, and O. Zahn. Thermal and optical characterization for polarbear-2 optical system, 2014.

[18] Yuki Inoue, Tomotake Matsumura, Masashi Hazumi, Adrian T. Lee, Takahiro Okamura, Aritoki Suzuki, Takayuki Tomaru, and Hiroshi Yamaguchi. Cryogenic infrared filter made of alumina for use at millimeter wavelength. *Appl. Opt.*, 53:1727, 2014.

[19] TICRA. GRASP. `http://www.ticra.com/products/software/grasp`.

[20] Scott Dodelson. *Modern Cosmology*. Academic Press, 2003.

[21] Ariel G. Sanchez, C.G. Scoccola, A.J. Ross, W. Percival, M. Manera, et al. The clustering of galaxies in the SDSS-III Baryon Oscillation Spectroscopic Survey: cosmological implications of the large-scale two-point correlation function. 2012.

[22] M. Sullivan, J. Guy, A. Conley, N. Regnault, P. Astier, et al. SNLS3: Constraints on Dark Energy Combining the Supernova Legacy Survey Three Year Data with Other Probes. *Astrophys.J.*, 737:102, 2011.

[23] A. Conley, J. Guy, M. Sullivan, N. Regnault, P. Astier, et al. Supernova Constraints and Systematic Uncertainties from the First 3 Years of the Supernova Legacy Survey. *Astrophys.J.Suppl.*, 192:1, 2011.

[24] Ruth Durrer. *The Cosmic Microwave Background.* Cambridge, 2008.

[25] NASA. LAMBDA. `http://lambda.gsfc.nasa.gov/product/`.

[26] D.J. Fixsen, E.S. Cheng, J.M. Gales, John C. Mather, R.A. Shafer, et al. The Cosmic Microwave Background spectrum from the full COBE FIRAS data set. *Astrophys.J.*, 473:576, 1996.

[27] P. A. R. Ade et al. Planck 2015 results. XIII. Cosmological parameters. 2015.

[28] Andrei D. Linde. A New Inflationary Universe Scenario: A Possible Solution of the Horizon, Flatness, Homogeneity, Isotropy and Primordial Monopole Problems. *Phys.Lett.*, B108:389–393, 1982.

[29] Hideo Kodama and Misao Sasaki. Cosmological Perturbation Theory. *Prog.Theor.Phys.Suppl.*, 78:1–166, 1984.

[30] David H. Lyth. What would we learn by detecting a gravitational wave signal in the cosmic microwave background anisotropy? *Phys. Rev. Lett.*, 78:1861–1863, 1997.

[31] Eugene Hecht. *Optics (4th Edition).* Addison-Wesley, 2001.

[32] The Polarbear Collaboration: P. A. R. Ade, Y. Akiba, A. E. Anthony, K. Arnold, M. Atlas, D. Barron, D. Boettger, J. Borrill, S. Chapman, Y. Chinone, M. Dobbs, T. Elleflot, J. Errard, G. Fabbian, C. Feng, D. Flanigan, A. Gilbert, W. Grainger, N. W. Halverson, M. Hasegawa, K. Hattori, M. Hazumi, W. L. Holzapfel, Y. Hori, J. Howard, P. Hyland, Y. Inoue, G. C. Jaehnig, A. H. Jaffe, B. Keating, Z. Kermish, R. Keskitalo, T. Kisner, M. Le Jeune, A. T. Lee, E. M. Leitch, E. Linder, M. Lungu, F. Matsuda, T. Matsumura, X. Meng, N. J. Miller, H. Morii, S. Moyerman, M. J. Myers, M. Navaroli, H. Nishino, A. Orlando, H. Paar, J. Peloton, D. Poletti, E. Quealy, G. Rebeiz, C. L. Reichardt, P. L. Richards, C. Ross, I. Schanning, D. E. Schenck, B. D. Sherwin, A. Shimizu, C. Shimmin, M. Shimon, P. Siritanasak, G. Smecher, H. Spieler, N. Stebor, B. Steinbach, R. Stompor, A. Suzuki, S. Takakura, T. Tomaru, B. Wilson, A. Yadav, and O. Zahn. A measurement of the cosmic microwave background b-mode polarization power spectrum at sub-degree scales with polarbear. *The Astrophysical Journal*, 794(2):171, 2014.

[33] LiteBIRD. `http://litebird.jp`.

[34] B. P. Abbott and et al. Observation of gravitational waves from a binary black hole merger. *Phys. Rev. Lett.*, 116:061102, Feb 2016.

[35] Robert Crittenden, Richard L. Davis, and Paul J. Steinhardt. Polarization of the microwave background due to primordial gravitational waves. *Astrophys.J.*, 417:L13–L16, 1993.

[36] E. M. George et al. A measurement of secondary cosmic microwave background anisotropies from the 2500-square-degree SPT-SZ survey. *Astrophys. J.*, 799(2):177, 2015.

[37] Sudeep Das, Blake D. Sherwin, Paula Aguirre, John W. Appel, J. Richard Bond, et al. Detection of the Power Spectrum of Cosmic Microwave Background Lensing by the Atacama Cosmology Telescope. *Phys.Rev.Lett.*, 107:021301, 2011.

[38] CAMB. CAMB. `http://camb.info`.

[39] B. Aharmim, S. N. Ahmed, J. F. Amsbaugh, A. E. Anthony, J. Banar, N. Barros, E. W. Beier, A. Bellerive, B. Beltran, M. Bergevin, S. D. Biller, K. Boudjemline, M. G. Boulay, T. J. Bowles, M. C. Browne, T. V. Bullard, T. H. Burritt, B. Cai, Y. D. Chan, D. Chauhan, M. Chen, B. T. Cleveland, G. A. Cox-Mobrand, C. A. Currat, X. Dai, H. Deng, J. Detwiler, M. DiMarco, P. J. Doe, G. Doucas, P.-L. Drouin, C. A. Duba, F. A. Duncan, M. Dunford, E. D. Earle, S. R. Elliott, H. C. Evans, G. T. Ewan, J. Farine, H. Fergani, F. Fleurot, R. J. Ford, J. A. Formaggio, M. M. Fowler, N. Gagnon, J. V. Germani, A. Goldschmidt, J. T. M. Goon, K. Graham, E. Guillian, S. Habib, R. L. Hahn, A. L. Hallin, E. D. Hallman, A. A. Hamian, G. C. Harper, P. J. Harvey, R. Hazama, K. M. Heeger, W. J. Heintzelman, J. Heise, R. L. Helmer, R. Henning, A. Hime, C. Howard, M. A. Howe, M. Huang, P. Jagam, B. Jamieson, N. A. Jelley, K. J. Keeter, J. R. Klein, L. L. Kormos, M. Kos, A. Krüger, C. Kraus, C. B. Krauss, T. Kutter, C. C. M. Kyba, R. Lange, J. Law, I. T. Lawson, K. T. Lesko, J. R. Leslie, J. C. Loach, R. MacLellan, S. Majerus, H. B. Mak, J. Maneira, R. Martin, K. McBryde, N. McCauley, A. B. McDonald, S. McGee, C. Mifflin, G. G. Miller, M. L. Miller, B. Monreal, J. Monroe, B. Morissette, A. Myers, B. G. Nickel, A. J. Noble, N. S. Oblath, H. M. O'Keeffe, R. W. Ollerhead, G. D. Orebi Gann, S. M. Oser, R. A. Ott, S. J. M. Peeters, A. W. P. Poon, G. Prior, S. D. Reitzner, K. Rielage, B. C. Robertson, R. G. H. Robertson, E. Rollin, M. H. Schwendener, J. A. Secrest, S. R. Seibert, O. Simard, J. J. Simpson, L. Sinclair, P. Skensved, M. W. E. Smith, T. D. Steiger, L. C. Stonehill, G. Tešić, P. M. Thornewell, N. Tolich, T. Tsui, C. D. Tunnell, T. Van Wechel, R. Van Berg, B. A. VanDevender, C. J. Virtue, T. J. Walker, B. L. Wall, D. Waller, H. Wan Chan Tseung, J. Wendland, N. West, J. B. Wilhelmy, J. F. Wilkerson, J. R. Wilson, J. M. Wouters, A. Wright, M. Yeh, F. Zhang, and K. Zuber. Independent measurement of the total active ^{8}B solar neutrino flux using an array of ^{3}He proportional counters at the sudbury neutrino observatory. *Phys. Rev. Lett.*, 101:111301, Sep 2008.

[40] P. Adamson et al. Measurement of Neutrino Oscillations with the MINOS Detectors in the NuMI Beam. *Phys. Rev. Lett.*, 101:131802, 2008.

[41] LLoyd Knox. Determination of inflationary observables by cosmic microwave background anisotropy experiments. *Phys. Rev.*, D52:4307–4318, 1995.

[42] Meir Shimon, Brian Keating, Nicolas Ponthieu, and Eric Hivon. CMB Polarization Systematics Due to Beam Asymmetry: Impact on Inflationary Science. *Phys. Rev.*, D77:083003, 2008.

[43] Zigmund David Kermish. *The POLARBEAR Experiment: Design and Characterization.* Ph.D., University of California, Berkeley, 2012.

[44] Yuki Inoue et al. Polarbear-2:an instrument for cmb polarization measurements, 2016.

[45] A. Suzuki, K. Arnold, J. Edwards, G. Engargiola, W. Holzapfel, B. Keating, A.T. Lee, X.F. Meng, M.J. Myers, R. O.Brient, E. Quealy, G. Rebeiz, P.L. Richards, D. Rosen, and P. Siritanasak. Multichroic dual-polarization bolometric detectors for studies of the cosmic microwave background. *Journal of Low Temperature Physics*, 176(5-6):650–656, 2014.

[46] N Stebor et al. The simons array cmb polarization experiment, 2016.

[47] Cryomec. PT415. `http://www.cryomech.com/products/cryorefrigerators/pulse-tube/pt415/`.

[48] Chase Cryogenics. He10 sorption cyocooler. `http://www.chasecryogenics.com`.

[49] SUMITOMO CHEMICAL. SUMITOMO CHEMICAL. `http://www.sumitomo-chem.co.jp`.

[50] Mitsubishi material. Mitsubishi material. `http://www.mmc.co.jp/corporate/en/`.

[51] KANEKA. KANEKA. `http://www.kaneka.co.jp`.

[52] T. Matsumura et al. POLARBEAR-2 optical and polarimeter design. *SPIE*, 2012.

[53] TICRA. QUAST. `http://www.ticra.com/products/software/grasp/quasi-optical-design-and-analysis-add`.

[54] Zotefoams plc. High Density Polyethylene Foam Property Data Sheet. `http://www.zotefoams.com/pages/de/datasheets/hd30.htm`.

[55] J. Choi, H. Ishitsuka, S. Mima, S. Oguri, K. Takahashi, and O. Tajima. Radio-transparent multilayer insulation for radiowave receivers. *Rev. Sci. Instrum.*, 84:114502, 2013.

[56] Peter A. R. Ade, Giampaolo Pisano, Carole Tucker, and Samuel Weaver. A review of metal mesh filters, 2006.

[57] Emerson and Cuming. Emerson and Cuming. `http://www.emersoncuming.com`.

[58] Mitsubishi carbon black. Mitsubishi carbon black #10. `http://www.carbonblack.jp/product/tokucho.html`.

[59] MOGU company. MOGU company. `http://mogus.jp`.

[60] Kaori Hattori et al. Adaptation of frequency-domain readout for Transition Edge Sensor bolometers for the POLARBEAR-2 Cosmic Microwave Background experiment. *Nucl. Instrum. Meth.*, A732:299–302, 2013.

[61] Darcy Barron, Matt Atlas, Brian Keating, Ron Quillin, Nathan Stebor, and Brandon Wilson. Performance of a 4 Kelvin pulse-tube cooled cryostat with dc SQUID amplifiers for bolometric detector testing. 2013.

[62] 香里 服部, Kam Arnold, and 祥希 秋葉. 招待講演周波数分割信号多重化による tes ボロメータアレイ読み出　システムの開発 (超伝導エレクトロニクス). 電子情報通信学会技術研究報告 = *IEICE technical report :* 信学技報, 115(242):23–28, oct 2015.

[63] D. Barron, P. A. R. Ade, Y. Akiba, C. Aleman, K. Arnold, M. Atlas, A. Bender, J. Borrill, S. Chapman, Y. Chinone, A. Cukierman, M. Dobbs, T. Elleflot, J. Errard, G. Fabbian, G. Feng, A. Gilbert, N. W. Halverson, M. Hasegawa, K. Hattori, M. Hazumi, W. L. Holzapfel, Y. Hori, Y. Inoue, G. C. Jaehnig, N. Katayama, B. Keating, Z. Kermish, R. Keskitalo, T. Kisner, M. Le Jeune, A. T. Lee, F. Matsuda, T. Matsumura, H. Morii, M. J. Myers, M. Navroli, H. Nishino, T. Okamura, J. Peloton, G. Rebeiz, C. L. Reichardt, P. L. Richards, C. Ross, M. Sholl, P. Siritanasak, G. Smecher, N. Stebor, B. Steinbach, R. Stompor, A. Suzuki, J. Suzuki, S. Takada, T. Takakura, T. Tomaru, B. Wilson, H. Yamaguchi, and O. Zahn. Development and characterization of the readout system for polarbear-2, 2014.

[64] Tijmen de Haan, Graeme Smecher, and Matt Dobbs. Improved performance of tes bolometers using digital feedback, 2012.

[65] Shaul Hanany, Michael D. Niemack, and Lyman Page. Cmb telescopes and optical systems. In TerryD. Oswalt and IanS. McLean, editors, *Planets, Stars and Stellar Systems*, pages 431–480. Springer Netherlands, 2013.

[66] R. W. Ogburn IV, P. A. R. Ade, R. W. Aikin, M. Amiri, S. J. Benton, J. J. Bock, J. A. Bonetti, J. A. Brevik, B. Burger, C. D. Dowell, L. Duband, J. P. Filippini, S. R. Golwala, M. Halpern, M. Hasselfield, G. Hilton, V. V. Hristov, K. Irwin, J. P. Kaufman, B. G. Keating, J. M. Kovac, C. L. Kuo, A. E. Lange, E. M. Leitch, C. B. Netterfield, H. T. Nguyen, A. Orlando, C. L. Pryke, C. Reintsema, S. Richter, J. E. Ruhl, M. C. Runyan, C. D. Sheehy, Z. K. Staniszewski, S. A. Stokes, R. V. Sudiwala, G. P. Teply, J. E. Tolan, A. D. Turner, P. Wilson, and C. L. Wong. The bicep2 cmb polarization experiment, 2010.

[67] Z. Kermish, P. Ade, A. Anthony, K. Arnold, K. Arnold, et al. The POLARBEAR Experiment. 2012.

[68] Britt Reichborn-Kjennerud, Asad M. Aboobaker, Peter Ade, Francois Aubin, Carlo Baccigalupi, Chaoyun Bao, Julian Borrill, Christopher Cantalupo, Daniel Chapman, Joy Didier, Matt Dobbs,

Julien Grain, William Grainger, Shaul Hanany, Seth Hillbrand, Johannes Hubmayr, Andrew Jaffe, Bradley Johnson, Terry Jones, Theodore Kisner, Jeff Klein, Andrei Korotkov, Sam Leach, Adrian Lee, Lorne Levinson, Michele Limon, Kevin MacDermid, Tomotake Matsumura, Xiaofan Meng, Amber Miller, Michael Milligan, Enzo Pascale, Daniel Polsgrove, Nicolas Ponthieu, Kate Raach, Ilan Sagiv, Graeme Smecher, Federico Stivoli, Radek Stompor, Huan Tran, Matthieu Tristram, Gregory S. Tucker, Yury Vinokurov, Amit Yadav, Matias Zaldarriaga, and Kyle Zilic. Ebex: a balloon-borne cmb polarization experiment, 2010.

[69] J. M. Lau et al. A millimeter-wave antireflection coating for cryogenic silicon lenses. *Appl. Opt.*, 45:3746–3751, 2006.

[70] James W. Lamb. Miscellaneous data on materials for millimetre and submillimetre optics. *International Journal of Infrared and Millimeter Waves*, 17(12):1997–2034, December 1996.

[71] Nihon Ceratech. Nihon Ceratech. `http://www.ceratech.co.jp`.

[72] The part number and output frequency of synthesized frequency generator are Agillent 83711B and 12-18 GHz, respectively. The frequency multiplier is made by AmTechs Corporation.

[73] NI DAQ. NI USB-6212. `http://www.ni.com/en-us.html`.

[74] Darin Rosen, Aritoki Suzuki, Brian Keating, William Krantz, Adrian T. Lee, Erin Quealy, Paul L. Richards, Praween Siritanasak, and William Walker. Epoxy-based broadband anti-reflection coating for millimeter-wave optics. *Appl. Opt.*, 52:8102, 2013.

[75] ZEISS UPMC. ZEISS UPMC. `http://www.hi-top.com.tw/TSK/UPMC.pdf`.

[76] Jordan D. Wheeler, Brian Koopman, Patricio Gallardo, Philip R. Maloney, Spencer Brugger, German Cortes-Medellin, Rahul Datta, C. Darren Dowell, Jason Glenn, Sunil Golwala, Chris McKenney, Jeffery J. McMahon, Charles D. Munson, Mike Niemack, Stephen Parshley, and Gordon Stacey. Antireflection coatings for submillimeter silicon lenses, 2014.

[77] Tomotake Matsumura, Karl Young, Qi Wen, Shaul Hanany, Hirokazu Ishino, Yuki Inoue, Masashi Hazumi, Jürgen Koch, Oliver Suttman, and Viktor Schütz. Millimeter-wave broadband antireflection coatings using laser ablation of subwavelength structures. *Appl. Opt.*, 55(13):3502–3509, May 2016.

[78] S. Bryan. Half-wave Plates for the Spider Cosmic Microwave Background Polarimeter. *ArXiv e-prints*, February 2014.

[79] Aritoki Suzuki. *Multichroic Bolometric Detector Architecture for Cosmic Microwave Background Polarimetry Experiments.* Ph.D., University of California, Berkeley, 2013.

[80] Tocalo. Tocalo. `http://www.tocalo.co.jp`.

[81] Ohad Levy and David Stroud. Maxwell garnett theory for mixtures of anisotropic inclusions: Application to conducting polymers. *Phys. Rev. B*, 56:8035–8046, Oct 1997.

[82] IST. IST. http://www.istcorp.jp/.

[83] Ohad Levy and David Stroud. Maxwell garnett theory for mixtures of anisotropic inclusions: Application to conducting polymers. *Phys. Rev. B*, 56:8035–8046, Oct 1997.

[84] Aritoki Suzuki, Kam Arnold, Jennifer Edwards, Greg Engargiola, Adnan Ghribi, et al. Multi-chroic dual-polarization bolometric detectors for studies of the Cosmic Microwave Background. *Proc.SPIE*, 2012.

[85] Z. Ahmed et al. BICEP3: a 95GHz refracting telescope for degree-scale CMB polarization. *Proc. SPIE Int. Soc. Opt. Eng.*, 9153:91531N, 2014.

[86] Satoki Matsushita and Hiroshi Matsuo. FTS measurements of submillimeter - wave atmospheric opacity at Pampa la Bola 3. Water vapor, liquid water, and 183 GHz water vapor line opacities. *Publ. Astron. Soc. Jap.*, 55:325–333, 2003.

[87] NIST. Cryogenics Material Properties. http://cryogenics.nist.gov/MPropsMAY/.

[88] Mills A.F. *Heat transfer second edition* . Prentice Hall, 1999.

[89] J.J. Bock. *Rocket-Borne Observation of Singly Ionized Carbon 158um Emission from the Diffuse Interstellar Medium.* Ph.D., University of California, Berkeley, 1994.

[90] B. A. Benson et al. SPT-3G: A Next-Generation Cosmic Microwave Background Polarization Experiment on the South Pole Telescope. *Proc. SPIE Int. Soc. Opt. Eng.*, 9153:91531P, 2014.

[91] M. D. Niemack, P. A. R. Ade, J. Aguirre, F. Barrientos, J. A. Beall, J. R. Bond, J. Britton, H. M. Cho, S. Das, M. J. Devlin, S. Dicker, J. Dunkley, R. Dunner, J. W. Fowler, A. Hajian, M. Halpern, M. Hasselfield, G. C. Hilton, M. Hilton, J. Hubmayr, J. P. Hughes, L. Infante, K. D. Irwin, N. Jarosik, J. Klein, A. Kosowsky, T. A. Marriage, J. McMahon, F. Menanteau, K. Moodley, J. P. Nibarger, M. R. Nolta, L. A. Page, B. Partridge, E. D. Reese, J. Sievers, D. N. Spergel, S. T. Staggs, R. Thornton, C. Tucker, E. Wollack, and K. W. Yoon. Actpol: a polarization-sensitive receiver for the atacama cosmology telescope, 2010.

[92] P. L. Richards. Bolometers for infrared and millimeter waves. *Journal of Applied Physics*, 76(1), 1994.

[93] Mario González-Cardel, Pedro Arguijo, and Rufino Díaz-Uribe. Gaussian beam radius measurement with a knife-edge: a polynomial approximation to the inverse error function. *Appl. Opt.*, 52(16):3849–3855, Jun 2013.

[94] T. Matsumura et al. Mission design of LiteBIRD. 2013.

[95] TSS-5X. TSS-5X. http://www.japansensor.co.jp/products/TSS-5X.html.

[96] T. S. Eriksson, A. Hjortsberg, G. A. Niklasson, and C. G. Granqvist. Infrared optical properties of evaporated alumina films. *Appl. Opt.*, 20(15):2742–2746, Aug 1981.

[97] R. Berman. The thermal conductivity of dielectric solids at low temperatures. *Advances in Physics*, 2(5):103–140, 1953.

[98] R Berman. The thermal conductivity of some polycrystalline solids at low temperatures. *Proceedings of the Physical Society. Section A*, 65(12):1029, 1952.

[99] P. G. Klemens. The thermal conductivity of dielectric solids at low temperatures (theoretical). *Proceedings of the Royal Society of London A: Mathematical, Physical and Engineering Sciences*, 208(1092):108–133, 1951.